Development of a novel targeted nanotherapy for the treatment of melanoma

by

Carl. A. Webster

A thesis submitted in partial fulfilment for the degree of Doctor of Philosophy

in the

Faculty of Science

School of Pharmacy

2016

For Sophie

Declaration of authorship

I declare that the work in this thesis submitted by me for the degree of Doctor of Philosophy is my work, except where due reference is made to other authors, and has not been previously submitted by me for a degree at this or any other university.

Carl. A. Webster

I. Abstract

Nanoparticles have been utilised in a wide range of applications and they provide unique advantages as drug delivery carriers and imaging agents in biomedicine. In particular, nanoparticles have been employed as therapeutic systems in oncology to overcome the limitations of conventional chemotherapeutics.

Melanoma is the cancer of pigment-producing cells in the basal layer of the epidermis. Once metastasised, melanoma is highly aggressive and notoriously difficult to treat with the currently available therapies. In order to improve the therapeutic options available for the treatment of melanoma, we developed iron oxide nanoparticles for use as a melanoma-specific drug delivery system. Iron oxide nanoparticles are useful tools in oncology as their superparamagnetic properties allow them to be used as a delivery system capable of acting as both an imaging contrast agent and a magnetic hyperthermia therapy agent.

Here, we developed a targeted iron oxide nanoparticle that exploits the overexpression of melanocortin 1 receptor, which is upregulated on the cell surface of melanoma cells. Surface functionalisation of iron oxide nanoparticles with the melanocortin 1 receptor agonist, α-melanocytes stimulating hormone, increased internalisation of nanoparticles in melanoma cells compared to non-melanoma and melanocyte cell lines. Moreover, the cytotoxic drug paclitaxel, was successfully encapsulated into the outer shell of the nanosystem. Delivery of paclitaxel via melanoma targeted iron oxide nanoparticles led to dose dependent cytotoxicity in melanoma cells.

A major limitation in the application of novel nanosystems in the clinic is the lack of an accurate and substantial toxicity assessment at the early stages of development. We addressed this issue by developing a hazard assessment protocol that combines cytotoxicity data with an embryonic vertebrate phenotypic assay to produce an overall toxicity index. Our iron oxide nanoparticle was assessed using this toxicity methodology to confirm they induced no toxic effects, and so were validated for further developed to be used as a therapeutic system.

II. Acknowledgements

I would like to start by thanking both my primary supervisors Dr Vicky Sherwood and Dr Francesca Baldelli Bombelli for all of their support during my PhD. Both have been extremely supportive and approachable throughout this time and I hope that I have been a credit to you both. I would especially like to thank Dr Chris Morris who adopted me as his supervisee for the latter stage of my PhD. Together, Vicky, Francesca, and Chris have helped me through both professional and personal challenges and their support has undoubtedly helped me to develop as a researcher.

I would also like to thank Grant Wheeler for the use of his lab during the *X. laevis* work, Elaine Barclay for microscopy support, and Alejandro Marín Menéndez for flow cytometry training. At the start of my PhD, I received a lot of support from Desirè Di Silvio and Kate Brown; to both, I am very grateful. Mehrnaz Behray has been a constant help during my PhD, particularly with chemistry advice; it has been an absolute pleasure to collaborate with you and I thank you wholeheartedly for your support and friendship.

Thanks to all the staff involved in the DNA-TRAP project, particularly those in Torino. Thank you to Paolo Gasco for welcoming me into your company and, above all, to Ana González Paredes for making my time in Italy an amazing experience. I couldn't have learnt from a better scientist and a nicer person.

I have met many fantastic people over the course of my PhD. In particular, I spent a lot of time with Mohammad Akbar and Melania Giorgetti drinking coffee and eating cake. Melania, *cosa farei senza di te*? I have enjoyed spending countless days talking about food with you and I hope to see you in sunny Battipaglia. It was an absolute pleasure to meet Matteo Staderini, *il lupo di mare*. I have never laughed so much in the lab than the time I spent with you. Matteo, I wish you the very best for the future.

I am particularly indebted to Paola Sánchez Moreno. At a difficult time of my PhD, Paola came to the rescue and reinstalled my motivation for the project and confidence in my abilities. I truly don't know how I would have got through the last year of my PhD without you.

The support I have received outside of work has been essential. So for this, I would like to thank my family, especially my parents, who have supported me unreservedly and I am forever grateful. I would also like to thank Simon and Jacci, your support and friendship has been extremely important to me over the course of my PhD. It has been a real pleasure spending time with you both. Finally, I would like to thank Sophie for all her help and encouragement. I feel I can tackle any problem with you by my side and I look forward to the future with you.

Table of contents

List of figures

IV. List of tables

V. List of abbreviations

AC	…	Adenylyl cyclase
ACN	…	Acetonitrile
ACTH	…	Adrenocorticotropic hormone
AFM	…	Atomic force microscopy
AFM	…	Alternating magnetic field
APS	…	Ammonium persulfate
ATR	…	Attenuated total reflection
BMDC	…	Bone marrow-derived cell
BMP	…	Bone morphogenetic protein
BPE	…	Bovine pituitary extract
CAF	…	Cancer-associated fibroblast
cAMP	…	Cyclic adenosine monophosphate
CRE	…	cAMP-response-element
CREB	…	cAMP-response-element binding protein
CSC	…	Cancer stem cell
CTC	…	Circulating tumour cell
CTLA-4	…	Cytotoxic T lymphocyte antigen
DIPEA	…	*N*,*N*-Dissopropylethylamine
DLS	…	Dynamic light scattering
DMF	…	*N*,*N*-Dimethylformamiode
DMSO	…	Dimethyl sulfoxide
DTIC	…	Dacarbazine
DTT	…	Dithiothreitol
DTX	…	Docetaxel
EC	…	Endothelial cell
ECL	…	Enhanced Chemi-Luminescence
ECM	…	Extracellular matrix
EDAC	…	1–ethyl–3–(3–dimethylaminopropyl) carbodiimide
EDTA	…	Ethylenediaminetetraacetic acid
EGFR	…	Epidermal growth factor receptor
EGTA	…	Ethylene glycol-bis(2-aminoethylether)-*N,N,N′,N′*-tetraacetic acid
EMT	…	Epithelial to mesenchymal transition
EPR	…	Enhanced permeability and retention
ERK	…	Extracellular signal-regulated kinase
FACS	…	Fluorescence-activated cell sorting
FCS	…	Fetal calf serum
FS	…	Forward scatter
FDA	…	Food and Drug Administration
FETAX	…	Frog teratogenesis assay-*Xenopus*
FGF	…	Fibroblast growth factor
FI	…	Fluorescent intensity
FT-IR	…	Fourier transform infra-red

GDP	…	Guanosine diphosphate
GM	…	Geometric mean
GPCR	…	G-protein coupled receptor
GTP	…	Guanosine triphosphate
HBSS	…	Hank's Balanced Salt solution
HCCA	…	α-cyano-4-hydroxycinnamic acid
hCG	…	Human chorionic gonadotrophin
HE	…	Hematoxylin and eosin
HEMA-lp	…	Human epidermal melanocytes, adult-lightly pigmented
HER-2	…	Human epidermal growth factor receptor 2
HMGS	…	Human melanocyte growth supplement
HPLC	…	High performance liquid chromatography
HPLC	…	High performance liquid chromatography
HRP	…	Horseradish peroxidase
HTS	…	High-throughput screening
IC	…	Immune inflammatory cell
ICP-OES	…	Inductively coupled plasma optical emission spectroscopy
IL	…	Interleukin
IRCCS	…	Istituto di Ricerche Farmacologiche “Mario Negri”
LON	…	Lonidamine
MALDI-TOF	…	Matrix-assisted laser desorption ionisation time-of-flight
MAPK	…	Mitogen-activated protein kinase
MC1R	…	Melanocortin-1 receptor
MCSP	…	Melanoma chondroitin sulphate proteoglycan
MET	…	Mesenchymal-epithelial transition
MITF	…	Microphthalmia-associated transcription factor
MMP	…	Matrix metalloproteinases
MMR	…	Marc's Modified Ringer's
MQW	…	Milli-Q water
MRI	…	Magnetic Resonance Imaging
MS	…	Mass spectrometry
MT1	…	Membrane type-1
MTT	…	3-(4,5-dimethylthiazolyl)-2,5-diphenyltetrazolium bromide
MWCO	…	Mw cut-off
NC	…	Neural crest
NF	…	Nieuwkoop and Faber
NG2	…	Anti-human neural/glial antigen 2
NK	…	Natural killer
NP	…	Nanoparticle
NR	…	Nile Red
NTD	…	Neural tube defect
OCT	…	Optimal cutting temperature
PARP-1	…	Poly [ADP-ribose] polymerase 1
PBS	…	Phosphate buffered saline

PC	…	Pericyte
PD-1	…	Programmed cell death protein 1
PDI	…	Polydispersity index
PEG	…	Poly(ethylene glycol)
PEP	…	Peptide
PI3K	…	Phosphoinositide 3-kinase
PKA	…	Protein-kinase A
PLGA	…	Poly(lactic-co-glycolic acid)
PMA	…	Phorbol 12-myristate 13-acetate
PMAO	…	Poly(maleic anhydride-alt-1-octadecene)
PMSG	…	Pregnant mare serum gonadotrophin
PS	…	Polystyrene
PTEN	…	Phosphatase and tensin homolog
PTX	…	Paclitaxel
QD	…	Quantum dot
RES	…	Reticuloendothelial system
RGF	…	Radial growth phase
RNAi	…	RNA interference
ROS	…	Reactive oxygen species
RPMI	…	Roswell Park Memorial Institute
RTK	…	Receptor protein-tyrosine kinase
SH2	…	Src-homology 2
siRNA	…	Small interfering RNA
SLN	…	Sentinal lymph node
SLNB	…	Sentinal lymph node biopsy
SPION	…	Superparamagnetic iron oxide nanoparticles
SPM	…	Superparamagnetic
SS	…	Side scatter
TBS(T)	…	Tris buffered saline (with added Tween)
TEM	…	Transmission electron microscopy
TEMED	…	*N*,*N*,*N'*,*N'*-Tetramethylethylenediamine
TERT	…	Telomerase reverse transcriptase
TF	…	Transcription factor
TFA	…	Triflouroacetic acid
TMAH	…	Tetramethylammonium hydroxide
UA	…	Uranyl acetate
UV	…	Ultraviolet
VEGF	…	Vascular endothelial growth factor
VGF	…	Vertical growth phase
α-MSH	…	Alpha-melanocyte-stimulating hormone

VI. Publications associated with this work

Ahire, J. H., Behray, M., **Webster, C. A**., Wang, Q., Sherwood, V., Saengkrit, N., Ruktanonchai, U., Woramongkolchai, N. & Chao, Y. 2015. Synthesis of Carbohydrate Capped Silicon Nanoparticles and their Reduced Cytotoxicity, In Vivo Toxicity, and Cellular Uptake. *Adv Healthc Mater,* 4**,** 1877-86.

Behray, M., **Webster, C. A**., Pereira, S., Ghosh, P., Krishnamurthy, S., Al-Jamal, W. T. & Chao, Y. 2016. Synthesis of Diagnostic Silicon Nanoparticles for Targeted Delivery of Thiourea to Epidermal Growth Factor Receptor-Expressing Cancer Cells. *ACS Appl Mater Interfaces,* 8**,** 8908-17.

Bombelli, F. B., **Webster, C. A**., Moncrieff, M. & Sherwood, V. 2014. The scope of nanoparticle therapies for future metastatic melanoma treatment. *Lancet Oncol,* 15**,** e22-32.

Webster, C. A., Di Silvio, D., Devarajan, A., Bigini, P., Micotti, E., Giudice, C., Salmona, M., Wheeler, G. N., Sherwood, V. & Bombelli, F. B. 2016. An early developmental vertebrate model for nanomaterial safety: bridging cell-based and mammalian toxicity assessment. *Nanomedicine (Lond),* 11**,** 643-56.

Al-Yousuf, K., **Webster, C. A**., Wheeler, G. N., Bombelli, F. B. & Sherwood, V. 2017. Combining Cytotoxicity Assessment and *Xenopus laevis* Phenotypic Abnormality Assay as a Predictor of Nanomaterial Safety. *Current Protocols in Toxicology,* (submitted).

Chapter 1.

Introduction

1.1 Cell cycle control and cancer

1.1.1 Genetic control of the cell cycle in the eukaryotic cell

Multicellular eukaryotic cells undergo an ordered sequence of events in order to proliferate, where the cell duplicates its chromosomes and divides. This process is known as the cell cycle and can be divided into four distinct phases (Whitfield et al., 2002). G1 is an intermediate phase preceding the end of cell division. In G1, the cell undertakes its normal physiological role. The chromosomes during G1 are in their extended form, thus genes are able to regulate the synthesis of RNA in order to mediate the metabolism of the cell (Bertoli et al., 2013). Following G1, S (synthesis) phase occurs. During this phase DNA is synthesised, resulting in each chromosome consisting of two sister chromatids joined by centrosomes required for cell division. G2 phase follows in which further proteins, notably microtubules, required for cell division are synthesised. G1, S, and G0 are all considered as interphase, the interval between nuclear divisions. Mitosis is the M phase of the cell cycle where nuclear division occurs and can be further subdivided into four stages; prophase, metaphase, anaphase, and telophase. The nuclear membrane is broken down in prophase and the chromosomes condense. Centrosomes duplicate and organise microtubules to form the mitotic spindle. During metaphase, the chromosomes line up at the equatorial plane at the midline of the cell *via* the centrosome and then align along the metaphase plate. The centromeres divide at anaphase and each sister chromatids are transported to opposite poles of the cell. At telophase, spindle fibres dissipate and the nuclear membrane reforms around the uncoiling chromosomes at the pole of the cell. After

telophase the cell undergoes cytokinesis, a process which sees the cell divide into two cells, each with a full set of chromosomes.

A cell may also go into a resting phase known as G0. After the G1 checkpoint, typically if there is a lack of growth factors or nutrients, a cell can enter G0 instead of passing into S phase. During G0, the cell is not preparing to divide but instead enters quiescence. Quiescence is a reversible state, and the cell can enter the cell cycle again if the conditions are right for it to divide (Morrison et al., 1997). Alternatively, if a cell is under stress from DNA damaging agents it will protect itself by loss of proliferative potential. If this is irreversible, the cell is said to be in senescence (Campisi and Di Fagagna, 2007).

Cell death is also an important physiological process that maintains cell numbers in tissues that are undergoing cell turnover (Bellamy et al., 1995). Broadly, cell death can occur as necrosis or apoptosis. Necrosis occurs due to pathological events that kill the cell in an uncontrolled manner leading to rupturing of the cell and the release of the cell's contents into the surrounding area resulting in inflammation. Apoptosis however, is an active and normal physiological event, which results in the controlled breaking up of the cell into membrane-enclosed fragments, known as apoptotic bodies, that are recognised by macrophages for phagocytosis (Canbay et al., 2003).

1.1.2 Cell signalling control and regulation

Cells in multi-cellular organisms are in continual communication with each other. This signalling regulates basic cellular activities and coordinates phenotypic response to external stimuli, most often a molecule secreted by another cell. The stimulus is

detected by a receptor on the surface of the target cell's plasma membrane and transfers this signal to the cytoplasmic side. Further transmission of the signal occurs through effector molecules that cascade down a signalling pathway to other proteins in the cytoplasm that undergo a conformational change often, but not exclusively, by phosphorylation or dephosphorylation. This cascade can terminate with the activation of transcription factors (TFs) that trigger a cellular response, such as the activation of gene transcription in the nucleus. The effector can also influence the biological activity of other proteins, leading to cellular changes such as cytoskeletal conformation and metabolic activity.

The type of signalling can be characterised by the distance the signalling molecules have to travel to the target cell and can be described as endocrine, paracrine, or autocrine signalling. In endocrine signalling, endocrine cells secrete hormones into the bloodstream to have an effect on distant target cells. Usually, this produces a slow but long lasting response. In paracrine signalling, the signalling molecule acts upon target cells that are in close proximity to that of the signal-releasing cell. In autocrine signalling, the signal releasing cell acts upon itself as the signalling molecule is secreted and targets receptors on the surface of the same cell.

There are four superfamilies of receptors that are used in different signalling pathways. These are the ligand-gated ion channels, intracellular receptors, G-protein coupled receptors (GPCRs), and enzyme-linked receptors. Ligand-gated ion channels control the flow of ions across cell membranes and are regulated by the binding of a ligand to the channel. The response to ligand-gated ion channels is extremely rapid (Cockcroft et al., 1990). Intracellular receptors, as the name suggests, are located intracellularly. As a result, the ligand must be able to diffuse into the cell in order to interact with the receptor to evoke a response (Starr et al., 1996).

With nearly 1000 different receptors in humans, GPCRs are the largest family of cell-surface molecules (Katritch et al., 2013). They are involved in key physiological functions and produce a vast array of biological responses such as cellular proliferation, survival, differentiation, and migration (figure 1.1.1; (Dorsam and Gutkind, 2007). All GPCRs have a single peptide that is embedded in the cell membrane. The peptide has seven-transmembrane spanning α-helices with an extracellular amine terminal and an intracellular carboxyl terminal (Kobilka, 2007). The GPCR is intracellularly linked to a G-protein that contains three subunits, α -, β - , and γ – subunits. Upon extracellular binding of a ligand, the GPCR activates the G protein by replacing the guanosine diphosphate (GDP) molecule, bound to the α – subunit, with guanosine triphosphate (GTP). Subsequently, the subunits dissociate to interact with downstream cellular effectors. Hydrolyses of GTP on the α – subunit causes the G protein to reassemble and return to its inactive state.

As with GPCRs, enzyme-linked receptors contain an extracellular binding site for signalling molecules. The intracellular domain is an enzyme and, upon binding of the ligand, the enzyme undergoes a conformational change to become activated or inhibited. Receptor protein-tyrosine kinases (RTKs) are an important example of enzyme-linked receptors. RTKs are membrane proteins containing a single transmembrane domain, an extracellular binding domain, and an intracellular protein kinase domain (figure 1.1.2; (Bier, 2005, Hubbard, 1999). Binding of a ligand leads to receptor dimerisation, where two inactive monomers come together through interaction with the bivalent ligand (Lemmon and Schlessinger, 2010).

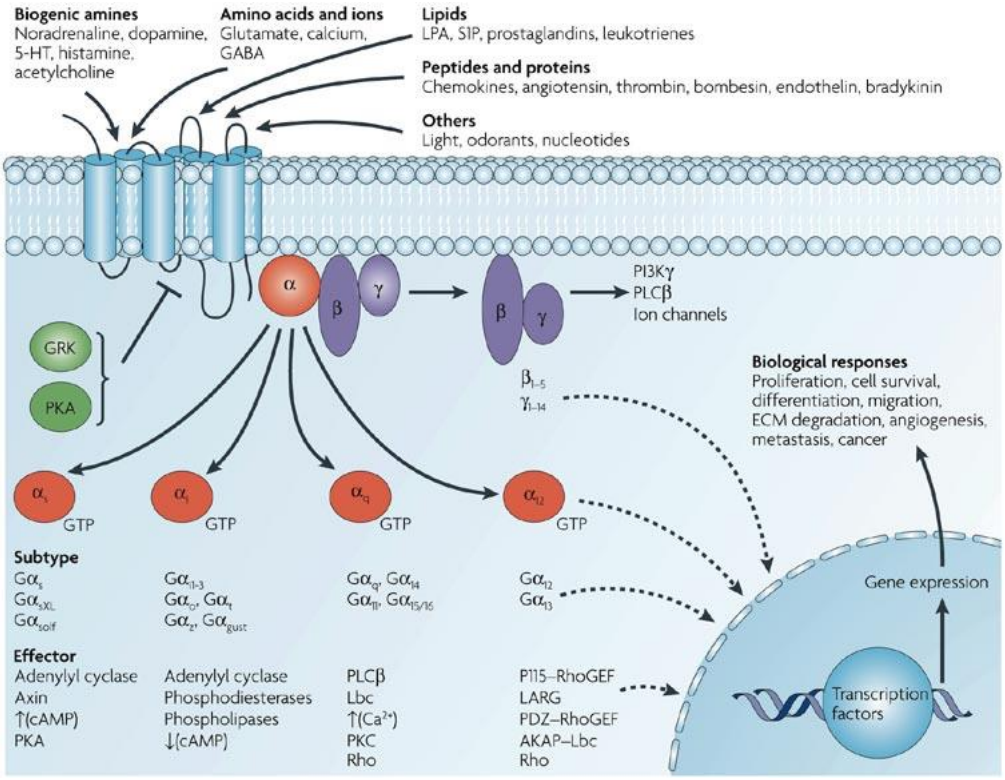

Figure 1.1.1 G-protein coupled receptors (GPCRs). Multiple ligands are used as agonists to GPCRs including bigenic amines, amino acids and ions, lipids, and peptides and proteins. After activation, GPCRs interact with heterotrimeric G proteins (comprising of α-, β-, and γ- subunits). After a conformational change of the receptor, GDP is exchanged for GTP on the α-subunit. G proteins have the ability to activate several downstream effectors including adenylyl cyclase, PKA, ion channels, and phospholipase C. Activated effector molecules ultimately activate TFs that alter gene regulation of key cellular events such as proliferation, cell survival, differentiation, migration, extracellular matrix (ECM) degradation, and angiogenesis. Abhorrent activation of any components within the signalling pathway can lead to dysregulation of these biological responses, potentially initiating tumorigenesis. Figure from Dorsam and Gutkind, 2007.

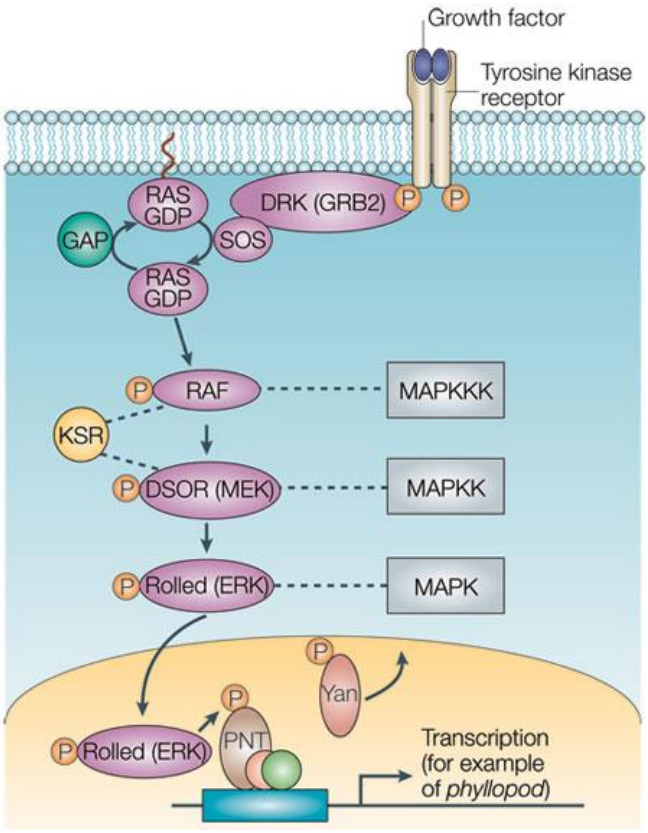

Figure 1.1.2 Receptor tyrosine kinases (RTKs). Activation of RTK is mediated through extracellular ligand binding. Upon binding, RTK monomers dimerise leading to intracellular trans-autophosphorylation. The adaptor protein, through the SH2 or PTB domain, interacts with the phosphorylated RTK residues. Downstream, ERK, is activated and translocates to the nucleus, where it is able to activate transcriptional targets. Figure from Bier, 2005.

After dimerisation, the intracellular kinase domains come in close contact with each other and trans-autophosphorylate, where the protein kinase of one monomer phosphorylates the tyrosine of the other and vice versa (Lemmon and Schlessinger, 2010). Intracellular signalling molecules, containing Src-homology 2 (SH2) domain or the phosphotyrosine-binding (PTB) domain (Pawson and Scott, 1997, Pendergast et al., 1993), interact with the phosphorylated tyrosine residues. These molecules regulate the phosphorylation of downstream signalling molecules to activate signalling pathways, including the mitogen-activated protein kinases (MAPK)/extracellular signal-regulated kinases (ERK) signalling pathway and the phosphatase and tensin homolog (PTEN)/phosphoinositide 3-kinase (PI3K)/AKT signalling pathway, eventuating with the activation of TFs.

1.1.3 Development of cancer

Cancer has had a huge impact on human health and, over the last few decades, there has been an exponential growth in the knowledge surrounding the mechanisms involved in cancer initiation and progression (Liotta and Petricoin, 2000, Tysnes and Bjerkvig, 2007). Cancer proves to be a complex group of genetic diseases that most often occurs in the DNA of somatic cells. Genetic mutations can provide an advantage to an individual cell, allowing it to outgrow and out compete the local tissue environment. The dominance of these mutated cells can lead to the death of neighbouring cells, loss of tissue/system function, and, ultimately, to the death of the organism. Every cell in the human body contains the machinery to transform into a cancer cell but ordinarily they are regulated to an extraordinary degree. The transformation from healthy cell to a highly malignant tumour cell, tumorigenesis, is

a multistep process of genetic modifications that sees the cell gain a certain set of biological capabilities. These capabilities, well known as the hallmarks of cancer (Hanahan and Weinberg, 2000), are alterations in the cell physiology that combine to dictate the extent of malignant growth. These include the ability to sustain proliferative signalling, evade growth suppressors, enable replicative immortality, resist cell death, induce angiogenesis, and activate invasion and metastasis (Hanahan and Weinberg, 2000). More recently, emerging hallmarks (including deregulation of cellular energetics and avoidance of immune destruction) and enabling characteristics (including tumour-promoting inflammation and genome instability and mutation) have been described as contributors to the pathogenesis of cancer (figure 1.1.3; (Hanahan and Weinberg, 2011). Tumour initiation is now regarded as a progressive multistep process were the cancer cell has an accumulation of genetic alterations and further genetic alterations are required for a pre-malignant lesion to form a primary tumour (Klein, 1998). At this early stage, the cells are not considered invasive or metastatic.

Figure 1.1.3 Biological capabilities of cancer. Normal cell proliferation and homeostasis is tightly regulated. There are distinct biological capabilities, or hallmarks, that cells acquire in order to be considered cancerous. The alterations in the cell physiology include the ability to sustain proliferative signalling, evade growth suppressors, avoid immune destruction, enable replicative immortality, tumour-promoting inflammation, activate invasion and metastasis, induce angiogenesis, genome instability and mutation, resist cell death, and deregulate cellular energetics. The combination of these hallmarks dictates the growth and progression of a tumour. Figure from Hanahan and Weinberg, 2011.

1.1.4 Pathology of the tumour microenvironment

Initially, a tumour was viewed as a rather simplistic homogenous group of cancer cells. However, the tumour proves to be a far more complex tissue that relies on the interaction between cancer cells and host cells (Egeblad et al., 2010, Liotta and Kohn, 2001). Within a solid tumour, there are a number of specialised cells that aid in tumour survival and progression. These specialised cells infiltrate at early tumorigenesis and include cancer-associated fibroblasts (CAF), cancer stem cells (CSC), cancer cells, immune inflammatory cells (ICs), endothelial cells (EC), pericytes (PC), invasive cancer cells, and bone marrow-derived cells (BMDCs) (Hanahan and Weinberg, 2011) that signal to each other and provide the scaffolding to support the survival and growth of cancer cells.

As the tumour tissue grows in size, angiogenesis (the formation of new blood vessels) is required to provide sufficient oxygen and nutrients. Without angiogenesis, tumour size is thought to be restricted to 1-2 mm^3 (Muthukkaruppan et al., 1982) and the tumour is likely to become necrotic (Parangi et al., 1996). Angiogenesis is promoted by secretion of growth factors from cancer cells. Vascular endothelial growth factor (VEGF) is a major angiogenic factor that is essential for the survival of vascular ECs. VEGF is upregulated in many tumours and overexpression is correlated to tumour progression and patient prognosis (Baillie et al., 2001, Itakura et al., 2000). Tumour cells and cells from the local stroma, release VEGF (agonist for the receptors VEGFR-1, VEGFR-2, and NRP1), angiopoietin ligands (agonist for Tie receptors), delta-like and jagged ligands (agonists for Notch receptors), ephrin ligands (agonist for Eph receptors), and slit ligands (agonist for Robo receptors) (Coultas et al., 2005,

Phng and Gerhardt, 2009). These ligands regulate the proliferation and migration of ECs in blood vessels underlying the tumour. This leads to branching of the vasculature towards the VEGF gradient emanating from the tumour cells (Blanco and Gerhardt, 2013). At the leading edge, the vascular sprout is comprised of stalk and tip cells (Weis and Cheresh, 2011). The stalk cells express Notch receptors and the tip cells, at the furthermost point of the vascular sprout, expresses Notch, VEGF, and Robo receptors (Blanco and Gerhardt, 2013). The established tumour vasculature allows the tumour to continue growing in size (Kim et al., 1993, Roskoski, 2007, Yancopoulos et al., 2000).

There are key physiological difference between normal tissue vasculature and the vasculature in the tumour environment (Siemann, 2011). In normal tissue, blood vessels form an ordered and efficient network, which work alongside an equally efficient systematic network of lymphatic vessels that drain waste metabolic fluid from the tissue (figure 1.1.4). The aggressive and hurried rate of tumour angiogenesis due to overexpression of pro-angiogenic factors such as VEGF, leads to a disorganised structure of blood vessels with irregular branching that are hyperpermeable (Gee et al., 2003, Roskoski, 2007, Tong et al., 2004). The lack of PC (perivascular cells that wrap around ECs) results in blood vessels that are haemorrhagic and hyperdilated (Bergers and Song, 2005). The accompanying lymphatic system is as leaky and dilated as the vasculature, providing poor and inefficient drainage of waste fluids from the tissue (Leu et al., 2000, Padera et al., 2002).

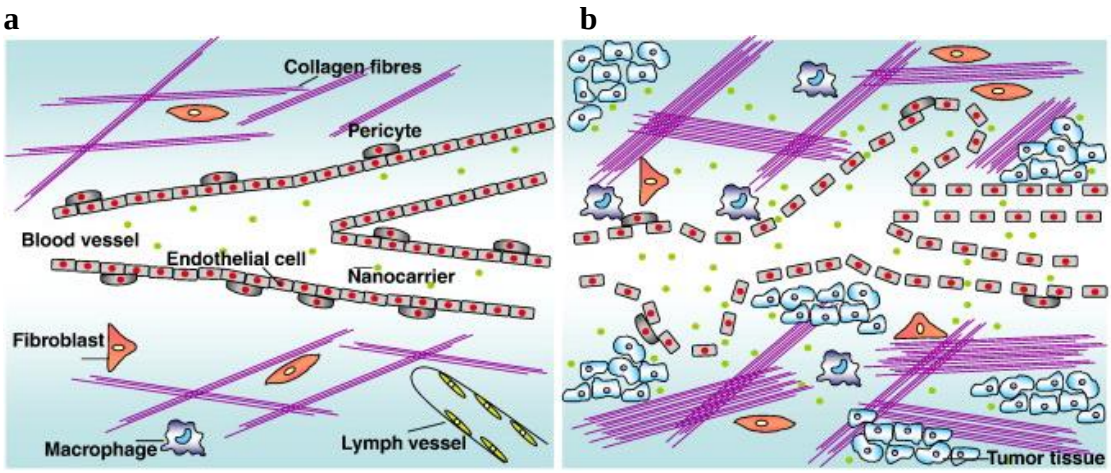

Figure 1.1.4 Vasculature structure in normal tissue and the tumour microenvironment. (a) In normal tissue, PCs help to maintain linear blood vessels by contraction around ECs. The surrounding ECM, containing fibroblasts, macrophages, and collagen fibres, is highly organised. Lymphatic vessels provide efficient drainage of waste fluid from the tissue. (b) Tumour tissues contain blood vessels that have disorganised branching, are hyperdilated, and have no constant blood flow or direction. The disruption in PC organisation contributes to tumour growth. The ECM has a higher density of collagen fibres, fibroblasts, and macrophages compared to normal tissue. There is also a lack of sufficient drainage due to the absence of lymph vessels. Figure from Danhier et al., 2010.

1.1.5 Invasion and metastasis

As the tumour mass continues to grow it can invade the local tissue and, in a process called metastasis, spread from the primary tumour site to secondary sites throughout the body (Schroeder et al., 2012). Metastasis of a tumour represents a great challenge. Rarely does the primary tumour alone lead to death; approximately 90% of cancer deaths are a result of cancer growth at secondary sites (Wittekind and Neid, 2005). The formation of the tumour vasculature and lymphatics give cancer cells access to the rest of the body. However, before the cancer cells can make use of these passage ways, they must first invade the local tissue and undergo intravasation into the lumina of blood or lymphatic vessels (figure 1.1.5; (Schroeder et al., 2012).

In order for intravasation to occur, tumour cells must exhibit a loss of cell-to-cell adhesion. This requires significant changes to the cell phenotype. The major change is the loss of epithelial-like phenotype by downregulation of cytokeratin, E-cadherin, and a loss of epithelial cell polarity (Onder et al., 2008, Thompson and Newgreen, 2005). This is in conjunction with the acquisition of a fibroblast-like phenotype, which is more motile and invasive. Upregulation of protease secretion (such as the matrix metalloproteinases MMP-2 and MMP-9) allows degradation of the surrounding ECM (Qin et al., 2008). The process from an epithelial phenotype to a fibroblast-like phenotype is called epithelial to mesenchymal transition (EMT). The TFs Slug and Snail are involved in the regulation of E-cadherin expression, as well as repressing the expression of genes encoding tight junction components.

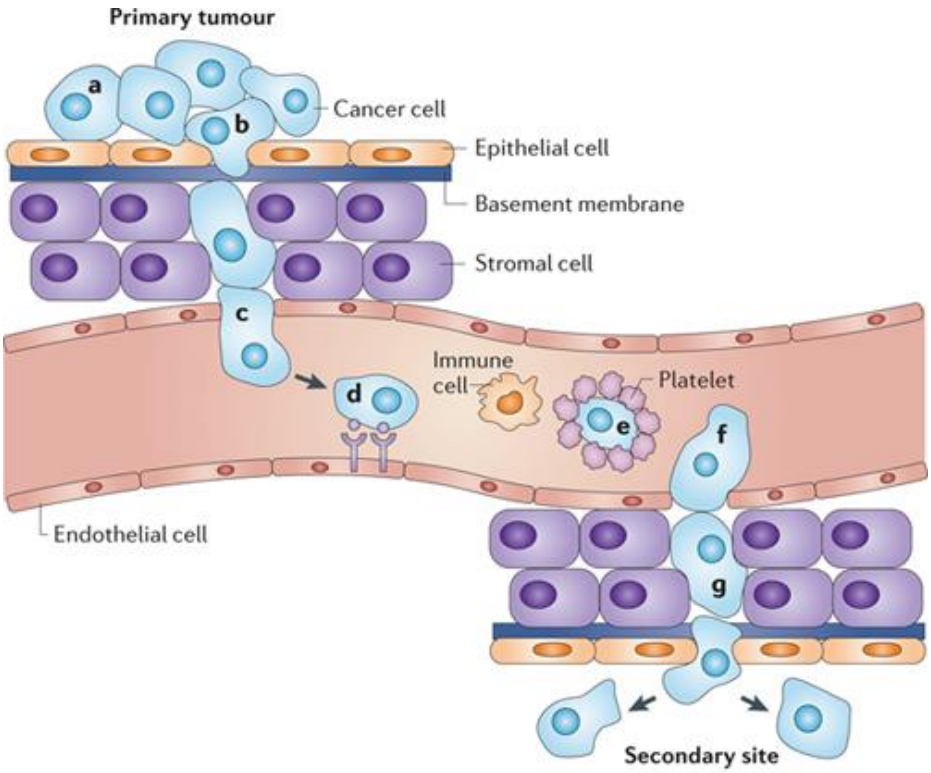

Figure 1.1.5 Stages of tumour cell metastasis. The process of cancer cells travelling from the original primary tumour to set up a secondary site of tumour growth, is called metastasis. Metastasis is a multistep process were the metastatic cells (a) escape from the primary tumour by inducing a loss of cell-cell adhesion through epithelial to mesenchymal transition (EMT). As a result, (b) the cell is more motile and begins to invade the local ECM. (c) Upregulation of several enzymes, such as MMP-1 is required for the cancer cell to intravasate through endothelial junctions into the lumen of the blood vessel. Within the blood stream, cancer cells are likely to be destroyed by the immune system. (d) Cancer cells can bind to receptors, such as E-selectin, N-cadherin, and integrin, on the surface of endothelial cells to mediate extravasation. (e) Aggregation of platelets on the surface of cancer cells can help to prevent detection by the immune system whilst travelling through the blood stream. (f) Extravasation is the movement of the cancer cell out of the blood vessel where, (g) the cell can undergo mesenchymal to epithelial transition (MET) and establish a secondary tumour site. Figure from Schroeder et al., 2012.

These TFs are vital for EMT and overexpression of both contributes to the acquisition of invasive and metastatic properties for the cancer cell (Jethwa et al., 2008, Sun et al., 2014, Zheng et al., 2015).

Once the tumour cells have undergone EMT and infiltrated the blood stream, they are known as circulating tumour cells (CTCs). Metastasis is a largely inefficient process and the immune system, haemodynamic forces, and/or apoptosis triggered by the loss of cell attachment, kills the majority of CTCs (Barok and Szöllősi, 2011); less than 0.01% of CTCs eventually form a secondary tumour growth (Fidler, 1970). As metastasis accounts for 90% of cancer patient deaths, analysis of the presence and quantity of CTCs has been shown to be a useful and accurate tool for prognosis (Williams, 2013). Furthermore, characterisation of CTCs can be used to gain vital molecular information of the tumour; useful for drug management (Krebs et al., 2010).

After arresting in microvascular beds, CTCs can undergo extravasation and establish a secondary tumour site, where they can interact with the local stromal cells to promote tumour growth. The reversal of EMT, mesenchymal-epithelial transition (MET), is required for metastatic colonisation (Brabletz, 2012). The cellular origin of the primary tumour often dictates where metastatic sites will occur as tumour cells appear to have an organ-preference for metastasis (Langley and Fidler, 2011). The theory that certain tumour types tend to metastasise to specific organs is not new. Stephen Paget's 1889 'soil and seed' hypothesis proposed that there were favourable interactions between the CTCs ('seed') and the secondary organ they occupy ('soil'). Lung cancer often metastasises to the brain, bone, adrenal gland, and liver; breast cancer to the bone, lungs, liver, and brain; prostate cancer to the bone; colorectal cancer to the liver and lungs; and melanoma often metastasises to the lung, brain, skin, and liver (Martin et al., 2000).

1.2 Melanoma

1.2.1 Epidemiology of melanoma

Cutaneous melanoma is a form of cancer that occurs as the result of uncontrolled proliferation of melanocytes; specialised melanin-producing cells located in the basal layer of the epidermis. Metastatic melanoma is the most lethal form of skin cancer and incident rates are rising faster than any other cancer (Lens and Dawes, 2004). Currently, malignant melanoma is the fifth most common cancer in the UK. Over the past several decades, the overall incidence rate of melanoma has increased significantly, reaching epidemic proportions (Canavan and Cantrell, 2016, Linos et al., 2009). In the United States, there was an increase in melanoma cases from 13.9 (per 100,000 person-years) in the period of 1989-1991, to 21.9 in the period of 2007-2009 (Shaikh et al., 2016). In the UK, melanoma represents approximately 4% of total cancer cases and in 2013, there were over 14,500 new cases of malignant melanoma. Alarmingly, there was an increase in incidence rate from 4.8 (per 100,000 person-year) to 23.0 in 2012 in the UK (Cancer Research UK). Incidence rates of melanoma is correlated to age; rates increase steadily from 20-24 years to a peak at 90 + years. However, unlike many other cancers, melanoma frequently affects people below 65 years old (~55%).

From 1971 to 2012, there has been a steady increase in melanoma related mortality in the UK from 1.2 (per 100,000 person-years) to 2.5. This increase is in line with the high rise of incidence rates, particularly in people aged over 75 (Ferlay, 2013).

This mortality rate equates to the 19th most common cause of cancer death in Europe, with over 22,000 deaths (Ferlay, 2013).

1.2.2 Development of Melanocytes

Melanocytes arise from the multipotent neural crest (NC) cells. The NC arises at the boarder of the closing neural tube and non-neural exoderm in vertebrate embryos (figure 1.2.1.a; (Shyamala et al., 2015). As a result of their stem cell-like multipotent potential, NC cells are able to differentiate into a range of cell types; these include melanocytes, neurons and glia cells of the nervous system, neuroendocrine cells of the adrenal medulla, and the craniofacial skeletal and connective tissue (Crane and Trainor, 2006). NC induction is a multistep process involving a variety of signalling pathways at specific time points in the developing embryo. Wnt, fibroblast growth factor (FGF), and bone morphogenetic protein (BMP) are inductive signalling ligands secreted from the underlying mesoderm and non-neural ectoderm that play a vital role in NC induction. BMP antagonists, such as chordin, noggin, and follistatin, are secreted factors from the Spemann's Organiser that set up a dorsal-ventral gradient of BMP activation (De Robertis, 2006). Inhibition of BMP signals in the dorsal ectoderm leads to neural fate, whereas high levels gives rise to epidermis. An intermediate level of BMP signal is required to induce NC. In addition, high levels of Wnt and FGF signalling from the underlying paraxial mesoderm, as well as Wnt signalling from non-neural ectoderm, are required (Labonne and Bronner-Fraser, 1998).

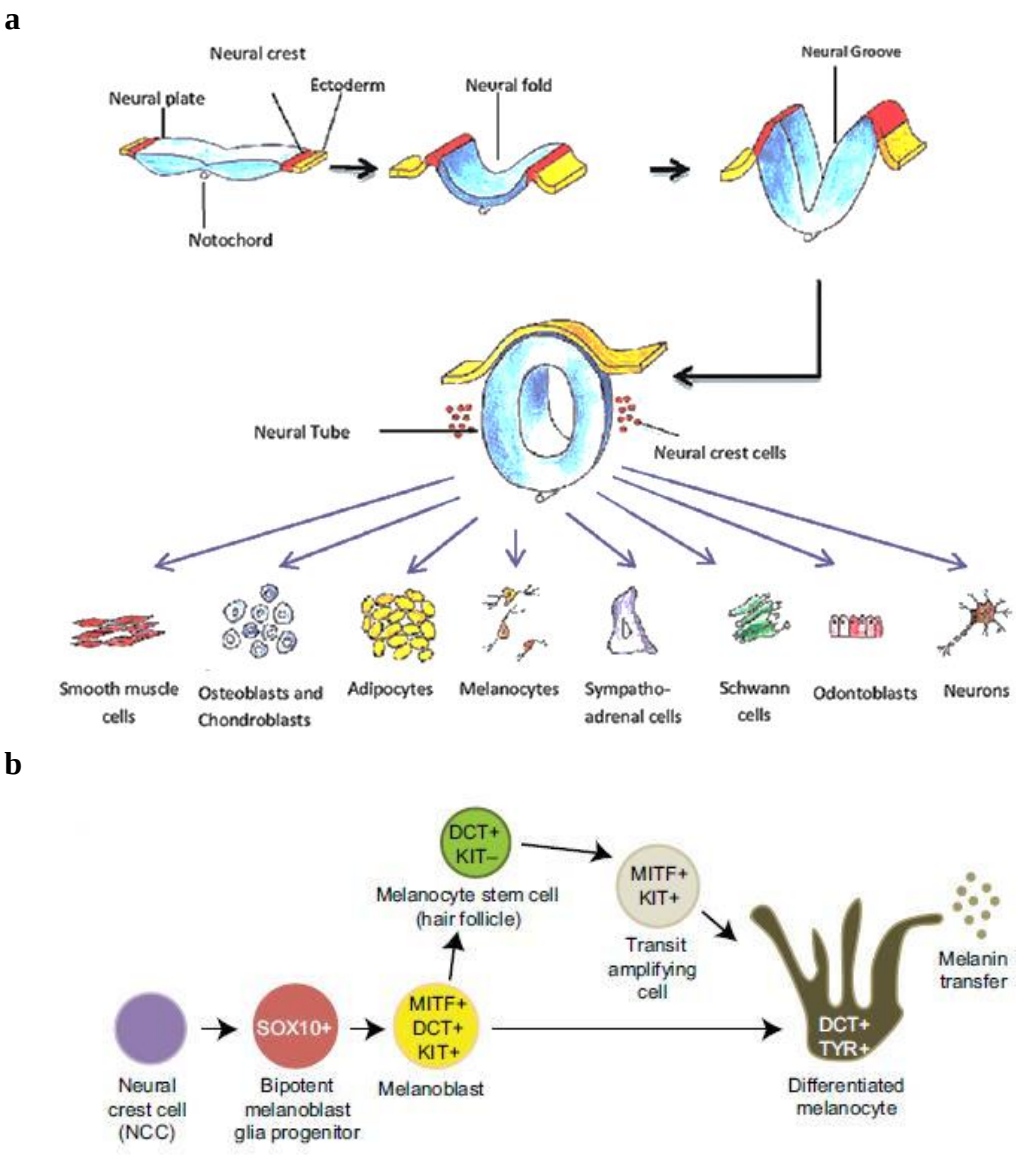

Figure 1.2.1 Formation of melanocytes from the NC. (a) The neural plate boarder is established by intermediate levels of BMPs, Wnt, and FGF from the underlying paraxial mesoderm, as well as Wnt signals from the non-neural ectoderm. Once the neural tube forms, NC cells undergo EMT and delaminate from the dorsal neural tube. NC cells then migrate to different areas of the embryo before differentiation to cell types such as melanocytes, neurons, osteoblasts, and Schwann cells. Figure adapted from Shyamala et al., 2015. (b) The TF MITF is required for NC differentiation into melanocytes. Figure adapted from Mort et al., 2015.

Introduction of Wnt/β-catenin signalling components, such as receptors (frizzled-3, frizzled-7, LRp6) and the intracellular signalling molecule, β-catenin, have been shown to induce NC (Abu-Elmagd et al., 2006, Deardorff et al., 2001, Labonne and Bronner-Fraser, 1998, Tamai et al., 2000). Once the neural boarder is established, TFs Zic1 and Pax3 activate early NC specifiers in a Wnt-dependent fashion. These include TF specifiers C-myc, Slug, Snail, FoxD3, and Sox9 (Honore et al., 2003). Early NC specifiers are in turn able to induce the expression of downstream NC specifiers such as SoxE (Honore et al., 2003). Sox10, a member of the SoxE family, is required for the survival of NC. Loss of Sox10 leads to a decrease in NC proliferation and an increase in apoptosis (Honore et al., 2003).

Following specification and closure of the neural tube, NC cells undergo an EMT, making the cells more migratory. Snail plays a vital role in NC EMT by down-regulating E-cadherin expression and claudins (Cano et al., 2000). Repression of E-caderin is essential for NC induction and failure to do this leads to an amassing of epithelial cells that are unable to migrate (Nieto et al., 1994). Once NC cells have lost polarity, MMPs are produced and secreted. In particular, the gelatinase MMP-2 is required to degrade the surrounding ECM allowing migrating NC cells to delaminate from the neuroepithelium. Knockdown of MMP-2 during *Xenopus* development results in a decrease in NC derived melanophore migration (Tomlinson et al., 2009). NC specifiers involved in differentiation of NC are not only expressed in premigratory cells, but also during migration. The SoxE family act upstream of many effector genes that promote terminal differentiation into one of the NC derived cell types. Other TFs can repress the differentiation of one cell type and lead the cell into a different cell lineage (Sauka-Spengler and Bronner-Fraser, 2008).

The fate of the premigratory NC is determined before delamination from the crest and there are thought to be two NC origins of melanocytes with different migration patterns. Firstly, there is a population of early differentiated melanoblasts that are derived from the NC and migrate dorsolaterally through the dermis between the somites (blocks of mesoderm in the developing embryo) and the developing epidermis (Mort et al., 2015). A second population of adult melanocytes is thought to originate from a glial-melanoblast precursor cell, that has the potential to differentiate into glia or melanocytes (Dupin et al., 2003), and migrate along the ventrolateral pathway (Mort et al., 2015).

The master regulator of melanocyte differentiation is the TF microphthalmia-associated transcription factor (MITF) and is absolutely required for melanocyte formation (figure 1.2.1.b; (Steingrimsson et al., 2004). MITF is a basic helix-loop-helix leucine zipper dimeric TF (Shibahara et al., 2001) that binds to the E-box promoter sequence CACGTG and CACATG (Hemesath et al., 1994, Yasumoto et al., 1994). MITF has a central role in melanocyte development, differentiation, survival, and growth, largely due to transcriptional target genes of MITF (Levy et al., 2006); figure 1.2.2). Progression of the cell cycle can be mediated MITF by regulation of CDK2, essential for transition through G1 to S phase (Du et al., 2004). Anti-apoptotic *Bcl2* is also mediated directly through MITF and a loss of MITF expression can lead to apoptosis in melanocytes (Mcgill et al., 2002). The promoter regions for the main pigmentation enzymes TYR, TYRP1, and DCP, all contain MITF E-box binding sites in melanocytes (Bentley et al., 1994, Bertolotto et al., 1996, Yasumoto et al., 1997).

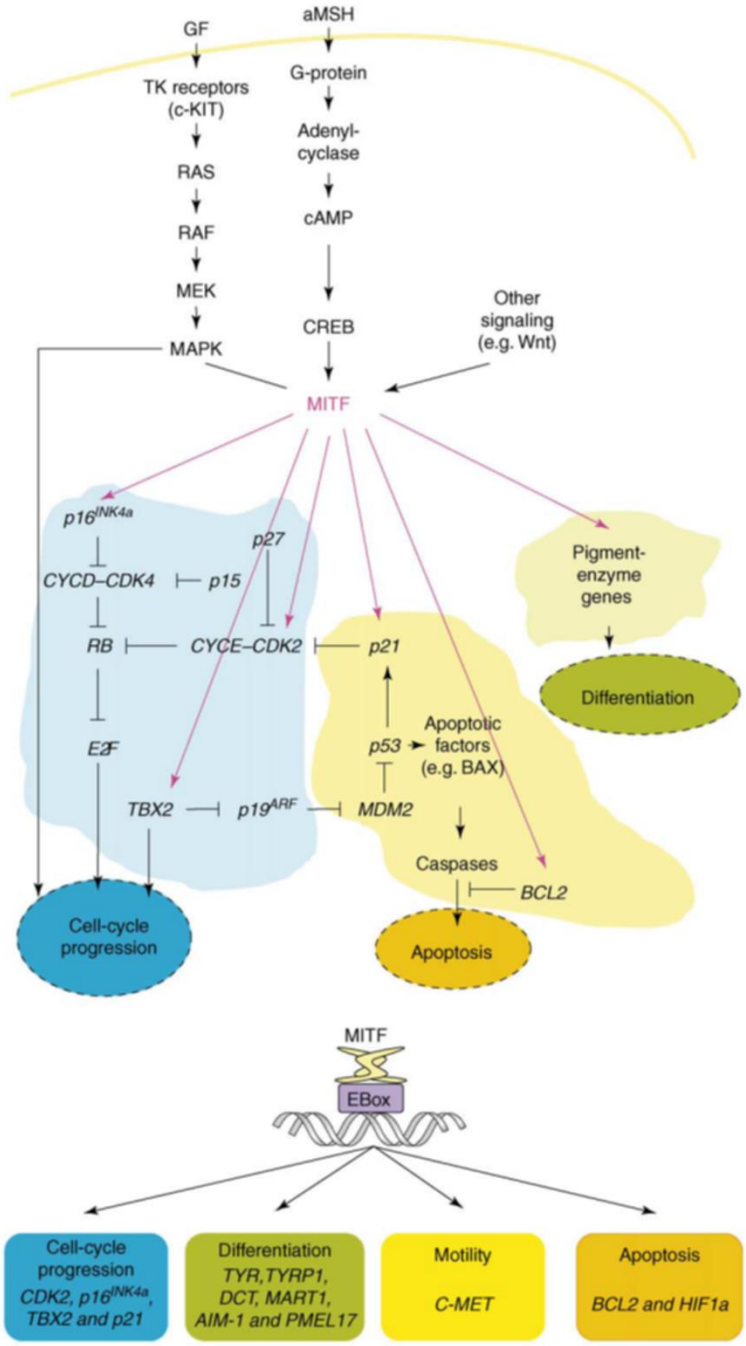

Figure 1.2.2 MITF target genes. (a) MITF plays a central role in the induction of melanoma, melanocyte differentiation, cell cycle progression, and melanocyte survival. MITF is downstream of both GPCRs and RTKs. MITF target genes include *p21* and *INK4a* (involved in cell cycle progression), *TBX2* and *CDK2* (involved in cell proliferation), *BCL2* (involved in cell survival), and *TYR* and *AIM-1* (involved in melanocyte differentiation. (b) The regulation of MITF target gene transcription occurs through MITF binding sequences (E-boxes) in the gene promoter region. Figure from Levy et al., 2006.

1.2.3 Initiation and progression of melanoma

Melanocyte proliferation can lead to a non-cancerous aggregation of cells known as a benign nevus, which commonly do not progress to melanoma due to cellular senescence. Melanoma typically progresses at first through a radial growth phase (RGP), during which they can be easily resected through surgery. During this phase, the tumour proliferates and invades the local epidermis but is restricted by the basement membrane which lies above the blood vessel containing dermis (figure 1.2.3;(Dye et al., 2013). If vertical growth phase (VGF) occurs, melanoma cells can invade the dermis and there is a greater risk of metastasis (Crowson et al., 2006).

The transformation of nevi to metastatic melanoma, as with all cancers, requires an accumulation of molecular mutations to influence cell proliferation, death, differentiation, angiogenesis, and invasiveness. Several factors and signalling pathways involved in the early development and survival of melanocytes are implicated in melanoma. UV radiation, a major environmental risk factor for melanoma initiation, typically leads to DNA damage *via* dimerisation of cytosine-thymine and thymine-thymine (De Gruijl et al., 2001). There are numerous genetic anomalies associated with metastatic melanoma. Amongst these, components of the MAPK/ERK and PTEN/PI3K/AKT signalling pathways are regularly involved. In 50-60% of melanomas, BRAF (a member of the MAPK/ERK pathway) is mutated leading to abhorrent signalling. In melanoma with BRAF wildtype, NRAS (another component of the MAPK/ERK pathway), is mutated at a frequency of 20-25%.

Figure 1.2.3 Initiation and progression of melanoma. Melanocytes are melanin-producing cells located at the base of the epidermis (1). Uncontrolled proliferation can result in a benign nevus, where growth is limited and restricted to the surrounding tissue (2). At this stage, whilst there is just radial growth, the tumour is easy to remove during surgery. If the cells begin to invade vertically through the basement membrane and into the underlying dermis (3), treatment options are limited and prognosis is poor. If the tumour continues to progress, cancer cells can dissociate from the primary tumour and invade the vascular or lymphatic system (4) and metastasise to a secondary site (5). Figure adapted from Dye et al., 2013.

Other notable genetic alterations include MITF (frequency 20%), telomerase reverse transcriptase (TERT) (frequency 70-80%), and PTEN (frequency 40-60%; (Shtivelman et al., 2014). Mutations in melanocortin-1 receptor (MC1R), a GPCR involved in melanogenesis, is also associated with an increased risk of melanoma (Kennedy et al., 2001, Palmer et al., 2000). Melanoma largely follows the standard model of progression for carcinomas (cancer of epithelial cells). Recruited cells from the surrounding environment, such as immune cells, help to induce angiogenesis. Macrophages promote angiogenesis by releasing pro-angiogenic molecules such as FGF-2 (Reiland et al., 2006) and interleukin-8 (IL-8) (Srivastava et al., 2015). Overexpression of both MMP-2 (Rotte et al., 2012) and MMP-9 (Tang et al., 2013) is indicative of a more invasive and metastatic phenotype, associated with a worsened patient prognosis.

The main route of melanoma metastasis is regarded as *via* the lymphatic system and whilst in transit, melanoma cells must evade detection by the immune system. Natural killer (NK) cells are one of the most efficient cells for the defence against cancer cells. NKD2D receptors are expressed on the surface of NK cells. NKD2D ligands are expressed at low levels on the surface of normal cells however, they are overexpressed on cells which are infected, transformed (as with cancer cells), or stressed (Fuertes et al., 2008). Melanoma cells are able to retain NKD2D ligands intracellularly to prevent their expression on the cell surface (Fuertes et al., 2008). In turn, this helps melanoma cells to evade destruction from NK cells (Zbytek et al., 2008). Melanoma cells can undergo different patterns of metastatic spread; the most frequent first metastasis is located at the regional lymph nodes (~50%; (Mervic, 2012, Zbytek et al., 2008), followed by distant sites (~25%), and satellite and/or in-transit metastasis (~24%; (Mervic, 2012).

1.2.4 Pathological staging of melanoma

Pathological staging of melanoma is used to indicate the extent of growth and spread of the tumour. There are several systems used to describe the stages of melanoma progression including the Breslow scale, TNM staging (Balch et al., 2009), and number staging. The Breslow scale measures the thickness of the melanoma in the skin (in millimetres). After dissection, the melanoma is analysed for the depth of invasion into the skin. In the UK, TNM staging is most frequently used in the clinical setting. TNM stands for tumour, node, and metastasis (table 1.2.1), where T is used to categorise the size of a primary tumour and is measured according to the Breslow scale. T can be further divided into groups a and b to characterise the tumour as ulcerated or not. Ulceration is defined as a breaking of the skin over the tumour and if the tumour is ulcerated (b) it has a higher risk of spreading from the primary site.

Table 1.2.1 TNM staging of melanoma. Adapted from Balch et al., 2009

T	**Thickness (mm)**	**Ulceration status/mitoses**
T*is*	n/a	n/a
T1	≤ 1.0	a. without ulceration and mitoses < 1/mm^2 b. with ulceration or mitoses ≥ 1/mm^2
T2	1.01-2.00	a. without ulceration b. with ulceration
T3	2.01-4.00	a. without ulceration b. with ulceration
T4	> 4.00	a. without ulceration b. with ulceration
N	**Number of nodes**	**Nodel metastatic burden**
N0	0	n/a
N1	1	a. micrometastasis b. macrometastasis
N2	2-3	a. micrometastasis b. macrometastasis c. in transit metastases/satellites without metastatic nodes
N3	4 +	metastatic nodes, or matted nodes, or in transit metastases/satellites with metastatic nodes
M	**Site**	**Serum LDH**
M0	no distant metastases	n/a
M1a	distant skin, subcutaneous or nodal metastases	normal
M1b	lung metastases	normal
M1c	all other visceral metastases	normal
	any distant metastasis	elevated

1.2.5 Current therapeutic options for the treatment of melanoma

Patient prognosis is generally good if melanoma is diagnosed early whilst it is still under RGP. If it is limited to the local epidermis with no sign of metastasis, melanoma can be cured by surgery. However, once the melanoma has metastasised and the tumour is unresectable, long-term prognosis is notoriously poor. After the tumour has developed into a late-stage metastatic disease, there are limited successful therapeutic options. Currently, the gold standard is surgery followed by sentinel lymph node (SLN) biopsy (SLNB), where the SLN (the first lymph node in which the cancer is likely to spread to from a primary tumour) is removed and examined for the presence of tumour cells. If the SLNB is positive, this indicates the cancer is in the SLN. This could also mean the melanoma has spread to regional lymph nodes and to other organs. If this is the case, the patient prognosis is poor; for stage 4 melanoma (table 1.2.2), 5-year survival rate is approximately 15-20% (Dickson and Gershenwald, 2011).

Traditionally, chemotherapeutics, such as the alkylating agent dacarbazine (DTIC), have been used as a general cytotoxic drug to help reduce the size of advanced melanoma. DTIC is typically administered intravenously at a dose of 150-200 mg/m^2/d for 5 days or as a single dose of 800-1,000 mg/m^2, with doses repeated every 3 to 4 weeks (Bhatia et al., 2009). Although the efficacy of DTIC is higher than other chemotherapeutic options, the survival benefits remain minimal and DTIC efficacy is relatively low, with less than 2% of patients treated with DTIC alone surviving 6 years (Hill et al., 1984).

Table 1.2.2 Number staging of melanoma (Cancer Research UK;

http://www.cancerresearchuk.org/about-cancer/type/melanoma/treatment/stages-of-melanoma).

Stage 0
In situ melanoma. Melanoma cells are only in the top surface layer of the epidermis and have not started to spread to deeper layers.

Stage 1A
The melanoma is less than 1 mm thick. The covering layer of skin over the tumour is not broken (it is not ulcerated). The melanoma is only in the skin and there is no sign that it has spread to the lymph nodes or other parts of the body.

Stage 1B
The melanoma is less than 1 mm thick and the skin is broken (ulcerated). Or it is between 1 and 2 mm and is not ulcerated. The melanoma is only in the skin and there is no sign that it has spread to lymph nodes or other parts of the body.

Stage 2A
The melanoma is between 1 and 2 mm thick and is ulcerated. Or it is between 2 and 4 mm and is not ulcerated. The melanoma is only in the skin and there is no sign that it has spread to lymph nodes or other parts of the body.

Stage 2B
The melanoma is between 2 and 4 mm thick and is ulcerated. Or it is thicker than 4 mm and is not ulcerated. The melanoma is only in the skin and there is no sign that it has spread to lymph nodes or other parts of the body.

Stage 2C
The melanoma is thicker than 4mm and is ulcerated. The melanoma is only in the skin and there is no sign that it has spread to lymph nodes or other parts of the body.

Stage 3A
The melanoma has spread into up to 3 lymph nodes near the primary tumour. But the nodes are not enlarged and the cells can only be seen under a microscope. The melanoma is not ulcerated and has not spread to other areas of the body.

Stage 3B
The melanoma is ulcerated and has spread to between 1 and 3 lymph nodes nearby but the nodes are not enlarged and the cells can only be seen under a microscope OR
The melanoma is not ulcerated and it has spread to between 1 and 3 lymph nodes nearby and the lymph nodes are enlarged OR
The melanoma is not ulcerated, has spread to small areas of skin or lymphatic channels, but nearby lymph nodes do not contain melanoma cells

Stage 3C
There are melanoma cells in the lymph nodes and small areas of melanoma cells in the skin or lymph channels close to the main melanoma OR
The melanoma is ulcerated and has spread to between 1 and 3 lymph nodes nearby which are enlarged OR
The melanoma may or may not be ulcerated and has spread to 4 or more nearby lymph nodes OR
The melanoma may or may not be ulcerated and has spread to lymph nodes that have joined together

Stage 4
These melanomas have spread elsewhere in the body, away from where they started (the primary site) and the nearby lymph nodes. The most common places for melanoma to spread are the lung, liver or brain or to distant lymph nodes or areas of the skin.

Over the past several years, with the increased understanding of the molecular mechanisms involved in the initiation and progression of melanoma, there has been significant advancement in the development of novel therapeutics for the treatment of metastatic melanoma (Johnson and Sosman, 2015). After the identification of the BRAF mutation in 40-50% of melanoma (Davies et al., 2002), BRAF has been explored as a potential therapeutic target and several BRAF inhibitors have been evaluated in clinical trials. The first, vemurafenib, improved patient survival rates and decreased death (Flaherty et al., 2010, Sosman et al., 2012). After phase III trials of vemurafenib, response rates were improved from 5% to 48% after treatment with vemurafenib (compared to DTIC alone; (Chapman et al., 2011). After the initial success of vemurafenib, relapse commonly occurred and nearly all of the patients treated with the BRAF inhibitor experienced tumour progression within 2 years of therapy. This is likely due to the formation of drug resistant cell populations that bypass BRAF through other MAPK components, such as NRAS, or parallel signalling pathways (Nazarian et al., 2010, Poulikakos et al., 2011, Rizos et al., 2014).

Recently, inhibitors of immune checkpoints have been developed for cancer therapy. Ordinarily, the immune system has the ability to distinguish healthy cells from cells it sees as 'foreign'. Cancer cells can often overcome these immune checkpoints to avoid destruction by the immune system (Chen and Mellman, 2013). Drugs that target these checkpoints aim to increase immune response to cancer cells (Pardoll, 2012a). An example of a potential immune checkpoint drug target is the cytotoxic T lymphocyte antigen (CTLA-4). CTLA-4 is a receptor expressed on the surface of T cells and is a negative regulator of T cell activation. Immune checkpoints are necessary to prevent excessive autoimmune response in healthy cells. In T helper cells, CTLA-4 suppresses T cell activity by preventing T cell activation *via* CD28. By inhibiting

CTLA-4, T cells are activated by CD28, leading to an increased immune response (Krummel and Allison, 1995). Ipilimumab is an immunotherapy that inhibits CTLA-4 (Acharya and Jeter, 2013) and has been shown to extend the overall survival rate from 4 to 36 months in melanoma patients (Hao et al., 2014, Pardoll, 2012b). However, the lack of clear clinical advantages and the occurrence of adverse side effects (documented as severe and long lasting) prevented the development of ipilimumab (Hodi et al., 2010).

Antibodies to programmed cell death protein 1 (PD-1) have been tested in melanoma and provide an alternative to CTLA-4 inhibitors. PD-1 is a membrane associated factor expressed by tumour cells that inhibits T-cell function (Gajewski, 2006). Nivolumab, the first anti-PD-1 to be developed as a therapeutic agent, provided an objective response in 29% of patients with melanoma with minimal adverse effects (as low as 6%; (Topalian et al., 2012). Another monoclonal antibody to PD-1, pembrolizumab, has been investigated for therapeutic benefits to melanoma patients (Robert et al.). After treatment with pembrolizumab, patients who had no success with ipilimumab treatment had a response rate of 26%. As these are relatively novel therapies, there is no long-term survival data. The combination of anti-CTLA-4 and anti-PD-1 has demonstrated complementary activity in patients with unresectable stage III or stage IV melanoma (Larkin et al., 2015).

1.3 Nanomedicine

1.3.1 Nanomaterials (NMs) in oncology

NMs are defined as sub-micronic colloidal systems comprising of organic, inorganic, or both, materials. Common organic NMs include dendrimers, cyclodextrin, micelles, and liposomes. Inorganic NMs include core-shelled NMs (such as iron oxide, gold, and silver), nanorods, fullerene, and carbon nanotubes (figure 1.3.1; (Bombelli et al., 2014). Nanotechnology has developed exponentially and is currently being utilised in numerous industries such as electronics, materials and textiles, energy, food, and pharmaceuticals (Bouwmeester et al., 2009, Gajewski, 2006, Mcintyre, 2012, Wagner et al., 2006). Due to the NM size range and the diversity of industries using nanomaterials, nanotechnology is a multi-disciplinary area of research. In terms of publications in subject specific journals, the discipline of material science accounts for around 50% of nano-publications. This is followed by chemistry (44%), physics (11%), and biomedical sciences (9%; (Porter and Youtie, 2009). Other disciplines using nanotechnology include environmental science, cognitive science, and computer science (Porter and Youtie, 2009). As NMs are on the same order of magnitude as proteins, they have the potential to be developed into powerful tools for biomedical use. These include applications such as fluorescent biological labels, drug and gene delivery systems, chemotherapy delivery, tissue engineering, detection of pathogens, detection of proteins, tumour hyperthermia, MRI contrast agents, and separation of biological molecules (Salata, 2004).

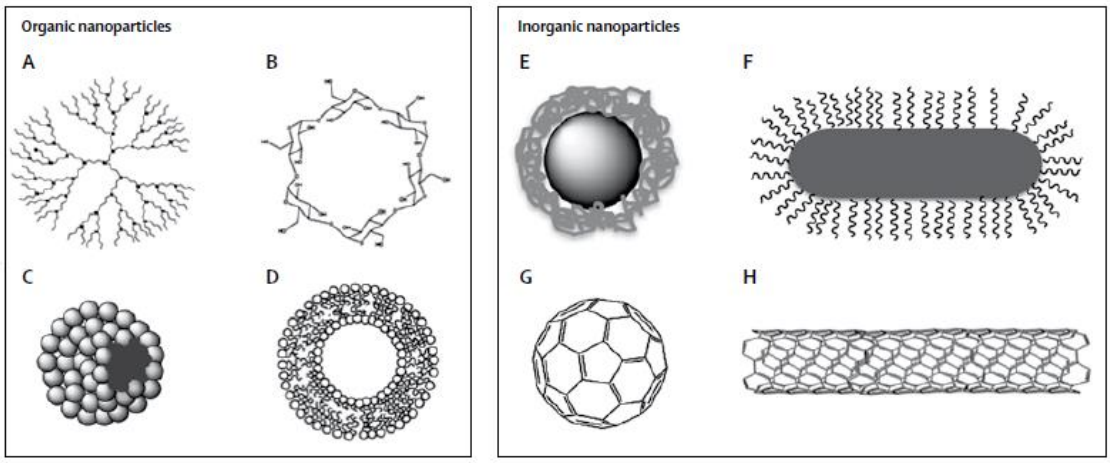

Figure 1.3.1 NMs used in oncology. Organic NMs frequently used as a drug delivery system for cancer therapy include (A) dendrimer, (B) cyclodextrin, (C) micelles, (D) liposomes. Inorganic NMs frequently used as nanocarriers in oncology include (E) core-shell NM, (F) nanorod, (G) fullerene, (H) carbon nanotube. Figure from Bombelli et al., 2014.

There has been an exponential increase in the number of biomedical multifunctional NMs that can act as both a therapeutic drug delivery system for the treatment of disease, and as a non-invasive diagnostic tool; the combination of therapeutic and diagnostics has coined the term ‘theranostics’ and is a key advantage for using NMs for a range of disease states.

For biomedical use, in particular oncology, NM size is in the range of 1 to 200 nm and they can be encapsulated with hydrophilic and/or hydrophobic drugs, depending on the NM and method of preparation. For polymer-based drug delivery systems, drugs can be physically entrapped within the formulation or covalently bound to the polymer matrix (Cho et al., 2008). Micelles are formed from amphiphilic molecules consisting of a hydrophobic core and a hydrophobic outer shell. The hydrophobic corecan act as a reservoir for hydrophobic drugs and the hydrophilic outer surface allows the micelle-drug formulation to be water-soluble. Liposomes are produced from self-assembled lipid bilayers that are then formed into spherical colloidal vesicles. As with micelles, liposomes have a hydrophilic surface allowing for dispersion in an aqueous solution. The inside of liposomes contain water, in which hydrophobic drugs can be dispersed. Lipophilic drugs can be trapped in the hydrophobic tails of the lipids, protected from the aqueous solution. Several liposomal drug formulations are approved or are in clinical trials (Suzuki et al., 2016). Drug association with metallic core nanoparticles (NPs) can be more complex than with self-assembling liposomes and micelles, and is largely dependent on the surface functionalisation of the metal core. Drug complexes can be achieved with reversible interactions between NPs and drugs, such as hydrophobic interaction with lipophilic drugs and hydrophobic regions of polymer coating. NP-drug conjugates can also be formed by covalent bonds by common covalent coupling such as between two thiol

groups, two primary amines, a carboxylic acid and primary amine, maleimide and thiol, hydrazide and aldehyde, and a primary amine and aldehyde (Werengowska-Ciećwierz et al., 2015).

Resistance to chemotherapy and targeted therapies is currently a major challenge in cancer research. Cancer cells inherently have unstable genomes and can become resistant to therapies by adapting the intended drug target (making the drug obsolete) or by abhorrent activation of other signalling components to bypass the molecular drug target. The one-dimensional approach to cancer therapy by using a single drug is fast being realised as ineffective and out-dated. Combinational NM formulations have been effective in the treatment of tumours by delivering chemosensitising agents alongside chemotherapeutics (Chiu et al., 2009, Hu and Zhang, 2012, Shapira et al., 2011). The ability to encapsulate hydrophobic and hydrophilic drugs in NMs means that drug combinations that had previously not been explored, can be developed (Zhang et al., 2007).

1.3.2 Passive targeting of NMs in cancer

One of the largest advantages of the use of NMs in oncology is the potential to specifically target cancer cells within the tumour tissue. Conventional chemotherapeutics often act upon proliferating cells as a means to prevent tumour growth and, unfortunately, this results in toxicity to healthy cells that typically have fast turn-over such as in the hair folicle, skin, blood, gastrointestinal tract, and immune system. This systemic toxicity leads to significant side effects and limits the chemotherapeutic dose administered.

NM-mediated delivery of anti-cancer drugs can passively target tumors *via* the enhanced permeability and retention (EPR) effect (Maeda et al., 2013). EPR exploits the solid tumor physiology, which differs from normal tissue. As described in 1.1.4, the blood vessels of tumours deviates from the normal physiology. Of considerable interest is the defective and leaky endothelium.

In most tumours, the tumour vasculature is of irregular diameter and contains abnormal branching patterns. This increase in blood vessel permeability in the tumour environment allows the accumulation of large molecules (10-500 nm) from the tumour vessels to the interstitial space (Peer et al., 2007). This effect is compounded by the lack of efficient drainage from the lymphatic system (figure 1.3.2; (Peer et al., 2007). As a result of tumour targeting, NM-drug systems aim to increase the drug concentration within the tumour environment and, as a result, limit the drug concentration in normal tissue. NMs can also improve the solubility drugs for intravenous administration, increase drug stability, and improve cellular uptake of drugs (Danhier et al., 2010). Several passively tumour-targeted NM systems are in the advanced stages of development or have been clinically approved (Cho et al., 2008). Genexol-PM is a polymeric micelle NM formulation containing the chemotherapeutic drug paclitaxel (PTX) and is currently in phase II-IV clinical trials for breast, lung, pancreatic, bladder cancer (Ahn et al., 2014, Lv et al., 2014). A study using Genexol-PM combined with doxorubicin is also recruiting for phase II clinical trials for metastatic breast cancer (NCT01784120). Abraxane is another polymeric micelle NM formulation containing PTX that passively targets tumours (Hersh et al., 2015). PTX alone is highly toxic due to the pharmacological formulation used and non-specific dispersal of the drug throughout the body (Gradishar et al., 2005).

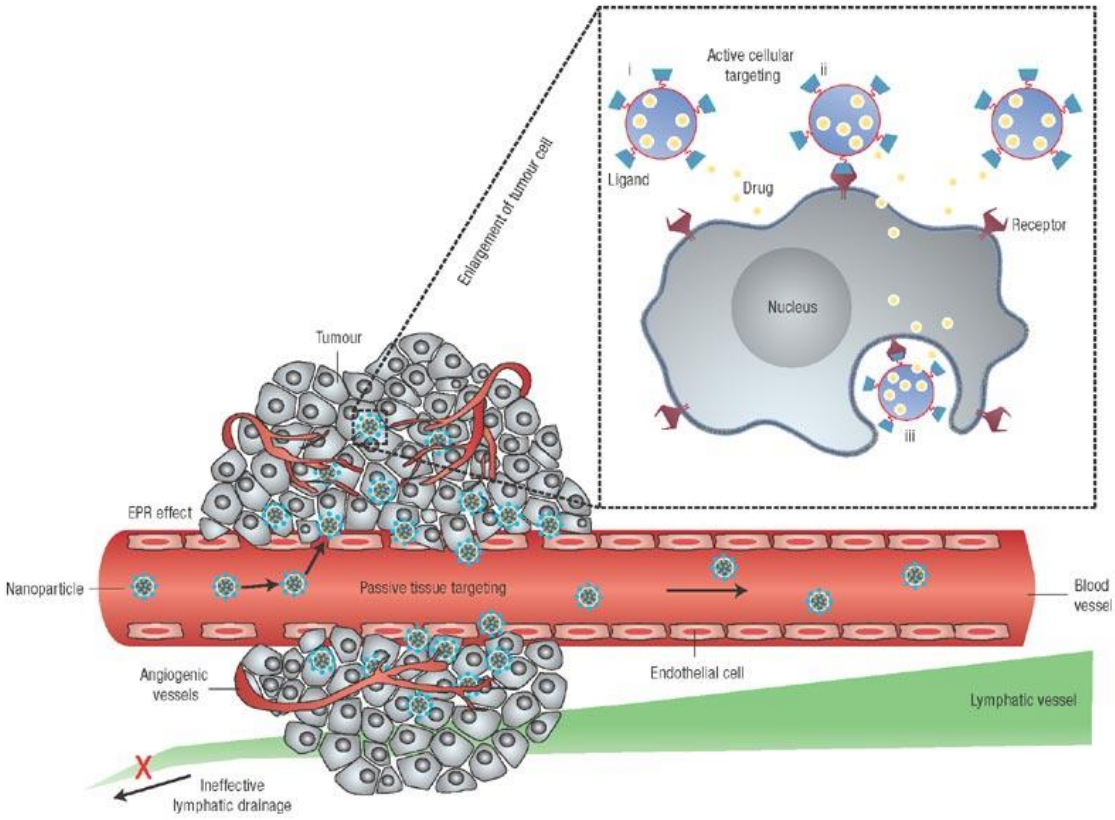

Figure 1.3.2 Passive and active targeting of NMs in the tumour microenvironment. Passive targeting of NMs is achieved by exploiting the tumour physiology. NMs are able to extravasate through the hyperpermeable vasculature and into the tumour tissue. The poor lymphatic drainage associated with solid tumours, increases the retention of the nanosystems in the tumour. Inset, NMs can actively target specific cell types ones they are located within the tumour. This is accomplished by the association of targeting moieties on the surface of the NMs that can interact with receptors on the surface of the target cell. The resulting interaction leads to receptor-mediated endocytosis of the NM and its payload. Figure from Peer et al., 2007.

Abraxane, containing non-covalently bound PTX, limits the toxicity by passively targeting the tumour (reducing systemic damage) and removes the need to use the toxic formulation of PTX. Abraxane is FDA approved for use in advanced pancreatic cancer, advanced non-small cell lung cancer, and advanced breast cancer (Miele et al., 2009). Passively tumour-targeted liposomes have also been FDA approved. Myocet (doxorubicin containing liposomes) is approved for breast cancer (Markman, 2006) and DaunoXome (daunorubicin containing liposomes) is approved for Kaposi sarcoma (Rivera, 2003, Rosenthal et al., 2002).

1.3.3 Active targeting of NMs in cancer

Despite the EPR effect being pre-clinically promising for increasing NM numbers at the tumour site, currently it does not appear to be as successful clinically (Prabhakar et al., 2013). There are concerns over relying solely on the EPR effect for the targeting of cancer therapeutics. Firstly, there is significant heterogenetity between tumours affecting pore size and blood vessel structure. Moreover, NMs do not passively target micro-metastasis before the tumour environment and its associated vasculature has been established. Furthermore, there is limited knowledge regarding which preclinical tumour models are reproducible in patient tumours and there is no guarantee that the drug payload will be to the cancer cells rather than the stroma. As a result, NM targeting can be unpredictable when depending on the EPR effect alone. Attention has therefore turned towards active targeting *via* cell-specific markers such as surface proteins (Byrne et al., 2008). Active targeting is achieved by conjugation of targeting moieties (such as proteins or antibodies) to the surface of the NM. Targeting moieties, rather than increasing NM tumour localisation, increase cellular internalisation

(Hatakeyama et al., 2007, Kirpotin et al., 2006). Increasing internalisation of NM-drug increases the therapeutic effect compared to the drug alone (Iinuma et al., 2002, Lopes De Menezes et al., 1998). Numerous targeted NMs are being developed for a range of cancers, comprising of different core materials, surface modifications, and targeting moieties (Byrne et al., 2008).

Potential targeting moieties are commonly surface located proteins that are upregulated on the target cell. General targets include proteins that are expressed in a range of tumours and look to exploit upregulated molecules associated with tumour-specific capabilities such as targeting angiogenesis and uncontrolled proliferation. Monoclonal antibodies to VEGF, overexpressed in cancers to promote tumour angiogenesis, have been conjugated to ferric oxide NPs to target glioma cells (Abakumov et al., 2015) and to silica NPs to selectively deliver the RTK inhibitor sunitinib to malignant glioblastoma xenograft mice (Goel et al., 2014). Other tumour vasculature targets include the integrin αvβ3 molecule, an endothelial cell receptor involved in cell-ECM interactions. The αvβ3 integrin is highly overexpressed on activated endothelial cells in the tumour-associated environment and has been demonstrated to be crucial for angiogenesis (Kumar, 2003). A cationic lipid-based NP conjugated to a small αvβ3 ligand and coupled showed specificity to αvβ3 through receptor-binding studies and cell adhesion experiments using melanoma cells (Hood et al., 2002). Moreover, after coupling to cDNA encoding ATP^{μ}-Raf, the αvβ3-targetted NPs lead to melanoma regression *in vitro* and regression of pulmonary and hepatic metastases of colon carcinoma after administration in mice (Hood et al., 2002). Like αvβ3 integrins, membrane type-1 (MT1) MMP is also expressed on the angiogenic endothelium and tumour cells (Sounni et al., 2002). MT1-MMP targeted liposomes suppressed colon carcinoma growth in xenograft mice (Kondo et al., 2004),

As uncontrolled proliferation is a major characteristic and biological capability of cancer cells, it is not surprising that there is great interest in targeting cell proliferation in oncology using NMs (as well as non-nanotheraputics). In breast cancer, the human epidermal growth factor receptor 2 (HER-2), a RTK, is a frequently investigated NP target as it is overexpressed in breast cancer and leads to uncontrolled proliferation. *In vitro* studies have shown poly(lactic-co-glycolic acid) (PLGA) conjugated with anti-HER-2 antibody fragments can internalise specifically in HER-2 positive cells (Chen et al., 2008). Significantly, the actively targeted PLGA-HER-2 NPs had a better therapeutic benefit compared to the drug alone after administration to HER-2 overexpressing tumour-bearing mice (Chen et al., 2008).

The epidermal growth factor receptor (EGFR) is a RTK expressed in over a third of solid tumours, including breast, lung, and colorectal, and is indicative of advanced disease and poor progression (Laskin and Sandler, 2004). PGLA NPs functionalised with an EGFR ligand and encapsulated with combinational drugs (including PTX and lonidamine (LON)). EGFR targeted PGLA-PTX/LON NPs decrease tumour volume and tumour weight in breast cancer xenograft mice, compared to the PTX/LON combination therapy (Milane et al., 2011).

As the molecular knowledge of individual tumour types expands, there has been an increase in the discovery of novel targets. Combination of specific targeting of distinct tumour types on a NM that increases cellular uptake of anti-cancer drugs, increases drug circulation times, a platform for combination therapy using multiple drugs, and acts as a theranostics agent, provides a powerful tool for drug delivery.

The fate of the NM after administration into an organism is determined by a number of factors, including the choice of targeting moiety on the NM surface (Coupland et al., 2009). Other physico-chemical properties identified as modulating

cellular uptake include the NM size (Jiang et al., 2008), shape, surface charge (Doherty and Mcmahon, 2009), and surface chemistry (Conner and Schmid, 2003, Jiang et al., 2011). The route of NM cellular uptake is important as it can influence the intracellular trafficking and ultimately the NM fate within the cell (Zhao et al., 2011). Generally, NMs are within a size range typical of cellular components and, as a result, can internalise into living cells by exploiting cellular endocytosis mechanisms (Conner and Schmid, 2003). The main endocytic pathways employed by NMs include macropinocytosis, caveolin-dependent endocytosis, clatherin-dependent endocytosis, and receptor-mediated endocytosis (Conner and Schmid, 2003). Macropinocytosis involves the engulfing of fluids and small materials, reported as between 0.5 – 10 µm, that reside in the extracellular environment through membrane invagination; inward folding of the plasma membrane over extracellular fluid containing materials such as NMs. The inward portion of the plasma membrane then buds off to form a macropinosome which internalises the engulfed material before transportation through the cytoplasm. In most cases the resulting macropinosome acidifies and decreases in size. In other cases, macropinosomes fuse with lysosomes (Canton and Battaglia, 2012). With receptor-mediated endocytosis, internalisation occurs from specific receptor-ligand interaction (Jiang et al., 2008). The most common receptor-mediated endocytic transport system is the clathrin-dependent pathway, where clathrin assembles into a lattice at the plasma membrane to form coated pits containing the internalised receptor and ligand (Conner and Schmid, 2003). Clathrin-mediated endocytosis can also occur as non-receptor mediated where clathrin proteins polymerise at the cell membrane without the presence of receptor-ligand interaction. In most cases of clathrin-dependent endocytosis, the endolysosomal pathway is

initiated and the engulfed material moves through intracellular compartments such as early endosomes, late endosomes, and lysosomes (Sandin et al., 2012).

1.3.4 NMs in a biological environment

The introduction of NMs in a biological environment (such as in the bloodstream after intravenous administration), results in biomolecules, such as lipids and proteins, associating with the NM surface. The NM coating formed is known as a protein corona (figure 1.3.3; (Walczyk et al., 2010). For NMs designed as theranostic agents, particularly those that are functionalised to interact with a specific cell type, the interface between the surface proteins of the cell and the surface of the NM dictates the physiological response of the cell. Once in a biological environment, the formation of the protein corona changes the characterisation of the NM and the cell can produce a different physiological response than predicted. By isolation of the associated proteins from the NM surface, it was observed that typically NM-protein interaction forms a hard corona composed of a few proteins that are strongly associated and slowly exchanging (Walczyk et al., 2010). The soft corona, on the other hand, provides an outer layer of weakly associated proteins that undergo rapid exchange with the free proteins in the biological environment (figure 1.3.3.a). The combination of proteins in the corona is likely to influence how the cell 'sees' the NM and the cellular response it evokes (figure 1.3.3.b; (Walczyk et al., 2010). The make-up of the absorbed proteins on the surface of a NM can determine its fate *in vivo*. Direct comparison of bare, PEGylated, and targeted liposomes with coronas formed from *in vivo* proteins and *in vitro* corona showed different composition of the resulting corona; *in vivo* coronas contained a wider range of proteins than coronas formed *in vitro* (Hadjidemetriou et al., 2015). Moreover, corona formation decreased receptor binding and cellular internalisation (Hadjidemetriou et al., 2015).

a

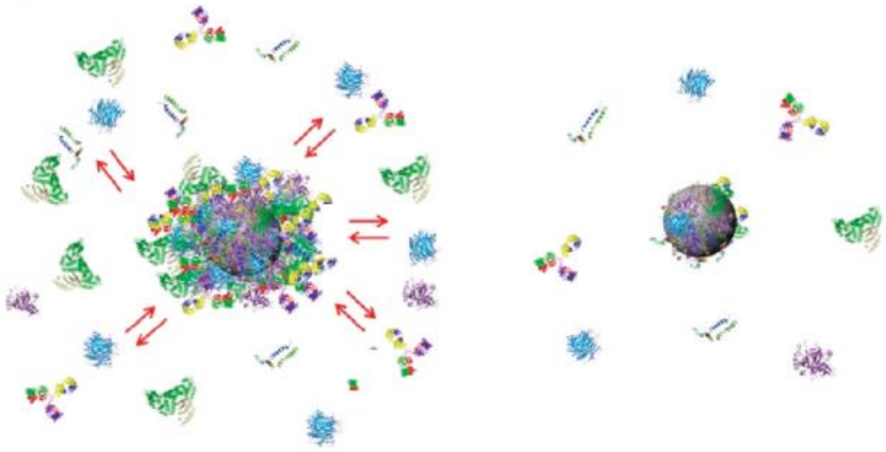

b

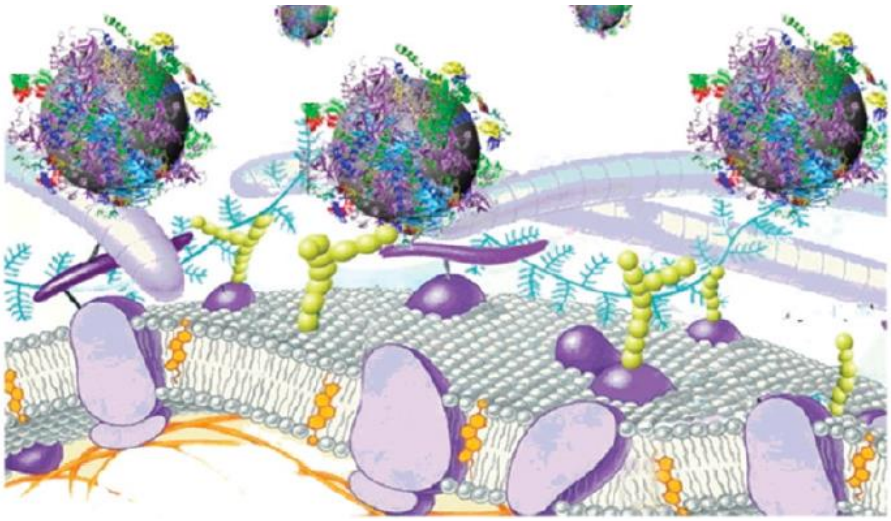

Figure 1.3.3 NMs in a biological environment and the protein corona. (a) In a biological environment, a NM forms a NM-protein complex. The associated protein on the surface of the NM is known as the protein corona. The outer layer is composed of weakly interacting proteins that undergo rapid exchange with free proteins in the local environment (top left). A hard corona, consisting of strongly associated proteins, is more stable and dissociates less readily from the surface of the NMs. (b) The formation of the protein corona affects how the cell recognises the NM at the bionanointerface. The protein corona may also mask any targeting moieties on the surface of the NM, and prevent interaction with a target receptor. Figure adapted from Walczyk et al., 2009.

Prolongation in circulation times of biomedical NMs is an important consideration, particularly in oncology where increased circulation time results in enhanced tumour drug uptake (Kwon et al., 1994, Lindner et al., 2004). A major hurdle is the avoidance of the reticuloendothelial system (RES). The RES is part of the immune system that consists of phagocytic cells. Macrophages, located in the liver and spleen, phagocytose NMs bound with serum protein (Moghimi et al., 2001). Specialised macrophages in the liver, called Kupffer cells, interact with NMs and remove them from the blood stream (Moghimi et al., 2001, Petros and Desimone, 2010). The design and surface functionalisation of biomedical NMs must therefore take into account the formation of a protein corona and consider how to increase circulation times. The development of 'stealth' NMs are thought to prevent opsonisation, increase circulation times *in vivo* (resulting in an increase in effectiveness of the EPR effect), and avoid rapid clearance from the RES (Larson et al., 2012). Hydrophilic polymers, such as poly(ethylene glycol) (PEG) have long been used to stabilise NMs and produce 'stealth' NMs (Klibanov et al., 1990, Uster et al., 1996, Woodle and Lasic, 1992).

1.3.5 NMs in the treatment of melanoma

Combining the aforementioned advantages of nanomaterials as drug delivery systems in oncology and the need for advancement in melanoma therapeutics, several groups have been investigating the use of nanotechnology for the treatment of melanoma. Strategies involve improving currently available cytotoxic drugs and making them less toxic to healthy cells. Docetaxel (DTX) is a potent broad-spectrum anti-tumour agent that is insoluble in water. As a result of its poor solubility, the drug is suspended in a

formulation vehicle containing Tween-80 and ethanol, which exhibits toxic effects (Yang et al., 2012). Ernsting et al. developed a NP formulation containing DTX (Ernsting et al., 2011). The NP formulation comprised a biocompatible carboxymethylcellulose polymer stabilised by conjugation of PEG, with DTX encapsulated. The formulation proved to induce less toxic side effects and improved accumulation of DTX in the tumour, resulting in improved efficacy (compared to the approved taxane nanoformulation, Abraxane) on the tumour burden in preclinical melanoma mouse model (Ernsting et al., 2012). Polycaprolactone NPs stabilised with PEG and encapsulated with DTX, also had significantly higher anti-tumour effect and lower systemic toxicity than DTX alone (Zheng et al., 2009).

Effective targeting of NMs to melanoma at the cellular level requires identification of upregulated surface markers. Functionalisation of the NM with a targeting moiety incites interaction between the NM and the melanoma cell. Several melanoma surface markers have been identified, providing promising targets for NM targeted therapy (Bombelli et al., 2014). The folate receptor is overexpressed on a range of cancerous cells, including melanoma (Skinner et al., 2016). NMs, with molecular imaging properties, conjugated to a folate ligand have shown to be selectively internalised in melanoma cell lines. Moreover, in a mouse subcutaneous B16 melanoma model, folate targeted NPs showed increased uptake in tumour tissue compared to the unconjugated NP alone (Rolfe et al., 2014). NMs have also been developed to target the tumour stroma and vasculature by aminopeptidase N (CD13) (Chen et al., 2010), neuropilin-1 (Sugahara et al., 2009), and CREKA to target fibrin-fibronectin and accumulate in the tumour vessels and stroma, resulting in clotting in the tumour blood vessels (Simberg et al., 2007). Amongst the most promising melanoma target is the MC1R. Numerous NMs with MC1R ligands have been

explored as potential therapeutic delivery systems for melanoma (Lu et al., 2009). The binding affinity of MC1R ligands was analysed in MC1R overexpressed cells. Selectivity to MC1R was confirmed by binding assays in cells with overexpressed members of the melanocortin family (MC2R, MC3R, MC4R, and MC5R; (Barkey et al., 2011). Furthermore, conjugation of the MC1R selective ligand to polymer micelle NP formulation did not affect the binding affinity to melanoma cells (Barkey et al., 2011). Interaction with MC1R ligands conjugated to NPs has been demonstrated to induce receptor-mediated transcytosis. PEGylated gold NPs surface functionalised with an MC1R agonist were internalised upon ligand-receptor binding, whereas NPs functionalised with an MC1R antagonist remained on the cell surface and were not internalised (Lu et al., 2012).

1.4 Thesis overview

The research aim of this project was to produce a targeted NM that could act as a drug delivery system for the treatment of metastatic melanoma. Ideally, the NM should act as a multi-model system, which acts as a therapeutic system as well as a diagnostic tool (a theranostic).

In Chapter 3, the synthesis of hydrophobic Fe_3O_4 NPs is described as well as the functionalisation of the resulting NPs to allow dispersion in an aqueous solution. Optimisation of the purification method is explored, to produce a biocompatible and safe nanosystem. NP surface modification to provide a stable system that is capable of targeting melanoma is also discussed before full characterisation.

In Chapter 4, due to the current lack of a full toxicity protocol to evaluate the safety of novel NMs, a comprehensive toxicity screening assay is presented. The

preclinical tool aims to quickly and accurately assess potential NM toxicity by combination of *in vitro* and *in vivo* toxicity models. Furthermore, the Fe_3O_4 NP developed in Chapter 3 will be subjected to this toxicity protocol in order to establish if it represents a safe and viable candidate for therapeutic use.

In Chapter 5, the effectiveness of Fe_3O_4 NPs as a biological tool will be assessed, including the cellular uptake of Fe_3O_4 NPs in melanoma cells. The NP will be further developed as a therapeutic agent by encapsulation of a chemotherapeutic drug before the efficacy of the system is evaluated.

Finally, in Chapter 6 all these findings are discussed in full detail within the wider content of the current literature.

1.5 References

Abakumov, M. A., Nukolova, N. V., Sokolsky-Papkov, M., Shein, S. A., Sandalova, T. O., Vishwasrao, H. M., Grinenko, N. F., Gubsky, I. L., Abakumov, A. M., Kabanov, A. V. & Chekhonin, V. P. 2015. VEGF-targeted magnetic nanoparticles for MRI visualization of brain tumor. *Nanomedicine,* 11**,** 825-33.

Abu-Elmagd, M., Garcia-Morales, C. & Wheeler, G. N. 2006. Frizzled7 mediates canonical Wnt signaling in neural crest induction. *Dev Biol,* 298**,** 285-98.

Acharya, U. H. & Jeter, J. M. 2013. Use of ipilimumab in the treatment of melanoma. *Clinical Pharmacology : Advances and Applications,* 5**,** 21-27.

Ahn, H. K., Jung, M., Sym, S. J., Shin, D. B., Kang, S. M., Kyung, S. Y., Park, J.-W., Jeong, S. H. & Cho, E. K. 2014. A phase II trial of Cremorphor EL-free paclitaxel (Genexol-PM) and gemcitabine in patients with advanced non-small cell lung cancer. *Cancer chemotherapy and pharmacology,* 74**,** 277-282.

Baillie, R., Carlile, J., Pendleton, N. & Schor, A. 2001. Prognostic value of vascularity and vascular endothelial growth factor expression in non-small cell lung cancer. *Journal of Clinical Pathology,* 54**,** 116-120.

Balch, C. M., Gershenwald, J. E., Soong, S.-J., Thompson, J. F., Atkins, M. B., Byrd, D. R., Buzaid, A. C., Cochran, A. J., Coit, D. G., Ding, S., Eggermont, A. M., Flaherty, K. T., Gimotty, P. A., Kirkwood, J. M., Mcmasters, K. M., Mihm, M. C., Morton, D. L., Ross, M. I., Sober, A. J. & Sondak, V. K. 2009. Final Version of 2009 AJCC Melanoma Staging and Classification. *Journal of Clinical Oncology,* 27**,** 6199-6206.

Barkey, N. M., Tafreshi, N. K., Josan, J. S., De Silva, C. R., Sill, K. N., Hruby, V. J., Gillies, R. J., Morse, D. L. & Vagner, J. 2011. Development of Melanoma-Targeted Polymer Micelles by Conjugation of a Melanocortin 1 Receptor (MC1R) Specific Ligand. *Journal of Medicinal Chemistry,* 54**,** 8078-8084.

Barok, M. & Szöllősi, J. 2011. Steps in metastasis research: Analyzing, collecting, and culturing circulating tumor cells. *Cytometry Part A,* 79A**,** 93-94.

Bellamy, C. O., Malcolmson, R. D., Harrison, D. J. & Wyllie, A. H. Cell death in health and disease: the biology and regulation of apoptosis. Seminars in cancer biology, 1995. Elsevier, 3-16.

Bentley, N. J., Eisen, T. & Goding, C. R. 1994. Melanocyte-specific expression of the human tyrosinase promoter: activation by the microphthalmia gene product and role of the initiator. *Mol Cell Biol,* 14**,** 7996-8006.

Bergers, G. & Song, S. 2005. The role of pericytes in blood-vessel formation and maintenance. *Neuro-Oncology,* 7**,** 452-464.

Bertoli, C., Skotheim, J. M. & De Bruin, R. a. M. 2013. Control of cell cycle transcription during G1 and S phases. *Nat Rev Mol Cell Biol,* 14**,** 518-528.

Bertolotto, C., Bille, K., Ortonne, J. P. & Ballotti, R. 1996. Regulation of tyrosinase gene expression by cAMP in B16 melanoma cells involves two CATGTG motifs surrounding the TATA box: implication of the microphthalmia gene product. *J Cell Biol,* 134**,** 747-55.

Bhatia, S., Tykodi, S. S. & Thompson, J. A. 2009. Treatment of Metastatic Melanoma: An Overview. *Oncology (Williston Park, N.Y.),* 23**,** 488-496.

Bier, E. 2005. Drosophila, the golden bug, emerges as a tool for human genetics. *Nat Rev Genet,* 6**,** 9-23.

Blanco, R. & Gerhardt, H. 2013. VEGF and Notch in Tip and Stalk Cell Selection. *Cold Spring Harbor Perspectives in Medicine,* 3**,** a006569.

Bombelli, F. B., Webster, C. A., Moncrieff, M. & Sherwood, V. 2014. The scope of nanoparticle therapies for future metastatic melanoma treatment. *Lancet Oncol,* 15**,** e22-32.

Bouwmeester, H., Dekkers, S., Noordam, M. Y., Hagens, W. I., Bulder, A. S., De Heer, C., Ten Voorde, S. E., Wijnhoven, S. W., Marvin, H. J. & Sips, A. J. 2009. Review of health safety aspects of nanotechnologies in food production. *Regul Toxicol Pharmacol,* 53**,** 52-62.

Brabletz, T. 2012. EMT and MET in Metastasis: Where Are the Cancer Stem Cells? *Cancer Cell,* 22**,** 699-701.

Byrne, J. D., Betancourt, T. & Brannon-Peppas, L. 2008. Active targeting schemes for nanoparticle systems in cancer therapeutics. *Adv Drug Deliv Rev,* 60**,** 1615-1626.

Campisi, J. & Di Fagagna, F. D. A. 2007. Cellular senescence: when bad things happen to good cells. *Nature reviews Molecular cell biology,* 8**,** 729-740.

Canavan, T. & Cantrell, W. 2016. Recognizing melanoma: Diagnosis and treatment options. *Nurse Pract,* 41**,** 24-9.

Canbay, A., Feldstein, A. E., Higuchi, H., Werneburg, N., Grambihler, A., Bronk, S. F. & Gores, G. J. 2003. Kupffer cell engulfment of apoptotic bodies stimulates death ligand and cytokine expression. *Hepatology,* 38**,** 1188-1198.

Cano, A., Perez-Moreno, M. A., Rodrigo, I., Locascio, A., Blanco, M. J., Del Barrio, M. G., Portillo, F. & Nieto, M. A. 2000. The transcription factor snail controls epithelial-mesenchymal transitions by repressing E-cadherin expression. *Nat Cell Biol,* 2**,** 76-83.

Canton, I. & Battaglia, G. 2012. Endocytosis at the nanoscale. *Chem Soc Rev,* 41**,** 2718-39.

Chapman , P. B., Hauschild , A., Robert , C., Haanen , J. B., Ascierto , P., Larkin , J., Dummer , R., Garbe , C., Testori , A., Maio , M., Hogg , D., Lorigan , P., Lebbe , C., Jouary , T., Schadendorf , D., Ribas , A., O'day , S. J., Sosman , J. A., Kirkwood , J. M., Eggermont , A. M. M., Dreno , B., Nolop , K., Li , J., Nelson , B., Hou , J., Lee , R. J., Flaherty , K. T. & Mcarthur , G. A. 2011. Improved Survival with Vemurafenib in Melanoma with BRAF V600E Mutation. *New England Journal of Medicine,* 364**,** 2507-2516.

Chen, Daniel s. & Mellman, I. 2013. Oncology Meets Immunology: The Cancer-Immunity Cycle. *Immunity,* 39**,** 1-10.

Chen, H., Gao, J., Lu, Y., Kou, G., Zhang, H., Fan, L., Sun, Z., Guo, Y. & Zhong, Y. 2008. Preparation and characterization of PE38KDEL-loaded anti-HER2 nanoparticles for targeted cancer therapy. *Journal of Controlled Release,* 128**,** 209-216.

Chen, Y., Wu, J. J. & Huang, L. 2010. Nanoparticles targeted with NGR motif deliver c-myc siRNA and doxorubicin for anticancer therapy. *Molecular Therapy,* 18**,** 828-834.

Chiu, G. N., Wong, M.-Y., Ling, L.-U., Shaikh, I. M., Tan, K.-B., Chaudhury, A. & Tan, B.-J. 2009. Lipid-based nanoparticulate systems for the delivery of anti-cancer drug cocktails: implications on pharmacokinetics and drug toxicities. *Current drug metabolism,* 10**,** 861-874.

Cho, K., Wang, X., Nie, S. & Shin, D. M. 2008. Therapeutic nanoparticles for drug delivery in cancer. *Clinical Cancer Research,* 14**,** 1310-1316.

Cockcroft, V., Osguthorpe, D., Barnard, E., Friday, A. & Lunt, G. 1990. Ligand-gated ion channels. *Molecular neurobiology,* 4**,** 129-169.

Conner, S. D. & Schmid, S. L. 2003. Regulated portals of entry into the cell. *Nature,* 422**,** 37-44.

Coultas, L., Chawengsaksophak, K. & Rossant, J. 2005. Endothelial cells and VEGF in vascular development. *Nature,* 438**,** 937-945.

Coupland, P. G., Briddon, S. J. & Aylott, J. W. 2009. Using fluorescent pH-sensitive nanosensors to report their intracellular location after Tat-mediated delivery. *Integr Biol (Camb),* 1**,** 318-23.

Crane, J. F. & Trainor, P. A. 2006. Neural crest stem and progenitor cells. *Annu Rev Cell Dev Biol,* 22**,** 267-86.

Crowson, A. N., Magro, C. M. & Mihm, M. C. 2006. Prognosticators of melanoma, the melanoma report, and the sentinel lymph node. *Mod Pathol,* 19**,** S71-S87.

Danhier, F., Feron, O. & Préat, V. 2010. To exploit the tumor microenvironment: Passive and active tumor targeting of nanocarriers for anti-cancer drug delivery. *Journal of Controlled Release,* 148**,** 135-146.

Davies, H., Bignell, G. R., Cox, C., Stephens, P., Edkins, S., Clegg, S., Teague, J., Woffendin, H., Garnett, M. J., Bottomley, W., Davis, N., Dicks, E., Ewing, R., Floyd, Y., Gray, K., Hall, S., Hawes, R., Hughes, J., Kosmidou, V., Menzies, A., Mould, C., Parker, A., Stevens, C., Watt, S., Hooper, S., Wilson, R., Jayatilake, H., Gusterson, B. A., Cooper, C., Shipley, J., Hargrave, D., Pritchard-Jones, K., Maitland, N., Chenevix-Trench, G., Riggins, G. J., Bigner, D. D., Palmieri, G., Cossu, A., Flanagan, A., Nicholson, A., Ho, J. W. C., Leung, S. Y., Yuen, S. T., Weber, B. L., Seigler, H. F., Darrow, T. L., Paterson, H., Marais, R., Marshall, C. J., Wooster, R., Stratton, M. R. & Futreal, P. A. 2002. Mutations of the BRAF gene in human cancer. *Nature,* 417**,** 949-954.

De Gruijl, F. R., Van Kranen, H. J. & Mullenders, L. H. F. 2001. UV-induced DNA damage, repair, mutations and oncogenic pathways in skin cancer. *Journal of Photochemistry and Photobiology B: Biology,* 63**,** 19-27.

De Robertis, E. M. 2006. Spemann's organizer and self-regulation in amphibian embryos. *Nat Rev Mol Cell Biol,* 7**,** 296-302.

Deardorff, M. A., Tan, C., Saint-Jeannet, J. P. & Klein, P. S. 2001. A role for frizzled 3 in neural crest development. *Development,* 128**,** 3655-63.

Dickson, P. V. & Gershenwald, J. E. 2011. Staging and Prognosis of Cutaneous Melanoma. *Surgical oncology clinics of North America,* 20**,** 1-17.

Doherty, G. J. & Mcmahon, H. T. 2009. Mechanisms of endocytosis. *Annu Rev Biochem,* 78**,** 857-902.

Dorsam, R. T. & Gutkind, J. S. 2007. G-protein-coupled receptors and cancer. *Nat Rev Cancer,* 7**,** 79-94.

Du, J., Widlund, H. R., Horstmann, M. A., Ramaswamy, S., Ross, K., Huber, W. E., Nishimura, E. K., Golub, T. R. & Fisher, D. E. 2004. Critical role of CDK2 for melanoma growth linked to its melanocyte-specific transcriptional regulation by MITF. *Cancer Cell,* 6**,** 565-576.

Dupin, E., Real, C., Glavieux-Pardanaud, C., Vaigot, P. & Le Douarin, N. M. 2003. Reversal of developmental restrictions in neural crest lineages: Transition from Schwann cells to glial-melanocytic precursors in vitro. *Proceedings of the National Academy of Sciences,* 100**,** 5229-5233.

Dye, D. E., Medic, S., Ziman, M. & Coombe, D. R. 2013. Melanoma biomolecules: independently identified but functionally intertwined. *Frontiers in Oncology,* 3.

Egeblad, M., Nakasone, E. S. & Werb, Z. 2010. Tumors as organs: complex tissues that interface with the entire organism. *Developmental cell,* 18**,** 884-901.

Ernsting, M. J., Murakami, M., Undzys, E., Aman, A., Press, B. & Li, S. D. 2012. A docetaxel-carboxymethylcellulose nanoparticle outperforms the approved taxane nanoformulation, Abraxane, in mouse tumor models with significant control of metastases. *J Control Release,* 162**,** 575-81.

Ernsting, M. J., Tang, W. L., Maccallum, N. & Li, S. D. 2011. Synthetic modification of carboxymethylcellulose and use thereof to prepare a nanoparticle forming conjugate of docetaxel for enhanced cytotoxicity against cancer cells. *Bioconjug Chem,* 22**,** 2474-86.

Ferlay, J., Soerjomataram, I., Ervik, M., Dikshit, R., Eser, S., Mathers, C., Rebelo, M., Parkin, Dm., Forman, D., Bray, F. 2013. *Cancer Incidence and Mortality Worldwide: IARC CancerBase No. 11 [Internet]* [Online]. Lyon, France: GLOBOCAN 2012 v1.0. Available: http://globocan.iarc.fr [Accessed 01/01/2016 2016].

Fidler, I. J. 1970. Metastasis: quantitative analysis of distribution and fate of tumor emboli labeled with 125 I-5-iodo-2'-deoxyuridine. *J Natl Cancer Inst,* 45**,** 773-82.

Flaherty , K. T., Puzanov , I., Kim , K. B., Ribas , A., Mcarthur , G. A., Sosman , J. A., O'dwyer , P. J., Lee , R. J., Grippo , J. F., Nolop , K. & Chapman , P. B. 2010. Inhibition of Mutated, Activated BRAF in Metastatic Melanoma. *New England Journal of Medicine,* 363**,** 809-819.

Fuertes, M. B., Girart, M. V., Molinero, L. L., Domaica, C. I., Rossi, L. E., Barrio, M. M., Mordoh, J., Rabinovich, G. A. & Zwirner, N. W. 2008. Intracellular retention of the NKG2D ligand MHC class I chain-related gene A in human melanomas confers immune privilege and prevents NK cell-mediated cytotoxicity. *J Immunol,* 180**,** 4606-14.

Gajewski, T. F. 2006. Identifying and overcoming immune resistance mechanisms in the melanoma tumor microenvironment. *Clinical Cancer Research,* 12**,** 2326s-2330s.

Gee, M. S., Procopio, W. N., Makonnen, S., Feldman, M. D., Yeilding, N. M. & Lee, W. M. F. 2003. Tumor Vessel Development and Maturation Impose Limits on the Effectiveness of Anti-Vascular Therapy. *The American Journal of Pathology,* 162**,** 183-193.

Goel, S., Chen, F., Hong, H., Valdovinos, H. F., Hernandez, R., Shi, S., Barnhart, T. E. & Cai, W. 2014. VEGF121-Conjugated Mesoporous Silica Nanoparticle: A Tumor Targeted Drug Delivery System. *ACS Applied Materials & Interfaces,* 6**,** 21677-21685.

Gradishar, W. J., Tjulandin, S., Davidson, N., Shaw, H., Desai, N., Bhar, P., Hawkins, M. & O'shaughnessy, J. 2005. Phase III trial of nanoparticle albumin-bound paclitaxel compared with polyethylated castor oil–based paclitaxel in women with breast cancer. *Journal of Clinical Oncology,* 23**,** 7794-7803.

Hadjidemetriou, M., Al-Ahmady, Z., Mazza, M., Collins, R. F., Dawson, K. & Kostarelos, K. 2015. In Vivo Biomolecule Corona around Blood-Circulating, Clinically Used and Antibody-Targeted Lipid Bilayer Nanoscale Vesicles. *ACS nano,* 9**,** 8142-8156.

Hanahan, D. & Weinberg, R. A. 2000. The Hallmarks of Cancer. *Cell,* 100**,** 57-70.

Hanahan, D. & Weinberg, Robert a. 2011. Hallmarks of Cancer: The Next Generation. *Cell,* 144**,** 646-674.

Hao, M.-Z., Zhou, W.-Y., Du, X.-L., Chen, K.-X., Wang, G.-W., Yang, Y. & Yang, J.-L. 2014. Novel anti-melanoma treatment: focus on immunotherapy. *Chinese Journal of Cancer,* 33**,** 458-465.

Hatakeyama, H., Akita, H., Ishida, E., Hashimoto, K., Kobayashi, H., Aoki, T., Yasuda, J., Obata, K., Kikuchi, H., Ishida, T., Kiwada, H. & Harashima, H. 2007. Tumor targeting of doxorubicin by anti-MT1-MMP antibody-modified PEG liposomes. *Int J Pharm,* 342**,** 194-200.

Hemesath, T. J., Steingrimsson, E., Mcgill, G., Hansen, M. J., Vaught, J., Hodgkinson, C. A., Arnheiter, H., Copeland, N. G., Jenkins, N. A. & Fisher, D. E. 1994. Microphthalmia, a critical factor in melanocyte development, defines a discrete transcription factor family. *Genes & development,* 8**,** 2770-2780.

Hersh, E. M., Del Vecchio, M., Brown, M., Kefford, R., Loquai, C., Testori, A., Bhatia, S., Gutzmer, R., Conry, R. & Haydon, A. 2015. A randomized, controlled phase III trial of nab-Paclitaxel versus dacarbazine in chemotherapy-naïve patients with metastatic melanoma. *Annals of Oncology***,** mdv324.

Hill, G. J., 2nd, Krementz, E. T. & Hill, H. Z. 1984. Dimethyl triazeno imidazole carboxamide and combination therapy for melanoma. IV. Late results after complete response to chemotherapy (Central Oncology Group protocols 7130, 7131, and 7131A). *Cancer,* 53**,** 1299-305.

Hodi, F. S., O'day, S. J., Mcdermott, D. F., Weber, R. W., Sosman, J. A., Haanen, J. B., Gonzalez, R., Robert, C., Schadendorf, D., Hassel, J. C., Akerley, W., Van Den Eertwegh, A. J., Lutzky, J., Lorigan, P., Vaubel, J. M., Linette, G. P., Hogg, D., Ottensmeier, C. H., Lebbe, C., Peschel, C., Quirt, I., Clark, J. I., Wolchok, J. D., Weber, J. S., Tian, J., Yellin, M. J., Nichol, G. M., Hoos, A. & Urba, W. J. 2010. Improved survival with ipilimumab in patients with metastatic melanoma. *N Engl J Med,* 363**,** 711-23.

Honore, S. M., Aybar, M. J. & Mayor, R. 2003. Sox10 is required for the early development of the prospective neural crest in Xenopus embryos. *Dev Biol,* 260**,** 79-96.

Hood, J. D., Bednarski, M., Frausto, R., Guccione, S., Reisfeld, R. A., Xiang, R. & Cheresh, D. A. 2002. Tumor Regression by Targeted Gene Delivery to the Neovasculature. *Science,* 296**,** 2404-2407.

Hu, C.-M. J. & Zhang, L. 2012. Nanoparticle-based combination therapy toward overcoming drug resistance in cancer. *Biochemical Pharmacology,* 83**,** 1104-1111.

Hubbard, S. R. 1999. Structural analysis of receptor tyrosine kinases. *Prog Biophys Mol Biol,* 71**,** 343-58.

Iinuma, H., Maruyama, K., Okinaga, K., Sasaki, K., Sekine, T., Ishida, O., Ogiwara, N., Johkura, K. & Yonemura, Y. 2002. Intracellular targeting therapy of cisplatin-encapsulated transferrin-polyethylene glycol liposome on peritoneal dissemination of gastric cancer. *Int J Cancer,* 99**,** 130-7.

Itakura, J., Ishiwata, T., Shen, B., Kornmann, M. & Korc, M. 2000. Concomitant over-expression of vascular endothelial growth factor and its receptors in pancreatic cancer. *Int J Cancer,* 85**,** 27-34.

Jethwa, P., Naqvi, M., Hardy, R. G., Hotchin, N. A., Roberts, S., Spychal, R. & Tselepis, C. 2008. Overexpression of Slug is associated with malignant progression of esophageal adenocarcinoma. *World Journal of Gastroenterology,* 14**,** 1044.

Jiang, W., Kimbetty, Y. S., Rutka, J. T. & Chanwarren, C. W. 2008. Nanoparticle-mediated cellular response is size-dependent. *Nat Nano,* 3**,** 145-150.

Jiang, X., Musyanovych, A., Rocker, C., Landfester, K., Mailander, V. & Nienhaus, G. U. 2011. Specific effects of surface carboxyl groups on anionic polystyrene particles in their interactions with mesenchymal stem cells. *Nanoscale,* 3**,** 2028-2035.

Johnson, D. B. & Sosman, J. A. 2015. Therapeutic advances and treatment options in metastatic melanoma. *JAMA Oncology,* 1**,** 380-386.

Katritch, V., Cherezov, V. & Stevens, R. C. 2013. Structure-Function of the G-protein-Coupled Receptor Superfamily. *Annual review of pharmacology and toxicology,* 53**,** 531-556.

Kennedy, C., Ter Huurne, J., Berkhout, M., Gruis, N., Bastiaens, M., Bergman, W., Willemze, R. & Bouwes Bavinck, J. N. 2001. Melanocortin 1 Receptor (MC1R) Gene Variants are Associated with an Increased Risk for Cutaneous Melanoma Which is Largely Independent of Skin Type and Hair Color. *Journal of Investigative Dermatology,* 117**,** 294-300.

Kim, K. J., Li, B., Winer, J., Armanini, M., Gillett, N., Phillips, H. S. & Ferrara, N. 1993. Inhibition of vascular endothelial growth factor-induced angiogenesis suppresses tumour growth in vivo. *Nature,* 362**,** 841-4.

Kirpotin, D. B., Drummond, D. C., Shao, Y., Shalaby, M. R., Hong, K., Nielsen, U. B., Marks, J. D., Benz, C. C. & Park, J. W. 2006. Antibody targeting of long-

circulating lipidic nanoparticles does not increase tumor localization but does increase internalization in animal models. *Cancer Res,* 66**,** 6732-40.

Klein, G. 1998. Foulds' dangerous idea revisited: the multistep development of tumors 40 years later. *Adv Cancer Res,* 72**,** 1-23.

Klibanov, A. L., Maruyama, K., Torchilin, V. P. & Huang, L. 1990. Amphipathic polyethyleneglycols effectively prolong the circulation time of liposomes. *FEBS Lett,* 268**,** 235-7.

Kobilka, B. K. 2007. G protein coupled receptor structure and activation. *Biochimica et Biophysica Acta (BBA) - Biomembranes,* 1768**,** 794-807.

Kondo, M., Asai, T., Katanasaka, Y., Sadzuka, Y., Tsukada, H., Ogino, K., Taki, T., Baba, K. & Oku, N. 2004. Anti-neovascular therapy by liposomal drug targeted to membrane type-1 matrix metalloproteinase. *Int J Cancer,* 108**,** 301-306.

Krebs, M. G., Hou, J.-M., Ward, T. H., Blackhall, F. H. & Dive, C. 2010. Circulating tumour cells: their utility in cancer management and predicting outcomes. *Therapeutic Advances in Medical Oncology,* 2**,** 351-365.

Krummel, M. F. & Allison, J. P. 1995. CD28 and CTLA-4 have opposing effects on the response of T cells to stimulation. *The journal of experimental medicine,* 182**,** 459-465.

Kumar, C. C. 2003. Integrin alpha v beta 3 as a therapeutic target for blocking tumor-induced angiogenesis. *Curr Drug Targets,* 4**,** 123-31.

Kwon, G., Suwa, S., Yokoyama, M., Okano, T., Sakurai, Y. & Kataoka, K. 1994. Enhanced tumor accumulation and prolonged circulation times of micelle-forming poly (ethylene oxide-aspartate) block copolymer-adriamycin conjugates. *Journal of Controlled Release,* 29**,** 17-23.

Labonne, C. & Bronner-Fraser, M. 1998. Neural crest induction in Xenopus: evidence for a two-signal model. *Development,* 125**,** 2403-14.

Langley, R. R. & Fidler, I. J. 2011. The seed and soil hypothesis revisited - the role of tumor-stroma interactions in metastasis to different organs. *International journal of cancer. Journal international du cancer,* 128**,** 2527-2535.

Larkin, J., Chiarion-Sileni, V., Gonzalez, R., Grob, J. J., Cowey, C. L., Lao, C. D., Schadendorf, D., Dummer, R., Smylie, M., Rutkowski, P., Ferrucci, P. F., Hill, A., Wagstaff, J., Carlino, M. S., Haanen, J. B., Maio, M., Marquez-Rodas, I., Mcarthur, G. A., Ascierto, P. A., Long, G. V., Callahan, M. K., Postow, M. A., Grossmann, K., Sznol, M., Dreno, B., Bastholt, L., Yang, A., Rollin, L. M.,

Horak, C., Hodi, F. S. & Wolchok, J. D. 2015. Combined Nivolumab and Ipilimumab or Monotherapy in Untreated Melanoma. *New England Journal of Medicine,* 373**,** 23-34.

Larson, T. A., Joshi, P. P. & Sokolov, K. 2012. Preventing Protein Adsorption and Macrophage Uptake of Gold Nanoparticles via a Hydrophobic Shield. *ACS nano,* 6**,** 9182-9190.

Laskin, J. J. & Sandler, A. B. 2004. Epidermal growth factor receptor: a promising target in solid tumours. *Cancer Treat Rev,* 30**,** 1-17.

Lemmon, M. A. & Schlessinger, J. 2010. Cell signaling by receptor tyrosine kinases. *Cell,* 141**,** 1117-1134.

Lens, M. B. & Dawes, M. 2004. Global perspectives of contemporary epidemiological trends of cutaneous malignant melanoma. *British Journal of Dermatology,* 150**,** 179-185.

Leu, A. J., Berk, D. A., Lymboussaki, A., Alitalo, K. & Jain, R. K. 2000. Absence of functional lymphatics within a murine sarcoma: a molecular and functional evaluation. *Cancer Res,* 60**,** 4324-7.

Levy, C., Khaled, M. & Fisher, D. E. 2006. MITF: master regulator of melanocyte development and melanoma oncogene. *Trends in Molecular Medicine,* 12**,** 406-414.

Lindner, L. H., Eichhorn, M. E., Eibl, H., Teichert, N., Schmitt-Sody, M., Issels, R. D. & Dellian, M. 2004. Novel temperature-sensitive liposomes with prolonged circulation time. *Clinical Cancer Research,* 10**,** 2168-2178.

Linos, E., Swetter, S. M., Cockburn, M. G., Colditz, G. A. & Clarke, C. A. 2009. Increasing Burden of Melanoma in the United States. *Journal of Investigative Dermatology,* 129**,** 1666-1674.

Liotta, L. & Petricoin, E. 2000. Molecular profiling of human cancer. *Nat Rev Genet,* 1**,** 48-56.

Liotta, L. A. & Kohn, E. C. 2001. The microenvironment of the tumour–host interface. *Nature,* 411**,** 375-379.

Lopes De Menezes, D. E., Pilarski, L. M. & Allen, T. M. 1998. In vitro and in vivo targeting of immunoliposomal doxorubicin to human B-cell lymphoma. *Cancer Res,* 58**,** 3320-30.

Lu, W., Xiong, C., Zhang, G., Huang, Q., Zhang, R., Zhang, J. Z. & Li, C. 2009. Targeted Photothermal Ablation of Murine Melanomas with Melanocyte-

Stimulating Hormone Analog-Conjugated Hollow Gold Nanospheres. *Clin Cancer Res,* 15**,** 876-886.

Lu, W., Xiong, C., Zhang, R., Shi, L., Huang, M., Zhang, G., Song, S., Huang, Q., Liu, G.-Y. & Li, C. 2012. Receptor-mediated transcytosis: A mechanism for active extravascular transport of nanoparticles in solid tumors. *Journal of Controlled Release,* 161**,** 959-966.

Lv, F., Cao, J., Zhang, J., Qian, J., Peng, W., Sun, S., Li, W., Zhang, W., Guo, W. & Li, J. 2014. Phase I and pharmacokinetic study of polymeric micelle-formulated paclitaxel in adult Chinese patients with advanced solid tumors. *Cancer chemotherapy and pharmacology,* 73**,** 1173-1179.

Maeda, H., Nakamura, H. & Fang, J. 2013. The EPR effect for macromolecular drug delivery to solid tumors: Improvement of tumor uptake, lowering of systemic toxicity, and distinct tumor imaging in vivo. *Adv Drug Deliv Rev,* 65**,** 71-9.

Markman, M. 2006. Pegylated liposomal doxorubicin in the treatment of cancers of the breast and ovary. *Expert Opin Pharmacother,* 7**,** 1469-74.

Martin, T. A., Ye, L., Sanders, A. J., Lane, J. & Jiang, W. G. 2000. Cancer invasion and metastasis: molecular and cellular perspective. *Madame Curie Bioscience Database [Internet]*.

Mcgill, G. G., Horstmann, M., Widlund, H. R., Du, J., Motyckova, G., Nishimura, E. K., Lin, Y. L., Ramaswamy, S., Avery, W., Ding, H. F., Jordan, S. A., Jackson, I. J., Korsmeyer, S. J., Golub, T. R. & Fisher, D. E. 2002. Bcl2 regulation by the melanocyte master regulator Mitf modulates lineage survival and melanoma cell viability. *Cell,* 109**,** 707-18.

Mcintyre, R. A. 2012. Common nano-materials and their use in real world applications. *Sci Prog,* 95**,** 1-22.

Mervic, L. 2012. Time Course and Pattern of Metastasis of Cutaneous Melanoma Differ between Men and Women. *PLoS ONE,* 7**,** e32955.

Miele, E., Spinelli, G. P., Miele, E., Tomao, F. & Tomao, S. 2009. Albumin-bound formulation of paclitaxel (Abraxane ABI-007) in the treatment of breast cancer. *Int J Nanomedicine,* 4**,** 99-105.

Milane, L., Duan, Z. & Amiji, M. 2011. Therapeutic Efficacy and Safety of Paclitaxel/Lonidamine Loaded EGFR-Targeted Nanoparticles for the Treatment of Multi-Drug Resistant Cancer. *PLoS ONE,* 6**,** e24075.

Moghimi, S. M., Hunter, A. C. & Murray, J. C. 2001. Long-circulating and target-specific nanoparticles: theory to practice. *Pharmacological reviews,* 53**,** 283-318.

Morrison, S. J., Shah, N. M. & Anderson, D. J. 1997. Regulatory mechanisms in stem cell biology. *Cell,* 88**,** 287-298.

Mort, R. L., Jackson, I. J. & Patton, E. E. 2015. The melanocyte lineage in development and disease. *Development,* 142**,** 620-632.

Muthukkaruppan, V. R., Kubai, L. & Auerbach, R. 1982. Tumor-induced neovascularization in the mouse eye. *J Natl Cancer Inst,* 69**,** 699-708.

Nazarian, R., Shi, H., Wang, Q., Kong, X., Koya, R. C., Lee, H., Chen, Z., Lee, M.-K., Attar, N. & Sazegar, H. 2010. Melanomas acquire resistance to B-RAF (V600E) inhibition by RTK or N-RAS upregulation. *Nature,* 468**,** 973-977.

Nieto, M. A., Sargent, M. G., Wilkinson, D. G. & Cooke, J. 1994. Control of cell behavior during vertebrate development by Slug, a zinc finger gene. *Science,* 264**,** 835-9.

Onder, T. T., Gupta, P. B., Mani, S. A., Yang, J., Lander, E. S. & Weinberg, R. A. 2008. Loss of E-cadherin promotes metastasis via multiple downstream transcriptional pathways. *Cancer Res,* 68**,** 3645-3654.

Padera, T. P., Kadambi, A., Di Tomaso, E., Carreira, C. M., Brown, E. B., Boucher, Y., Choi, N. C., Mathisen, D., Wain, J., Mark, E. J., Munn, L. L. & Jain, R. K. 2002. Lymphatic metastasis in the absence of functional intratumor lymphatics. *Science,* 296**,** 1883-6.

Palmer, J. S., Duffy, D. L., Box, N. F., Aitken, J. F., O'gorman, L. E., Green, A. C., Hayward, N. K., Martin, N. G. & Sturm, R. A. 2000. Melanocortin-1 receptor polymorphisms and risk of melanoma: is the association explained solely by pigmentation phenotype? *Am J Hum Genet,* 66**,** 176-86.

Parangi, S., O'reilly, M., Christofori, G., Holmgren, L., Grosfeld, J., Folkman, J. & Hanahan, D. 1996. Antiangiogenic therapy of transgenic mice impairs de novo tumor growth. *Proc Natl Acad Sci U S A,* 93**,** 2002-7.

Pardoll, D. M. 2012a. The blockade of immune checkpoints in cancer immunotherapy. *Nature Reviews Cancer,* 12**,** 252-264.

Pardoll, D. M. 2012b. The blockade of immune checkpoints in cancer immunotherapy. *Nat Rev Cancer,* 12**,** 252-64.

Pawson, T. & Scott, J. D. 1997. Signaling through scaffold, anchoring, and adaptor proteins. *Science,* 278**,** 2075-2080.

Peer, D., Karp, J. M., Hong, S., Farokhzad, O. C., Margalit, R. & Langer, R. 2007. Nanocarriers as an emerging platform for cancer therapy. *Nat Nano,* 2**,** 751-760.

Pendergast, A. M., Quilliam, L. A., Cripe, L. D., Bassing, C. H., Dai, Z., Li, N., Batzer, A., Rabun, K. M., Der, C. J. & Schlessinger, J. 1993. BCR-ABL-induced oncogenesis is mediated by direct interaction with the SH2 domain of the GRB-2 adaptor protein. *Cell,* 75**,** 175-185.

Petros, R. A. & Desimone, J. M. 2010. Strategies in the design of nanoparticles for therapeutic applications. *Nat Rev Drug Discov,* 9**,** 615-627.

Phng, L.-K. & Gerhardt, H. 2009. Angiogenesis: a team effort coordinated by notch. *Developmental cell,* 16**,** 196-208.

Porter, A. L. & Youtie, J. 2009. How interdisciplinary is nanotechnology? *Journal of Nanoparticle Research,* 11**,** 1023-1041.

Poulikakos, P. I., Persaud, Y., Janakiraman, M., Kong, X., Ng, C., Moriceau, G., Shi, H., Atefi, M., Titz, B. & Gabay, M. T. 2011. RAF inhibitor resistance is mediated by dimerization of aberrantly spliced BRAF (V600E). *Nature,* 480**,** 387-390.

Prabhakar, U., Maeda, H., Jain, R. K., Sevick-Muraca, E. M., Zamboni, W., Farokhzad, O. C., Barry, S. T., Gabizon, A., Grodzinski, P. & Blakey, D. C. 2013. Challenges and key considerations of the enhanced permeability and retention effect for nanomedicine drug delivery in oncology. *Cancer Res,* 73**,** 2412-7.

Qin, L., Liao, L., Redmond, A., Young, L., Yuan, Y., Chen, H., O'malley, B. W. & Xu, J. 2008. The AIB1 oncogene promotes breast cancer metastasis by activation of PEA3-mediated matrix metalloproteinase 2 (MMP2) and MMP9 expression. *Molecular and cellular biology,* 28**,** 5937-5950.

Reiland, J., Kempf, D., Roy, M., Denkins, Y. & Marchetti, D. 2006. FGF2 binding, signaling, and angiogenesis are modulated by heparanase in metastatic melanoma cells. *Neoplasia,* 8**,** 596-606.

Rivera, E. 2003. Current status of liposomal anthracycline therapy in metastatic breast cancer. *Clin Breast Cancer,* 4 Suppl 2**,** S76-83.

Rizos, H., Menzies, A. M., Pupo, G. M., Carlino, M. S., Fung, C., Hyman, J., Haydu, L. E., Mijatov, B., Becker, T. M., Boyd, S. C., Howle, J., Saw, R., Thompson, J. F., Kefford, R. F., Scolyer, R. A. & Long, G. V. 2014. BRAF inhibitor resistance mechanisms in metastatic melanoma: spectrum and clinical impact. *Clin Cancer Res,* 20**,** 1965-77.

Robert, C., Ribas, A., Wolchok, J. D., Hodi, F. S., Hamid, O., Kefford, R., Weber, J. S., Joshua, A. M., Hwu, W.-J., Gangadhar, T. C., Patnaik, A., Dronca, R., Zarour, H., Joseph, R. W., Boasberg, P., Chmielowski, B., Mateus, C., Postow, M. A., Gergich, K., Elassaiss-Schaap, J., Li, X. N., Iannone, R., Ebbinghaus, S. W., Kang, S. P. & Daud, A. Anti-programmed-death-receptor-1 treatment with pembrolizumab in ipilimumab-refractory advanced melanoma: a randomised dose-comparison cohort of a phase 1 trial. *The Lancet,* 384**,** 1109-1117.

Rolfe, B. E., Blakey, I., Squires, O., Peng, H., Boase, N. R. B., Alexander, C., Parsons, P. G., Boyle, G. M., Whittaker, A. K. & Thurecht, K. J. 2014. Multimodal Polymer Nanoparticles with Combined 19F Magnetic Resonance and Optical Detection for Tunable, Targeted, Multimodal Imaging in Vivo. *J Am Chem Soc,* 136**,** 2413-2419.

Rosenthal, E., Poizot-Martin, I., Saint-Marc, T., Spano, J. P. & Cacoub, P. 2002. Phase IV study of liposomal daunorubicin (DaunoXome) in AIDS-related Kaposi sarcoma. *Am J Clin Oncol,* 25**,** 57-9.

Roskoski, R. 2007. Vascular endothelial growth factor (VEGF) signaling in tumor progression. *Critical reviews in oncology/hematology,* 62**,** 179-213.

Rotte, A., Martinka, M. & Li, G. 2012. MMP2 expression is a prognostic marker for primary melanoma patients. *Cell Oncol (Dordr),* 35**,** 207-16.

Salata, O. 2004. Applications of nanoparticles in biology and medicine. *Journal of Nanobiotechnology,* 2**,** 1-6.

Sandin, P., Fitzpatrick, L. W., Simpson, J. C. & Dawson, K. A. 2012. High-Speed Imaging of Rab Family Small GTPases Reveals Rare Events in Nanoparticle Trafficking in Living Cells. *ACS nano,* 6**,** 1513-1521.

Sauka-Spengler, T. & Bronner-Fraser, M. 2008. A gene regulatory network orchestrates neural crest formation. *Nature reviews Molecular cell biology,* 9**,** 557-568.

Schroeder, A., Heller, D. A., Winslow, M. M., Dahlman, J. E., Pratt, G. W., Langer, R., Jacks, T. & Anderson, D. G. 2012. Treating metastatic cancer with nanotechnology. *Nat Rev Cancer,* 12**,** 39-50.

Shaikh, W. R., Dusza, S. W., Weinstock, M. A., Oliveria, S. A., Geller, A. C. & Halpern, A. C. 2016. Melanoma Thickness and Survival Trends in the United States, 1989 to 2009. *J Natl Cancer Inst,* 108.

Shapira, A., Livney, Y. D., Broxterman, H. J. & Assaraf, Y. G. 2011. Nanomedicine for targeted cancer therapy: towards the overcoming of drug resistance. *Drug resistance updates,* 14**,** 150-163.

Shibahara, S., Takeda, K., Yasumoto, K.-I., Udono, T., Watanabe, K.-I., Saito, H. & Takahashi, K. Microphthalmia-associated transcription factor (MITF): multiplicity in structure, function, and regulation. Journal of Investigative Dermatology Symposium Proceedings, 2001. Nature Publishing Group, 99-104.

Shtivelman, E., Davies, M. A., Hwu, P., Yang, J., Lotem, M., Oren, M., Flaherty, K. T. & Fisher, D. E. 2014. *Pathways and therapeutic targets in melanoma*, Oncotarget.

Shyamala, K., Yanduri, S., Girish, H. C. & Murgod, S. 2015. Neural crest: The fourth germ layer. *J Oral Maxillofac Pathol,* 19**,** 221-9.

Siemann, D. W. 2011. The unique characteristics of tumor vasculature and preclinical evidence for its selective disruption by Tumor-Vascular Disrupting Agents. *Cancer treatment reviews,* 37**,** 63-74.

Simberg, D., Duza, T., Park, J. H., Essler, M., Pilch, J., Zhang, L., Derfus, A. M., Yang, M., Hoffman, R. M. & Bhatia, S. 2007. Biomimetic amplification of nanoparticle homing to tumors. *Proceedings of the National Academy of Sciences,* 104**,** 932-936.

Skinner, C. C., Mcmichael, E. L., Jaime-Ramirez, A. C., Abrams, Z. B., Lee, R. J. & Carson, W. E., 3rd 2016. Folate-conjugated immunoglobulin targets melanoma tumor cells for NK cell effector functions. *Melanoma Res*.

Sosman , J. A., Kim , K. B., Schuchter , L., Gonzalez , R., Pavlick , A. C., Weber , J. S., Mcarthur , G. A., Hutson , T. E., Moschos , S. J., Flaherty , K. T., Hersey , P., Kefford , R., Lawrence , D., Puzanov , I., Lewis , K. D., Amaravadi , R. K., Chmielowski , B., Lawrence , H. J., Shyr , Y., Ye , F., Li , J., Nolop , K. B., Lee , R. J., Joe , A. K. & Ribas , A. 2012. Survival in BRAF V600–Mutant

Advanced Melanoma Treated with Vemurafenib. *New England Journal of Medicine,* 366**,** 707-714.

Sounni, N. E., Devy, L., Hajitou, A., Frankenne, F., Munaut, C., Gilles, C., Deroanne, C., Thompson, E. W., Foidart, J.-M. & Noël, A. 2002. MT1-MMP expression promotes tumor growth and angiogenesis through an up-regulation of vascular endothelial growth factor expression. *The FASEB Journal,* 16**,** 555-564.

Srivastava, S., Bhardwaj, A., Arora, S., Tyagi, N., Singh, A., Carter, J., Scammell, J., Fodstad, Ø. & Singh, S. 2015. Interleukin-8 is a key mediator of FKBP51-induced melanoma growth, angiogenesis and metastasis. *British journal of cancer,* 112**,** 1772-1781.

Starr, D. B., Matsui, W., Thomas, J. R. & Yamamoto, K. R. 1996. Intracellular receptors use a common mechanism to interpret signaling information at response elements. *Genes & development,* 10**,** 1271-1283.

Steingrimsson, E., Copeland, N. G. & Jenkins, N. A. 2004. Melanocytes and the microphthalmia transcription factor network. *Annu Rev Genet,* 38**,** 365-411.

Sugahara, K. N., Teesalu, T., Karmali, P. P., Kotamraju, V. R., Agemy, L., Girard, O. M., Hanahan, D., Mattrey, R. F. & Ruoslahti, E. 2009. Tissue-penetrating delivery of compounds and nanoparticles into tumors. *Cancer Cell,* 16**,** 510-520.

Sun, Y., Song, G. D., Sun, N., Chen, J. Q. & Yang, S. S. 2014. Slug overexpression induces stemness and promotes hepatocellular carcinoma cell invasion and metastasis. *Oncol Lett,* 7**,** 1936-1940.

Suzuki, R., Omata, D., Oda, Y., Unga, J., Negishi, Y. & Maruyama, K. 2016. Cancer Therapy with Nanotechnology-Based Drug Delivery Systems: Applications and Challenges of Liposome Technologies for Advanced Cancer Therapy. *Nanomaterials in Pharmacology,* 1**,** 457-482.

Tamai, K., Semenov, M., Kato, Y., Spokony, R., Liu, C., Katsuyama, Y., Hess, F., Saint-Jeannet, J. P. & He, X. 2000. LDL-receptor-related proteins in Wnt signal transduction. *Nature,* 407**,** 530-5.

Tang, Z. Y., Liu, Y., Liu, L. X., Ding, X. Y., Zhang, H. & Fang, L. Q. 2013. RNAi-mediated MMP-9 silencing inhibits mouse melanoma cell invasion and migration in vitro and in vivo. *Cell Biol Int,* 37**,** 849-54.

Thompson, E. W. & Newgreen, D. F. 2005. Carcinoma invasion and metastasis: a role for epithelial-mesenchymal transition? *Cancer Res,* 65**,** 5991-5995.

Tomlinson, M. L., Guan, P., Morris, R. J., Fidock, M. D., Rejzek, M., Garcia-Morales, C., Field, R. A. & Wheeler, G. N. 2009. A chemical genomic approach identifies matrix metalloproteinases as playing an essential and specific role in Xenopus melanophore migration. *Chem Biol,* 16**,** 93-104.

Tong, R. T., Boucher, Y., Kozin, S. V., Winkler, F., Hicklin, D. J. & Jain, R. K. 2004. Vascular normalization by vascular endothelial growth factor receptor 2 blockade induces a pressure gradient across the vasculature and improves drug penetration in tumors. *Cancer Res,* 64**,** 3731-6.

Topalian , S. L., Hodi , F. S., Brahmer , J. R., Gettinger , S. N., Smith , D. C., Mcdermott , D. F., Powderly , J. D., Carvajal , R. D., Sosman , J. A., Atkins , M. B., Leming , P. D., Spigel , D. R., Antonia , S. J., Horn , L., Drake , C. G., Pardoll , D. M., Chen , L., Sharfman , W. H., Anders , R. A., Taube , J. M., Mcmiller , T. L., Xu , H., Korman , A. J., Jure-Kunkel , M., Agrawal , S., Mcdonald , D., Kollia , G. D., Gupta , A., Wigginton , J. M. & Sznol , M. 2012. Safety, Activity, and Immune Correlates of Anti–PD-1 Antibody in Cancer. *New England Journal of Medicine,* 366**,** 2443-2454.

Tysnes, B. B. & Bjerkvig, R. 2007. Cancer initiation and progression: involvement of stem cells and the microenvironment. *Biochimica et Biophysica Acta (BBA)-Reviews on Cancer,* 1775**,** 283-297.

Uster, P. S., Allen, T. M., Daniel, B. E., Mendez, C. J., Newman, M. S. & Zhu, G. Z. 1996. Insertion of poly(ethylene glycol) derivatized phospholipid into pre-formed liposomes results in prolonged in vivo circulation time. *FEBS Lett,* 386**,** 243-6.

Wagner, J. B., Willinger, M. G., Muller, J. O., Su, D. S. & Schlogl, R. 2006. Surface-charge-induced reversible phase transitions of Bi nanoparticles. *Small,* 2**,** 230-4.

Walczyk, D., Bombelli, F. B., Monopoli, M. P., Lynch, I. & Dawson, K. A. 2010. What the cell "sees" in bionanoscience. *J Am Chem Soc,* 132**,** 5761-8.

Weis, S. M. & Cheresh, D. A. 2011. Tumor angiogenesis: molecular pathways and therapeutic targets. *Nat Med,* 17**,** 1359-1370.

Werengowska-Ciećwierz, K., Wiśniewski, M., Terzyk, A. P. & Furmaniak, S. 2015. The chemistry of bioconjugation in nanoparticles-based drug delivery system. *Advances in Condensed Matter Physics,* 2015**,** 27.

Whitfield, M. L., Sherlock, G., Saldanha, A. J., Murray, J. I., Ball, C. A., Alexander, K. E., Matese, J. C., Perou, C. M., Hurt, M. M. & Brown, P. O. 2002. Identification of genes periodically expressed in the human cell cycle and their expression in tumors. *Molecular biology of the cell,* 13**,** 1977-2000.

Williams, S. C. P. 2013. Circulating tumor cells. *Proceedings of the National Academy of Sciences,* 110**,** 4861.

Wittekind, C. & Neid, M. 2005. Cancer invasion and metastasis. *Oncology,* 69 Suppl 1**,** 14-6.

Woodle, M. C. & Lasic, D. D. 1992. Sterically stabilized liposomes. *Biochimica et Biophysica Acta (BBA)-Reviews on Biomembranes,* 1113**,** 171-199.

Yancopoulos, G. D., Davis, S., Gale, N. W., Rudge, J. S., Wiegand, S. J. & Holash, J. 2000. Vascular-specific growth factors and blood vessel formation. *Nature,* 407**,** 242-248.

Yang, D., Van, S., Shu, Y., Liu, X., Ge, Y., Jiang, X., Jin, Y. & Yu, L. 2012. Synthesis, characterization, and in vivo efficacy evaluation of PGG–docetaxel conjugate for potential cancer chemotherapy. *International Journal of Nanomedicine,* 7**,** 581-589.

Yasumoto, K.-I., Yokoyama, K., Shibata, K., Tomita, Y. & Shibahara, S. 1994. Microphthalmia-associated transcription factor as a regulator for melanocyte-specific transcription of the human tyrosinase gene. *Molecular and cellular biology,* 14**,** 8058-8070.

Yasumoto, K., Yokoyama, K., Takahashi, K., Tomita, Y. & Shibahara, S. 1997. Functional analysis of microphthalmia-associated transcription factor in pigment cell-specific transcription of the human tyrosinase family genes. *J Biol Chem,* 272**,** 503-9.

Zbytek, B., Carlson, J. A., Granese, J., Ross, J., Mihm, M. C. & Slominski, A. 2008. Current concepts of metastasis in melanoma. *Expert review of dermatology,* 3**,** 569-585.

Zhang, L., Radovic‐Moreno, A. F., Alexis, F., Gu, F. X., Basto, P. A., Bagalkot, V., Jon, S., Langer, R. S. & Farokhzad, O. C. 2007. Co‐delivery of hydrophobic and hydrophilic drugs from nanoparticle–aptamer bioconjugates. *ChemMedChem,* 2**,** 1268-1271.

Zhao, F., Zhao, Y., Liu, Y., Chang, X., Chen, C. & Zhao, Y. 2011. Cellular uptake, intracellular trafficking, and cytotoxicity of nanomaterials. *Small,* 7**,** 1322-37.

Zheng, D., Li, X., Xu, H., Lu, X., Hu, Y. & Fan, W. 2009. Study on docetaxel-loaded nanoparticles with high antitumor efficacy against malignant melanoma. *Acta biochimica et biophysica Sinica,* 41**,** 578-587.

Zheng, M., Jiang, Y.-P., Chen, W., Li, K.-D., Liu, X., Gao, S.-Y., Feng, H., Wang, S.-S., Jiang, J., Ma, X.-R., Cen, X., Tang, Y.-J., Chen, Y., Lin, Y.-F., Tang, Y.-L. & Liang, X.-H. 2015. Snail and Slug collaborate on EMT and tumor metastasis through miR-101-mediated EZH2 axis in oral tongue squamous cell carcinoma. *Oncotarget,* 6**,** 6794-6810.

Chapter 2.

Materials and methods

Materials and methods

The following chapter describes the experimental methods and chemicals (table 2.0.1) used for the work presented in this thesis. This includes the synthesis, functionalisation, and purification of Fe_3O_4 NPs; NP and peptide characterisation; cell culture conditions and *in vitro* experiments; *in vivo* toxicity assessment, including NP uptake in mammalian models; *in vitro* targeting of NP to melanoma cells; digestion and sorting of human lymphadectomy tissue.

Table 2.0.1 List of materials. Materials used throughout this thesis with their supplier and catalogue number stated.

Materials used for NP synthesis, functionalisation, and purification

Product	**Supplier**	**Catalog No.**
1,2-tetradecanediol	Sigma-Aldrich	260290
1–ethyl–3–(3–dimethylaminopropyl) carbodiimide (EDAC)	Sigma-Aldrich	E1769
Benzyl ether	Sigma-Aldrich	108014
Cellulose Ester dialysis membrane, 100 kDa	Spectrum Labs	131414
Cellulose Ester dialysis membrane, 3.5-5 kDa	Spectrum Labs	131198
Centrifuge tube, thinwall, polypropylene (for rotor SW 28)	Beckman Coulter	326823
Chloroform ($CHCl_3$)	Sigma-Aldrich	C2432
$Fe(acac)^3$	Sigma-Aldrich	F300
FluidMAG-Amine	Chemicell	4121
FluoSphere, 20 nm	Molecular Probes	F8787
HCl 4 M in dioxane	Sigma-Aldrich	345547
Nile red	Sigma-Aldrich	19123
N,*N*-Dimethylformamiode (DMF)	Sigma-Aldrich	PHR1553
N,*N*-Dissopropylethylamine (DIPEA)	Sigma-Aldrich	496219
Oleic Acid	Sigma-Aldrich	O1008
Oleylamine	Sigma-Aldrich	O7805
PEG succinimidyl carboxymethyl ester, Mw 2000	Jenkem Technology	M-SCM-2000
Poly(maleic anhydride-*alt*-1-octadecene) (PMAO)	Sigma-Aldrich	419117
Sephacryl S-300 high resolution	GE Life Sciences	17-0599-01
Sodium azide (NaN_3)	Sigma-Aldrich	S2002
Sucrose	Sigma-Aldrich	S0389
t-Boc amine PEG NHS ester, Mw 2000	Jenkem Technology	TBOC-PEG2000-NHS
Tetramethylammonium hydroxide (TMAH)	Sigma-Aldrich	426318
Toluene	Sigma-Aldrich	179417

Materials used for NP and peptide characterisation

Product	**Supplier**	**Catalog No.**
1,10-phenathroline	Sigma-Aldrich	P9375
Acetonitrile (ACN)	Sigma-Aldrich	271004
Citric acid monohydrate	Sigma-Aldrich	C1909
Hydrochloric acid (HCl), 37%	Sigma-Aldrich	320331
Hydroxylamine hydrochloride	Sigma-Aldrich	379921
Iron (II) sulphate heptahydrate	Sigma-Aldrich	215422

Sodium citrate	Sigma-Aldrich	PHA1416
Sulphuric acid	Sigma-Aldrich	339741
TEM copper grids, 70 µm square holes	Agar Scientific	AGG203
Thioglycolic acid	Sigma-Aldrich	T3758
Triflouroacetic acid (TFA)	Sigma-Aldrich	271004
Uranyl acetate dihydrate	Sigma-Aldrich	73943
α-cyano-4-hydroxycinnamic acid (HCCA)	Sigma-Aldrich	C2020

Materials used for cell culture and *in vitro* experiments

Product	**Supplier**	**Catalog No.**
3-(4,5-dimethylthiazolyl)-2,5-diphenyltetrazolium bromide	Sigma-Aldrich	M2128
Acrylamide/bis-aceylamide, 40%	Sigma-Aldrich	A7168
Agarose, genetic analysis grade	Fisher Scientific	10688973
Ammonium chloride (NH_4Cl)	Sigma-Aldrich	A9434
Ammonium persulfate (APS)	Sigma-Aldrich	248614
BCA Protein Assay Kit	Pierce	23225
Bovine serum albumin (BSA)	Fisher Scientific	12861630
Cell strainer 70 µm pore size	Fisher Scientific	15370801
Collagenase IV	Fisher Scientific	17104019
cOmplete mini Tablets protease inhibitor cocktail	Roche	4693124001
Coverslip, borosilicate glass, ø 18 mm	VWR	631-0153
Deoxyribonuclease I from bovine pancreas	Sigma-Aldrich	D5025
Dimethyl sulfoxide (DMSO)	Fisher Scientific	10213810
Dithiothreitol (DTT)	Sigma-Aldrich	D0632
ECL Prime Western Blotting Detection	GE Healthcare	RPN2232
EZ-PCR Mycoplasma Test Kit	GeneFlow	K1-0210
Fermentas Spectra ™, multicolour broad range protein ladder	Fisher Scientific	11842124
Fetal calf serum (FCS) (Lot # RVJ35882)	Hyclone	SV30160
Gel Red ™ nucleic acid stain	VWR	BT41003
Hank's Balanced Salt solution (HBSS)	Sigma-Aldrich	55021C
Human melanocyte growth supplement (HMGS)	Fisher Scientific	10378213
Hyaluronidase from bovine testes	Sigma-Aldrich	H3506
L-glutamine, 20 mM sterile filtered	Sigma-Aldrich	G7513
Marvel Milk Powder	Marvel	n/a
Medium 254	Fisher Scientific	10236533
N,*N*,*N'*,*N'*-Tetramethylethylenediamine (TEMED)	Sigma-Aldrich	T9281
Nitrocellulose 0.45 µm 300 mm x 3.5 m	Fisher Scientific	10773485
Paraformaldehyde, 95%	Sigma-Aldrich	158127
Penicillin (10000 units/ml), Streptomycin (10 mg/ml)	Sigma-Aldrich	P0781
Phosphate buffered saline (PBS) tablets	Fisher Scientific	12821680
PhosSTOP phosphatase inhibitor cocktail tablet	Roche	4906837001
Quick load 1 Kb DNA ladder	Fisher Scientific	10787018

Quick load 100 bp DNA ladder	NEB	H04675
RPMI-1640	Hyclone	SH30096.01
SDS loading buffer	Cell Signalling Technology	7722
Sodium dodecyl sulfate (SDS)	Sigma-Aldrich	71725
Sodium phosphare dibasic anhydrous (Na_2HPO_4)	Sigma-Aldrich	RES20908-A7
Sodium phosphare monobasic (NaH_2PO_4)	Sigma-Aldrich	S5011
Trizma hydrochloride	Sigma-Aldrich	T5941
Trypan Blue solution, 0.4% in PBS	Fisher Scientific	10593524
Trypsin Neutralizer Solution	Fisher Scientific	11667104
Trypsin-EDTA, 0.5%	Fisher Scientific	FF01058J
Vectashield antifade mounting medium	Vector Laboratories	H1000

Antibodies and cell stains

Product	**Supplier**	**Catalog No.**
anti-human CD45, Alexa Fluor® 610	Fisher Scientific	10518173
anti-human neural/glial antigen 2 (NG2), Alexa Fluor® 488	eBioscience	53-6504
anti-MC1R, rabbit	Abcam	AB125031
anti-MelanA, rabbit	Abcam	AB51061
anti-mouse, HRP conjugated, horse	Cell Signaling	7076
anti-PARP-1, rabbit	Santa Cruz	SC-25780
anti-rabbit, HRP conjugated, goat	Cell Signaling	7074
anti-α-tubulin, mouse	Cell Signaling	3873
Hoechst 33342 trihydrocholride trihydrate	Fisher Scientific	11534886
Phalloidin, Alexa Fluor 568	Invitrogen	10135092

Materials used for *in vivo* experiments

Product	**Supplier**	**Catalog No.**
Calcium chloride ($CaCl_2$)	Sigma-Aldrich	C1016
Cystine	Sigma-Aldrich	C33000000
Ethyl 3–aminobenzoate methanesulfonate	Sigma-Aldrich	E10521
Ethylene glycol-bis(2-aminoethylether)-*N,N,N′,N′*-tetraacetic acid (EGTA)	Sigma-Aldrich	E2889
Ethylenediaminetetraacetic acid (EDTA)	Sigma-Aldrich	E9884
Gentamicin	Fisher Scientific	15710049
Glutaraldehyde solution, 8%	Sigma-Aldrich	G7526
HEPES	Sigma-Aldrich	H4034
Magnesium sulfate ($MgSO_4$)	Sigma-Aldrich	M7506
Methanol (MeOH)	Sigma-Aldrich	322415
MOPS	Sigma-Aldrich	M1254
Optimal cutting temperature (OCT) compound	Agar Scientific	AGR1180
Osmium tetroxide solution, 4%	Sigma-Aldrich	75632

Potassium cholride (KCl)	Sigma-Aldrich	P9333
Potassium dihydrogen phosphate (KH_2PO_4)	Sigma-Aldrich	PHR1330
Propylene oxide	Sigma-Aldrich	110205
Sodium cacodylate trihydrate	Sigma-Aldrich	C0250
Sodium chloride (NaCl)	Sigma-Aldrich	S7653
Tween-20	Sigma-Aldrich	P1379

Laboratory consumables

Product	**Supplier**	**Catalog No.**
Centrifuge tube, sterile, 15 ml	Fisher Scientific	11849650
Centrifuge tube, sterile, 50 ml	Fisher Scientific	11819650
Chromatography paper, pure cellulose, 20 cm x 20 cm	Fisher Scientific	11320744
Ethanol, 95.0%	Sigma-Aldrich	652261
Microcentrifuge tube, 1.5 ml	Fisher Scientific	11558232
Microplate, sterile, 96 well	Fisher Scientific	10567131
Parafilm M,10 cm x 76 cm	Fisher Scientific	10018130
Pipette serological, sterile, 10 ml	Fisher Scientific	11839660
Pipette serological, sterile, 25 ml	Fisher Scientific	11517752
Pipette serological, sterile, 5 ml	Fisher Scientific	11829660
Pipettor tip, 0.1-10 µl	Fisher Scientific	11933416
Pipettor tip, 100-1250 µl	Fisher Scientific	11548442
Pipettor tip, 1-200 µl	Fisher Scientific	11538422
Test tube, Falcon, round bottom polystyrene, 5 ml	Fisher Scientific	10186360
Tissue culture dish, sterile, ø 10 cm	Fisher Scientific	10508921
Tissue culture dish, sterile, 12 well	Fisher Scientific	10098870
Tissue culture dish, sterile, 24 well	Fisher Scientific	10376912
Tissue culture dish, sterile, 6 well	Fisher Scientific	10119831
Tissue culture flask, sterile, 25 cm^2 culture area	Fisher Scientific	10490033

Table 2.02 List of recipes. Recipes used throughout this thesis**.**

Name		**Final Volume**	**Final pH**
Lysis buffer	50 mM Tris-HCl 1% Triton X-100 150 mM NaCl	200 ml PBS	pH 7.4
Note: store at 4 ºC			
MEMFA	Formaldehyde (3.7%) MOPS (0.1 M) EGTA (2 mM) $MgSO_4$ (1 mM)	100 ml MQW	pH 7.4
MMR, 1 x	NaCl (100 mM) HEPES (5 nM) $CaCl_2$ (2 nM) $MgCl_2$ (1 mM)	1000 ml MQW	pH 7.5
Paraformaldehyde (PFA), 4%	8 g Paraformaldehyde	200 ml PBS	pH 7.3
Note: dissolve PFA in initial 150 ml PBS at 60 ºC in fume cupboard			
PBS, 1 x	1 PBS tablet consisting of: 137 mM NaCl 10 mM Phosphate Buffer 2.7 mM KCl	100 ml MQW	pH 7.4
PBST	8 g NaCl 0.2 g KCl 1.44 g Na_2HPO_4 0.24 g KH_2PO_4 2 ml Tween-20	800 ml MQW	pH 7.4
Ponceau stain	5 ml glacial acetic acid 0.2 g Ponceau S	100 ml MQW	-
Note: store at 4 ºC			
Running buffer, 10 x	30.2 g Tris-base (25 mM) 144 g Glycine (190 mM) 0.1% SDS	1000 ml MQW	pH 8.3
SDS, 10%	20 g SDS	200 ml MQW	-
Sørensen's glycine buffer	39.0 ml NaH_2PO_4 (0.2 M) 61.0 ml Na_2HPO_4 (0.2 M)	100 ml MQW	pH 7.0
TAE, 50 x	121 g Tris Base 28.55 ml Acetic Acid 50 ml, 0.5 M EDTA	500 ml MQW	pH 8.0

TBS, 10 x	24.23 g Tris-HCl 80.6 g NaCl	1000 ml MQW	pH 7.6
Note: TBST, 0.1% Tween-20 to be added to 1 x TBS.			
Transfer buffer, 10 x	30.2 g Tris-base (25 mM) 144 g Glycine (190 mM) 0.1% SDS	1000 ml MQW	pH 8.3
Note: 20% Methanol added to 1 x Transfer buffer. Store at 4^{o}C			
Tris-HCl, 0.5 M	19.7 g Tris-HCl	200 ml MQW	pH 6.8
Tris-HCl, 1.5 M	36.4 g Tris-HCl	200 ml MQW	pH 8.8

2.1 Nanoparticle synthesis, functionalisation, and purification

2.1.1 Cadmium selenide quantum dot (CdSe QD) synthesis

CdSe QDs were synthesised by microwave heating, in a conventional microwave oven, of an aqueous 0.1 M cadmium perchlorate with 0.01 M *N, N*-dimethyl seleno-urea in the presence of a stabiliser, 0.1% (w/v) sodium citrate (Wang et al., 2008). This resulted in uncoated 10:1 CdSe QDs.

Initially, 0.025 g of sodium citrate was dissolved in ~ 50 mL filtered Milli-Q water (MQW) and the pH was adjusted to 9.2. Cadmium ions were obtained by the addition of 2 mL cadmium perchlorate, and selenium ions from 2 mL *N, N*-dimethyl seleno-urea, and the pH was readjusted back to 9.2. The solution was heated in a microwave oven at 800 W continuously for 60 s before gently mixing and heated for a further 30 s. The particles where then left in the dark for 3 days.

2.1.2 Fe_3O_4 NP synthesis

Monodispersed magnetic Fe_3O_4 NPs were synthesised by high-temperature phase reaction of iron salts in the presence of oleic acid and oleylamine (Sun et al., 2004). Gradual heating during thermal decomposition of salts allowed control over particle diameter and a better size distribution. This method resulted in hydrophobic particles in an organic solvent (Sun et al., 2004).

$Fe(acac)_3$ (2 mmol, 706 mg),1,2-tetradecanediol (10 mmol, 2 g), benzyl ether (20 mL), oleic acid (2 mmol, 565 mg), and oleylamine (2 mmol, 935 mg) were mixed

and magnetically stirred under a flow of N_2 and initially heated to 100^{o}C over 45 min (figure 2.1.1). The mixture was kept at 100 ^{o}C for 45 min before gradually heating to 200 ^{o}C over 40 min and kept at this temperature for 2 h. Finally, the mixture was heated to reflux at 300 ^{o}C; the reflux temperature is dependent on the boiling temperature of benzyl ether (298 ^{o}C). After 30 min at 300 ^{o}C, the mixture was cooled to room temperature and left overnight.

The black-brown mixture was transferred using a small volume of toluene to centrifuge tubes and centrifuged at 6000 rpm for 10 min to remove any insoluble residue. Particles were then precipitated from the supernatant by centrifugation in an excess of ethanol at 8500 rpm for 20 min. After the removal of ethanol, the particles were resuspended in 5 ml of toluene and filtered with a 0.22 μm pore syringe filter.

Figure 2.1.1 Fe_3O_4 synthesis apparatus. A round bottom flask was placed in a heating mantle, attached to a resistor to control temperature, above a magnetic stir plate. Temperature was monitored via a thermal probe entering the second neck of the round bottom flask. For reflux, a condenser was attached to 0 ^oC pumped water. The top of the condenser was attached to a nitrogen line and the reaction occurred under a constant flow of N_2.

2.1.3 Fe_3O_4 NP phase transfer using PMAO

Iron oxide NPs were prepared as described in method 2.1.2, resulting in hydrophobic particles that were soluble in an organic solvent. For use in biological application, Fe_3O_4 NPs had to undergo a phase transfer by surface functionalisation to allow solubility in an aqueous solution. This was achieved by the addition of an amphiphilic polymer, poly(maleic anhydride-*alt*-1-octadecene) (PMAO), to the surface of the particle (Di Corato et al., 2008). The hydrophobic alkyl groups of the octatedecene chain in PMAO were able to intercalate with the surfactant chains of the oleate and dodecanethiol chains from the Fe_3O_4 NPs via hydrophobic interactions. The resulting particle was wrapped in a polymeric shell where the hydrophilic group was exposed on the outside, allowing the Fe_3O_4 NPs to be soluble in an aqueous solution.

To achieve this, Fe_3O_4 NPs in toluene were precipitated by centrifugation in an excess of ethanol at 8000 rpm for 20 min. PMAO was dissolved in chloroform and added in excess to the dried particles. The solution was mixed for 30 mins at 20 ^oC at 210 mbar, to evaporate off the chloroform. The pressure was then lowered to 180 mbar until the particles appeared dry before a final pressure of 70 mbar for 10 min. To ensure all chloroform had been evaporated, the particles were further dried through a stream of nitrogen for 1 h. An excess of PMAO in 0.1 M tetramethylammonium hydroxide (TMAH) was added at a concentration of 1 mg/ml at a volume ratio of 1:10 (PMAO : Fe_3O_4) for 1 h. The base, TMAH, was used to hydrolyse the anhydride ring resulting in a charged COO^- group, increasing solubility and acting as an anchor for the convenient attachment of other molecules. The solution was sonicated for a minimum of 20 mins to disperse the Fe_3O_4-PMAO NPs in the aqueous solution and the mixture was shaken overnight at room temperature.

Fe_3O_4-PMAO NPs were dialysed against PBS pH 7.4, (10 mM NaCl) 0.31 osmol using a dialysis membrane with Mw cut-off (MWCO) of 100 kDa to remove part of the unbounded polymer for 3 days.

2.1.4 Fe_3O_4-PMAO purification by size exclusion chromatography

Addition of excess polymer (150 mg/ml) during coating and functionalisation led to the formation of micelles. As a result, the sample appeared polydispersed by dynamic light scattering (DLS) analysis suggesting the formation of aggregates. Before use in any biological assay, the sample was first purified to remove micelles and possible NP-polymer aggregates and create a monodispersed population. Size exclusion chromatography was used to separate Fe_3O_4-PMAO from PMAO micelles. A Sephacryl S-300 High Resolution column was used with a cross sectional area of 5 cm^2 and a length of 25 cm with a single pump. The column was washed 3 times with 100 mM PBS before the sample was loaded. The eluent was pumped at a rate of 0.6 ml per minute and the fractions were collected in collection tubes at a rate of 1.5 min per tube.

2.1.5 Fe_3O_4-PMAO purification by ultracentrifugation

Purification was achieved by ultracentrifugation of the particles through a sucrose gradient. This method had previously been shown to produce highly pure monodispersed NPs of a variety of particle types (Di Corato et al., 2008). Particles move through the sucrose gradient until they reach a comparable density. As a result, NPs are separated by size and excess polymer is removed from the NPs.

A 2% to 66% sucrose gradient was used. The stock solution of 66% (w/w) sucrose was made using 66 g of sucrose in a total weight of 100 g MQW and gently stirred on a low heat. A range of sucrose concentrations were made by diluting the stock solution in MQW to make the fractions 58.9%, 51.8%, 44.7%, 37.6%, 30.5%, 23.4%, 16.3%, 9.2%, and 2%. The addition of 0.05 M sodium azide was added to each fraction to prevent any contamination whilst NPs were passed through the sucrose gradient. Starting with 66%, decreasing concentrations were layered on top of each other in a centrifuge tube. The gradient was left overnight for the sucrose to equilibrate and form a continuous gradient. The NPs were carefully added on top of the sucrose gradient and spun at 25000 rpm for 4 h in a Beckman Coulter SW 28 swinging bucket rotor.

After size exclusion and removal of excess polymer by ultracentrifugation, fractions were removed from the tube using a syringe and needle. Confirmation of the presence of excess polymer in a fraction was done by electrophoresis through 1.5% agarose gel. Each fraction was loaded with 3 x SDS sample buffer and run for 1 h at 90 V. Excess polymer fluoresced blue after ultraviolet (UV) excitation whereas bound polymer did not as it was quenched by the NP, and so any fraction containing excess polymer was visualised by UV irradiation after electrophoresis. DLS was instead used for fractions with no excess polymer to determine the size of the NPs, fractions with a similar size distribution at DLS were grouped together. To remove the sucrose from the sample, NPs were dialysed against PBS pH 7.4, (10 mM NaCl) 0.31 osmol using a dialysis membrane with MWCO of 2 kDa for 3 days.

Finally, the particles were filtered using a 0.22 μm pore syringe filter and concentrated by centrifugation with 50 kDa Amicon filter units at 4000 rpm until they reached the desired concentration.

2.1.6 PEGylation of Fe_3O_4-PMAO NPs

The maleic anhydride ring allows easy functionalisation of the particle. PEGylation of a NP has been shown to stabilise the particle in a biological environment by reducing the interaction of proteins with the surface of the NP, reduce cytoxicity, and prolong circulation time (Gref et al., 2000).

Carboxylated Fe_3O_4 cores were synthesised and purified as previously described (method 2.1.2, 2.1.3, and 2.1.5). Coupling of Fe_3O_4-PMAO to PEG was done using an excess of methoxy PEG succinimidyl carboxymethyl ester (Mw 2000) in the presence of the catalyst 1–ethyl–3–(3–dimethylaminopropyl) carbodiimide (EDAC). Solutions of 20 mM PEG (2000 kDa-NH_2) and 0.15 M EDAC were made up beforehand in PBS. These were added to 250 µl of carboxylated Fe_3O_4-PMAO NPs using 100 µl of both PEG-NH_2 and EDAC in a final volume of 1000 µl; final concentration of 2 mM (PEG) and 15 mM (EDAC). The solution was placed on a shaking block at room temperature and agitated overnight.

To remove excess PEG, Fe_3O_4-PEG NPs were dialysed against PBS pH 7.4, (10 mM NaCl) 0.31 osmol using a dialysis membrane with MWCO of 2 kDa for 24 h.

2.1.7 Conjugation of α-MSH peptide and PEG

The α-MSH peptide (PEP) (H-Ser-Tyr-Ser-Nle-Glu-His-d-Phe-Arg-Trp-Gly-Lys(Dde)-Pro-Val-NH_2; (Lu et al., 2009) and scrambled peptide were purchased from Jenkem Technology. CH_3-PEG-NH_2 was attached to PEP via the N terminal serine residue. In a 10 ml round bottom flask, 5.3 mg of peptide (0.0033 mmol) and 13.2 mg

t-Boc mono-amine PEG N-hydroxylsuccinimide (NHS) ester (0.0066 mmol) were dissolved in DMF (1.5 ml) and *N, N*-Dissopropylethylamine (DIPEA) (30 µl). The reaction was stirred at room temperature for 24 h. DMF solvent was then removed by evaporation at 37 °C under vacuum resulting in a white powder. The powder was then dissolved in 3 ml H_2O and dialysed in a 3.5-5 kDa dialysis membrane against H_2O for 3 days at 4 °C.

Deprotection of the *tert*-butoxycarbonyl (Boc) group was achieved using HCl/dioxane as previously described (Han et al., 2001). First, protected PEG-PEP was lyophilised to return it to a powder. In a solution of 4 M HCl in dioxane, 0.2 mmol protected PEG-PEP was added to a 25 ml round bottom flask at 4 °C and mixed using a magnetic stir bar. The reaction was removed from ice and left mixing overnight at room temperature. After the reaction was complete, the solution was lyophilised under vacuum until a powder. The deprotected PEG-PEP was then prepared as a 20 mM stock in PBS pH 7.4, (10 mM NaCl) 0.31 osmol.

2.1.8 Conjugation of PEG-PEP to Fe_3O_4-PMAO

After deprotection, the conjugated PEG-PEP was attached to Fe_3O_4-PMAO using the same method as PEGylation of Fe_3O_4-PMAO NPs (method 2.1.6). In place of 100 µl PEG, 10% 20 mM deprotected PEG-PEP and 90% 20 mM PEG was used in the presence of the catalyst EDAC. Solutions of 10 % 20 mM PEG-PEP (2000 kDa-NH_2), 90 % 20 mM mono-amine PEG, and 0.15 M EDAC were made up beforehand in PBS. These were added to 250 µl of carboxylated Fe_3O_4-PMAO NPs using 100 µl of both PEG-NH_2/deprotected PEG-PEP and EDAC in a final volume of 1000 µl; final

concentration of 2 mM (PEG/PEG-PEP) and 15 mM (EDAC). The solution was placed on a shaking block at room temperature and agitated overnight.

To remove excess PEG, PEG-PEP, and reaction byproducts such as urea, Fe_3O_4-PEG-PEP NPs were dialysed against PBS pH 7.4, (10 mM NaCl) 0.31 osmol using a dialysis membrane with MWCO of 2 kDa for 24 h.

2.1.9 Nanoparticle drug encapsulation

Hydrophobic molecules were encapsulated into the hydrophobic shell of Fe_3O_4-PEG and Fe_3O_4-PEP NPs. For NP cellular uptake that was performed using confocal microscopy (method 2.5.1) and flow cytometry (method 2.5.2) nile red (NR) was encapsulated in the hydrophobic shell. NR has a λ_{ex} 552 nm and λ_{em} 600-700 nm and was made into 1 mg/ml stock in $CHCl_3$. To Fe_3O_4-PEG or Fe_3O_4-PEP in PBS, 0.5% (v/v) of NR in $CHCl_3$ was added and left overnight at room temperature for the small volume of $CHCl_3$ to evaporate fully. Successful encapsulation of NR was evaluated using a Horiba Yobin FluoroLog-3 spectrophotometer.

Paclitaxel (PTX) was also encapsulated via this method. A stock of 5 mM PTX in $CHCl_3$ was added to $10^{12.4}$ NP/ml Fe_3O_4 NPs to a final concentration of 50 μM and left overnight for $CHCl_3$ to evaporate. NPs were then dialysed against PBS pH 7.4, (10 mM NaCl) 0.31 osmol using a dialysis membrane with Mw cut-off (MWCO) of 100 kDa for 3 days.

2.1.10 Commercial NPs

FluidMAG-Amine magnetic NPs were purchased from Chemicell Gmbh (Berlin, Germany), stated as size (hydrodynamic diameter) 50 nm. FluoSphere fluorescent carboxylated-modified microspheres yellow-green (λ_{ex}, 505 nm; λ_{em}, 515 nm) were purchased from Molecular Probes at a stated hydrodynamic diameter of 20 nm.

2.2 Nanoparticle and peptide characterisation

2.2.1 Dynamic light scattering (DLS)

DLS, also known as Photon Correlation Spectroscopy, is an important tool for determining the hydrodynamic size and size distribution of particles within a solution. Typically, DLS is used to measure particles in the sub-micron region and can measure particles down to a few nanometres in diameter. DLS measures size and size distribution by shining a monochrome coherent light beam onto spherical particles that are in Brownian motion. As the particles undergo Brownian motion their relative position to each other changes and consequently the scattered light intensity changes. This variation in scattered light intensity is then analysed as a function of time.. The extent of this change in wave frequency is related to the size of the moving particles. Smaller particles, moving fast, exhibit a larger Doppler shift than larger, slow moving particles (Hiemenz and Rajagopalan, 1997). When the combined scattered light from several particles is added together, there is time-dependent fluctuation in the intensity of the scattered light that can be measured on a photo counter.

The velocity of the Brownian motion is defined by the translational diffusion coefficient and so the sizes of the spherical particles can be calculated using the Stokes – Einstein equation:

$$D_h = \frac{k_B T}{3\pi\eta D_t} \qquad \textbf{Equation 2.1}$$

Where D_h is hydrodynamic diameter, D_t is the translational diffusion coefficient, k is Boltzmann's constant, T absolute temperature, and η is viscosity. The scattered light was detected at an angle under an angle of 173°. DLS was performed using Malvern Zetasizer Nano ZS (Malvern Instruments, Malvern, UK).

2.2.2 ζ-potential

ζ-potential is the potential difference between the surface of a solid particle in a colloidal system and the liquid. The value given can be used to assess the stability of the particle. Particles with a large positive or negative value, often >30 mV, are considered stable. This is due to the repulsion between particles. Below this value there is a limited force among the particles to repel each other, leading to instability and aggregation. ζ-potential was measured using Malvern Zetasizer Nano ZS (Malvern Instruments, Malvern, UK).

2.2.3 Inductively coupled plasma optical emission spectroscopy (ICP-OES)

Inductively coupled plasma optical emission spectroscopy (ICP-OES) was used to determine the concentration of Fe_3O_4 NPs and CdSe QDs. A radio frequency generator

surrounds a quartz torch. When the torch is initiated, a large electromagnetic field is created by the radio frequency in the coil. An argon gas is ionised to produce positive ions. This is the used to excite atoms in a sample that produces a unique emission spectrum specific to the element. Quantitative analysis of the resulting emission spectrum is used to gain the concentration of the metal in the sample. For ICP-OES analysis, samples were sent to the School of Environment Science, University of East Anglia.

2.2.4 Iron concentration using o-phenanthroline

The concentration of Fe^{2+} in a sample of Fe_3O_4 NPs was determined colourimetrically using the compound 1, 10-phenathroline (Nitin et al., 2004). 1, 10-phenathroline is a colourless tricyclic nitrogen heterocyclic compound that forms a complex with Fe^{2+} via two nitrogen atoms with available electron pairs (figure 2.2.1). The resulting complex is a red colour that can be measured at 510 nm.

In order to release the iron, thioglycolic acid was added to the sample. The resulting Fe^{3+} ions are reduced using hydroxylamine hydrochloride. Sodium citrate was used to maintain an acidic pH required for Fe-phenanthroline complex formation. A hydroxylamine hydrochloride (reducing agent) working stock was made using hydroxylamine hydrochloride 1.4 mol/L prepared in 2 mol/L analytical grade HCl.

Iron standards were made from a stock solution of iron (II) sulphate heptahydrate in sulfuric acid (200 mg iron (II) sulphate heptahydrate in 10 mls 1:1000 H_2SO_4). For the stock, 200 mg of iron (II) sulphate heptahydrate was dissolved in 8 ml of H_2O in a 10 ml volumetric flask. Concentrated H_2SO_4, 10 µl, was added before making up to the mark with H_2O. The resulting 20 mg/ml solution contained 400 mg/L

Fe. The iron solution was diluted in a total volume of 100 µl (after addition of all reagents) to the concentrations in table 2.2.1.

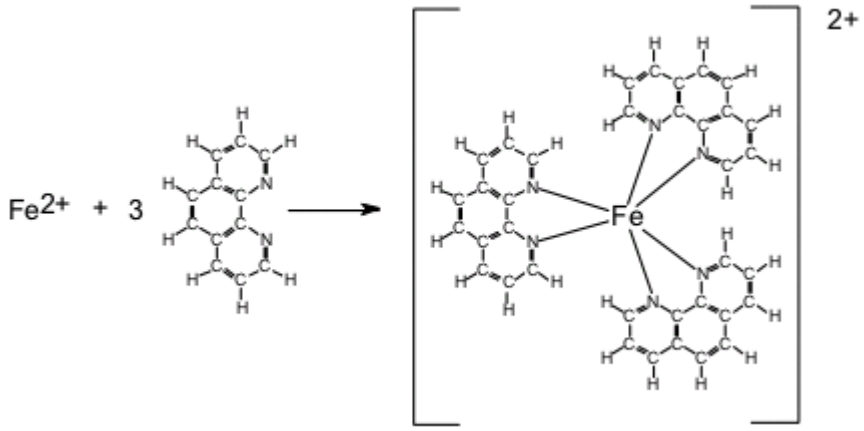

Figure 2.2.1 Fe^{2+} and phenathroline complex used to determine iron concentration. Fe^{2+} in excess is able to bind to both N atoms of 1, 10-phenathroline. Each Fe binds to three 1, 10-phenathroline molecules. The resulting complex was used to determine Fe concentration by measuring absorption at 510 nm.

Table 2.2.1 Fe standard concentrations for determination of iron concentration using *o*-phenanthroline.

	mg/L Fe	Volume standard solution	Volume of H_2O
A	400	50 µl	20 µl
B	360	45 µl	25 µl
C	320	40 µl	30 µl
D	280	35 µl	35 µl
E	240	30 µl	40 µl
F	200	50 µl 1:2	20 µl
G	160	40 µl 1:2	30 µl
H	120	30 µl 1:2	40 µl
I	80	20 µl 1:2	50 µl
J	40	10 µl 1:2	60 µl
K	0	0 µl	70 µl

Thioglycolic acid, 1 µl, was added to each standard solution of iron. Unknown iron oxide samples were diluted into a range of dilutions before the addition of thioglycolic acid to break up the nanoparticles for at least 2 h. To each standard and sample, 10 µl of hydroxylamine hydrochloride reducing agent (1.4 mol/L prepared in 2 mol/L analytical grade HCl), 1, 10-phenathroline (0.25% (w/v) 1, 10-phenothroline in 50% EtOH), and sodium citrate was added and left for at least an hour at room temperature for the colour to fully develop before measuring at 510 nm. Sodium citrate buffer stock was prepared by dissolving 21 g citrate acid monohydride in 200 ml 1 M NaOH and made up to 1 L H_2O. A working solution of the sodium citrate buffer was prepared by addition of 40.3 ml of sodium citrate buffer stock to 0.1 M HCl in 100 ml, pH adjusted to the range of 2.9 to 3.5.

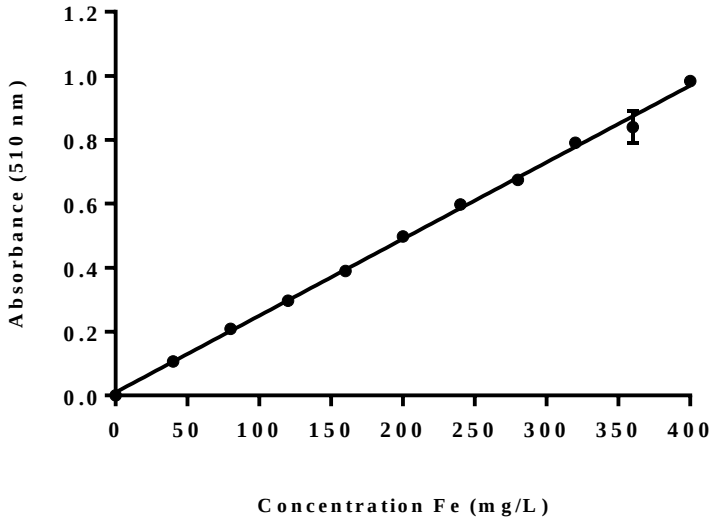

Figure 2.2.2 Calibration curve for assessing iron concentration. Typical calibration curve for standards used to calculate the iron concentration of Fe_3O_4 cored NPs. Y= 0.002433*X + 0.005364, R^2 = 0.9994. Mean ± SD.

2.2.5 Transmission electron microscopy (TEM)

Transmission electron microscopy (TEM) is an electron-based imaging technique that is often used in nanotechnology. Unlike light microscopes, TEM uses a beam of electrons as a light source that, due to the small wavelength of electrons, results in a higher resolution. The beam of electrons interacts strongly with sample matter whilst under vacuum to prevent electron scattering. Materials that are electron transparent are shown as light areas on an image and where the electrons cannot transmit, the image is dark (figure 2.2.3).

Tecnai 20 TEM with AMT cameras, operating at an accelerating voltage of 200 kV, provided images of the dried NPs to assess particle diameter. TEM provided images containing a large number of particles that were statistically analysed. TEM samples were prepared by dropping a dilute suspension of NP onto carbon-coated 300 – mesh copper grids and left to dry for 30 s at room temperature. Samples were then counterstained with 2% uranyl acetate (UA). UA was left to evaporate for a further 30 s at room temperature. A minimum of 100 particles were counted for each sample. Fiji Image J software was used to analyse the resulting images.

2.2.6 Atomic force microscopy (AFM) Fe_3O_4 NPs

Atomic force microscopy (AFM) is a scanning probe microscopy technique (Binnig et al., 1986) that utilises forces between a probe tip mounted on a cantilever and the surface in which it is interacting (Hoo et al., 2008, Wang et al., 2007). Unlike TEM, AFM is able to measure NP size in a vertical dimension. The tip is placed above the

surface at a distance in which it is able to interact with the different forces from the sample. The AFM tip keeps a constant force from the sample surface, and so as the topography of the sample changes, the cantilever is bent (figure 2.2.3). A laser refracting off the back of the cantilever detects this movement, which in turn is read by a photo-detector. The resulting data characterises shape and size distribution of a particle population.

NanoWizard II AFM (JPK, Germany) operating in contact mode under ambient conditions provided AFM images of Fe_3O_4 NPs. A sample of 100 µl was dropped on a glass slide and allowed to dry for 5 min. AFM images were taken with tipless Si cantilevers with a nominal length of 225 µm, force constant 48 N/m, and a nominal resonance frequency of 190 kHz. All measurements were exported to JPK image processing software.

2.2.7 Fourier Transform-Infra-Red (FT-IR) spectroscopy.

Mid infra-red radiation, with a wavelength spectral range of 4000 cm^{-1} to 500 cm^{-1}, can be absorbed by molecules at specific frequencies. Absorption spectra from Fourier transform infra-red (FT-IR) spectroscopy can be used to identify chemical bonds within the molecule by comparison to reference absorptions wavenumber of common functional groups. This can then be used to characterise the compound and identify functional groups within the molecule (Bekyarova et al., 2009, Fang et al., 2009, Nagesha et al., 2009). For samples in a dry state, attenuated total reflection FT-IR (ATR-FT-IR) is used, providing a better signal than with molecules suspended in a medium.

For this work, Perkin-Elmer ATR-FT-IR spectrometer was used. The samples were placed in round bottom flasks and dried under a flow of nitrogen until all solvent was removed. The powder samples were recorded after 16 scans by correcting the background.

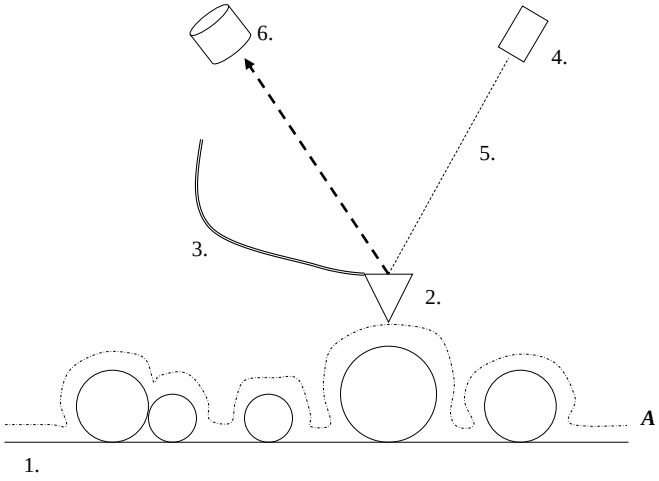

Figure 2.2.3 Basic diagram showing the workings of AFM. Adapted from Binnig *et al.*, 1986. The AFM tip, on the end of the cantilever, was passed along the sample surface. The force between the tip and the sample deflected the cantilever. 1. Sample surface; 2. AFM tip; 3. Cantilever; 4. Diode laser 5. Laser light path 6. Position-sensitive photo-detector; *A.* Contour of AFM tip movement due to attraction or repulsion from sample surface.

2.2.8 High performance liquid chromatography (HPLC)

High performance liquid chromatography (HPLC) is a powerful analytical technique that is based on column chromatography. In normal phase HPLC, a non-polar solvent mobile phase, containing the sample, is passed through a stationary phase, often a porous silica gel bonded with alkyl chains on the surface. The stationary phase provides a chemical environment for the sample within the solvent to interact with. Polar compounds within the sample interact with the stationary phase and so are retained in the column for a longer period of time compared to less, or non-polar, compounds. The time taken for a compound to pass through the column to the detector is known as the retention time and can be varied by the pressure of the system, the column (material used, length, pore size), composition of the solvent, and the temperature of the column. In reverse phase HPLC, the silica stationary phase is modified by the attachment of hydrocarbon chains to make it non-polar and a polar solvent is used as the mobile phase. As a result, polar molecules will travel through the column more quickly than non-polar molecules which tend to form attractions with the hydrocarbon groups in the stationary phase.

To analyse the peptide reverse phase HPLC was used. APhenomenex C18 column was used with a particle size of 5 μm, pore size 100 Å, length of 150 mm, and an internal diameter of 4.60 nm. A UV absorption detection was use at 230 nm. For the mobile phase a gradient elusion was used consisting of 0-5 min 95% H_2O, 5-35 min 95% MeOH, 35-45 min 95% H_2O at a flow rate of 1 ml/min at 25 ^oC. Both eluents contained 0.1% TFA.

2.2.9 Matrix-assisted laser desorption ionisation time-of-flight (MALDI-TOF)

Matrix-assisted laser desorption ionisation time-of-flight (MALDI-TOF) is a mass analysis technique that can be used to identify the mass of a variety of biomolecules, such as whole proteins and peptides (Caprioli et al., 1997). The sample is dispersed in a matrix material containing a chromophore to absorb the laser incident light. The sample and matrix is dried on a MALDI target plate. After inserting the target plate and initiating the MALDI-TOF, short pulses of laser light is focused onto the sample. Energy from the incident light causes the sample and matrix to volatilise and form ions. The ions are then accelerated by high voltage before drifting through the flight tube towards the detector. The time of flight before detection at the end of the flight tube is dependent on the mass of the ions. Mass is then calculated using the following equation:

$$m/Z = B\,(t-A)^2$$

Where, m is mass, Z is calculated from the charge of the ion, A and B are calibration constants determined by calibration to a known m/Z, and t is time of flight.

In this work, a Shimadzu Axima-CFR MADLI-TOF with a variable repetition rate 50 Hz N_2 laser with a wavelength of 337 nm was used to analyse the mass of PEG, peptide, and successful conjugation of both. A matrix material was prepared containing 10 g α-cyano-4-hydroxycinnamic acid (HCCA) added to 1 ml 50:50 water/acetonitrile (ACN) with 0.1% triflouroacetic acid (TFA) in a 1.5 ml

microcentrifuge tube. The sample solution, at a concentration of 1 mg/ml in water, was diluted 1:1 with ACN and 0.1% TFA before adding to the matrix at a ratio of 1:1. The combined sample and matrix was dropped onto a metal target plate and dried before analysis using Shimadzu Axima-CFR MADLI-TOF.

2.3 Cell culture conditions and *in vitro* experiments

2.3.1 General cell culture conditions

All cells were incubated at 37ºC, 5% CO_2 / 95% air. In this work, all cell lines used were monolayer cells attached to tissue culture flasks. General cell culture conditions were adapted from Basic Principles of Cancer Cell Culture (Langdon, 2004).

Continuous cultures are single cell types that are immortalised and grow indefinitely. Usually however, they will grow for a limited time before growth is affected and in this study continuous cultures were grown to passage 30 after which time they are likely to senesce. The continuous cultures used were A375 (human malignant melanoma), SK-MEL-28 (human malignant melanoma), M202 (human malignant melanoma), M229 (human malignant melanoma), M285 (human malignant melanoma), A2058 (human malignant melanoma), B16F10 (mouse malignant melanoma), MDCK (canine kidney), and A549 (human lung carcinoma). Cells were gifted by Prof. Chien and Prof. Moon, University of Washington (A375, SK-MEL-28, M202, M229, M285, and A2058); Dr. Al-Jamal, University of East Anglia (B16F10); Dr. Mogensen, University of East Anglia (MDCK); and Dr. Morris, University of East Anglia (A549). These cells lines were cultured in Roswell Park Memorial Institute (RPMI) 1640 cell culture media with 25 mM HEPES zwitterion to maintain a pH range of 7.0-7.6, phenol red pH indicator, carbohydrates in the form of glucose (1.8-2.2 g/l), and essential amino acids and vitamins.

RPMI-1640 was supplemented with 10% heat-inactivated foetal calf serum (FCS) which contained a mixture of albumins, growth factors, and growth inhibitors,

which are all important for supporting the growth of cells, maintaining cell characteristics and increasing the buffering capacity of the media. Also added to the culture media was 2 mM L-glutamine, 100 µg/ml penicillin, and 100 µg/ml streptomycin. Continuous adherent cells were subcultured using the protease 0.25% trypsin/EDTA in HBSS without Ca^{2+}/Mg^{2+} at 70-80% cell confluency.

Human epidermal melanocytes lightly pigmented (HEMA-lp) used in this work were commercial primary cells isolated from lightly pigmented human tissue obtained from ThermoFisher Scientific (#C0245C). Medium 254 with 200 µM calcium chloride was used for HEMA-lp cell culture and supplemented with human melanocyte growth supplement (HMGS). After addition of HMGS to a 500 ml bottle, Medium 254 contained a final concentration of bovine pituitary extract (BPE; 0.2% v/v), fetal calf serum (0.5% v/v), recombinant human insulin-like growth factor-1 (1 µg/ml), bovine transferrin (5 µg/ml) basic fibroblast growth factor (3 ng/ml), hydrocortisone (0.18 µg/ml), heparin (3 µg/ml), and phorbol 12-myristate 13-acetate (PMA; 10 ng/ml). As HEMA-lp cells are sensitive to trypsin, the subculturing of cells was done with trypsin neutraliser after 0.25% trypsin/EDTA in HBSS without Ca^{2+}/Mg^{2+}.

2.3.2 Seed stock preparation of cell lines

All cell lines were stored as a seed stock in sterile cryovials in liquid nitrogen. The cells were suspended in FCS with 10% DMSO at a concentration of approximately 0.75×10^6 cells/ml. Subsequent freezing of the cells was achieved in a Mr Frosty freezing container (ThermoFisher Scientific) containing 100% isopropanol and transferred to a -80 ^oC freezer. The freezing container was used to insure the cells froze

at the optimal rate for cell preservation (-1 ^{o}C/min). Once at -80 ^{o}C, cryovials were transferred to the liquid nitrogen dewar for long-term storage.

Resuscitation of the cells was achieved by rapid thawing of cryovials in a 37 ^{o}C water bath. As soon as the cell suspension had thawed, 5 ml of appropriate growth media was added to dilute the DMSO and the cells seed in a cell culture flask. After the cells had adhered to the culture flask, the DMSO containing media was removed, the cells gently washed with PBS, and fresh media was added.

2.3.3 PCR detection of mycoplasma

Routine inspection for mycoplasma contamination was carried out on all cell lines. Mycoplasmas can impact the analysis of biological assays and are a particular problem in cell culture as, unlike most bacterial or fungal contamination, they can be very difficult to detect without specific screening. Testing for mycoplasma contamination was performed using EZ-PCR mycoplasma test kit following manufacturer's instructions as well as with PCR primers (Van Kuppeveld et al., 1994, Van Kuppeveld et al., 1993):

Forward Primer (GPO-3) 5' - 3': GGGAGCAAACAGGATTAGATACCCT

Reverse Primer (MGSO): 5' - 3': TGCACCATCTGTCACTCTGTTAACCTC

Briefly, media, was removed from the cell culture flask after being in contact with the adherent cells for a minimum of 48 h. A positive control of *Mycoplasma hominis* DNA and a negative control of nuclease free sterile water was used. After DNA amplification using a thermal cycler, samples were analysed using

electrophoresis through a 2% agarose gel (2% w/v agarose in TAE buffer). The gel was run at 90 V for approximately 30 min with 5 µl Quick-Load 1 kb DNA ladder. Using the DNA intercalating agent GelRed (0.004% v/v) in the agarose gel, the amplified DNA was visualised under UV light using a BioRad Molecular Imager ChemiDoc XRS. A positive sample was confirmed by a band at 270 bp.

2.3.4 Trypan Blue exclusion assay

Cell viability after stimulation with different NPs was assessed using Trypan Blue exclusion assay (Strober, 2001). Trypan Blue is a dye that is able to penetrate through the cell membrane of dead cells. Trypan Blue is unable to penetrate live cells. A549 and SK-MEL-28 cell lines were seeded at a seeding density of 26550 cells per well and MDCK cells at 20000 cells per well in a 24-well plate. Cells were exposed to NPs at different concentrations for 72 h. After 72 h the cells were detached from the wells using 100 µl trypsin/EDTA. Once detached, 10 µl of cell suspension and 10 µl of Trypan Blue were loaded into a haemocytometer and counted using a light microscope. Results were expressed as percent cell viability normalised to a control of unstimulated cells.

2.3.5 Cell viability MTT assay

Tetrazolium salts, such as 3-(4,5-dimethylthiazolyl)-2,5-diphenyltetrazolium bromide (MTT), are reduced to formazan by the cytochrome of viable cells (Berridge and Tan, 1993). The resulting dark blue formazan product can be easily measured using a spectrophotometer (λ_{max} 565), allowing viable cells to be quantified.

A549, SK-MEL-28, and MDCK cells were seeded at a density of 4500 cells per well in 96 well plates and incubated overnight. After incubation, the media was discarded and the cells were washed once with PBS before 140 µl of fresh media was added to each well. Different concentrations of NPs were achieved by dilution in either PBS or autoclaved MQW and added to the appropriate wells, of which the final volume was 150 µl. The cells were stimulated with the NPs for 72 h. After stimulation, the media containing NPs was discarded and the cells washed with PBS. Fresh media and 50 µl of MTT (2 mg/ml), in autoclaved MQW, was added to a total volume of 250 µl per well and incubated for 4 h. The media was then removed, leaving the insoluble formazan product. DMSO (200 µl per well) and Sørensen's glycine buffer (25 µl) per well was used to resuspend the formazan before reading at absorbance 570 nm on a spectrophotometer. Percentage viability of the cells was calculated as a ratio of mean absorbance from quadruplicate readings with respect to the control wells of non-stimulated cells:

$$\text{Percentage cell viability} = (I_{sample}/I_{control}) \times 100$$

2.3.6 Protein extraction and quantification

Cells were removed from the flask or well plate using EDTA/Typsin and suspended in media. The cells were then centrifuged at 1200 rpm for 5 mins and the supernatant aspirated. The resulting cell pellets were lysed in lysis buffer with the addition of PhosSTOP phosphatase inhibitor and cOmplete protease inhibitor for 30 mins on ice, and then centrifuged at 16000 x *g* for 10 mins at 4 ^{o}C. Protein concentration was calculated from the crude protein supernatant using the colourimetric BCA Protein Assay Kit (Walker, 2009). Dilutions of the supplied BSA with known protein

concentrations are used to produce a standard curve at an absorbance of 562 nm using POLARstar Optima microplate reader (BMG Labtech) after colour development reaction with BCA. This was then used to determine the protein concentration of the cell lysates.

2.3.7 SDS-polyacrylamide gel electrophoresis

Protein concentrations were equalised in lysis buffer before adding dithiothritol (DTT) reducing agent, to reducing disulphide bridges, and SDS Loading Buffer and heated at 90 °C for 10 mins (Jenei et al., 2009). Samples were then loaded onto a 12% resolving polyacrylamide gel, overlaid with a 5% stacking gel (table 2.3.1) set in Biorad mini PROTEAN 3 cell apparatus. The total amount of protein loaded was in the range of 20-30 µg. Gels were loaded into the Biorad Electrode Assembly and placed into the Mini Tank with running buffer.

Protein samples were run through the 5% polyacrylamide stacking gel at 90 V until they reached the interface between the upper and lower gels using 1 x running buffer. Once at the 12% resolving gel, the voltage was increased to 120 V until the proteins had fully resolved through the gel and electrophoresis was terminated.

Table 2.3.1 Reagents of resolving and stacking polyacrylamide gels for electrophoresis

12% resolving (lower) gel	**5% stacking (upper) gel**
MQW - *3.45 ml*	MQW - *2.90 ml*
40% acrylamide - *2.40 ml*	40% acrylamide – *0.75 ml*
1.5 M Tris (pH 8.8) - *2.00 ml*	0.5 M Tris (pH 6.8) - *1.25 ml*
10% SDS – *80 µl*	10% SDS – *50 µl*
10% APS – *80 µl*	10% APS – *50 µl*
TEMED – *8 µl*	TEMED – *5 µl*

2.3.8 Western Immunoblotting

Following electrophoresis, protein was transferred from the polyacrylamide gel to a nitrocellulose membrane in accordance with BioRad Mini protean 3 transfer system in a transfer buffer for 2 h at 250 mA. Successful transfer of proteins onto the nitrocellulose membrane was checked using Ponceau S red staining. The nitrocellulose membrane was then blocked to prevent non-specific binding of primary and/or secondary HRP-conjugated antibodies to the membrane; leading to a high background and a low signal-to-noise ratio. Depending on the primary antibody, the membrane was blocked for 1 h at room temperature in either 5% milk powder in PBS or 3% FCS in TBST (Safholm et al., 2006). Primary antibody, diluted in the relevant blocking buffer, was added overnight at 4 °C.

Following incubation with the primary antibody, the membrane was washed three times, each wash for 10 mins, in TBST to remove any unbound primary antibody. The applicable HRP-conjugated secondary antibody was then added for 1 hour at room temperature. Again, the membrane was washed three times in TBST to remove any unbound secondary antibody before Pierce Enhanced Chemi-Luminescence (ECL) Western Blotting Substrate to detect HRP activity. After addition of the peroxidase substrate, the HRP activity was visualised using BioRad Molecular Imager ChemiDoc XRS. A loading control of α-tubulin was used to check that protein concentrations were even across the samples and that even transfer occurred.

2.3.9 Reverse transfection of siRNA

MC1R siRNA (ThermoFisher Scientific) was transfected into A2058 cells by adaptation of a previously described reverse transfection protocol (Chien et al., 2009). A RNA interference (RNAi) duplex was made to a final concentration of 20 nM siRNA in 100 µl serum free media with the addition of 1 µl Lipofectamine transfection reagent per well. The siRNA and Lipofectamine was incubated together at room temperature for 20 min to allow for the formation of siRNA-Lipofectamine complexes. The cells were prepared in complete growth media (without antibiotics) so that the cells were 50% confluent in a 12-well plate. Cells were incubated for 48, 72, and 96 h.

2.4 In vivo analysis

2.4.1 Obtaining embryos

Female *Xenopus laevis* adults were primed by injection of 100 units of pregnant mare serum gonadotrophin (PMSG) into the dorsal lymph sac 5-7 days before the eggs were required. To induce ovulation, 250 µl of human chorionic gonadotrophin (hCG) was injected into each dorsal lymph sac. After approximately 14 h at 18 ^{o}C, manual squeezing of the female *X. laevis* abdomen to encourage egg release into a petri dish. Testis were removed from a sacrificed male and stored in testes buffer (100% FCS, MMR (4:1)). The eggs were then covered, for 5 m at 18 ^{o}C with testes that had been homogenised in MMR. Concentration of the salt solution was reduced to 0.1 x MMR

and the eggs are left for 20 m at 18 ºC for fertilisation. The eggs were then placed in a beaker containing 2% cysteine (pH 8.0) dissolved in MMR and gently stirred to remove the jelly coat that the eggs are encased in. Cysteine was removed by washing in MMR followed by a wash of 0.1 x MMR. Procedures described thus far were undertaken by a member of the Wheeler lab with the appropriate animal licence for the handling of adult *Xenopus laevis.* All experiments were performed in compliance with the relevant laws and institutional guidelines at the University of East Anglia. The research had approval by the local ethical review committee according to UK Home Office regulations.

Embryos were left at 18 ºC and monitored until they had reached the required stage for the phenotypic assay, according to Nieuwkoop and Faber (NF; Nieuwkoop and Faber, 1956). The eggs were cleaned once every hour in 0.1 x MMR and 1:1000 gentamycin until they have reached the necessary stage. Any dead embryos were removed twice daily.

2.4.2 Xenopus phenotypic assay

Live embryos were collected for exposure to NPs at NF stages 4, 15, and 38, as described in 2.4.1. The stages of *X. laevis* were selected to assess NP toxicity during key stages of development an organism. These stages correlate to pre-gastrulation (NF stage 4), pre-neuralation (NF stage 15), and pre-tadpole (NF stage 38). Concentrations of NPs were made up using serial dilutions 0.1 x MMR, total volume 500 µl per well. In a 24-well plate, 5 embryos per well were collected in 500 µl of 0.1 x MMR and added to the NPs, total volume 1000 µl per well.

Embryos were incubated and exposed to NPs at 18 ºC until the required NF stage. Embryos exposed to NPs at NF stages 4 and 15 were fixed at NF stage 38. Those that were exposed to NPs at NF stage 38 were fixed at NF stage 45. Once the embryos reached the required stage they were washed in 0.1 x MMR and anesthetised with 0.6 mg/ml ethyl 3–aminobenzoate methanesulfonate salt before fixing in MEMFA. The embryos are left in MEMFA for 1 h at room temperature or overnight at 4 ºC. After 2 washes in PBST all embryos were ranked by phenotypic abnormalities. Once ranked, the embryos were dehydrated in increasing concentrations of methanol, 25%, 50%, and 75%, before being stored at -20 ºC in 100% MeOH. The embryos were rehydrated using decreasing concentrations of MeOH, 75%, 50%, and 25% and 2 washes of PBST, before imaging or sectioning (method 2.4.3-2.4.5).

2.4.3 Cryosection of embryos

Embryos were placed in 30% sucrose overnight at 4 ºC. They were then transferred to cryomoulds containing optimal cutting temperature (OCT) solution or 15% fish gelatin. The embryos were then orientated in the correct position for cutting. Once orientated, the samples were flash frozen by surrounding the cryomoulds with dry ice until the OCT or fish gelatin had completely solidified. Samples were then stored at -80 ºC until needed. Using a LEICA CM 1950 Cryostat, the embryos were sectioned at 10 μm and kept on 5% TESPA coated slides overnight at room temperature. The slides were then washed with PBS, stained with Hoescht 33342, before hydromount was used to secure a cover slip over the samples.

2.4.4 X. laevis whole mount fluorescence microscopy

To investigate internalisation of the fluorescent PS-COOH NPs in *X. laevis,* NF stage 38 embryos were exposed to 10^{15} NP/ml until they had developed to NF stage 45. Embryos were then anesthetised with 0.6 mg/ml ethyl 3–aminobenzoate methanesulfonate salt. PS-COOH particles were imaged in the bloodstream of anaesthetised embryos using Nikon Eclipse 600 with a CCD digital camera, with an emission filter of 509–547 nm**.**

2.4.5 X. laevis TEM

Internalisation of Fe_3O_4-core NPs (Fe_3O_4-PEG and Fe_3O_4-NH_2) was assessed using TEM microscopy, as previously described (2.2.5). Embryos were exposed to $10^{15.3}$ Fe_3O_4 NPs from NF stage 38 to NF stage 45. Embryos were then fixed in 4% paraformaldehyde and 2% glutaraldehyde in 0.1 M sodium cacodylate (Bacchetta et al., 2012). A post fix of 1% osmium tetroxide (OsO_4) for 1.5 h at 4 ^{o}C was used to increase electron density in lipids and proteins. Fixed embryos were then dehydrated in decreasing concentrations of MeOH before being washed in 100% propylene oxide before infiltration in propylene oxide resin overnight. Embryos were then submersed in resin and polymerisation occurred at 60 ^{o}C for 48 h. Sections, at 1 μm thickness, were mounted onto carbon-coated 300 – mesh copper grids and observed using a Tecnai 20 TEM with AMT cameras, operating at an acceleration voltage of 200 kV.

2.4.6 Mouse Magnetic Resonance Imaging (MRI)

Fe_3O_4-core NPs were sent to Institute for Pharmacological Research "Mario Negri" (IRCCS) in Milan for murine toxicology and uptake assays. All experiments involving mice was conducted in compliance with national (Decreto Legge nr 116/92, Gazzetta Ufficiale, supplement 40, February 18, 1992; Circolare nr 8, Gazzetta Ufficiale, July 14, 1994) and international laws and policies (EEC Council Directive 86/609, OJL 358, 1, Dec. 12, 1987; Guide for the Care and Use of Laboratory Animals, US National Research Council, 8th edition, 2011). The work was reviewed by IRCCS-IRFMN Animal Care and Use Committee (IACUC) and then approved by the Italian 'Istituto Superiore di Sanità' code 17/01 D Appl 3. NFR mice were bred until 3 months old and maintained under pathogen-free conditions at the IRCCS Animal Care Facility. A total of 15 mice were used and were randomly divided into three experimental groups PBS-treated control group (n=3), Fe_3O_4-NH_2 (n=6) and Fe_3O_4-PEG treated mice (n=6). NP solution at a concentration of 15 µg Fe_3O_4/ml and control was injected as a single 150 µl dose in the tail vein.

MRI was performed on mice pre and post NP treatment on 7 T/30 cm horizontal bore magnet (Bruker-Biospin) with a 12 cm gradient set, capable of supplying a maximum of 400 mT/m. Mice were anesthetised with isoflurane, 30% oxygen, and 70% nitrous oxide during MRI analysis and body temperature stabilised with a warmed cradle at 36 ± 1 ^{o}C. A total of three mice were used for each group and MRI was performed after 24 h and 120 h after NP injection. Intensity was normalised to signal from the dorsal muscle as this is an area where NPs do not accumulate and analysis was concentrated on the liver and kidney tissues using Fuji Image J imaging

software. Post MRI scan, all animals were sacrificed with an overdose of 75 mg/kg ketamine and 1 mg/kg medetotimine.

Following MRI analysis, liver and kidney tissue was removed from the animals and post fixed with 4% paraformaldehyde for 24 h. Samples were then paraffin embedded and processed for histopathology. Sections, 5 µm in thickness, were stained with hematoxylin and eosin (HE) before observation using a light microscope. Perl's staining (Diapath Perl's Staining Kit; (Katsnelson et al., 2011, Song et al., 2015) was used to highlight Fe_3O_4 in the tissue.

2.5 NPs *in vitro*

2.5.1 Confocal microscopy

Cells were seeded at seeding density of 2 x 10^4 cells per well in a 12 well plate, each well containing a sterile ø 18 mm borosilicate glass cover slip. The cells were left overnight at 37 ^oC to adhere to the glass cover slips before addition of NPs.

At the assay endpoint, the media was removed and the cells were washed in 3 times PBS before fixation in 4% paraformaldehyde. Coverslips were then washed a further 3 times with PBS and any reactive aldehydes from the fixative were quenched with a wash of 50 mM NH_4Cl. Coverslips were than mounted on a glass slide using Hydromount and secured. Cells were imaged using a Zeiss LSM510 META confocal microscope.

2.5.2 Flow cytometry

Flow cytometry is a technique used to analyse physical properties of NPs with a size range of 0.2-150 μm. The most common application is the analysis of cells and, for this work, flow cytometry was employed to analyse the uptake of NPs in mammalian cells (Suzuki et al., 2007, Zucker and Daniel, 2012). The suspended cells are transported in the fluidics of the flow cytometer and are focused as a stream of individual cells by the sheath fluid, and directed through the flow cell where it is hit by a laser beam. As the sample stream is pressurised, the flow rate can be controlled by changing the pressure (figure 2.5.1).

When the cells are hit by the laser the light is deflected. The extent at which the light is scattered is a result of the surface area or size of the cell, measured by the forward scatter (FCS) and the internal compartments, or granulation measured by side scatter (SSC). Once the correct population of single cells has been established fluorescent activity can be analysed.

For NP uptake analysis we encapsulated the fluorescent dye NR into the hydrophobic shell of the Fe_3O_4-core NP (method 2.1.8). As a fluorescent compound, NR absorbs light from the argon ion laser beam emitting light at 488 nm, which was used for this work. The absorption of light causes an electron in NR to be raised to a higher energy level. The return of this electron to the ground state results in a release of energy that is emitted at a longer wavelength to the 488 nm originally absorbed by the compound at a maximum λ_{em} 635 nm. We detected the emission of NR using one of the machine detectors, FL-4.

Cells were seeded at a seed density of 5 x 10^4 cells per well in a 24-well plate and left to adhere overnight. After the cells had adhered, they were washed with PBS before exposure to NPs at a final concentration of 1.4 x 10^{12} NP/ml. At the assay endpoint, the cell media was removed and the cells washed with 1 x PBS before de-adherence of cells using 0.2% trypsin/EDTA. Once the cells were resuspended, they were transferred to a 1.5 ml microcentrifuge tube and pelleted by centrifugation at 200 x *g* for 5 mins. The supernatant was then removed and the resulting cell pellet was resuspended in media. The cells were then washed with PBS before fixation in 4% paraformaldehyde in PBS for 30 mins at room temperature with agitation. After fixation, cells were washed by pelleting at 1500 rpm and resuspending in PBS. This was repeated three times. Finally, the cells were suspended in PBS + 2% FCS and transferred to 5 ml round bottom polystyrene test tube before measuring using Beckman Coulter Cytomics FC 500 flow cytometer. Analysis was performed using Kaluza Analysis 1.3 (Beckman Coulter) software.

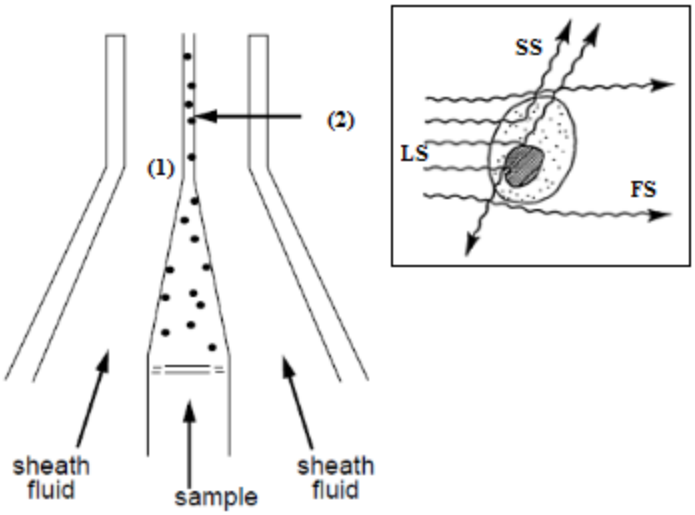

Figure 2.5.1 Flow cytometry fluidics. The sample of cells is injected into the fluidics of the flow cytometer and directed into a single stream of cells via the sheath fluid (1). Once directed into a hydrodynamic focus the sample is hit by a laser beam (2). Increasing the pressure of the fluidics leads to a wider stream of sample through the laser beam. This can cause the laser to hit the cells at a below optimal angle, resulting in a lower accuracy. Decreasing pressure insures a single cell stream of sample through the laser beam resulting in a higher accuracy. Multiple detectors are used to identify SS, FS, and fluorescence. Image from Becton, Dickinson, and Company.

2.6 Human lymphadectomy tissue

2.6.1 Tissue digestion

Patients diagnosed with cutaneous melanoma had given prior consent for biopsied tissue, after sentinel lymph node biopsy, to be used for our research. HTA-compliant Norwich Biorepository (HTA licence 11208; National Research Ethics Service reference, 08/H0304/85) ethical approval was obtained. All procedures of patient-derived melanoma cells were approved by the UEA Faculty of Medicine and Health ethics committee (Ref: 2013/2014-03HT).

Tissue was collected from the Norfolk and Norwich University Hospital and transported to the lab in a sterile 50 ml centrifuge tube containing 1 x HBSS, 2% FCS, 100 U/ml penicillin, and 100 μg/ml streptomycin. Once in the cell culture laboratory, the sample was weighed and characterised according to its general appearance. The tissue was washed twice and vortexed in PBS to remove any blood and/or debris; the tissue was decanted and the liquid discarded. After transfer to a sterile petri dish, the tissue was finely minced using forceps and scissors. A digestion solution containing 0.075% collagenase IV in PBS, 0.01% hyaluronidase from bovine testes, and 0.01% deoxyribonuclease I from bovine pancreas, was added to a small beaker along with the minced tissue sample and a magnetic stir bar. The digesting sample was placed in a water bath at 37 ^{o}C and mixed for 30 mins. During this time the majority of the tissue should be digested, however the sample was strained through a 70 μm nylon mesh filter into a 50 ml centrifuge tube to remove any large undigested material. After filtration, the cells were pelleted from the digestion solution by centrifugation at 200

x *g* for 10 mins. The supernatant was discarded and the cell pellet was resuspended in PBS to wash.

2.6.2 Cell staining of digested lymphadectomy tissue for FACS

Cells were stained with anti-human neural/glial antigen 2 (NG2) Alexa Fluor® 488, melanoma marker (Li et al., 2003, Yang et al., 2004), and anti-human CD45 Alexa Fluor® 610, lymphocyte marker (Bouma-Ter Steege et al., 2004, Ninomiya et al., 2007), directly conjugated primary antibodies. After digestion, primary cells in PBS were centrifuged at 200 x *g* for 10 mins to pellet the cells. The supernatant was removed and the cells resuspended in HBSS containing 2% FCS as a blocking buffer and incubated at room temperature for 20 mins.

Following blocking, the cell suspension was transferred to two sterile micro-centrifuge tubes; an unlabelled control, and an antibody-labelled sample. The cells were centrifuged at 450 x *g* for 5 mins and, after discarding the supernatant, then resuspended in 100 µl of HBSS 2% FCS. NG2 and CD45 antibodies were added to the microcentrifuge tube for the labelled sample and incubated, in the dark at room temperature, for 30 mins.

After staining, cells were pelleted at 450 x *g* for 5 mins and washed twice in HBSS 2% FCS. For each wash the cells were centrifuged at 450 x *g* for 5 mins at room temperature and the supernatant was discarded between washes. Following the last wash, the cells were resuspended in 500 µl HBSS 0.5% FCS.

The samples were taken directly to a Sony SH800 cell sorter (Institute of Food Research, Norwich Research Park) contained in a BioMat class II biological safety cabinet and sorted into $NG2^{+}$ /$CD45^{-}$ and $NG2^{-}$ populations.

2.7 References

Bacchetta, R., Tremolada, P., Di Benedetto, C., Santo, N., Fascio, U., Chirico, G., Colombo, A., Camatini, M. & Mantecca, P. 2012. Does carbon nanopowder threaten amphibian development? *Carbon,* 50**,** 4607-4618.

Bekyarova, E., Itkis, M. E., Ramesh, P., Berger, C., Sprinkle, M., De Heer, W. A. & Haddon, R. C. 2009. Chemical modification of epitaxial graphene: spontaneous grafting of aryl groups. *Journal of the American Chemical Society,* 131**,** 1336-1337.

Berridge, M. V. & Tan, A. S. 1993. Characterization of the cellular reduction of 3-(4,5-dimethylthiazol-2-yl)-2,5-diphenyltetrazolium bromide (MTT): subcellular localization, substrate dependence, and involvement of mitochondrial electron transport in MTT reduction. *Arch Biochem Biophys,* 303**,** 474-82.

Binnig, G., Quate, C. F. & Gerber, C. 1986. Atomic force microscope. *Phys Rev Lett,* 56**,** 930-933.

Bouma-Ter Steege, J. C., Baeten, C. I., Thijssen, V. L., Satijn, S. A., Verhoeven, I. C., Hillen, H. F., Wagstaff, J. & Griffioen, A. W. 2004. Angiogenic profile of breast carcinoma determines leukocyte infiltration. *Clin Cancer Res,* 10**,** 7171-8.

Caprioli, R. M., Farmer, T. B. & Gile, J. 1997. Molecular imaging of biological samples: localization of peptides and proteins using MALDI-TOF MS. *Analytical chemistry,* 69**,** 4751-4760.

Chien, A. J., Moore, E. C., Lonsdorf, A. S., Kulikauskas, R. M., Rothberg, B. G., Berger, A. J., Major, M. B., Hwang, S. T., Rimm, D. L. & Moon, R. T. 2009. Activated Wnt/beta-catenin signaling in melanoma is associated with decreased proliferation in patient tumors and a murine melanoma model. *Proc Natl Acad Sci U S A,* 106**,** 1193-8.

Di Corato, R., Quarta, A., Piacenza, P., Ragusa, A., Figuerola, A., Buonsanti, R., Cingolani, R., Manna, L. & Pellegrino, T. 2008. Water solubilization of hydrophobic nanocrystals by means of poly(maleic anhydride-alt-1-octadecene). *Journal of Materials Chemistry,* 18**,** 1991-1996.

Fang, C., Bhattarai, N., Sun, C. & Zhang, M. 2009. Functionalized Nanoparticles with Long‐Term Stability in Biological Media. *Small,* 5**,** 1637-1641.

Gref, R., Luck, M., Quellec, P., Marchand, M., Dellacherie, E., Harnisch, S., Blunk, T. & Muller, R. H. 2000. 'Stealth' corona-core nanoparticles surface modified by polyethylene glycol (PEG): influences of the corona (PEG chain length and surface density) and of the core composition on phagocytic uptake and plasma protein adsorption. *Colloids and Surfaces B-Biointerfaces,* 18**,** 301-313.

Han, G., Tamaki, M. & Hruby, V. J. 2001. Fast, efficient and selective deprotection of the tert-butoxycarbonyl (Boc) group using HCl/dioxane (4 m). *J Pept Res,* 58**,** 338-41.

Hiemenz, P. C. & Rajagopalan, R. 1997. *Principles of colloid and surface chemistry,* New York, Marcel Dekker.

Hoo, C. M., Starostin, N., West, P. & Mecartney, M. L. 2008. A comparison of atomic force microscopy (AFM) and dynamic light scattering (DLS) methods to characterize nanoparticle size distributions. *Journal of Nanoparticle Research,* 10**,** 89-96.

Jenei, V., Sherwood, V., Howlin, J., Linnskog, R., Safholm, A., Axelsson, L. & Andersson, T. 2009. A t-butyloxycarbonyl-modified Wnt5a-derived hexapeptide functions as a potent antagonist of Wnt5a-dependent melanoma cell invasion. *Proc Natl Acad Sci U S A,* 106**,** 19473-8.

Katsnelson, B. A., Degtyareva, T. D., Minigalieva, I. I., Privalova, L. I., Kuzmin, S. V., Yeremenko, O. S., Kireyeva, E. P., Sutunkova, M. P., Valamina, I. I. & Khodos, M. Y. 2011. Subchronic systemic toxicity and bioaccumulation of Fe3O4 nano-and microparticles following repeated intraperitoneal administration to rats. *International journal of toxicology,* 30**,** 59-68.

Langdon, S. P. 2004. Basic principles of cancer cell culture. *Methods Mol Med,* 88**,** 3-15.

Li, Y., Madigan, M. C., Lai, K., Conway, R. M., Billson, F. A., Crouch, R. & Allen, B. J. 2003. Human uveal melanoma expresses NG2 immunoreactivity. *Br J Ophthalmol,* 87**,** 629-32.

Lu, W., Xiong, C., Zhang, G., Huang, Q., Zhang, R., Zhang, J. Z. & Li, C. 2009. Targeted photothermal ablation of murine melanomas with melanocyte-

stimulating hormone analog-conjugated hollow gold nanospheres. *Clin Cancer Res,* 15**,** 876-86.

Nagesha, D. K., Plouffe, B. D., Phan, M., Lewis, L. H., Sridhar, S. & Murthy, S. K. 2009. Functionalization-induced improvement in magnetic properties of Fe3O4 nanoparticles for biomedical applications. *Journal of Applied Physics,* 105**,** 07B317.

Ninomiya, M., Abe, A., Katsumi, A., Xu, J., Ito, M., Arai, F., Suda, T., Ito, M., Kiyoi, H., Kinoshita, T. & Naoe, T. 2007. Homing, proliferation and survival sites of human leukemia cells in vivo in immunodeficient mice. *Leukemia,* 21**,** 136-42.

Nitin, N., Laconte, L. E., Zurkiya, O., Hu, X. & Bao, G. 2004. Functionalization and peptide-based delivery of magnetic nanoparticles as an intracellular MRI contrast agent. *J Biol Inorg Chem,* 9**,** 706-12.

Safholm, A., Leandersson, K., Dejmek, J., Nielsen, C. K., Villoutreix, B. O. & Andersson, T. 2006. A formylated hexapeptide ligand mimics the ability of Wnt-5a to impair migration of human breast epithelial cells. *J Biol Chem,* 281**,** 2740-9.

Song, L., Zang, F., Song, M., Chen, G. & Zhang, Y. 2015. Effective PEGylation of Fe3O4 nanomicelles for in vivo MR imaging. *Journal of nanoscience and nanotechnology,* 15**,** 4111-4118.

Strober, W. 2001. Trypan blue exclusion test of cell viability. *Current protocols in immunology***,** A3. B. 1-A3. B. 3.

Sun, S., Zeng, H., Robinson, D. B., Raoux, S., Rice, P. M., Wang, S. X. & Li, G. 2004. Monodisperse MFe2O4 (M = Fe, Co, Mn) nanoparticles. *J Am Chem Soc,* 126**,** 273-9.

Suzuki, H., Toyooka, T. & Ibuki, Y. 2007. Simple and easy method to evaluate uptake potential of nanoparticles in mammalian cells using a flow cytometric light scatter analysis. *Environmental Science & Technology,* 41**,** 3018-3024.

Van Kuppeveld, F. J., Johansson, K. E., Galama, J. M., Kissing, J., Bolske, G., Hjelm, E., Van Der Logt, J. T. & Melchers, W. J. 1994. 16S rRNA based polymerase chain reaction compared with culture and serological methods for diagnosis of Mycoplasma pneumoniae infection. *Eur J Clin Microbiol Infect Dis,* 13**,** 401-5.

Van Kuppeveld, F. J., Van Der Logt, J. T., Angulo, A. F., Van Zoest, M. J., Quint, W. G., Niesters, H. G., Galama, J. M. & Melchers, W. J. 1993. Genus- and species-

specific identification of mycoplasmas by 16S rRNA amplification. *Appl Environ Microbiol,* 59**,** 655.

Walker, J. M. 2009. The bicinchoninic acid (BCA) assay for protein quantitation. *The Protein Protocols Handbook***,** 11-15.

Wang, L., Nagesha, D. K., Selvarasah, S., Dokmeci, M. R. & Carrier, R. L. 2008. Toxicity of CdSe Nanoparticles in Caco-2 Cell Cultures. *J Nanobiotechnology,* 6**,** 11.

Wang, X., Zhang, R., Wu, C., Dai, Y., Song, M., Gutmann, S., Gao, F., Lv, G., Li, J. & Li, X. 2007. The application of Fe3O4 nanoparticles in cancer research: a new strategy to inhibit drug resistance. *Journal of Biomedical Materials Research Part A,* 80**,** 852-860.

Yang, J., Price, M. A., Neudauer, C. L., Wilson, C., Ferrone, S., Xia, H., Iida, J., Simpson, M. A. & Mccarthy, J. B. 2004. Melanoma chondroitin sulfate proteoglycan enhances FAK and ERK activation by distinct mechanisms. *J Cell Biol,* 165**,** 881-91.

Zucker, R. M. & Daniel, K. M. 2012. Detection of TiO2 nanoparticles in cells by flow cytometry. *Methods Mol Biol,* 906**,** 497-509.

Chapter 3.

Synthesis, functionalisation, and purification of Fe_3O_4 nanoparticles

3. Synthesis, functionalisation, and purification of Fe_3O_4 nanoparticles

3.1 Introduction

Iron oxides in the nanometre range have been explored for a variety of applications including catalysis (Li et al., 2003), magnetic data storage (Terris and Thomson, 2005), materials (Lu et al., 2002), and, in biomedicine as drug delivery systems and contrast imaging agents (Figuerola et al., 2010, Li et al., 2013). As a biomedical tool, in particular for oncotherapy (Peng et al., 2008, Zhang and Kievit, 2012), iron oxide nanoparticles (NPs) have many advantages over other nanomaterials, such as their biocompatibility (Hanini et al., 2011). The combined magnetic and optical function of Fe_3O_4 NPs allow simultaneous diagnostic and therapeutic benefits. Among the different iron oxides, magnetite (Fe_3O_4) has attracted increasing interest as Fe_3O_4 NPs for biomedical application largely due to their superparamagnetic (SPM) properties where, under an alternating magnetic current, the NP can evoke therapeutic hyperthermia (Sonvico et al., 2005). Once there is Fe_3O_4 NP uptake in cells, intracellular magnetic heating of tumour cells can be achieved by the application of an external alternating magnetic field (AMF). The electromagnetic field transfers energy to the NP, which in turn can deliver cytotoxic amounts of thermal energy. Tumour cells are particularly sensitive to increased physiological temperatures of 42-45 ^{o}C (Overgaard and Overgaard, 1972).

A further advantage of Fe_3O_4 core NPs as an oncology drug delivery system is the exploitation of their unique properties for the use as magnetic resonance imaging (MRI) tools (Bulte et al., 1999). As a targeted MRI contrast agent, the progression of

a tumour can be monitored in a non-invasive and real-time manner; providing improved diagnostics. Several Fe_3O_4 NPs have been developed as MRI contrast agents for a range of disease states (Arsalani et al., 2010, Kim et al., 2001, Lee et al., 2004, Tromsdorf et al., 2009).

The integration of a NP that can be used as both a diagnostic and a therapeutic agent is termed 'theranostic' (Xie et al., 2010). In order to be used for therapeutic hyperthermia and as an MRI contrast agent Fe_3O_4 NPs, and other ferromagnetic or ferrimagnetic NPs, must be under a critical size to exhibit SPM activity. Magnetite reaches this critical size at diameters less than 10 nm, when the particle becomes a single-domain structure and, principally, magnetisation does not vary across the NP; all atoms within an individual NP are aligned and the particle is the sum of all these magnetic moments (Jordan et al., 2009). As a result, the NPs display anisotropy energy where the energy is directionally dependent. Generally, there is a preference for NP direction known as uniaxial anisotropy. Fe_3O_4 NPs with uniaxial anisotropy flip in the direction of their magnetisation to a stable orientation (Fannin, 1991). There are two stable orientations with minimum energy states antiparallel to each other. Thermal excitation is required to reverse the magnetisation over time where the average time to undergo this flip is known as Néel's relaxation time (τ_N) (Fannin, 1991):

$$\boldsymbol{\tau N = \tau 0\, exp\left(\frac{kV}{k_B T}\right)} \qquad \textbf{Equation 3.1}$$

Where,

- τ_0: The time constant specific to the material related to atomic reorganisation time (typically between 10^{-9} to 10^{-12} s).
- *kV*: The energy barrier of which the magnetisation flip has to overcome from k as an anisotropy constant and *V* as volume.
- k_B: The Boltzmann constant.
- *T*: The Temperature

An applied AMF can flip the orientation of the particles along the magnetic axis if it is able to surpass the energy barrier *(kV)*. Under an AMF, rotation of the overall magnetic moment of the NPs away from the stable orientation minimises its potential energy leading to internal friction from the movement of the magnetic moment (Jordan et al., 2009).

In order for Fe_3O_4 NPs to display SPM properties required for therapeutic hyperthermia, the size and size distribution of the NP core is particularly important. As defined by the above equation, the smaller the NP, the stronger the influence of thermal energy upon it. A particle diameter between 10 – 13 nm leads to intermediate superparamagnetic – ferromagnetic properties, whereas above 13 nm is in the ferromagnetic region (Bakoglidis et al., 2012). In addition, as the temperature released from the system is dependent on the sum of the magnetic moment a monodispersed population of NPs is required to have an effect (Bakoglidis et al., 2012). Therefore, in order to acquire superparamagnetic properties, the synthesis method for Fe_3O_4 NPs must be able to control the size of NPs and produce a narrow size distribution.

There are many recognised methods for the production of superparamagnetic iron oxide nanoparticles (SPIONs). Broadly, these methods can be divided into three

different routes of synthesis: physical, chemical, and biological. Chemical synthesis being the most popular method by publication. Within the route of chemical synthesis, co-precipitation, microemulsion, hydrothermal, and thermal decomposition are particularly proven (Hyeon, 2003). Co-precipitation is amongst the simplest and most established method, the Massart procedure (Bee et al., 1995), has changed very little over time. The method requires the addition of a base to an aqueous solution of Fe^{2+} and Fe^{3+} ions (1:2 stoichiometry). This results in a magnetite precipitate in a basic solution. However, due to magnetite readiness to oxidise to ferric hydroxide, the synthesis must occur in an inert gas. Disadvantageously, this method can be difficult to control size and size distribution.

Highly monodispersed NPs can be synthesised by thermal decomposition of organic iron precursors (Sun et al., 2004). The precursors are decomposed at high temperature in the presence of a non-polar solvent and a capping agent at the boiling point of the solvent. The size of the resulting hydrophobic NPs can be easily controlled by modifying the reactions conditions such as the reflux time. Synthesised in this way, the NP core presents a narrow size distribution and the correct diameter to exhibit SPM.

Before use in a biological assay, hydrophobic Fe_3O_4 NPs must undergo a phase transfer to allow them to disperse in an aqueous solution. Amphiphilic molecules contain regions of hydrophobic and hydrophilic properties. Amphiphilic polymers can be used to functionalise the surface of NPs;where the hydrophobic regions of the polymer interact with the alkyl chains on the surface of the NP.h As the amphiphilic polymer intercalates and wraps around the surface of the NP, the hydrophilic regions are exposed to the outside. This completes phase transfer and allows the NP to be dispersed in an aqueous solution.

In a biological environment, the NP surface can accumulate biomolecules. Proteins are one of the major constituents of biological fluids and when they become adsorbed on the surface of a NP, as they often do, a protein corona will form (Walczyk et al., 2010). The formation of a protein corona is largely dependent on particle size (Deng et al., 2011), surface charge (Hühn et al., 2013), and NP colloidal stability (Gebauer et al., 2012). For a targeted NP, the formation of a protein corona can change how the NP and cell interacts with one another (Walczyk et al., 2010).

An approach to promote specific uptake of the NPs by tumour cells is to functionalise the NP surface with biological ligands that selectively interact with receptors overexpressed by the cancer cells. To avoid the formation of a protein corona, which can hamper the target of the ligand and destabilise the NP, a non-ionic hydrophilic polymer is often used: poly(ethyleneglycol) (PEG) being one of the most studied polymers used for the stabilisation of a range of NPs (Allen et al., 1995, Bhattarai et al., 2003, Sheng et al., 2009).

This project aims to produce a monodispersed population of Fe_3O_4-core NPs that can be dispersed in an aqueous solution. The NPs will be stabilised using PEG (Fe_3O_4-PEG) and further functionalised with a targeting peptide to melanoma cells (Fe_3O_4-PEP). In this work, we have chosen to use a maleic anhydride polymer. Poly(maleic anhydride-*alt*-1-octadecene) (PMAO) is a polymer containing an anhydride ring and a 18-carbon long alkyl side chain. Copolymers of maleic anhydride have been used to for aqueous dispersion and further surface functionalisation of different NPs (Di Corato et al., 2008, Pellegrino et al., 2004), including Fe_3O_4 NPs (William et al., 2006). Furthermore, an added advantage of using a maleic anhydride polymer is that the maleic anhydride ring can be opened in a basic environment. Once the ring is open, additional functionalisation is easily achieved. Ethanolamine (Lees et

al., 2009), Jeffamine M-1000 (Lees et al., 2009), NH_2 terminated poly(*N*-isopropylacrylamide) (Qin et al., 2009), NH_2 terminated PEG (Bronstein et al., 2010, Moros et al., 2012, Muir et al., 2009), and 4-aminophenyl β-D-galactopyranoside (Moros et al., 2010) have all been successfully attached via the maleic anhydride.

3.2 Synthesis and phase transfer of Fe_3O_4 NPs

Fe_3O_4 core NPs were synthesised as previously described (Sun et al., 2004); section 2.1.2) by high-temperature solution phase reaction of iron salts (iron (iii) acetylacetonate, $Fe(acac)_3$) and 1,2-hexadecanediol, with oleic acid and oleylamine. This method has previously been used to produce a monodispersed population of Fe_3O_4 NPs (Sun et al., 2004). The reaction conditions can be modified by changing the temperature of the reaction to adjust the final diameter of the magnetite core. In this work, we performed high-temperature solution phase reaction at a reflux temperature 300 ^oC using benzyl ether to produce NPs with a diameter of 8 nm. AFM gave a clear representation of the NP size and size distribution after synthesis (figure 3.2.1). The actual average diameter of the Fe_3O_4 core, after AFM analysis, was 6 ± 1 nm. Residual material from the reaction was removed and the Fe_3O_4 NPs were dispersed in toluene. In order to use the NPs in biological assays, a phase transfer reaction was used to disperse the Fe_3O_4 NPs in an aqueous solution. Amphiphilic coating of Fe_3O_4 NPs was achieved using PMAO. PMAO, as an amphiphilic compound, was able to intercalate the alkyl chains with the hydrophilic chains of the oleate ligand on the surface of the Fe_3O_4 NP (figure 3.2.2). Fe_3O_4 NPs, as a result, were wrapped in the PMAO with the anhydride ring on the surface of the NP.

a

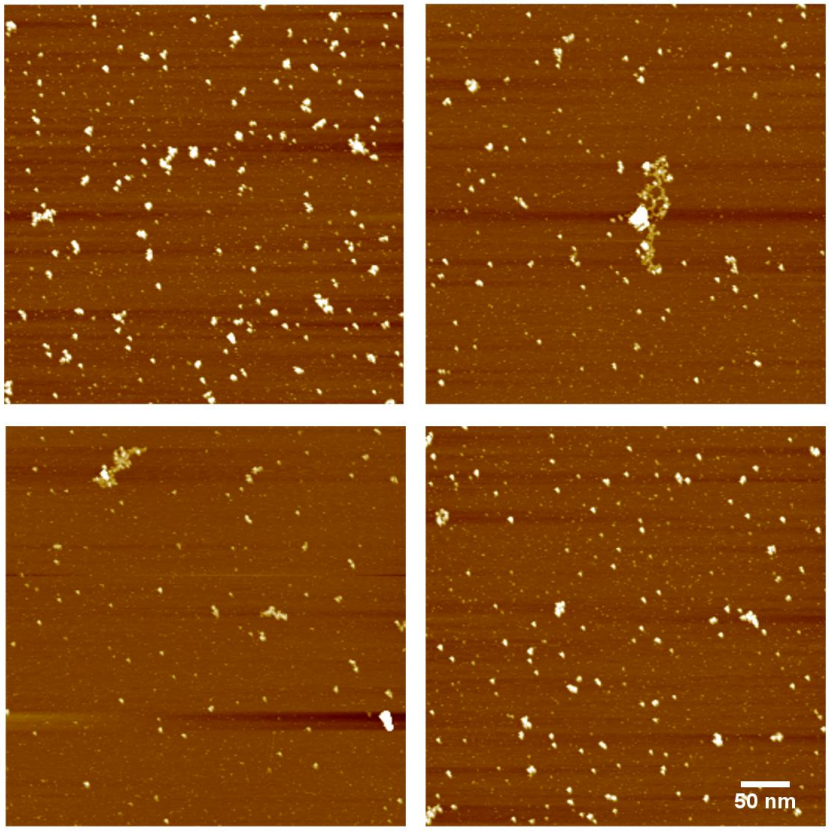

b

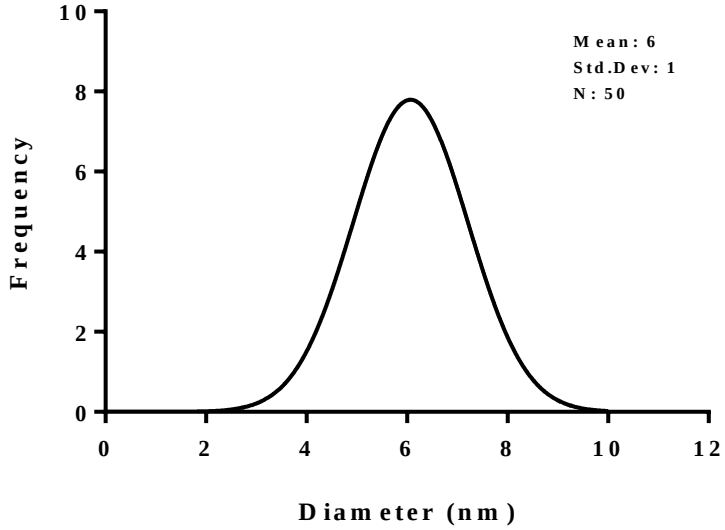

Figure 3.2.1 AFM characterisation of Fe_3O_4 NPs. (a) Representative images of Fe_3O_4 NPs from AFM topography. (b) Fe_3O_4 NP size distribution showing a mean diameter of 6 nm ± 1 SD after AFM analysis of 50 NPs.

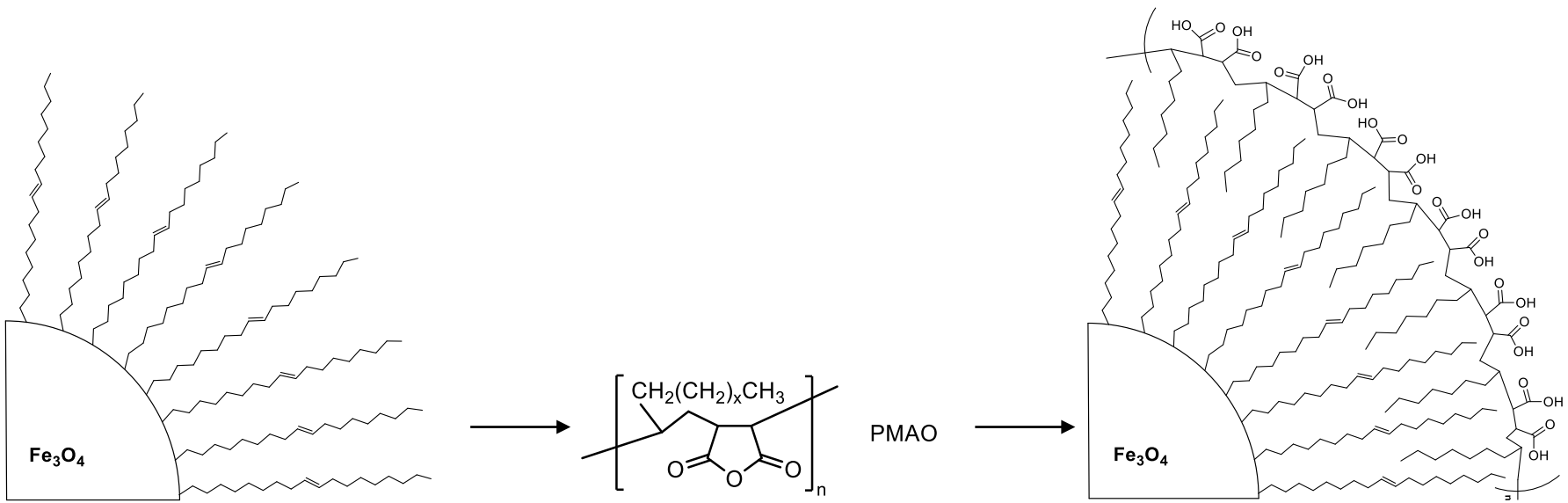

Figure 3.2.2 Amphiphilic coating of Fe_3O_4 NPs. Iron salts in the presence of oleic acid, oleylamine, and benzyl ether solvent were heated gradually to 200 ^oC and refluxed at 300 ^oC resulting in monodispersed hydrophobic Fe_3O_4 NPs with oleate on the surface. The hydrophobic chains of the oleate surfactant and the alkyl chains of PMAO intercalated, leaving the hydrophilic maleic anhydride ring exposed to the surface of the Fe_3O_4 NPs.

The hydrodynamic diameter of Fe_3O_4 NPs in toluene, before PMAO coating, was 12 nm with a PDI of 0.1 (figure 3.2.3.a). The size distribution suggests a highly monodisperse population of NPs. After phase transfer with PMAO, the DLS profile became more polydisperse and contained two populations with different size distributions; 26 nm and a larger population at 193 nm (figure 3.2.3.b). As PMAO was added in excess, it is likely that this second population is due to the formation of polymer micelles or to polymer-NP aggregates. PMAO micelles can self-assemble, were the non-polar alkyl chains of multiple PMAO molecules bunch together in the centre of a sphere-like structure with the hydrophilic regions facing outwards (Di Corato et al., 2008). Therefore, it is important that in our methodology to effectively purify the monodispersed coated NPs from other aggregates and micelles.

a

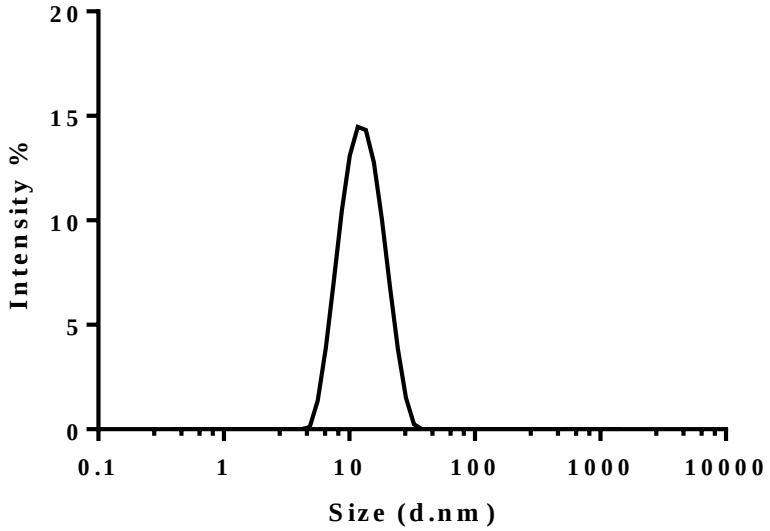

b

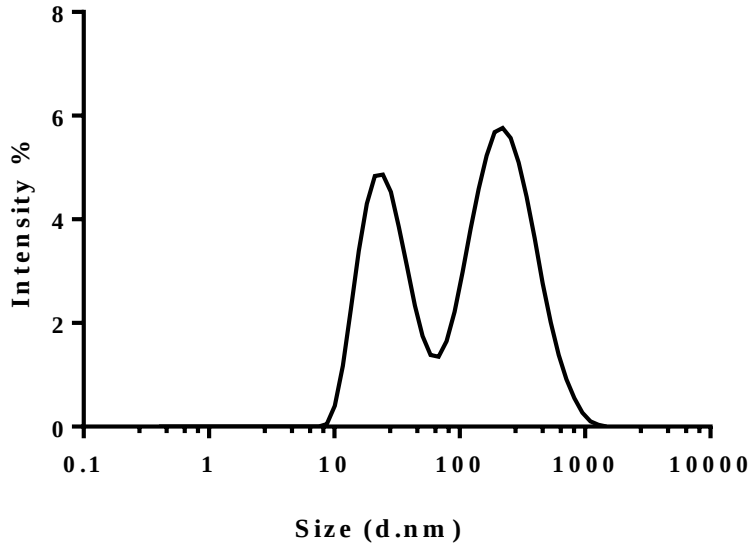

Figure 3.2.3 Size distribution of Fe_3O_4 NPs before purification. (a) Representative DLS measurement of Fe_3O_4 NPs in toluene, Z-Ave 12 nm (b) Representative DLS measurement of Fe_3O_4 NPs in PBS in the presence of excess PMAO.

3.3 Purification of Fe_3O_4-PMAO nanoparticles

To purify Fe_3O_4 NPs and remove the second population of larger aggregates, firstly size exclusion chromatography was used. Fe_3O_4 NPs were passed through a Sephacryl S-300 column. The size and polydispersity index (PDI) for each fraction containing Fe_3O_4 NPs was analysed using DLS. The size range of the fractions containing Fe_3O_4 NPs (fractions 1-24; table 3.3.1) varied from ~ 20 nm to 127 nm. Combined, the size distribution was too large, however for each fraction the PDI was low; mean PDI 0.14. Although size exclusion chromatography led to each fraction being an acceptable monodisperse population of Fe_3O_4 NPs, each fraction was ~ 1 ml of diluted NPs. Overall, this method of purification was time consuming and led to a low concentration of sample and so other approaches were investigated.

Ultracentrifugation through a sucrose gradient has been described as a more efficient method of removing excess polymer from NPs in solution (Di Corato et al., 2008). Sucrose gradient density and centrifugation time was adjusted for Fe_3O_4 NPs. We used a gradient of 10% to 66% (v/v) sucrose that was left to equilibrate, forming a continuous gradient. Unpurified Fe_3O_4 NPs were loaded on top of the sucrose gradient (10% sucrose) and centrifuged at 25000 rpm for 4 h. After centrifugation, the Fe_3O_4 NPs had clearly travelled through the sucrose as seen by the yellow/orange band of NPs in the gradient (figure 3.3.1). As PMAO micelles are less dense than Fe_3O_4 NPs they passed a shorter distance through the sucrose gradient than the NPs. UV light showed the presence of free polymer above the band of NPs (figure 3.3.1) as free PMAO absorbs UV light while when PMAO is attached on the surface of the NPs it is quenched (Di Corato et al., 2008).

Table 3.3.1 Size and size distribution of Fe_3O_4 NPs after size exclusion chromatography.

IOX-PMAO		
Fraction	**Z-Ave (d.nm)**	**PDI**
1	127	0.2
2	93	0.2
3	122	0.3
4	78	0.2
5	82	0.2
6	63	0.1
7	60	0.1
8	59	0.1
9	53	0.1
10	49	0.1
11	46	0.1
12	43	0.1
13	39	0.1
14	38	0.1
15	35	0.1
16	33	0.1
17	31	0.1
18	29	0.1
19	27	0.1
20	26	0.1
21	25	0.1
22	23	0.1
23	32	0.3
24	22	0.1

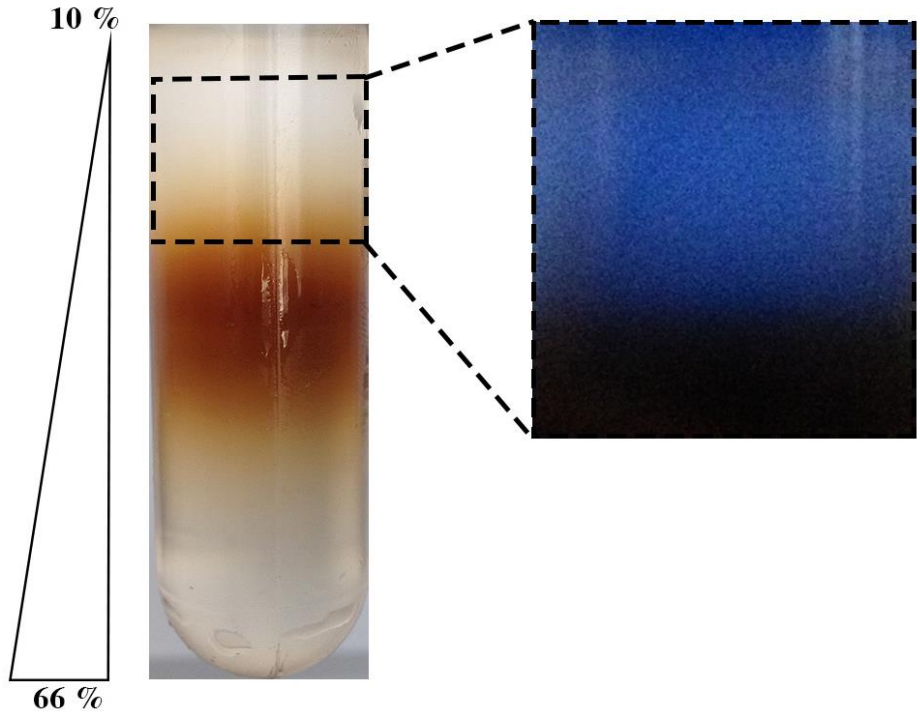

Figure 3.3.1 Fe_3O_4 purification via ultracentrifugation through a sucrose gradient. After ultracentrifugation, Fe_3O_4 NPs travelled further through the sucrose gradient (10 – 66%) than the PMAO polymer alone. Free polymer was visualised above the NP population using UV light (right hand panel). Following ultracentrifugation, Fe_3O_4 NPs (brown coloured fractions) were extracted from the free polymer using a syringe and needle.

Layers from the centrifuge tube were removed for characterisation. After gel electrophoresis through an agarose gel, free PMAO was found in lanes 2 – 5 from the first fractions (figure 3.3.2.a). Layers 1-3 (lanes 2-4) contained no traces of Fe_3O_4 NPs, however lane 5 (fraction 4) had a low concentration of Fe_3O_4 NPs, as seen by a faint yellow/orange colouring. Both fractions 5 and 6 (lane 6 and 7) contained the majority of Fe_3O_4 NPs extracted from the ultracentrifugation tube with no free PMAO visible. Size and size distribution of fractions 5 and 6 were analysed using DLS (figure 3.3.2.b). Fe_3O_4-PMAO NPs in fraction 5 had a Z-ave of 23nm and a PDI of 0.2. In fraction 6, Fe_3O_4-PMAO NPs had a Z-ave of 25 nm and a PDI of 0.2. Both fractions had an acceptable monodispersed population of Fe_3O_4-PMAO NPs with the free PMAO polymer removed.

a

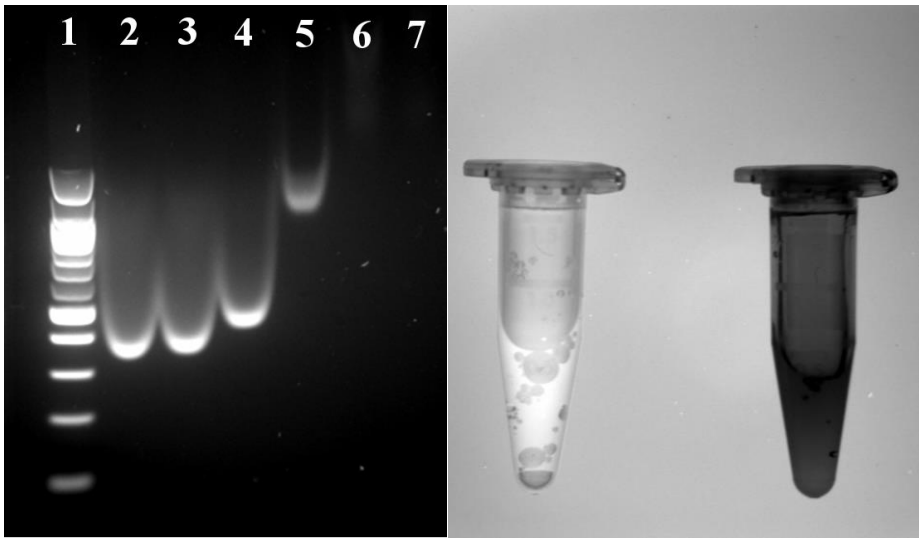

b

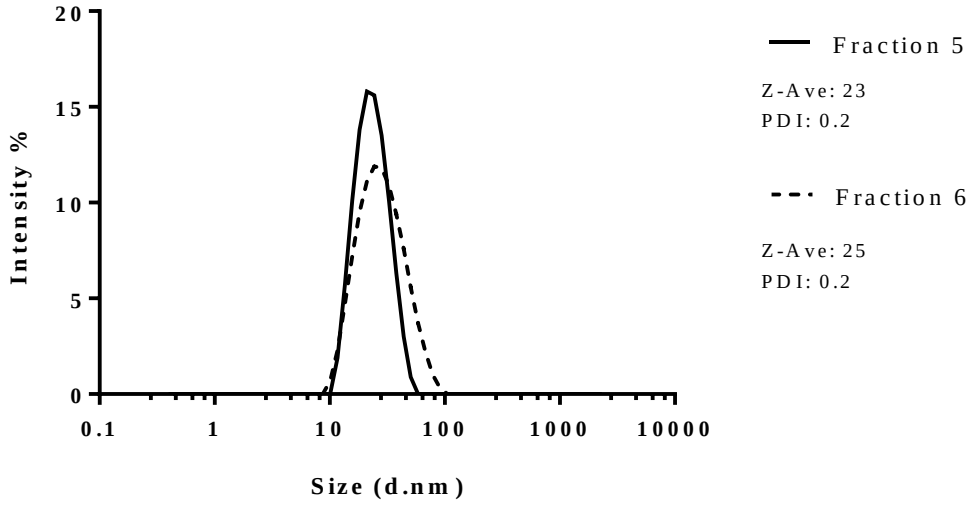

Figure 3.3.2 Separation of Fe_3O_4 NPs from free PMAO. (a) Free PMAO can be visualised using UV light on a 1.5% agarose gel. After removal of different fractions from the centrifuge tube, gel electrophoresis was used to assess free PMAO. Lane 1 contained 100 base pair ladder and subsequent lanes contained fractions collected after ultracentrifugation (lane 2 starting from the top of the centrifuge tube). Both fractions 5 and 6 contained NPs, extracted from ~ 35 % sucrose. The combined fractions 2-4 (left microcentrifuge tube) was compared to fraction 6 (right microcentrifuge tube) under UV light. (b) DLS size population measurements of fraction 5 and 6 retrieved after ultracentrifugation.

3.4 PEGylation of Fe_3O_4 NPs

To stabilise Fe_3O_4 NPs in physiological conditions, PEG chains were linked to the NP surface. When Fe_3O_4-PMAO NPs were in a basic environment, the anhydride ring opened. Tetramethylammonium hydroxide (TMAH), 0.1 M, was used to do this. Once the anhydride ring was open, carboxyl functional groups are exposed and can react with the amine terminal of PEG through EDAC activation; this results in surface attachment of PEG to the Fe_3O_4-PMAO NP (figure 3.4.1). TEM analysis provided images of the resulting Fe_3O_4-PEG NPs (figure 3.4.2.a). Images show the core Fe_3O_4 of the NP and the outer shell consisting of the PMAO and PEG. TEM shows monodispersed NPs with little-to-no aggregation. Using ImageJ software, the size and size distribution of both the Fe_3O_4 core alone and the Fe_3O_4 with the shell was analysed. Fe_3O_4 core was a mean diameter was 8 ± 1 nm (figure 3.4.2.b). This is comparable to the proposed size of 8 nm from the synthesis method used (Di Corato et al., 2008), and to 6 ± 1 nm from AFM analysis of the synthesised Fe_3O_4 NPs in toluene (figure 3.2.1). With the PMAO-PEG outer shell, the diameter increased to 21 ± 3 nm (figure 3.4.2.b) from TEM.

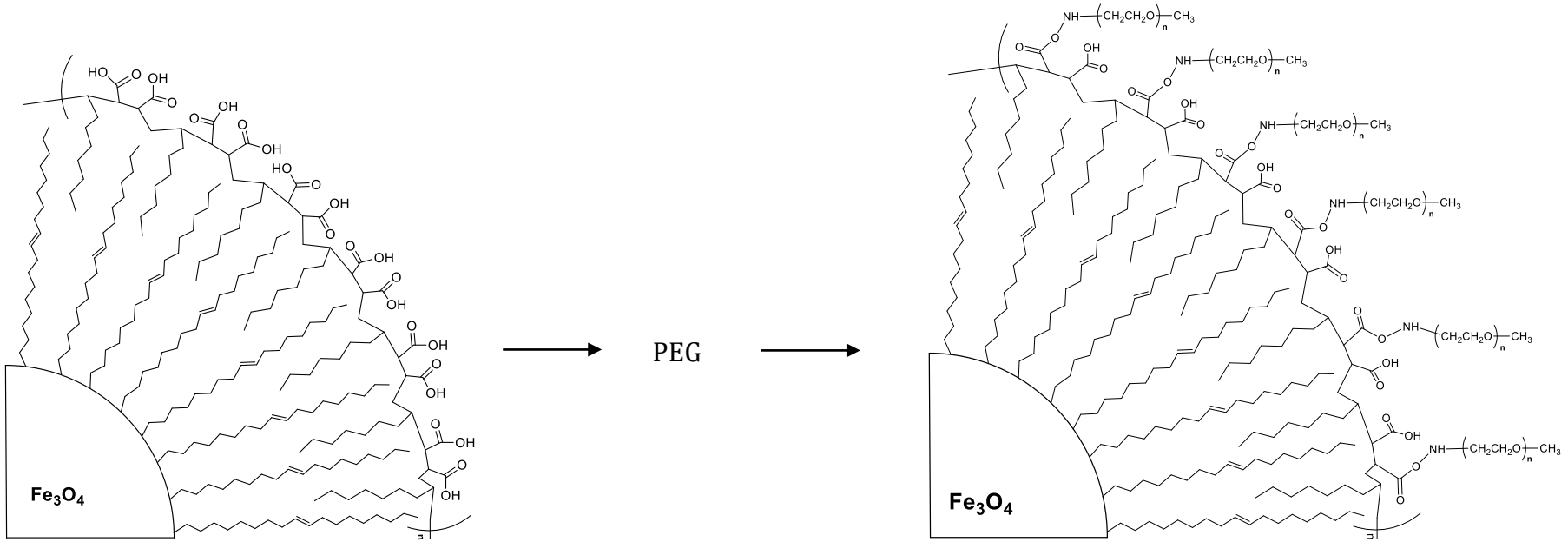

Figure 3.4.1 PEGylation of Fe_3O_4 NPs. The open anhydride ring allowed easy attachment of monoamine PEG via the amine terminal.

a

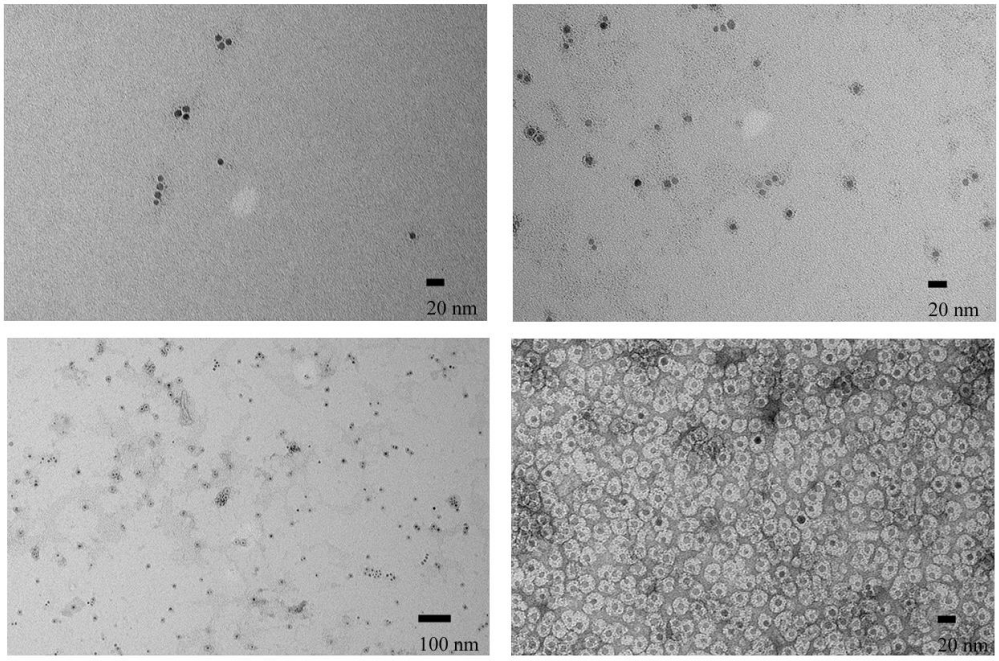

b

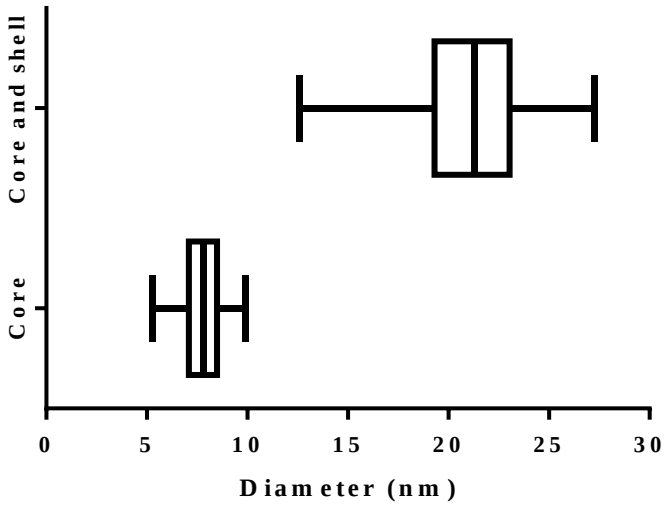

Figure 3.4.2 TEM characterisation of Fe_3O_4-PEG. (a) TEM analysis shows the high contrast from Fe_3O_4 core and the outer shell after PEGylation. Representative images from different grids, scale bars indicated (b) Size distribution, measured from the TEM images, was used to compare Fe_3O_4 core size against Fe_3O_4-PMAO with the outer shell. Mean diameter of Fe_3O_4 core alone was 8 nm (SD ± 1) and with the outer core mean diameter was 21 nm (SD ± 3); 100 NPs were analysed using ImageJ software.

3.5 Conjugation of PEG and α-MSH peptide

The α-MSH peptide was identified as a suitable targeting molecule for the desired application of Fe_3O_4-NPs (see chapter 5). Prior to attachment to Fe_3O_4-PEG NPs, α-MSH peptide and a scrambled control were tested to see if they promoted cell proliferation or caused toxicity. As a targeting molecule for a chemotherapeutic drug delivery system, it would not be advantageous for it to promote cell proliferation to non-targeted cells. The α-MSH peptide is an agonist for the receptor melanocortin 1 (MC1R) expressed on the cell surface of melanocytes and melanoma cells (Kennedy et al., 2001). Upon interaction with α-MSH peptide, MC1R initiates a signalling cascade that ultimately leads to the activation of genes for a cellular response, including initiating cell proliferation (Busca and Ballotti, 2000). As a result, cell viability was tested using MTT assay in melanoma cell lines (M202, SK-MEL-28, and A375) and a non-melanoma cell line (A549). After exposure up to 100 µg/ml of both α-MSH and a scrambled version of the same peptide for 24 h, there was no significant loss of cell viability or evidence of promotion (figure 3.5.1). As a result, it was a viable peptide for attachment to Fe_3O_4-PEG.

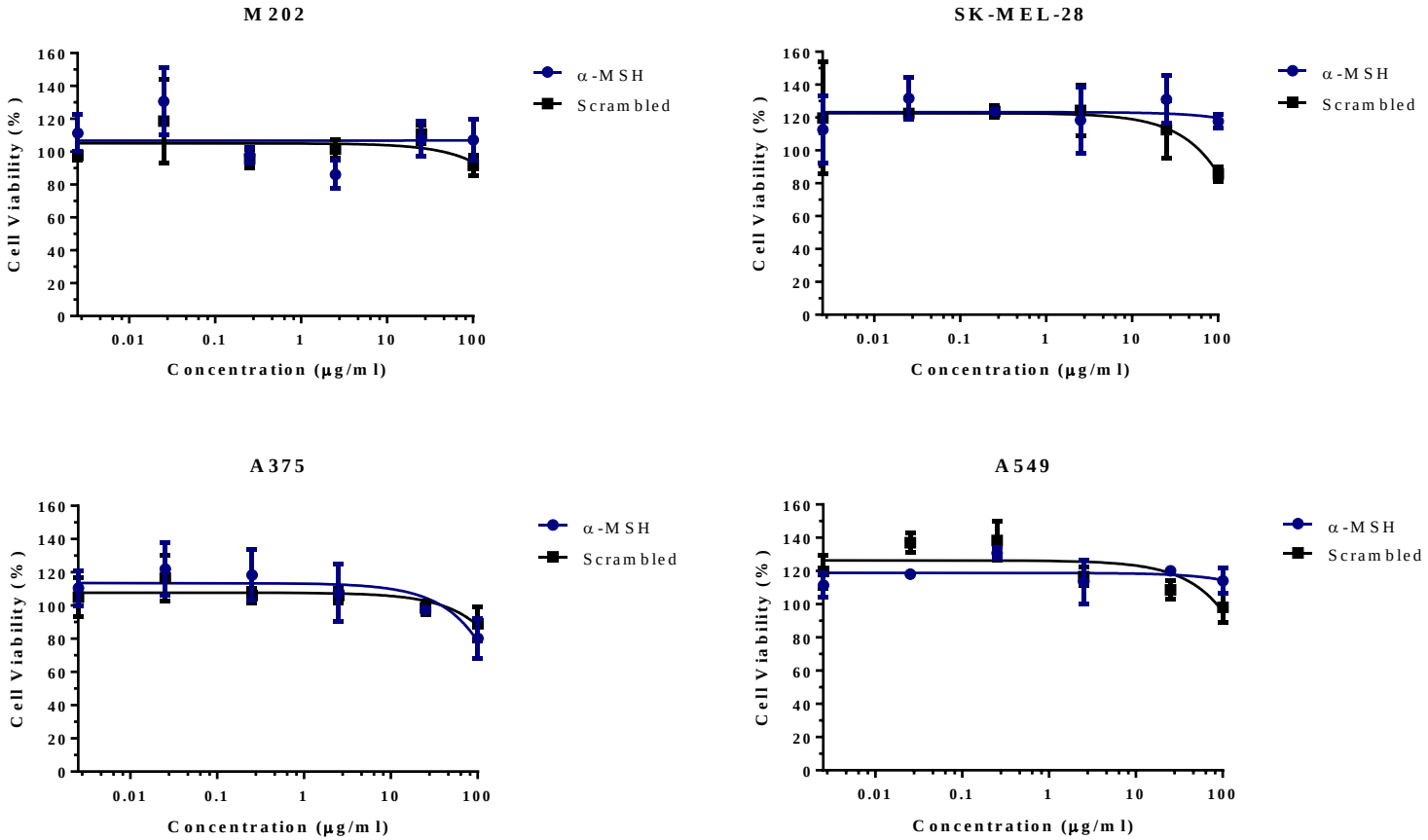

Figure 3.5.1. Cell viability assay after exposure to α-MSH and scrambled peptide. Melanoma (M202, SK-MEL-28, and A375) and non-melanoma (A549) cell lines were exposed to α-MSH and scrambled peptide for 24 h before cell viability was assessed using MTT assay. All values normalised to vehicle, mean ± SEM, n = 3.

For functionalisation of Fe_3O_4 with α-MSH, firstly α-MSH was conjugated to t-Boc amine PEG NHS ester using *N*, *N*-Diisopropylethylamine (DIPEA) to produce PEG-PEP (figure 3.5.2; (Hamley, 2014)). The PEG t-Boc protection group was then removed to expose the amine at the PEG end of PEG-PEP. Deprotection of tBoc was achieved by using 4 M HCl in anhydrous dioxane solution (method 2.1.7; (Han et al., 2001)). MALDI mass spectrometry (MS) was used to characterise PEG, PEP, and to confirm conjugation of both. MALDI MS of PEG 2000 contained a main peak just above 2000 Da, as expected (figure 3.5.3). A peak was also seen at ~ 4000 D due to a small population of dimerised PEG. α-MSH peptide alone had a MALDI mass spectra with a peak at 1770 Da as expected (figure 3.5.4). After conjugation using DIPEA, MALDI mass spectrometry showed a peak at ~ 4000 Da as a result of the 1700 Da PEP with the 2000 Da PEG (figure 3.5.5). There was also a peak related to the unreacted PEP and a peak at ~ 6000 Da where PEP had attached to the small population of dimerised PEG. After purification by dialysis through a 2 kDa nitrocellulose membrane, the excess PEP was removed from the sample as seen from the lack of a peak at 1700 Da on the MALDI mass spectra (figure 3.5.6).

a

*H-SER-TYR-SER-NLE-GLU-HIS-DPHE-ARG-TRP-GLY-LYS(DDE)-PRO-VAL-OH

b

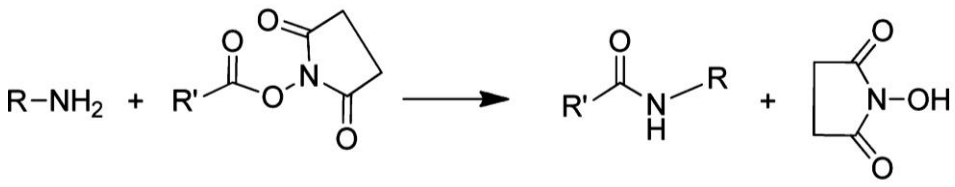

c

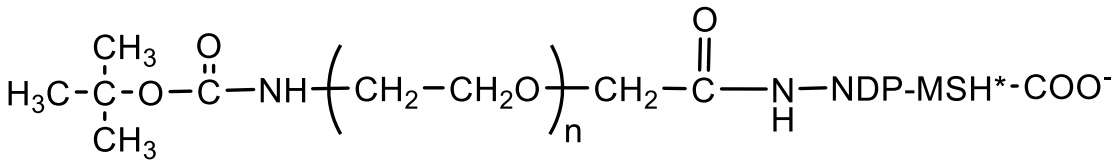

Figure 3.5.2 Structure of the conjugated PEG α-MSH peptide. (a) Amino acid composition of α-MSH (NDP-MSH) with the NH_2 of the lysine protected with Dde group. (b) The NH_2 terminal of the peptide chain (R) reacts with the NHS ester on the PEG (R') to form a peptide bond (Hamley, 2014). (c) The resulting conjugated PEG-PEP.

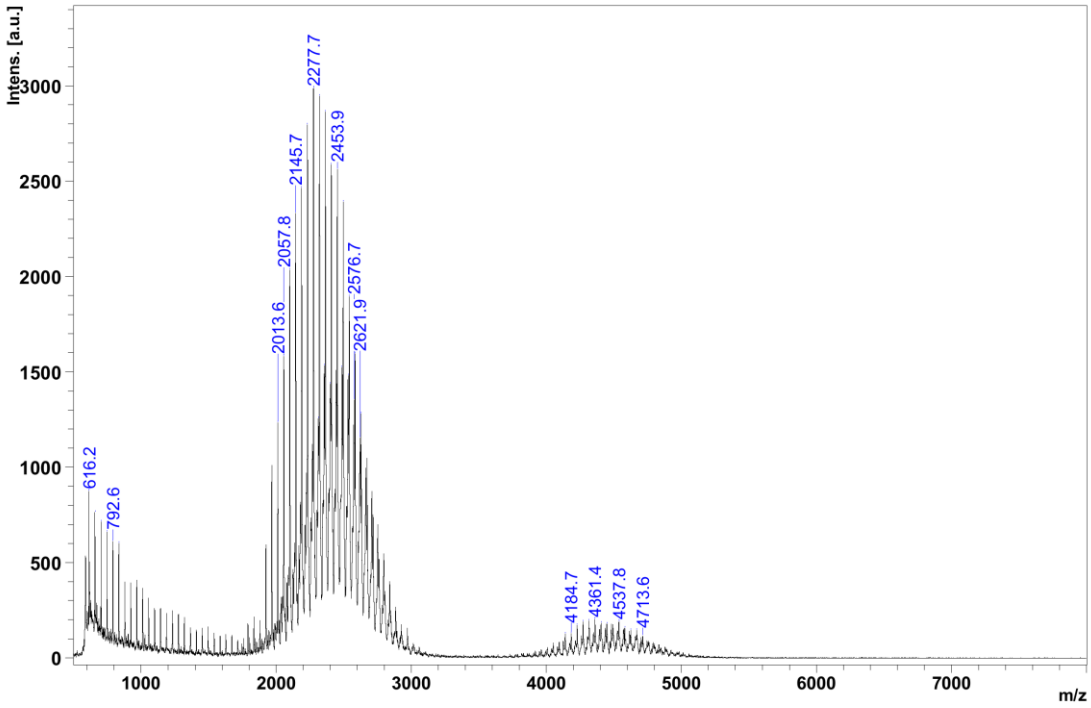

Figure 3.5.3 MALDI mass spectrum of PEG 2000. A large peak at ~ 2280 Da showed the PEG 2000 before purification. A peak at ~ 4360 Da represented dimerised PEG 2000.

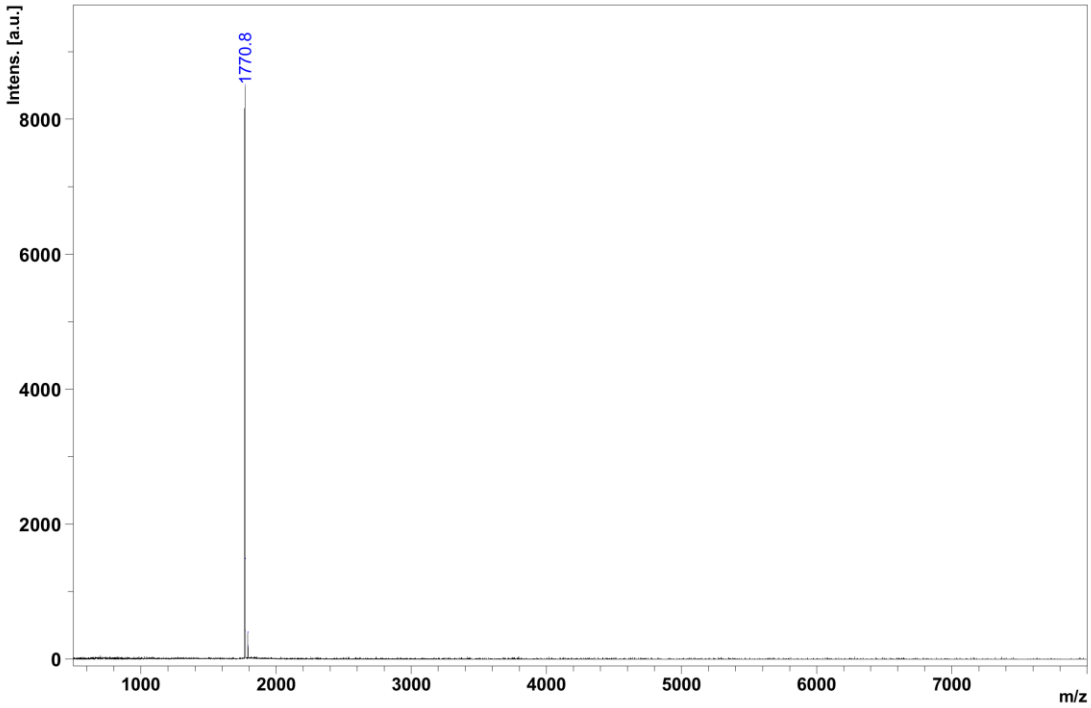

Figure 3.5.4 MALDI mass spectrum of α-MSH peptide. A single peak at ~ 1770 Da confirmed the presence of α-MSH peptide.

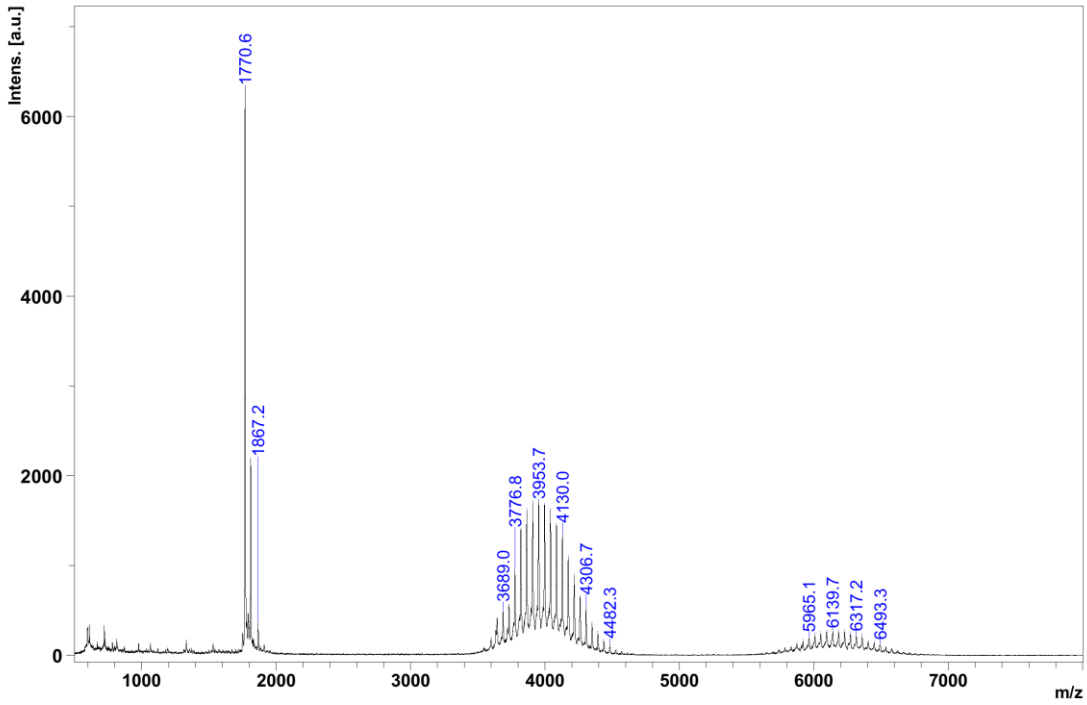

Figure 3.5.5 MALDI mass spectrum of PEG 2000 and α-MSH in the reaction mix. The reaction mix before purification, contained α-MSH PEP alone (peak at ~ 1770 Da), conjugated PEG-PEP (peak at ~ 4000 Da), and the dimerised PEG conjugated to PEP (peak at ~ 6200 Da).

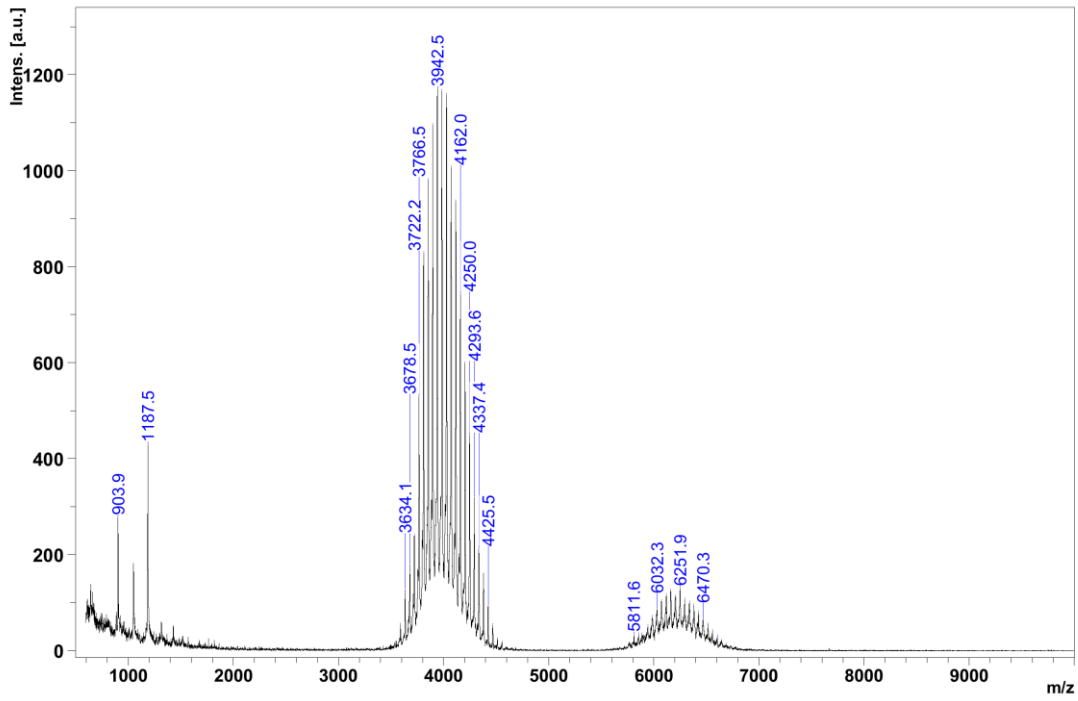

Figure 3.5.6 MALDI mass spectrum of PEG 2000 conjugated to α-MSH. PEG-PEP was purified by dialysis for 3 days in a 2 kDa nitrocellulose membrane. Dialysis was performed against PBS at room temperature. The purified reaction mix contained conjugated PEG-PEP (peak at ~ 4000 Da) and the dimerised PEG conjugated to PEP (peak at ~ 6200 Da).

Further characterisation was achieved by high performance liquid chromatography (HPLC) analysis. HPLC retention time for PEP alone through a Phenomenex C18 column (conditions stated in methods 2.2.8) was ~ 1000 s (figure 3.5.7). After conjugation of PEG-PEP, HPLC retention times were ~ 80 s for free PEG, ~ 1000 s for free PEP, ~ 1250 sfor PEG-PEP, and ~ 1400 s for the dimerised PEG-PEP. Again, PEG-PEP was purified by dialysis through a 2 kDa nitrocellulose membrane (figure 3.5.8.a). The HPLC chromatograph shows that the free PEG and free PEP had been removed from the sample as there is no peak at 80 and 1000 s (figure 3.5.8.b).

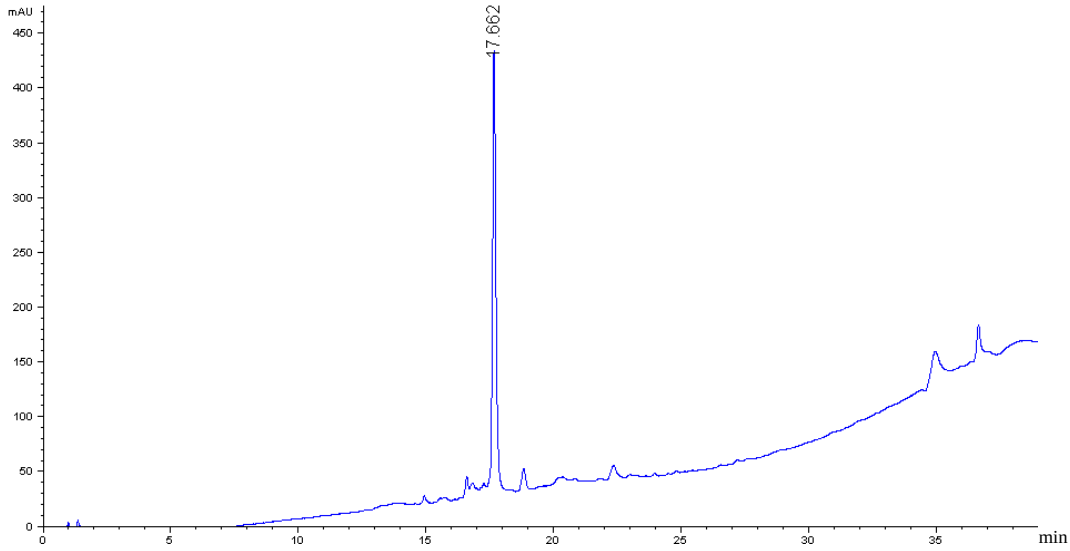

Figure 3.5.7 HPLC chromatogram of α-MSH peptide. Peptide alone had a retention time of ~ 18 min (1000 s).

a

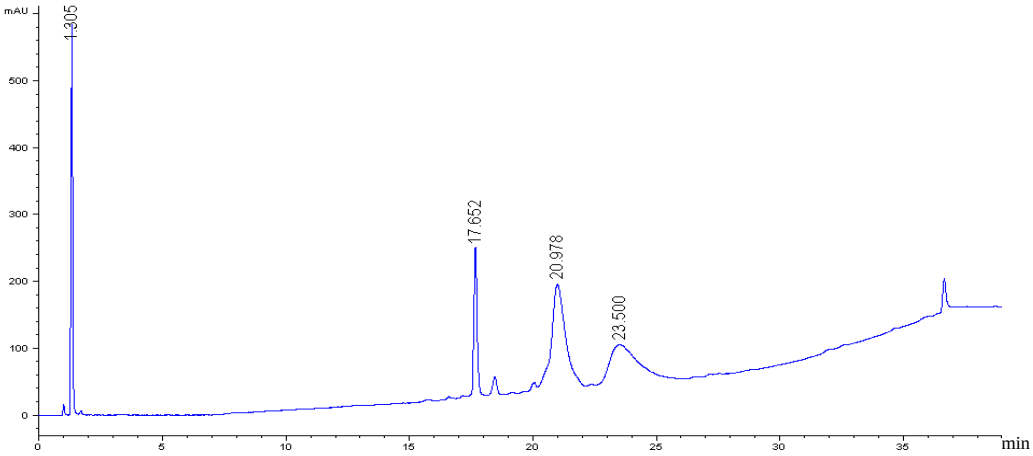

b

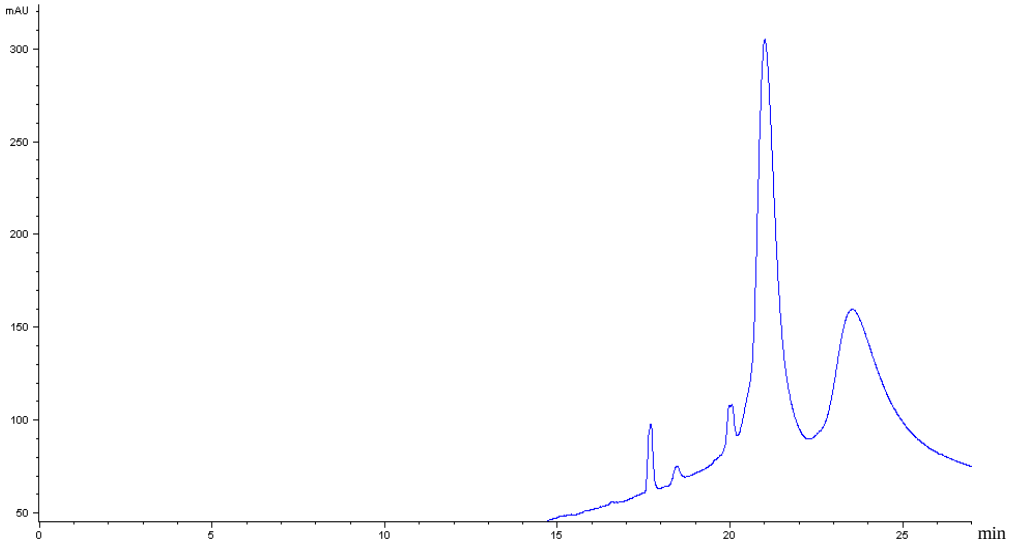

Figure 3.5.8 HPLC chromatogram of PEG 2000 and α-MSH. (a) PEG 2000 and α-MSH in the reaction mix. The peaks represent free PEG (80 s), free PEP (1250 s), and PEG-PEP (1400 s). (b) PEG-PEP was purified by dialysis for 3 days in a 2 kDa nitrocellulose membrane. Dialysis was performed against PBS at room temperature.

3.6 Attachment of PEG-PEP to Fe_3O_4-PMAO

Commercial α-MSH peptide was conjugated to PEG as previously described (figure 3.5.2 and method 2.1.7). Excess PEG-PEP was removed from Fe_3O_4-PEP by dialysis against PBS pH 7.4, 0.31 osmol using a dialysis membrane with MWCO of 2 kDa for 24 h. To assess the attachment of PEG-PEP to Fe_3O_4-PMAO, samples for ATR-FT-IR were dried under vacuum using a Schlenk line. Powdered samples were then measured on the optically dense diamond crystal of a Perkin-Elmer ATR-FT-IR spectrometer.

First, Fe_3O_4 oleate NPs were analysed. FT-IR spectrum showed peaks at 2852 and 2922 cm^{-1} which were attributed to the asymmetrical CH_2 and the symmetrical CH_2 bands associated to the stretching vibrations from the oleic acid coating the Fe_3O_4 NP (Yang et al., 2010); figure 3.5.9). Further evidence of oleic acid from CH_3 can be seen at 1409 cm^{-1} as well as the C=O stretching vibration at 1710 cm^{-1} (Wu et al., 2004). A broad peak could be seen at ~ 3400 cm^{-1} attributed to the carboxylic acid from the oleic acid on the surface of the Fe_3O_4 NPs (Sun et al., 2007). There is a large peak at 580 cm^{-1} due to the Fe–O bonds from the Fe_3O_4 core.

After coating with PMAO and PEG, Fe_3O_4-PEG NP FT-IR spectrum showed a decrease in the peaks at 2852 and 2922 cm^{-1} (from the oleic acid), and 580 cm^{-1} (from the Fe_3O_4 core) due to the core and oleic acid being masked by the PMAO and PEG (figure 3.5.10). Moreover, a peak at 1217 cm^{-1} , attributed to C-O-C present in PEG, confirmed the presence of PEG on the surface of Fe_3O_4 NPs (Le Thi Mai et al., 2009).

FT-IR was also used to confirm successful attachment of PEG-PEP to Fe_3O_4-PMAO (to produce Fe_3O_4-PEP NPs). As with Fe_3O_4-PEG (figure 3.5.10), there was a decrease in the oleic acid peaks 2852 and 2922 cm^{-1}, and the peak from the Fe_3O_4 core

at 580 cm^{-1}, due to the masking of the inner most molecules after addition of PEG-PEP (figure 3.5.11). The peak at 1217 cm^{-1}, attributed to C-O-C in PEG, remained, again suggesting PEG-PEP was conjugated to Fe_3O_4-PMAO NPs. Furthermore, the FT-IR spectrum for Fe_3O_4-PEP showed peaks at both 1642 and 1559 cm^{-1} which were assigned to amide I (1600-1700 cm^{-1}) and amide II (1500-1560 cm^{-1}) bonds (Cai and Chen, 2007, Kouassi et al., 2005, Le Thi Mai et al., 2009), due to the amine groups of the amino acids in the peptide chain (figure 3.5.11). Overall, this data shows that the PEG-MSH peptide could be easily conjugated on to the surface of Fe_3O_4-PMAO NPs.

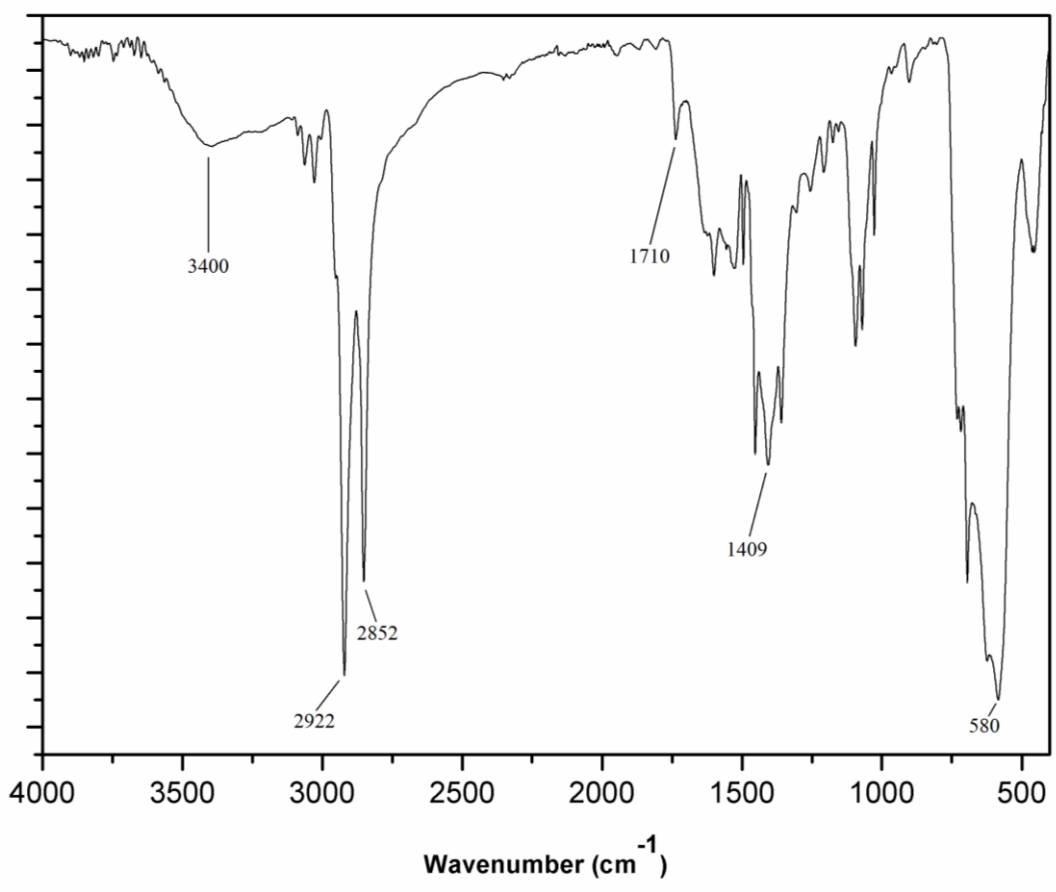

Figure 3.5.9 FTIR spectrum of Fe_3O_4. The large peak at 580 cm^{-1} is indicative of the Fe-O from the Fe_3O_4 core. Other important peaks from bonds found in the oleic acid, demonstrating that oleic acid is on the surface of the NP, include CH_2 (2852 and 2922 cm^{-1}), CH_3 (1409 cm^{-1}), C=O (1710 cm^{-1}), and the OH (broad peak at 3400 cm^{-1}).

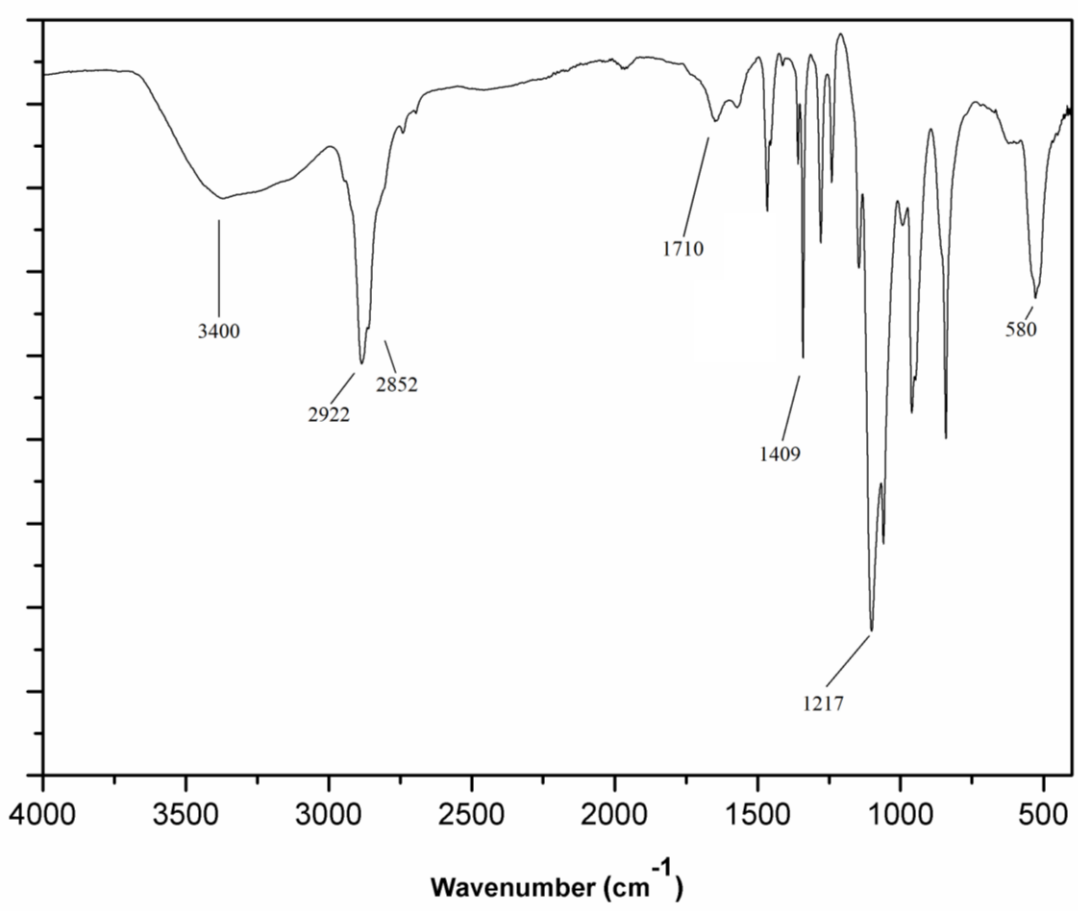

Figure 3.5.10 FTIR spectrum of Fe_3O_4-PEG. A peak at 580 cm^{-1} is indicative of the Fe-O from the Fe_3O_4 core. The oleic acid can be seen from bonds such as the CH_2 (2852 and 2922 cm^{-1}), CH_3 (1409 cm^{-1}), C=O (1710 cm^{-1}), and the OH (broad peak at 3400 cm^{-1}). The addition of PEG led to a peak at 1217 cm^{-1} due to the C-O-C bond.

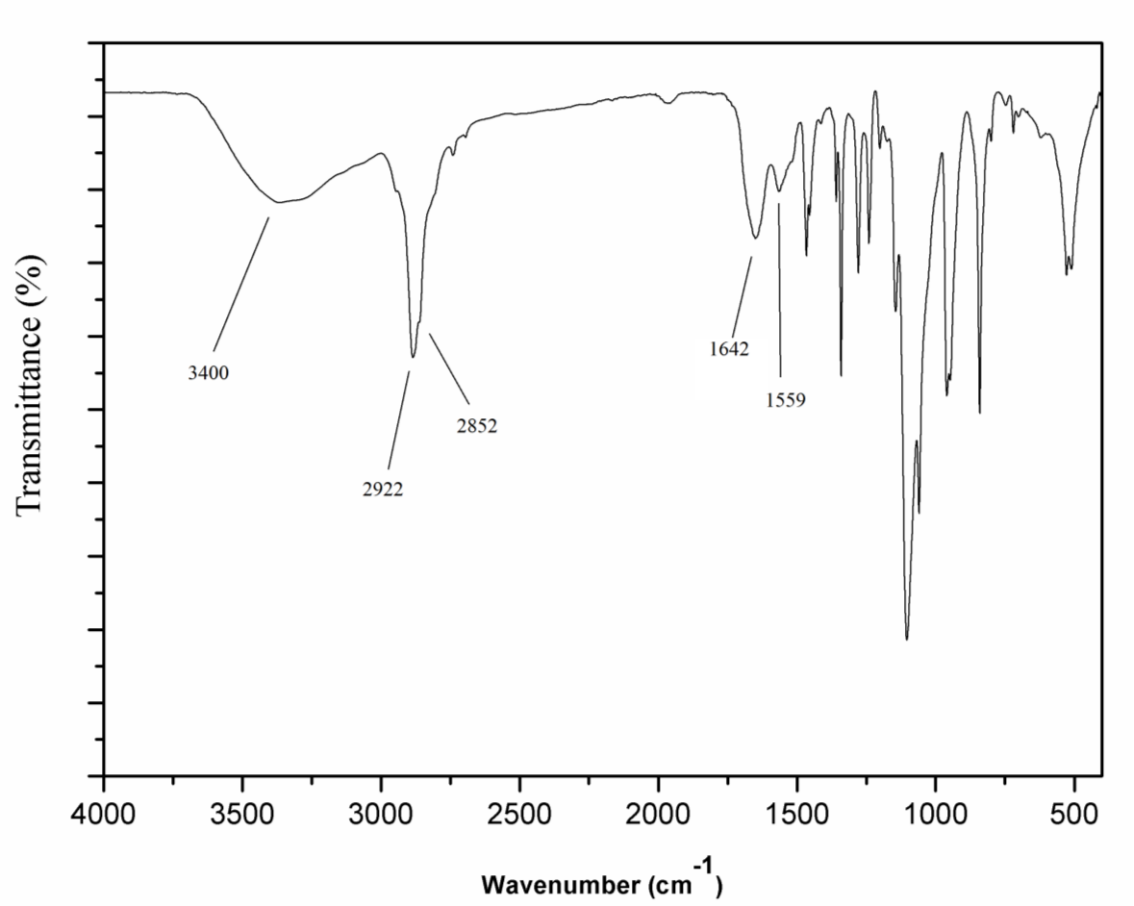

Figure 3.5.11 FTIR spectrum of Fe_3O_4-PEG-PEP. A peak at 580 cm^{-1} is indicative of the Fe-O from the Fe_3O_4 core. The oleic acid can be seen from bonds such as the CH_2 (2852 and 2922 cm^{-1}), CH_3 (1409 cm^{-1}), C=O (1710 cm^{-1}), and the OH (broad peak at 3400 cm^{-1}). A peak at 1217 cm^{-1} is visible due to the C-O-C bond in PEG. Peaks at 1642 and 1559 cm^{-1} (from amide I and II bonds) confirm the presence of PEP on the surface of the NP.

3.7 Discussion

Due to their SPM properties, Fe_3O_4 NPs are useful tools in biomedical applications (Cheng et al., 2005, Gao et al., 2009). In particular, these properties can be exploited in the field of oncology and utilised as both therapeutic and diagnostic tools (Wang et al., 2007). In order to achieve this, the Fe_3O_4 core of the NP must be within a certain size range and, more importantly, with a limited size distribution. This uniformity allows Fe_3O_4 NPs to act in unison to produce a SPM effect (Jordan et al., 2009).

A major challenge in the use of Fe_3O_4 NPs in biomedicine is the lack of control of shape, size, and size distribution during synthesis (Mohapatra and Anand, 2010). Chemical precipitation is a simple and efficient method of Fe_3O_4 NP synthesis, however there is limited control of size distribution (Tartaj et al., 2006). Hydrothermal decomposition of iron salts, as used in this work, produced Fe_3O_4 NPs with the core mean diameter > 10 nm (7.8 ± 1.0 nm, figure 3.3.1) and a highly monodispersed size population. Within this size range, Fe_3O_4 should exhibit SPM properties required for MRI diagnostics and thermal ablation therapy. Furthermore, Fe_3O_4 NPs were easily functionalised for phase transfer with PMAO via the oleate on the NP surface.

Although purification by size exclusion chromatography resulted in NP fractions with narrow size distributions (table 3.2.1), the process was inefficient and lead to a loss in yield. Ultracentrifugation through a sucrose gradient was used as an alternative purification method (figure 3.2.4) which provided a quick and efficient way to remove excess PMAO micelles from the NP sample. Ultracentrifugation resulted in a monodispersed population of Fe_3O_4-PMAO NPs (PDI ~ 1.7) that were dispersed in aqueous phase.

Further functionalisation was achieved by the attachment of PEG (MW 2000) to the surface of the NP. PEG has previously been shown to increase NP stability and improve circulation time of the NPs (Jokerst et al., 2011, Otsuka et al., 2003, Yoo et al., 2010). FT-IR confirmed the presence of PEG on the surface of Fe_3O_4 NPs, to produce Fe_3O_4-PEG NPs, by identification of key chemical bonds. The targeting peptide (α-MSH) was added to PEG prior to attachment to the NPs. MALDI mass spectrometry and HPLC confirmed the conjugation of the 1700 Da peptide to the 2000 Da PEG (figure 3.4.6, 3.5.8.a). PEG-PEP was then purified which successfully removed both the free PEG and free PEP (figure 3.5.7, 3.5.8.b). After conjugation of PEG-PEP with DIPEA, the tBoc group on the N terminal of the PEG was deprotected using 4 M HCl in dioxane. Successful attachment of PEG-PEP to Fe_3O_4-PMAO using carbodiimide was measured using FT-IR. As with Fe_3O_4-PEG, FT-IR showed a reduction in the peaks caused by bonds from oleic acid (1409 cm^{-1}, 1710 cm^{-1}, 2852 cm^{-1}, and 2922 cm^{-1}) and Fe_3O_4 (580 cm^{-1}). This reduction was due to masking of the inner most molecules as a result of addiction molecules added to the surface. A peak at 1217 cm^{-1} was also indicative of the C-O-C bond found in PEG. Furthermore, peaks at 1642 and 1559 cm^{-1}, assigned to amide I and amide II respectively, found in peptide bonds, were observed in the Fe_3O_4-PEP NPs. This suggests that there was an increase in peptide bonds on the surface of Fe_3O_4 NPs from effective conjugation of PEG-PEP. While FT-IR confirmed the presence of PEP on the surface of Fe_3O_4-PEP NPs, it does not quantify the amount of peptide that was successfully attached. The amount of targeting peptide available on the surface of the NP has a direct impact on cellular uptake and specificity (Broda et al., 2015, Gao et al., 2013). HPLC can be used to quantify the amount of free peptide in order to calculate the concentration of peptide attached to the surface of the NP (Zhang et al., 2014). Other groups have measured the

amount of protein on the NP surface directly using protein quantitation kits (Yu et al., 2010).

Although PEG is well established as a stabilising agent for Fe_3O_4 NPs (Amstad et al., 2011), more work must be done to identify the stability of Fe_3O_4-PEG NPs (and after conjugation with PEG-PEP). The colloidal stability of the NPs was assessed before each biological assay (table 3.7.1), but no formal identification as to the long term stability was established. Lu et al., using NPs conjugated with the α-MSH peptide and PEG, found the NPs were stable for at least 24 h at 37 ^{o}C in 2.5 mM sodium citrate, PBS, 10% serum, and 100% serum (Lu et al., 2009). The results were comparable between NP-PEG and NP-PEG- α-MSH, suggesting the α-MSH peptide did not alter the colloidal stability within the first 24 h. NPs without the PEG coating aggregated in PBS, 10% serum, and 100% serum (Lu et al., 2009).

Table 3.7.1 Size summary of Fe_3O_4 NPs from AFM, TEM, and DLS. Errors shown as ± SD.

	AFM	TEM	DLS
Fe_3O_4 NP	6 nm ± 1	8 nm ± 1	-
Fe_3O_4-PMAO	-	21 nm ± 3	25 nm ± 2
Fe_3O_4-PEG	-	-	55 nm ± 1
Fe_3O_4-PEP	-	-	57 nm ± 4

The scope of this work did not require large volumes of Fe_3O_4 NPs, and so it was focused on the synthesis of highly monodispersed population of NPs. However, for future applications, the scale-up of this methodology must be considered. As previously discussed, the size and size distribution of biomedical Fe_3O_4 NPs must be carefully controlled in order to produce NPs capable of exploiting the enhanced permeability and retention (EPR) effect (Maeda et al., 2013); section 1.3.2) and displaying SPM properties (Sonvico et al., 2005). In this respect, the method of synthesis is critical. The different synthesis methods for Fe_3O_4 NPs have their advantages and disadvantages. Although co-precipitation method is simple and could be easily scaled-up, the resulting NPs often have a broad size distribution. Synthesis by thermal decomposition, as demonstrated in this work, produces a narrow size distribution and provides a method which allows easy control of NP size; important if the NP is used for biomedical applications (Gonzalez-Moragas et al., 2015). However, the high temperature and long reaction times may make it difficult to be scale-up efficiently. Other methods of thermal decomposition to produce Fe_3O_4 NPs have been explored, specifically with the aim of scale-up (Gonzalez-Moragas et al., 2015). In this work, we have demonstrated that purification via ultracentrifugation through a sucrose gradient produced a NP population free of excess polymer and aggregates. However, using this method limits the volume of NP solution that can be purified at one time and the dialysis times between steps is long. An alternative to the extended waiting time whilst the sample is dialysing is to use a tangential flow filtration system; this has previously been used to remove excess surfactant from PEGylated NPs (Dalwadi and Sunderland, 2007) and did not have any adverse effects on the SPM properties of Fe_3O_4 NPs (Zaloga et al., 2015).

Overall, this chapter has demonstrated the successful synthesis, purification, and functionalisation of Fe_3O_4-PEP NPs. These NPs can be further developed to contain hydrophobic drugs in their polymeric shell to produce a theranostic NP able to function as both a diagnostic agent and as an anti-melanoma therapeutic system.

3.8 References

Allen, T. M., Hansen, C. B. & De Menezes, D. E. L. 1995. Pharmacokinetics of long-circulating liposomes. *Advanced drug delivery reviews,* 16**,** 267-284.

Amstad, E., Textor, M. & Reimhult, E. 2011. Stabilization and functionalization of iron oxide nanoparticles for biomedical applications. *Nanoscale,* 3**,** 2819-2843.

Arsalani, N., Fattahi, H. & Nazarpoor, M. 2010. Synthesis and characterization of PVP-functionalized superparamagnetic Fe3O4 nanoparticles as an MRI contrast agent. *Express Polym Lett,* 4**,** 329-38.

Bakoglidis, K. D., Simeonidis, K., Sakellari, D., Stefanou, G. & Angelakeris, M. 2012. Size-Dependent Mechanisms in AC Magnetic Hyperthermia Response of Iron-Oxide Nanoparticles. *Ieee Transactions on Magnetics,* 48**,** 1320-1323.

Bee, A., Massart, R. & Neveu, S. 1995. Synthesis of very fine maghemite particles. *Journal of Magnetism and Magnetic Materials,* 149**,** 6-9.

Bhattarai, N., Bhattarai, S. R., Khil, M. S., Lee, D. R. & Kim, H. Y. 2003. Aqueous solution properties of amphiphilic triblock copolymer poly(p-dioxanone-co-l-lactide)-block-poly(ethylene glycol). *European Polymer Journal,* 39**,** 1603-1608.

Broda, E., Mickler, F. M., Lächelt, U., Morys, S., Wagner, E. & Bräuchle, C. 2015. Assessing potential peptide targeting ligands by quantification of cellular adhesion of model nanoparticles under flow conditions. *Journal of Controlled Release,* 213**,** 79-85.

Bronstein, L. M., Shtykova, E. V., Malyutin, A., Dyke, J. C., Gunn, E., Gao, X., Stein, B., Konarev, P. V., Dragnea, B. & Svergun, D. I. 2010. Hydrophilization of Magnetic Nanoparticles with Modified Alternating Copolymers. Part 1: The Influence of the Grafting. *The journal of physical chemistry. C, Nanomaterials and interfaces,* 114**,** 21900-21907.

Bulte, J. W. M., Brooks, R. A., Moskowitz, B. M., Bryant, L. H. & Frank, J. A. 1999. Relaxometry and magnetometry of the MR contrast agent MION-46L. *Magnetic Resonance in Medicine,* 42**,** 379-384.

Busca, R. & Ballotti, R. 2000. Cyclic AMP a key messenger in the regulation of skin pigmentation. *Pigment Cell Research,* 13**,** 60-69.

Cai, W. & Chen, X. 2007. Nanoplatforms for Targeted Molecular Imaging in Living Subjects. *Small,* 3**,** 1840-1854.

Cheng, F.-Y., Su, C.-H., Yang, Y.-S., Yeh, C.-S., Tsai, C.-Y., Wu, C.-L., Wu, M.-T. & Shieh, D.-B. 2005. Characterization of aqueous dispersions of Fe3O4 nanoparticles and their biomedical applications. *Biomaterials,* 26**,** 729-738.

Dalwadi, G. & Sunderland, V. B. 2007. Purification of PEGylated nanoparticles using tangential flow filtration (TFF). *Drug Dev Ind Pharm,* 33**,** 1030-9.

Deng, Z. J., Liang, M., Monteiro, M., Toth, I. & Minchin, R. F. 2011. Nanoparticle-induced unfolding of fibrinogen promotes Mac-1 receptor activation and inflammation. *Nature nanotechnology,* 6**,** 39-44.

Di Corato, R., Quarta, A., Piacenza, P., Ragusa, A., Figuerola, A., Buonsanti, R., Cingolani, R., Manna, L. & Pellegrino, T. 2008. Water solubilization of hydrophobic nanocrystals by means of poly(maleic anhydride-alt-1-octadecene). *Journal of Materials Chemistry,* 18**,** 1991-1996.

Fannin, P. C. 1991. Measurement of the Neel relaxation of magnetic particles in the frequency range 1 kHz to 160 MHz. *Journal of Physics D: Applied Physics,* 24**,** 76.

Figuerola, A., Di Corato, R., Manna, L. & Pellegrino, T. 2010. From iron oxide nanoparticles towards advanced iron-based inorganic materials designed for biomedical applications. *Pharmacological Research,* 62**,** 126-143.

Gao, H., Yang, Z., Zhang, S., Cao, S., Shen, S., Pang, Z. & Jiang, X. 2013. Ligand modified nanoparticles increases cell uptake, alters endocytosis and elevates glioma distribution and internalization. *Scientific reports,* 3.

Gao, J., Gu, H. & Xu, B. 2009. Multifunctional Magnetic Nanoparticles: Design, Synthesis, and Biomedical Applications. *Accounts of Chemical Research,* 42**,** 1097-1107.

Gebauer, J. S., Malissek, M., Simon, S., Knauer, S. K., Maskos, M., Stauber, R. H., Peukert, W. & Treuel, L. 2012. Impact of the Nanoparticle–Protein Corona on Colloidal Stability and Protein Structure. *Langmuir,* 28**,** 9673-9679.

Gonzalez-Moragas, L., Yu, S.-M., Murillo-Cremaes, N., Laromaine, A. & Roig, A. 2015. Scale-up synthesis of iron oxide nanoparticles by microwave-assisted thermal decomposition. *Chemical Engineering Journal,* 281**,** 87-95.

Hamley, I. W. 2014. PEG–Peptide Conjugates. *Biomacromolecules,* 15**,** 1543-1559.

Han, G., Tamaki, M. & Hruby, V. J. 2001. Fast, efficient and selective deprotection of the tert-butoxycarbonyl (Boc) group using HCl/dioxane (4 m). *The Journal of Peptide Research,* 58**,** 338-341.

Hanini, A., Schmitt, A., Kacem, K., Chau, F., Ammar, S. & Gavard, J. 2011. Evaluation of iron oxide nanoparticle biocompatibility. *International Journal of Nanomedicine,* 6**,** 787-794.

Hühn, D., Kantner, K., Geidel, C., Brandholt, S., De Cock, I., Soenen, S. J. H., Rivera_Gil, P., Montenegro, J.-M., Braeckmans, K., Müllen, K., Nienhaus, G. U., Klapper, M. & Parak, W. J. 2013. Polymer-Coated Nanoparticles Interacting with Proteins and Cells: Focusing on the Sign of the Net Charge. *ACS Nano,* 7**,** 3253-3263.

Hyeon, T. 2003. Chemical synthesis of magnetic nanoparticles. *Chem Commun (Camb)***,** 927-34.

Jokerst, J. V., Lobovkina, T., Zare, R. N. & Gambhir, S. S. 2011. Nanoparticle PEGylation for imaging and therapy. *Nanomedicine (London, England),* 6**,** 715-728.

Jordan, A., Wust, P., Fahling, H., John, W., Hinz, A. & Felix, R. 2009. Inductive heating of ferrimagnetic particles and magnetic fluids: Physical evaluation of their potential for hyperthermia. *International Journal of Hyperthermia,* 25**,** 499-511.

Kennedy, C., Ter Huurne, J., Berkhout, M., Gruis, N., Bastiaens, M., Bergman, W., Willemze, R. & Bavinck, J. N. B. 2001. Melanocortin 1 receptor (MC1R) gene variants are associated with an increased risk for cutaneous melanoma which is largely independent of skin type and hair color. *Journal of Investigative Dermatology,* 117**,** 294-300.

Kim, D. K., Zhang, Y., Kehr, J., Klason, T., Bjelke, B. & Muhammed, M. 2001. Characterization and MRI study of surfactant-coated superparamagnetic nanoparticles administered into the rat brain. *Journal of Magnetism and Magnetic Materials,* 225**,** 256-261.

Kouassi, G. K., Irudayaraj, J. & Mccarty, G. 2005. Examination of Cholesterol oxidase attachment to magnetic nanoparticles. *Journal of Nanobiotechnology,* 3**,** 1-1.

Le Thi Mai, H., Tran Thi, D., Tran Mau, D., Nguyen Huu, D. & Dang Mau, C. 2009. Preparation and characterization of magnetic nanoparticles coated with polyethylene glycol. *Journal of Physics: Conference Series,* 187**,** 012048.

Lee, S.-J., Jeong, J.-R., Shin, S.-C., Kim, J.-C., Chang, Y.-H., Chang, Y.-M. & Kim, J.-D. 2004. Nanoparticles of magnetic ferric oxides encapsulated with poly(D,L latide-co-glycolide) and their applications to magnetic resonance imaging contrast agent. *Journal of Magnetism and Magnetic Materials,* 272–276, Part 3**,** 2432-2433.

Lees, E. E., Nguyen, T.-L., Clayton, A. H. A. & Mulvaney, P. 2009. The Preparation of Colloidally Stable, Water-Soluble, Biocompatible, Semiconductor Nanocrystals with a Small Hydrodynamic Diameter. *ACS Nano,* 3**,** 1121-1128.

Li, L., Jiang, W., Luo, K., Song, H., Lan, F., Wu, Y. & Gu, Z. 2013. Superparamagnetic iron oxide nanoparticles as MRI contrast agents for non-invasive stem cell labeling and tracking. *Theranostics,* 3**,** 595-615.

Li, P., Miser, D. E., Rabiei, S., Yadav, R. T. & Hajaligol, M. R. 2003. The removal of carbon monoxide by iron oxide nanoparticles. *Applied Catalysis B-Environmental,* 43**,** 151-162.

Lu, W., Xiong, C., Zhang, G., Huang, Q., Zhang, R., Zhang, J. Z. & Li, C. 2009. Targeted photothermal ablation of murine melanomas with melanocyte-stimulating hormone analog-conjugated hollow gold nanospheres. *Clin Cancer Res,* 15**,** 876-86.

Lu, Y., Yin, Y. D., Mayers, B. T. & Xia, Y. N. 2002. Modifying the surface properties of superparamagnetic iron oxide nanoparticles through a sol-gel approach. *Nano Letters,* 2**,** 183-186.

Maeda, H., Nakamura, H. & Fang, J. 2013. The EPR effect for macromolecular drug delivery to solid tumors: Improvement of tumor uptake, lowering of systemic toxicity, and distinct tumor imaging in vivo. *Adv Drug Deliv Rev,* 65**,** 71-9.

Mohapatra, M. & Anand, S. 2010. Synthesis and applications of nano-structured iron oxides/hydroxides–a review. *International Journal of Engineering, Science and Technology,* 2.

Moros, M., Hernáez, B., Garet, E., Dias, J. T., Sáez, B., Grazú, V., González-Fernández, Á., Alonso, C. & De La Fuente, J. M. 2012. Monosaccharides versus PEG-Functionalized NPs: Influence in the Cellular Uptake. *ACS Nano,* 6**,** 1565-1577.

Moros, M., Pelaz, B., Lopez-Larrubia, P., Garcia-Martin, M. L., Grazu, V. & De La Fuente, J. M. 2010. Engineering biofunctional magnetic nanoparticles for biotechnological applications. *Nanoscale,* 2**,** 1746-1755.

Muir, B. W., Moffat, B. A., Harbour, P., Coia, G., Zhen, G., Waddington, L., Scoble, J., Krah, D., Thang, S. H., Chong, Y. K., Mulvaney, P. & Hartley, P. 2009. Combinatorial Discovery of Novel Amphiphilic Polymers for the Phase Transfer of Magnetic Nanoparticles. *The Journal of Physical Chemistry C,* 113**,** 16615-16624.

Otsuka, H., Nagasaki, Y. & Kataoka, K. 2003. PEGylated nanoparticles for biological and pharmaceutical applications. *Advanced drug delivery reviews,* 55**,** 403-419.

Overgaard, K. & Overgaard, J. 1972. Investigations on the possibility of a thermic tumour therapy. I. Short-wave treatment of a transplanted isologous mouse mammary carcinoma. *Eur J Cancer,* 8**,** 65-78.

Pellegrino, T., Manna, L., Kudera, S., Liedl, T., Koktysh, D., Rogach, A. L., Keller, S., Rädler, J., Natile, G. & Parak, W. J. 2004. Hydrophobic Nanocrystals Coated with an Amphiphilic Polymer Shell: A General Route to Water Soluble Nanocrystals. *Nano Letters,* 4**,** 703-707.

Peng, X. H., Qian, X. M., Mao, H., Wang, A. Y., Chen, Z., Nie, S. M. & Shin, D. M. 2008. Targeted magnetic iron oxide nanoparticles for tumor imaging and therapy. *International Journal of Nanomedicine,* 3**,** 311-321.

Qin, J., Jo, Y. S. & Muhammed, M. 2009. Coating Nanocrystals with Amphiphilic Thermosensitive Copolymers. *Angewandte Chemie International Edition,* 48**,** 7845-7849.

Sheng, Y., Yuan, Y., Liu, C., Tao, X., Shan, X. & Xu, F. 2009. In vitro macrophage uptake and in vivo biodistribution of PLA–PEG nanoparticles loaded with hemoglobin as blood substitutes: effect of PEG content. *Journal of Materials Science: Materials in Medicine,* 20**,** 1881-1891.

Sonvico, F., Mornet, S., Vasseur, S., Dubernet, C., Jaillard, D., Degrouard, J., Hoebeke, J., Duguet, E., Colombo, P. & Couvreur, P. 2005. Folate-conjugated iron oxide nanoparticles for solid tumor targeting as potential specific magnetic hyperthermia mediators: Synthesis, physicochemical characterization, and in vitro experiments. *Bioconjugate Chemistry,* 16**,** 1181-1188.

Sun, J., Zhou, S., Hou, P., Yang, Y., Weng, J., Li, X. & Li, M. 2007. Synthesis and characterization of biocompatible Fe3O4 nanoparticles. *Journal of Biomedical Materials Research Part A,* 80A**,** 333-341.

Sun, S., Zeng, H., Robinson, D. B., Raoux, S., Rice, P. M., Wang, S. X. & Li, G. 2004. Monodisperse MFe2O4 (M = Fe, Co, Mn) nanoparticles. *J Am Chem Soc,* 126**,** 273-9.

Tartaj, P., Morales, M. P., Veintemillas-Verdaguer, S., Gonzalez-Carreño, T. & Serna, C. J. 2006. Synthesis, properties and biomedical applications of magnetic nanoparticles. *Handbook of magnetic materials,* 16**,** 403-482.

Terris, B. D. & Thomson, T. 2005. Nanofabricated and self-assembled magnetic structures as data storage media. *Journal of Physics D-Applied Physics,* 38**,** R199-R222.

Tromsdorf, U. I., Bruns, O. T., Salmen, S. C., Beisiegel, U. & Weller, H. 2009. A Highly Effective, Nontoxic T1 MR Contrast Agent Based on Ultrasmall PEGylated Iron Oxide Nanoparticles. *Nano Letters,* 9**,** 4434-4440.

Walczyk, D., Bombelli, F. B., Monopoli, M. P., Lynch, I. & Dawson, K. A. 2010. What the cell "sees" in bionanoscience. *J Am Chem Soc,* 132**,** 5761-8.

Wang, X., Zhang, R., Wu, C., Dai, Y., Song, M., Gutmann, S., Gao, F., Lv, G., Li, J., Li, X., Guan, Z., Fu, D. & Chen, B. 2007. The application of Fe3O4 nanoparticles in cancer research: A new strategy to inhibit drug resistance. *Journal of Biomedical Materials Research Part A,* 80A**,** 852-860.

William, W. Y., Emmanuel, C., Christie, M. S., Rebekah, D. & Vicki, L. C. 2006. Aqueous dispersion of monodisperse magnetic iron oxide nanocrystals through phase transfer. *Nanotechnology,* 17**,** 4483.

Wu, N., Fu, L., Su, M., Aslam, M., Wong, K. C. & Dravid, V. P. 2004. Interaction of Fatty Acid Monolayers with Cobalt Nanoparticles. *Nano Letters,* 4**,** 383-386.

Xie, J., Lee, S. & Chen, X. 2010. Nanoparticle-based theranostic agents. *Advanced drug delivery reviews,* 62**,** 1064-1079.

Yang, K., Peng, H., Wen, Y. & Li, N. 2010. Re-examination of characteristic FTIR spectrum of secondary layer in bilayer oleic acid-coated Fe3O4 nanoparticles. *Applied Surface Science,* 256**,** 3093-3097.

Yoo, J.-W., Chambers, E. & Mitragotri, S. 2010. Factors that control the circulation time of nanoparticles in blood: challenges, solutions and future prospects. *Current pharmaceutical design,* 16**,** 2298-2307.

Yu, D.-H., Lu, Q., Xie, J., Fang, C. & Chen, H.-Z. 2010. Peptide-conjugated biodegradable nanoparticles as a carrier to target paclitaxel to tumor neovasculature. *Biomaterials,* 31**,** 2278-2292.

Zaloga, J., Stapf, M., Nowak, J., Pöttler, M., Friedrich, R. P., Tietze, R., Lyer, S., Lee, G., Odenbach, S. & Hilger, I. 2015. Tangential flow ultrafiltration allows purification and concentration of lauric acid-/albumin-coated particles for improved magnetic treatment. *International journal of molecular sciences,* 16**,** 19291-19307.

Zhang, B., Shen, S., Liao, Z., Shi, W., Wang, Y., Zhao, J., Hu, Y., Yang, J., Chen, J., Mei, H., Hu, Y., Pang, Z. & Jiang, X. 2014. Targeting fibronectins of glioma extracellular matrix by CLT1 peptide-conjugated nanoparticles. *Biomaterials,* 35**,** 4088-4098.

Zhang, M. Q. & Kievit, F. M. 2012. Surface engineering of iron oxide nanoparticles for targeted cancer therapy. *Abstracts of Papers of the American Chemical Society,* 243.

Chapter 4.

Development of a preclinical tool for predictive analysis of nanomaterial safety

4. Development of a preclinical tool for predictive analysis of nanomaterial safety

4.1 Introduction

Research and development of biomedical nanomaterials (NMs) is currently amongst the most rapidly evolving area in drug delivery and biomedical imaging. Biomedical NMs are being developed for a vast number of disease states, notably cancer, infectious diseases, cardiovascular disorders, and immune and degenerative diseases (Brigger et al., 2012, Heckman et al., 2013, Lanza et al., 2006, Lin et al., 2013). The unique physico-chemical properties of NMs, such as size, composition, and surface area-to-volume ratio, contribute to their desirability as a drug delivery system. Although these characteristics can be advantageous to a drug delivery system they can also add to the complexity when investigating potential toxicity. Size, in particular, has been highlighted as an important physical characteristic of a NM when predicting potential toxicity (Nel et al., 2006, Oberdorster et al., 2005). Size-dependent toxicity has been demonstrated in a number of NMs, notably silver (Ivask et al., 2014, Kasemets et al., 2014, Kim et al., 2012) and gold (Coradeghini et al., 2013). The small size and high surface area-to-volume ratio contributes to the highly reactive nature of NMs (Oberdorster et al., 2005).

As well as delivering therapeutic compounds, multi-model NMs can be functionalised with imaging agents to be used as both a diagnostic and therapeutic tools (Boisselier and Astruc, 2009, Brigger et al., 2012, Mornet et al., 2004). Systemic toxicity, caused by non-specificity of drugs, can be overcome by functionalisation with

targeting moieties, such as peptides or antibodies, to target specific cell types or abhorrent proteins as part of a mutated cellular signalling pathway. Nevertheless, there are innumerable core materials and surface modifications, often non-FDA approved components, available to consider when designing NPs for biomedical use. This leads to vast permutations of physico-chemical properties and a complex task to predict potential toxicity.

Despite the ever-increasing production of novel NMs for biomedical use, few have been approved by the Food and Drug Administration (Anselmo and Mitragotri, 2016, Venditto and Szoka, 2013). The lack of a regulatory framework to assess the potential toxicity of a novel NM is restricting the transfer of many promising nanotherapeutics into a clinical environment (Desai, 2012). It is often difficult to acquire accurate toxicity results on novel engineered nanoparticles due to their poor physical chemical characterisation, which is frequently unpredictable in biological environments, and a lack of pre-clinical screening.

Although *in vitro* models provide a quick and easy assessment of potential nanotoxicity, there can often be disagreement between *in vitro* and mammalian *in vivo* toxicology results (Joris et al., 2013). Mammalian models, such as the mouse or rat, provide detailed assessment of toxicity; however at the early stage of a novel NM's development it is not often feasible to use a higher organism model, which is considered expensive and time consuming. Furthermore, it would not be in keeping with the 3R's (replacement, reduction, and refinement) outlined by the National Centre for the Replacement Refinement and Reduction of Animals in Research, which provides a framework for human animal research. Current initiatives such as 'Tox 21' aim to change the way toxicology is performed, providing alternatives to using rodent models and prioritising chemicals, which would need more extensive and costly

toxicological evaluation (Hsieh et al., 2015). It would be advantageous to use an *in vivo* model that could bridge the gap between *in vitro* cell based assays and a mammalian model. As a result, more primitive organisms such as *Caenorhabditis elegans* (a nematode) (Mohan et al., 2010, Wang et al., 2009), *Danio rerio* (zebrafish) (Asharani et al., 2008, George et al., 2011, Kim et al., 2013), and *Xenopus laevis* (African clawed frog) (Leconte and Mouche, 2013, Marcon et al., 2010), are being investigated as potential *in vivo* toxicity models.

C. elegans has been an important model organism since the early 1960s when it was introduced as a tool for research (Brenner, 1974). In particular, it has been a successful model in developmental biology (including programmed cell death and ageing) and neurology (Bargmann, 1998), in part due to the short life cycle and the complete fate mapping of somatic cells. It has also been proposed as an inexpensive animal model for drug screening as it is easy to administer water-soluble compounds and screen for resulting apoptotic responses. However, as with other invertebrates, there is little correlation between the anatomy of *C. elegans* and that of humans. Specifically, the lack of vascular and digestive systems, including the liver, kidneys, and pancreas, restricts *C. elegans'* use as an appropriate system for assessing the potential risk of NMs to human health. The vertebrate systems of *Danio rerio* and *Xenopus laevis* both have considerable advantages as tools for assessing potential NM toxicity. As vertebrates, they have digestive, skeletal, and nervous systems, as well as a closed circulatory system. The analysis of these systems after nanoparticle exposure is important to ascertain any potential toxicity to human health. *Xenopus* has a long-running history in toxicity testing, such as the frog teratogenesis assay-*Xenopus* (FETAX) assay, which provides high predictability of teratogens in mammals (Mouche et al., 2011).

We propose using the African clawed frog *Xenopus* as a suitable *in vivo* system for the toxicity assessment of novel NMs (Bacchetta et al., 2012, Nations et al., 2011). *Xenopus* is a higher vertebrate system that has been used at the forefront of developmental biology and has been highlighted for its use as a model for chemical genetic screening (Wheeler and Liu, 2012). There are many benefits to using *Xenopus* as an *in vivo* toxicity model including a relatively simple procedure to generate embryos resulting in high yields, an important consideration if the model is to be used in a high-throughput screening (HTS) assay. *Xenopus* start-up and maintenance costs are relatively low, making them a cost effective model compared to mammalian alternatives (Wheeler and Brändli, 2009). External development of the embryo allows for temporal control over the exposure to NMs, allowing investigation into the toxic affects during significant stages during embryogenesis, such as gastrulation and neurulation. Many embryos can be externally exposed to NM solution during their development. Exposure through embryogenesis can be used to determine any teratogenic effects, or the embryo can be exposed after organogenesis in order to determine any toxicity to organs simulating a more 'adult' model. Furthermore, the *Xenopus* developmental stages are well characterised making it an ideal model for phenotypic assays (Tomlinson et al., 2012). The sensitivity of embryos during development can be exploited to identify varying degrees of toxicity by a range of phenotypic abnormalities and give an indication into safe dosages, information not often accurately known before assessment in a mammalian model.

This chapter will outline the methodology a nanotoxicity screening assay (figure 4.1.1) that involves an initial physico-chemical characterisation of the NMs in the biological environment and combines the sensitivity of *X. laevis* embryos during development in parallel with *in vitro* testing in mammalian cell lines to provide a

hierarchical, rapid, and low cost approach to assess NM toxicity. The system has been tested using four different nanoparticles (NPs); CdSe NPs (QDs), PEGylated magnetite NPs (Fe_3O_4-PEG), amine-functionalised magnetite NPs (Fe_3O_4-NH_2), and fluorescent carboxylated polystyrene NPs (PS-COOH).

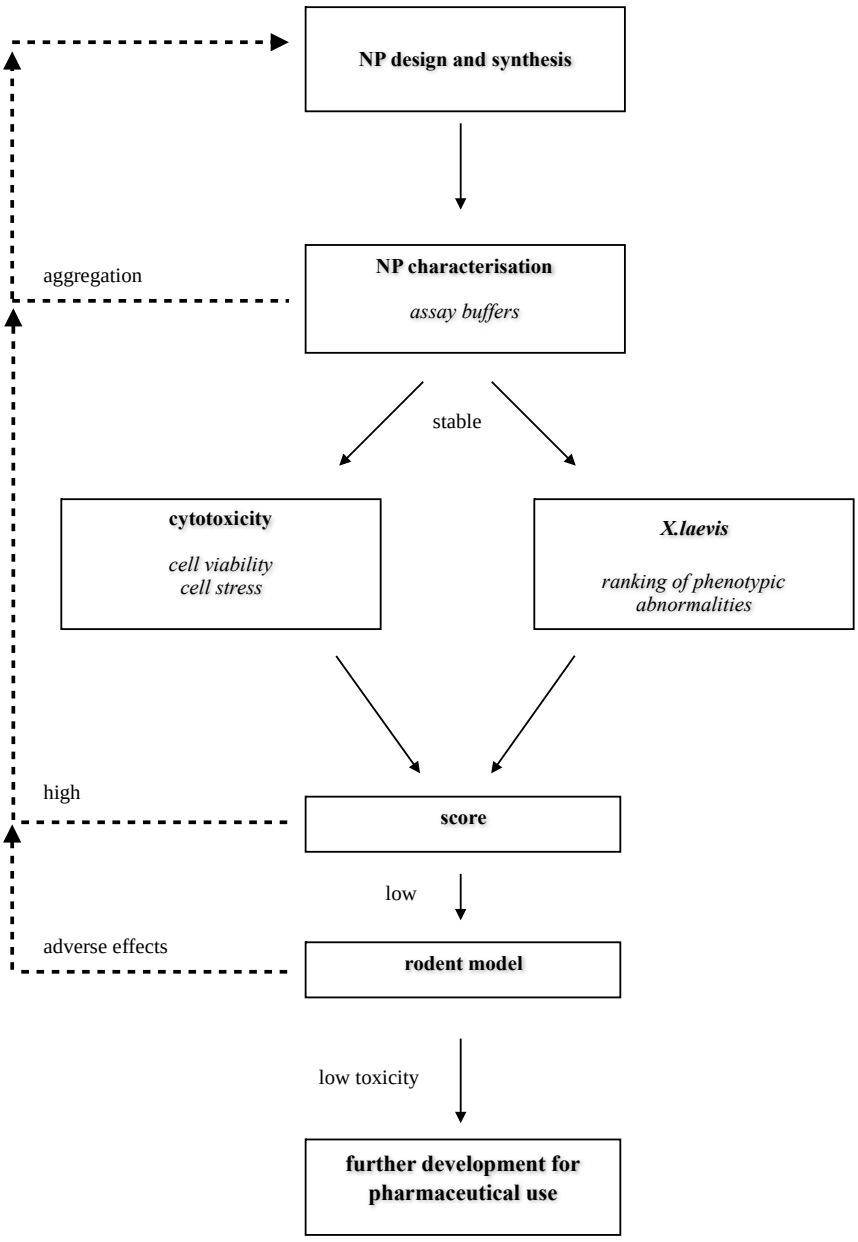

Figure 4.1.1 Nanotoxicology assay workflow. A NP in the early stages of development is firstly characterised in the assay buffers, cell media (RPMI + supplements) and embryos culture media (0.1 x MMR). Particles that are unstable and aggregate in assay buffers must be redesigned or modified to increase stability. Once a stable particle is fully characterised, it will undergo an integrated toxicity screening protocol combining, in parallel, cytotoxicity assays in a range of cell lines and *X. laevis* ranking of phenotypic abnormalities. The combined results produce a hazard ranking that indicates if the NP should advance for further development and toxicity screening in a rodent model.

4.2 Nanoparticle characterisation

Several core materials are unsuitable for use in a biological system. Cadmium selenide quantum dots (QD), for example, show high levels of toxicity in several cell lines (Guo et al., 2007). Other Cd based core QD, such as CdTe, also show toxicity (Lovric et al., 2005). The mechanism of toxicity for Cd core based QD is unknown but thought to be due to leaching of Cd^{2+} ions after core degradation in the cell. To this end, Derfus *et al.* demonstrated a correlation between surface oxidation, leading to the release of Cd ions and toxicity (Derfus et al., 2004). As it is well established that CdSe QD are highly toxic, we have used these NPs as a positive control in our assay. There are core materials thought to be biocompatible due to lack of toxicity, which as a result have high potential as drug delivery systems. Amongst these are iron oxide NPs, currently the only clinically approved metal oxide core (Qiao et al., 2009), and polystyrene nanoparticles (Fahmy et al., 2005). We have used two iron oxide NPs with different surface functionalisation and physical chemical stability, as well as inert polystyrene particles to test the suitability of the methodology in detecting any possible related toxicity effects.

QDs were synthesised in house as described in materials and methods 2.1.1 (Ahire et al., 2015). Typically, core diameter for QD was 5 nm from TEM (figure 4.2.1 and 4.2.2) with a hydrodynamic diameter in aqueous solution of 21 nm and a PDI of 0.1 from DLS (figure 4.2.3). Commercial PS-COOH had a mean core diameter of 23 nm and a hydrodynamic diameter in water of 345 nm, PDI 0.2 (figure 4.2.3).

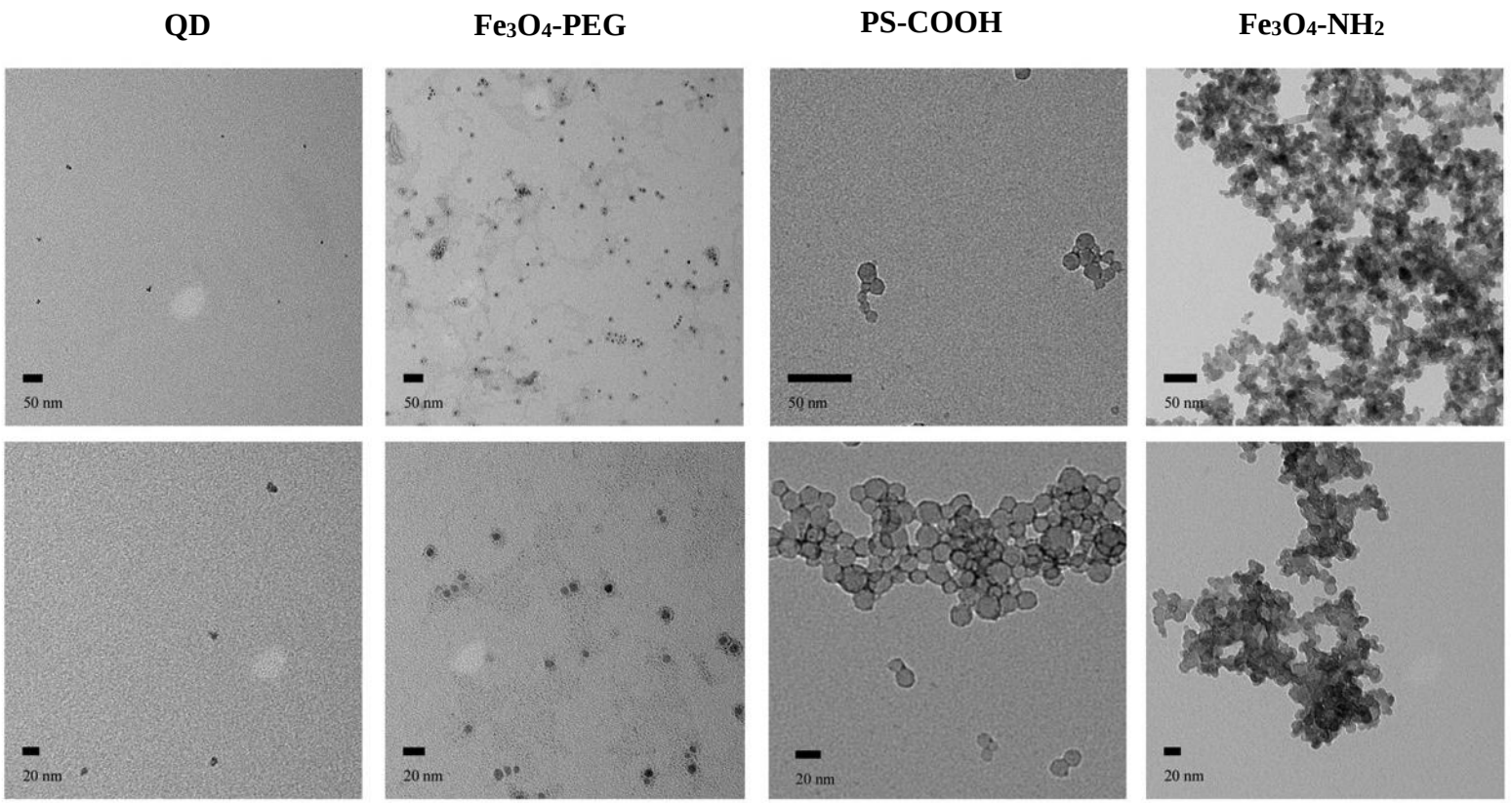

Figure 4.2.1 TEM analysis of NPs. Representative images of QD, Fe_3O_4-PEG, PS-COOH and Fe_3O_4-NH_2 NPs.

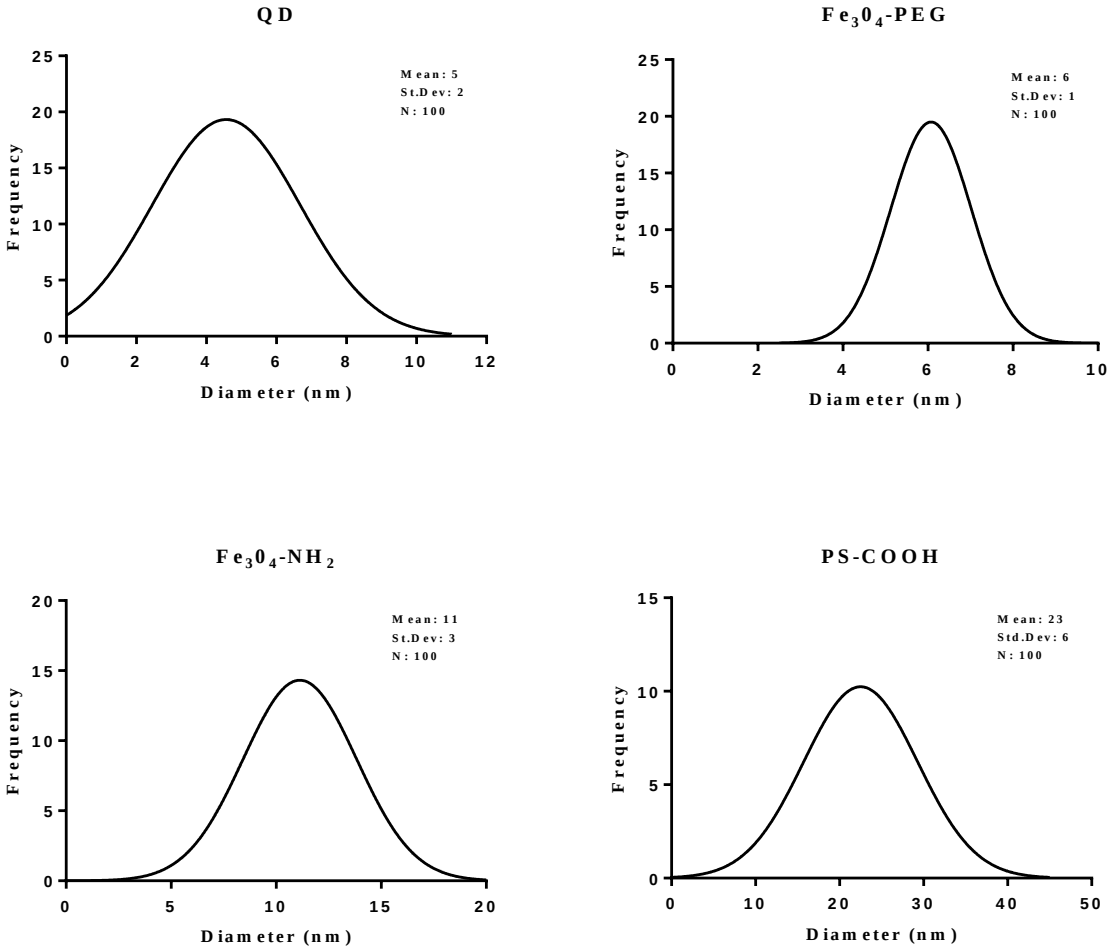

Figure 4.2.2 Size distribution of NPs. Distribution of NP diameter (nm) from TEM analysis. For each NP, 100 particles were analysed from representative TEM images with respective mean diameters of 5, 6, 23, and 11 nm for QD, Fe_3O_4-PEG, PS-COOH, and Fe_3O_4-NH_2 NPs. NPs were measured from different areas of the copper grid.

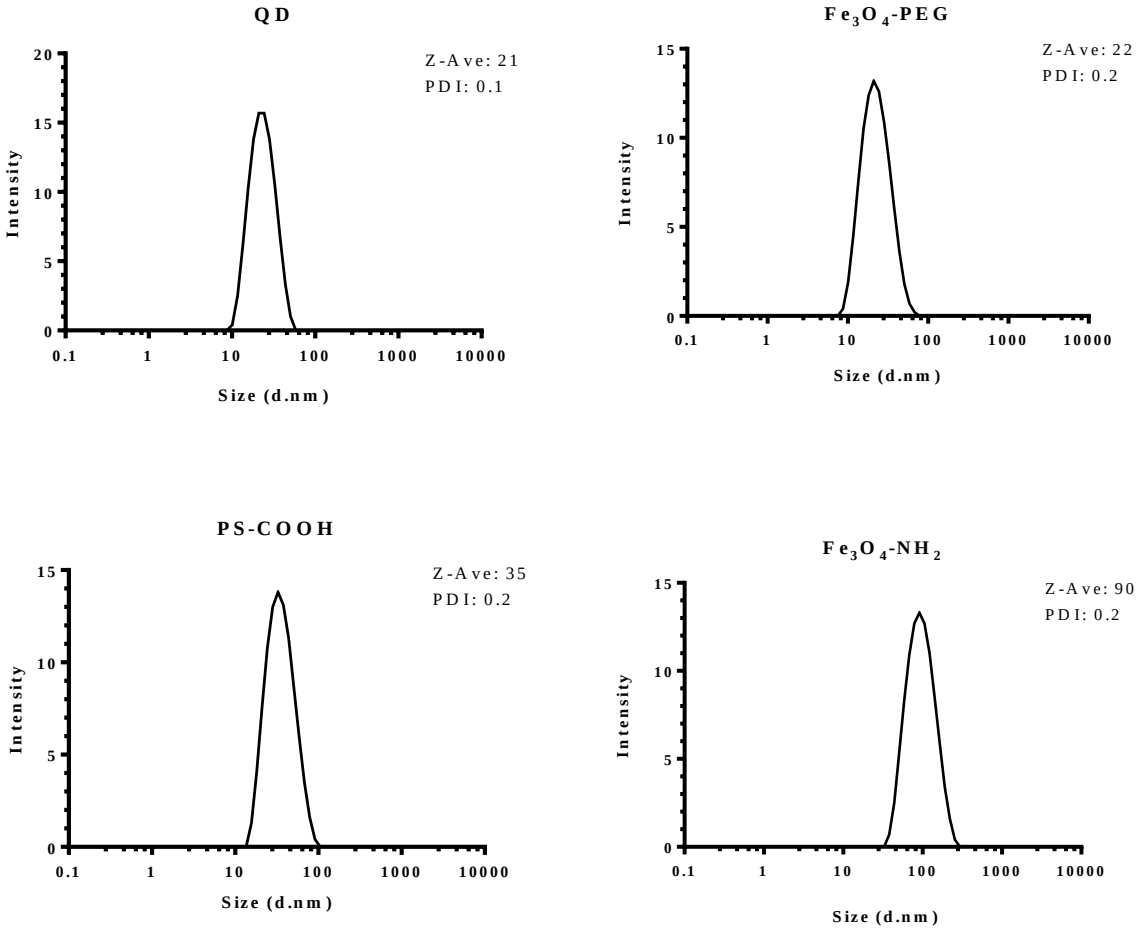

Figure 4.2.3 NP hydrodynamic size distribution from DLS. NPs were dispersed into MQW apart from Fe_3O_4-PEG which was dispersed in PBS. Respective hydrodynamic diameters (Z-ave) of 21, 22, 35, and 90 nm for QD, Fe_3O_4-PEG, PS-COOH and Fe_3O_4-NH_2 NPs.

Table 4.2.1 Summary of NP characterisation in different buffers. NPs were dispersed in the different assay mediums, water (PBS*), RPMI-1640, and 0.1 x MMR. Hydrodynamic diameter, analysed using DLS, was compared to the core size using TEM. Error shown as standard deviation**.**

	TEM	**Water (PBS*)**			**RMPI-1640 10% FBS**		**0.1 x MMR**	
	D (nm)	D_H (nm)	PDI	ζ-potential (mV)	D_H (nm)	PDI	D_H (nm)	PDI
QD	5 ± 2	21 ± 2	0.1	- 27 ± 0	108 ± 1	0.7	122 ± 2	0.1
Fe_3O_4-PEG	6 ± 1	22 ± 0	0.2	- 4 ± 2	33 ± 3	0.2	22 ± 1	0.2
PS-COOH	23 ± 6	35 ± 1	0.2	- 37 ± 2	75 ± 1	0.2	35 ± 1	0.2
Fe_3O_4- NH_2	11 ± 3	90 ± 1	0.2	+ 30 ± 4	294 ± 2	0.4	2268 ± 96	0.2

*Fe_3O_4-PEG analysis in PBS

Characterisation of the commercial Fe_3O_4-NH_2 showed a mean core diameter of 11 nm and a greatly increased hydrodynamic diameter of 90 nm, PDI 0.2, from the DLS (figure 4.2.3); indicative of the formation of Fe_3O_4-NH_2 clusters in aqueous solution. On the other hand, the in-house synthesised Fe_3O_4 NPs, mean core diameter 6 nm, were stabilised using a PEG coating. This is evident in the low hydrodynamic diameter of 22 nm, PDI 0.2 (figure 4.2.3).

It is also important to characterise the physico-chemical properties of the NPs in the relevant assay buffers to surmise if toxicity profiles are dependent on the material and components of the NP or due to aggregation. The salt buffer (0.1 x MMR) and cell growth media with 10% FCS was used to simulate conditions of each assay, including incubation over 72 h at 18 ^oC and 37 ^oC respectively. Although stable in aqueous solution, in the assay buffers QD and Fe_3O_4-NH_2 showed some instability and aggregation (table 4.2.1). It is evident that the stability of these electrostatically stabilised NPs (table 4.2.1) is affected by the salt concentration in the MMR. In the presence of proteins, from the FCS supplemented media, aggregation in electrostatically stabilised NPs is reduced. This is due to the formation of NP-protein complexes to form a protein corona (Di Silvio et al., 2015, Walczyk et al., 2010). NP-protein can be seen in all particles (table 4.2.1 and figure 4.2.4); however, after the initial increase in size when exposed to RPMI 10% FCS the size remained stable over the 72 hr at 37 ^oC.

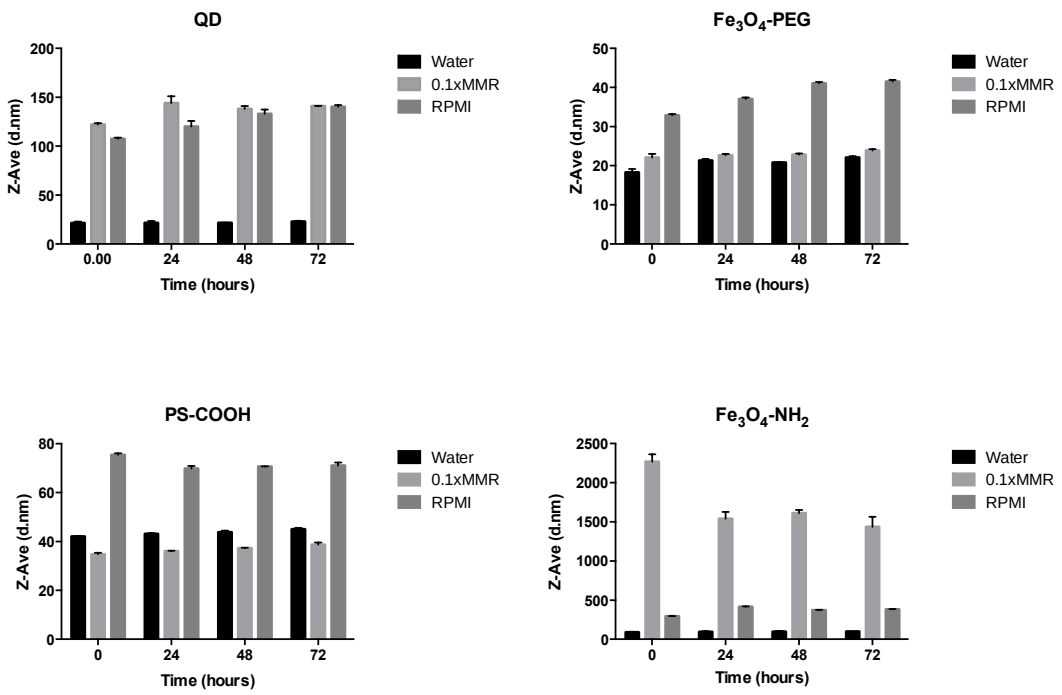

Figure 4.2.4 Stability of NPs in assay buffers. Mean hydrodynamic diameters of NPs dispersed in assay buffers over 72 hr to assess colloidal stability. Error bars shown are SD.

4.3 Cell-based cytotoxicity analysis

Cell-based assays are routinely used as a platform to evaluate the potential toxicity of a novel NM and, typically, they are used as a first screen in toxicological assessment (Monteiro-Riviere et al., 2009). Cytotoxicity assays are often based on identifying cell viability and/or cell stress after immortalised cell lines are exposed to NMs in a monoculture. The cell line used is often dependent on the target organ expected to experience NM exposure *in vivo.* After acute exposure to NMs, commonly ranging from 3 to 48 hr, the resulting cell viability is assessed by a biochemical assay. We have used 3 cell lines; A549 lung cancer, SK-MEL-28 melanoma, and MDCK canine kidney. These cell lines were selected as they represent easy to grow lines that are readily available for most research groups.

Initially, cell morphology was observed after 72 hr exposure to the four NPs at high concentrations in the three lines (figure 4.3.1). The control, without NP exposure, shows the healthy morphology and confluency of the cells. After exposure to $10^{15.8}$ NP/ml QD, there is a significant loss in cell viability and the remaining cells appear rounded and unhealthy. Fe_3O_4-PEG at $10^{15.3}$ NP/ml had no significant visible effect on morphology and confluency across all three cell lines. At relevant concentrations, PS-COOH appears to have a small toxic effect, especially on the SK-MEL-28; the morphology is more rounded as they become detached from the plate and there is a noticeable loss of cells. Fe_3O_4-NH_2 also showed signs of toxicity. Noticeably, aggregates of Fe_3O_4-NH_2 can be seen on the surface on the cells.

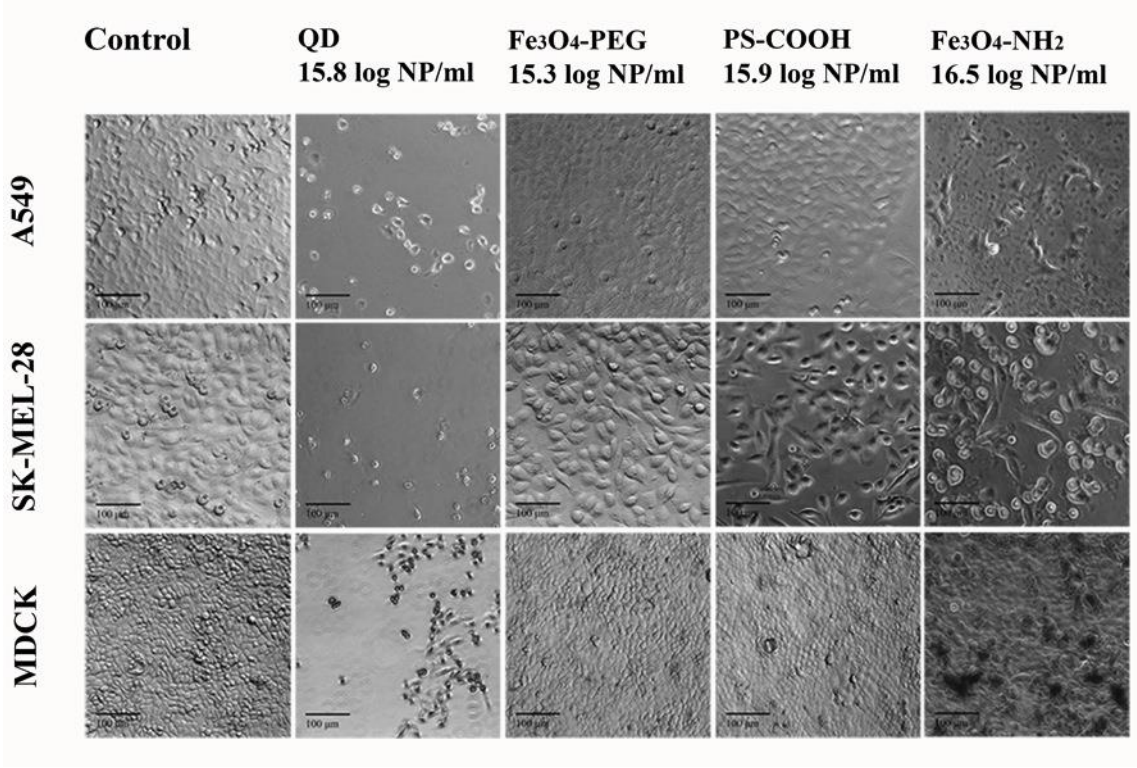

Figure 4.3.1 Cell morphology after exposure to NPs. Cells were exposed to $10^{15.8}$ NP/ml QD, $10^{15.3}$ Fe_3O_4-PEG, $10^{15.9}$ PS-COOH, and $10^{16.5}$ Fe_3O_4-NH_2 NPs for 72 hr. Shown are the resulting representative bright field images of the cell monolayers at 10 x magnification. Size bars 100 µm.

Basic cell viability assays, such as the Trypan Blue exclusion assay, are convenient as preliminary screening tools to identify potential toxicity. Trypan Blue is a diazo dye that is excluded by the intact membrane of healthy cells. The dye is able to pass the membranes of non-viable cells with a compromised membrane (Strober, 2001), resulting in accumulation of the blue dye in the cytoplasm of the cell. Counting the stained cells, using a haemocytometer, indicates cell viability after exposure to NPs. Fe_3O_4-PEG and PS-COOH showed no significant toxicity up to the highest concentration of $10^{15.3}$ NP/ml and $10^{15.9}$ NP/ml respectively (figure 4.3.2). QD showed a loss of 50% viability in all cell lines at ~10^{13} NP/ml and dose dependent toxicity was observed; cell viability was reduced to >15% after exposure to 10^{15} NP/ml. Fe_3O_4-NH_2 at $10^{13.8}$ and $10^{14.2}$ showed minimal (A549) and no significant toxicity (SK-MEL-28 and MDCK). However, after 72 hr exposure to $10^{15.5}$ NP/ml, Fe_3O_4-NH_2 causes significant toxicity and in the three cell lines there was a mean cell viability of between 45-52% (figure 4.3.2).

It is important that different cytotoxicity assays are employed to determine the potential toxicity of a NP. Whilst the Trypan Blue may indicate no toxicity due to an intact membrane, other damage, such as mitochondrial damage or cell stress may occur. Enzymatic assays with a spectrophotometric read out, such as MTT (3-[4,5-dimethylthiazol-2-yl]-2,5 diphenyl tetrazolium bromide), are quick and easy, and can provide an abundance of data for statistical analysis. The MTT assay relies on the reduction of tetrazolium salt to a formazan product by the cytochrome in the mitochondria of viable cells (Mosmann, 1983). The resulting formazan product, a dark blue precipitate, can be easily measured using a spectrophotometer (λmax 565 nm), allowing viable cells to be quantified. MTT was able to detect dose dependent toxicity of the positive control QD after 72 hr exposure at concentration range between $10^{12.8}$

and $10^{15.8}$ NP/ml (figure 4.3.3). At $10^{15.8}$ NP/ml QD cell viability for A549, SK-MEL-28, and MDCK was reduced to 11.7%, 15.8%, and 21.7%, respectively.

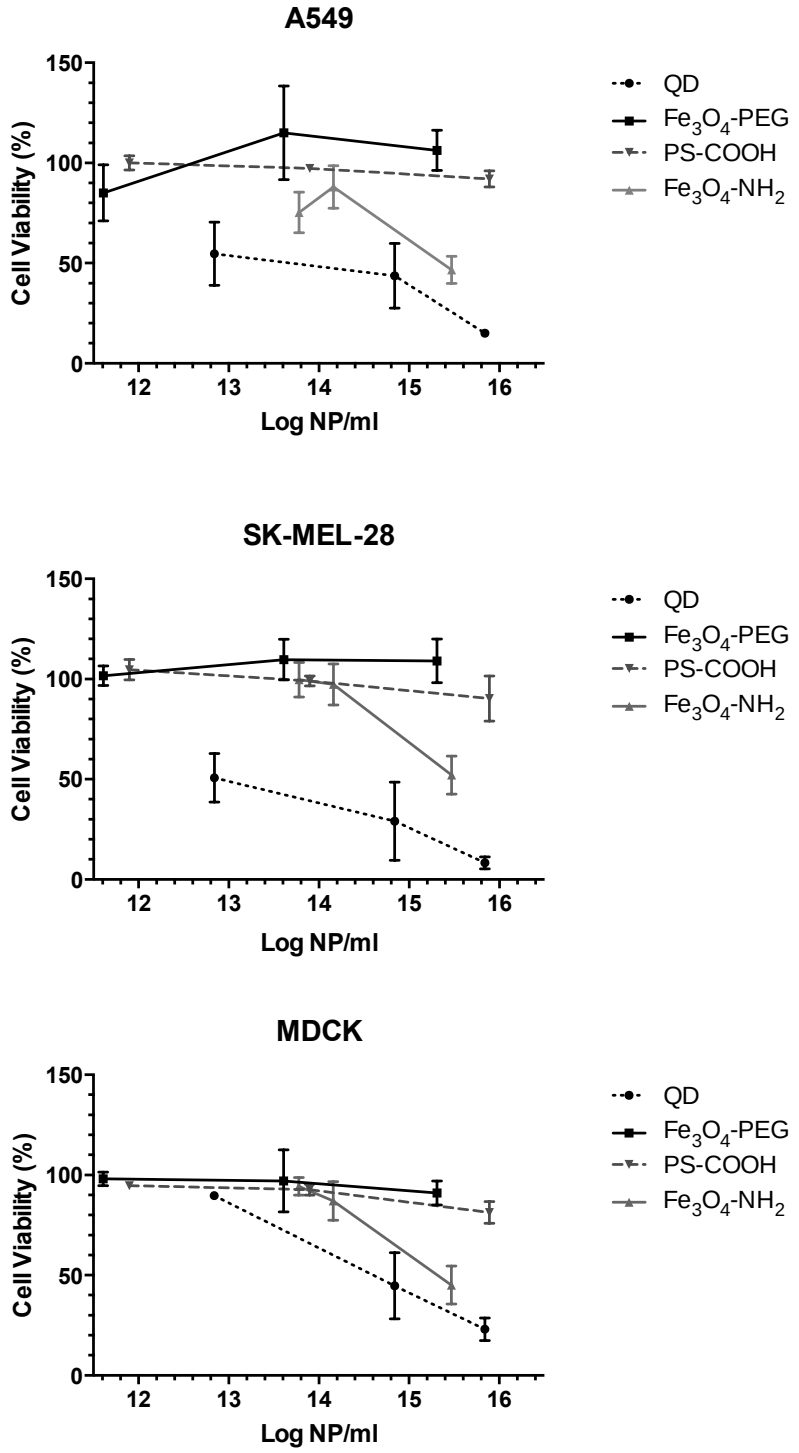

Figure 4.3.2 Trypan blue analysis after NP treatment. A549, SK-MEL-28, and MDCK cell lines were exposed to different concentrations of QD, Fe_3O_4-PEG, PS-COOH, and Fe_3O_4-NH_2 NPs. Cytotoxicity was evaluated by counting the number of viable cells using Trypan Blue after 72 h NP exposure. Percentage cell viability was calculated by normalising cell count to control cells. Error bars show SEM.

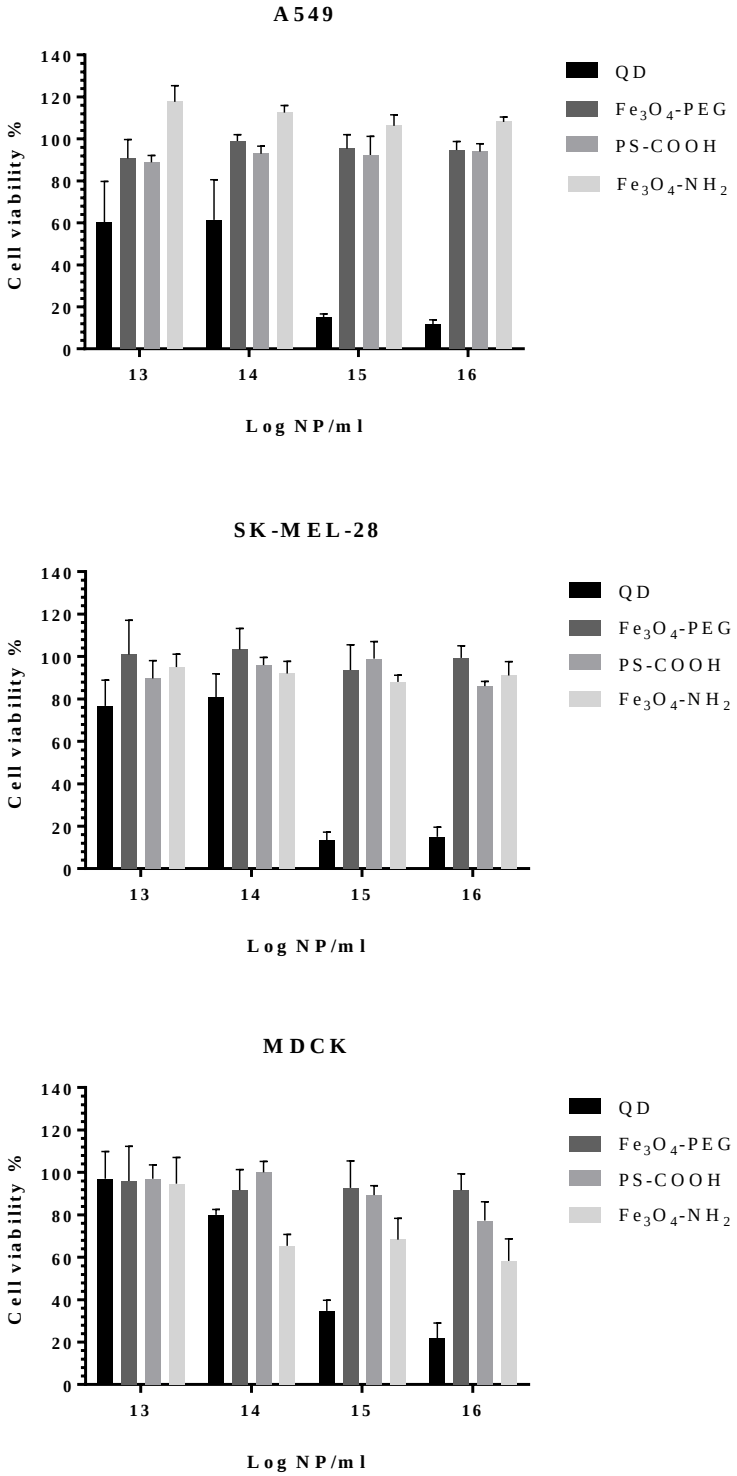

Figure 4.3.3 MTT analysis after NP treatment. A549, SK-MEL-28, and MDCK cell lines were exposed to different concentrations of QD, Fe_3O_4-PEG, PS-COOH, and Fe_3O_4-NH_2 NPs. Cytotoxicity was evaluated MTT assay after 72 h NP exposure. Percentage cell viability was calculated by normalising cell count to control cells. Error bars show SEM.

In A549 and SK-MEL-28 cell lines, Fe_3O_4-PEG, Fe_3O_4-NH_2, and PS-COOH induced no significant loss of cell viability. As the only non-cancerous cell line (yet immortalised), MDCKs appeared to be more sensitive to NP exposure. MDCK cell viability was reduced to ~58% after exposure to $10^{16.5}$ NP/ml Fe_3O_4-NH_2 and after exposure to $10^{15.9}$ NP/ml PS-COOH cell viability was 77%.

In nanotoxicology it is important to consider different concentration metrics to better understand the interaction between the nanomaterials and the cells. Currently, there is no metric that is recognised as an international standard. Mass, surface area, and number of NPs are the most common dose metrics for nanomaterial toxicity. For drug toxicology, mass concentration is perhaps the easiest and most common. A major difficultly with using mass-based dose metrics for nanotoxicology is Avogadro's law; the molar mass of a solute is equal to 6.022×10^{23} NPs per mole. NPs in the nanoscale do not follow this law. Decreasing NP size, at a given mass, exponentially increases the NP number and surface area available to interact with a cell's surface. The total surface area of the particulate material and the total number of NPs that are accessible to interact with the cell's surface have been used as an alternative metrics (figure 4.3.4) (Hull et al., 2012, Zou et al., 2015). The number of NPs per ml was calculated by working out the mass of a single NP using the density of the material used. The concentration, in mg/L from ICP-MS analysis, divided by the mass of a single NP results in the number of NPs in a given volume.

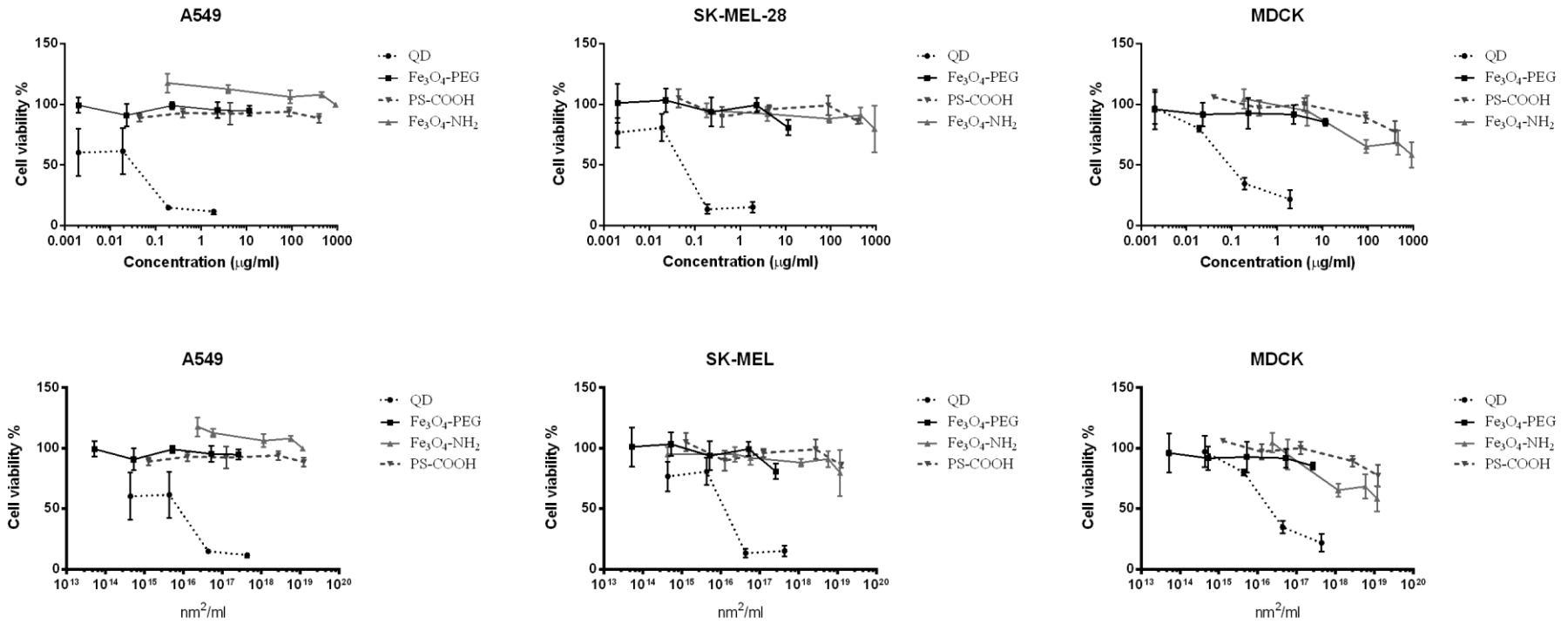

Figure 4.3.4 MTT alternative concentration matrices. Analysis of MTT cell viability assay after A549, SK-MEL-28, and MDCK cell lines were exposed to different concentrations of QD, Fe_3O_4-PEG, PS-COOH, and Fe_3O_4-NH_2 NPs. Cytotoxicity was evaluated after 72 h NP exposure. (a) NP concentration expressed as weight to volume (μg/ml). (b) NP concentration expressed as surface area to volume (nm^2/ml). Percentage cell viability was calculated by normalising cell count to control cells. Error bars show SEM.

Previous studies have shown that, despite a lack of cell death, exposure to nanomaterials can lead to cellular stress and an increase in reactive oxygen species (ROS) (Carlson et al., 2008, Filippi et al., 2015, Hussain et al., 2005). Evaluating levels of activated poly [ADP-ribose] polymerase 1 (PARP-1) is one way to determine if cells are under stress after exposure to NPs. PARP-1, a substrate for active cysteinyl-aspartate protease cleavage, is activated by internal and external stress stimulus, such as the production ROS, and mediates DNA damage response and apoptosis (Tewari et al., 1995). In this study, we have evaluated the abundance of the active cleaved PARP-1 protein as a marker for apoptosis in the response to exposure to NPs. Full length PARP-1 protein (116 kDa) is involved in DNA repair and differentiation (Javle and Curtin, 2011). Following apoptosis initiation, PARP-1 is cleaved by caspases, notably caspase-3, at the C-terminal to an active form (89 kDa). After NP treatment we found QDs and the cytotoxic drug cisplatin, the latter used as a positive control, induced apoptosis as shown through increased levels of cleaved PARP-1 protein (figure 4.3.5) using western immunoblotting. Lower levels of cleaved PARP-1 can be seen in A549 when compared to SK-MEL-28 and MDCK cell lines after treatment with cisplatin and QDs. This shows the importance of using a range of cell lines for cytotoxicity analysis to avoid false negative results.

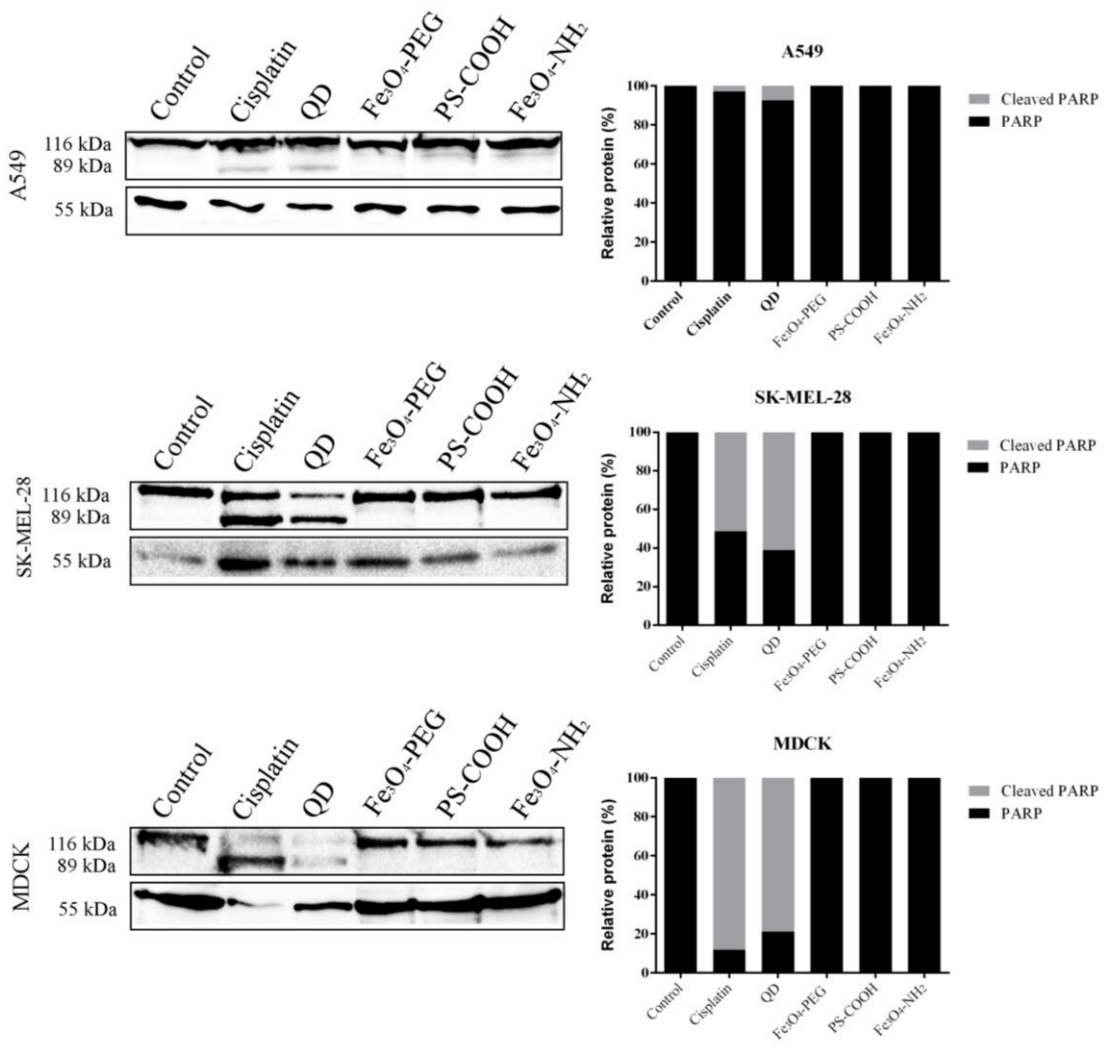

Figure 4.3.5 Western blot analysis of PARP-1 cleavage. Protein expression of full length (116 kDa) and cleaved (89 kDa) PARP-1 using Western Immunoblotting in A549, SK-MEL-28, and MDCK cell lines. Relative levels of full length and cleaved PARP-1 protein were analysed in whole cell lysates after 24 h NP stimulation with 70 μM cisplatin (positive control), $10^{15.8}$ NP/ml QD, $10^{15.3}$ NP/ml PEG-Fe_3O_4, $10^{15.9}$ NP/ml PS-COOH, and $10^{15.5}$ NP/ml NH_2-Fe_3O_4 NPs. Control cells were vehicle treated. β-tubulin (55 kDa) was used as a loading control. Graphs show normalised levels of the full length and cleaved PARP-1 calculated from densitometry analysis of the Western Immunoblot.

4.4 *X. laevis* as a multiparametric nanotoxicity assessment tool

X. laevis embryos were exposed to a range of NP concentrations during different stages of development (figure 4.4.1). Embryos were selected at NF stage 4 and were incubated with NPs until NF stage 38 (NF 4 – 38). At NF stage 4 the *X. laevis* embryo is at 8 cells and continues to undergo cleavage, increasing the cell number. The embryo is considered a blastula once at 128 cells and the blastocoel, a fluid-filled cavity, forms within the embryo. After cleavage the embryo undergoes gastrulation. 'It is not birth, marriage, or death, but gastrulation, which is truly the most important time in your life'. This statement by Lewis Wolpert, a leading developmental biologist, highlights the importance and sensitivity of this process. During gastrulation the three primary germ layers, the outer ectoderm, inner endoderm, and interstitial mesoderm, are produced. The process is sensitive due to the large amount of cell movement throughout the embryo, including invagination of bottle cells to form the primitive gut (Hardin and Keller, 1988).

We also selected embryos at NF stage 15 for NP exposure until NF stage 38. At NF stage 15, embryos undergo neurulation to form the neural tube. This is also a very sensitive stage of embryo development as the neural tube develops into the brain, spinal column and neural crest (Davidson and Keller, 1999). Due to the extended period of organogenesis, the central nervous system, in particular, is sensitive to teratogenic effects. Neural tube defects (NTDs) can occur during neuralation when the neural tube fails to close. Common NTDs include spinal bifida and anencephaly (Greene and Copp, 2014). Finally, *X. laevis* at NF stage 38 were selected for exposure to NPs until NF stage 45 (figure 4.4.0). For our aim, it is important to look at these

later stages of the embryo development, as there are key organs that have been developed after NF stage 38. By NF stage 38 the embryonic kidney is functioning with a fully formed glomus, which is the filtration device of the *X. laevis* pronephros, the pronephric tubules, which collects filtrate from the glomus, and the pronephric duct (Dressler, 2006). The primitive embryonic gut, formed during gastrulation, starts to elongate and rotate to form the epithelium-lined lumen of the gut coils at NF stage 41 through to NF stage 45. Later in *X. laevis* development, around NF stage 45, the liver bud differentiates and starts to display characteristics of hepatic tissue (Blitz et al., 2006). Therefore, embryos exposed to NPs at the tadpole stage (NF 38-45) are an embryonic *in vivo* system, which more accurately represents an adult system.

Embryos were exposed to a range of NP concentrations and left to develop until they had reached the required NF stage. After fixation, morphological scoring of a range of observed phenotypic abnormalities was carried out on 30 embryos per NP, concentration, and NF stage. Typical abnormalities recorded included edema, blistering, eye deformities, loss of melanocytes, loss of melanocyte migration, tail loss, stunted growth, axial defects (such as bent spine), degradation of tissue, and delayed development (figure 4.4.1). Grading of toxicity was based on these phenotypic abnormalities and embryos were scored as non-abnormal (healthy), abnormal (with phenotypic abnormalities), or dead.

After exposure to QDs, *X. laevis* showed severe abnormalities even at the lowest concentrations and dose dependant toxicity can be seen across all NF stages (figure 4.4.2, 4.4.3, and 4.4.4).

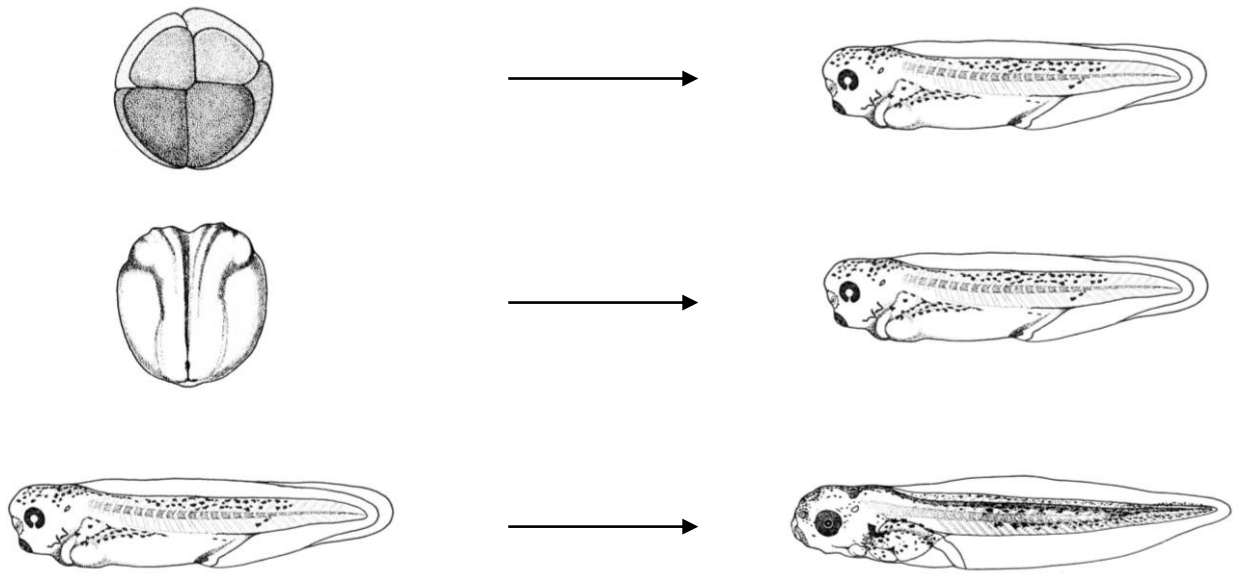

	Embryo at nanoparticle exposure	Embryo fixed
NF 4 – 38	NF 4: Eight cell	NF 38: Late tailbud
NF 15 – 38	NF 15: Undergoing neuralation	
NF 38 - 45	NF 38: Late tailbud	NF 45: Tadpole

Figure 4.4.0 Staging of *X. laevis* embryos. Cartoons depict *X. laevis* embryos during the different stages of normal development that we selected for NP treatment. Diagrams taken from Xenbase and *Xenopus laevis* staging is based on Nieuwkoop and Faber (1994) Normal Table of *Xenopus laevis* (Daudin).

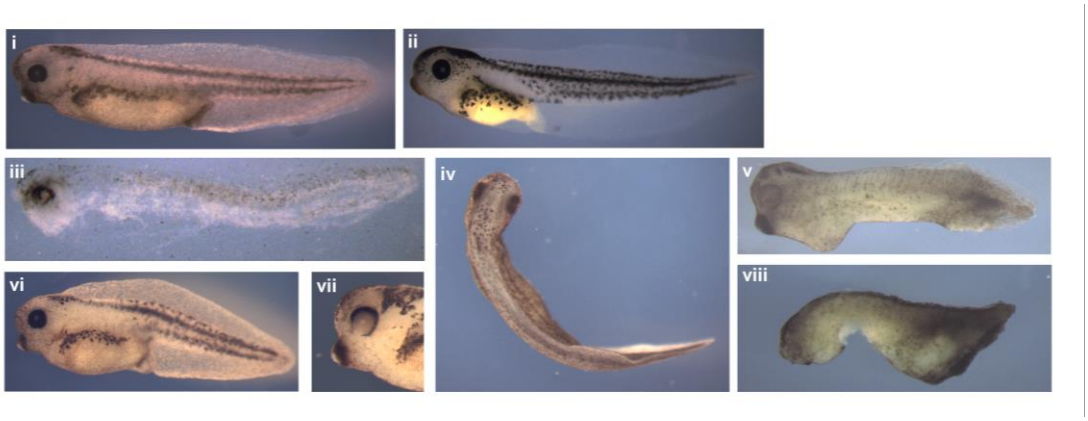

Figure 4.4.1 Examples of phenotypic abnormalities. Representative images of abnormalities observed in the *X. laevis* phenotypic assay; (i) NF stage 38 control embryo, (ii) NF stage 45 control embryo, (iii) embryo exposed to $10^{15.8}$ NP/ml QD at NF stage 38 and fixed at NF stage 45, showing embryo lethality and tissue degradation, (iv) dorsal view of *X. laevis* with bent tail, embryo fixed at NF stage 38 after exposure to $10^{14.2}$ NP/ml, (v and viii) *X. laevis* exposed to $10^{15.8}$ NP/ml QD at NF stage 4 and fixed when control embryos reached NF stage 38. Abnormalities include eye deformities, stunted growth/development, edema, blistering, and melanocyte deformities, (vi and vii) embryo exposed to $10^{14.2}$ NP/ml QD, abnormalities include stunted growth, bent spin, and loss of pigmentation in the eye.

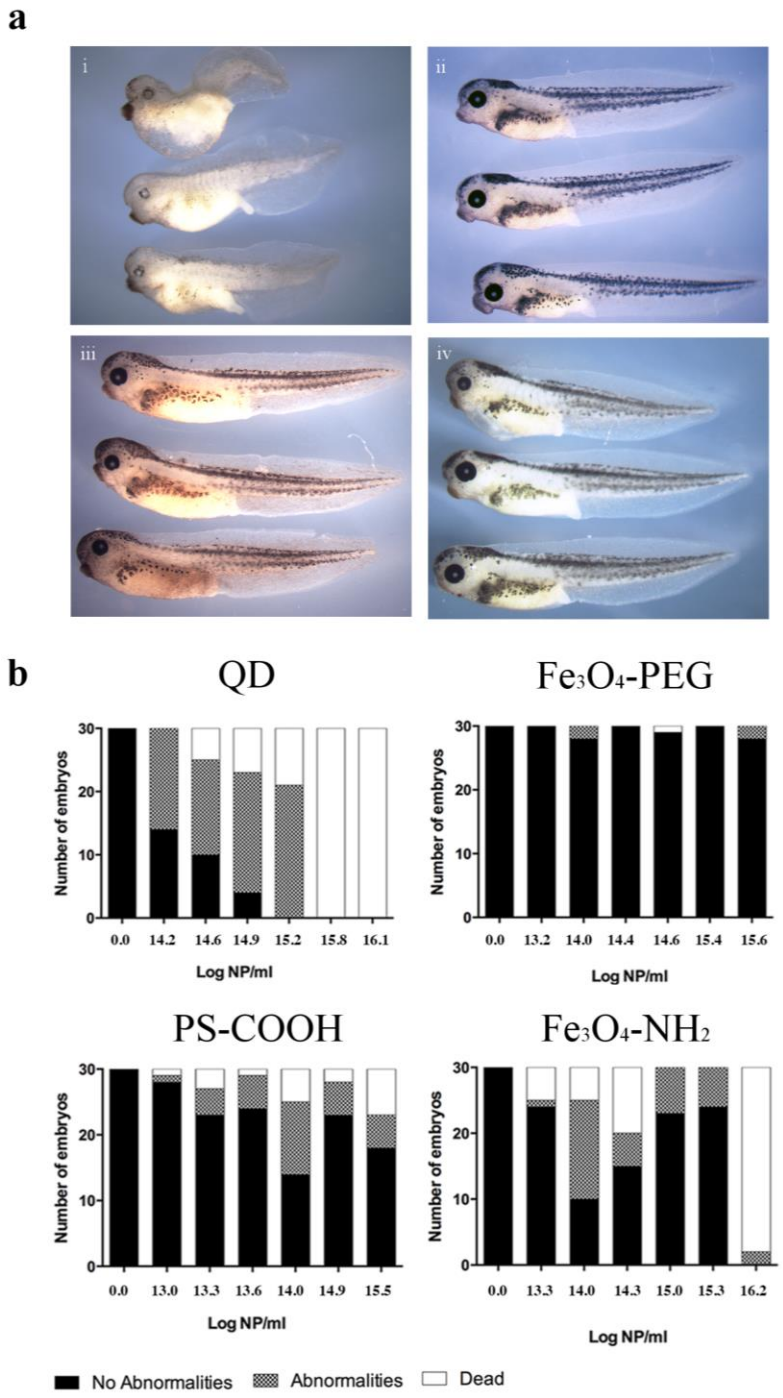

Figure 4.4.2. *X. laevis* phenotypic assay at NF 4 – 38. (a) Representative images of embryos selected at NF stage 4 and left to develop in $10^{15.8}$ NP/ml QD, $10^{15.6}$ NP/ml Fe_3O_4-PEG, $10^{15.5}$ NP/ml PS-COOH, and $10^{15.3}$ NP/ml Fe_3O_4-NH_2 NP solution until NF stage 38. After fixation embryos were imaged and analysed for any developmental abnormalities or death. (b) A total of 30 embryos were analysed for each concentration of NP to semi-quantify NP toxicity in *X. laevis.*

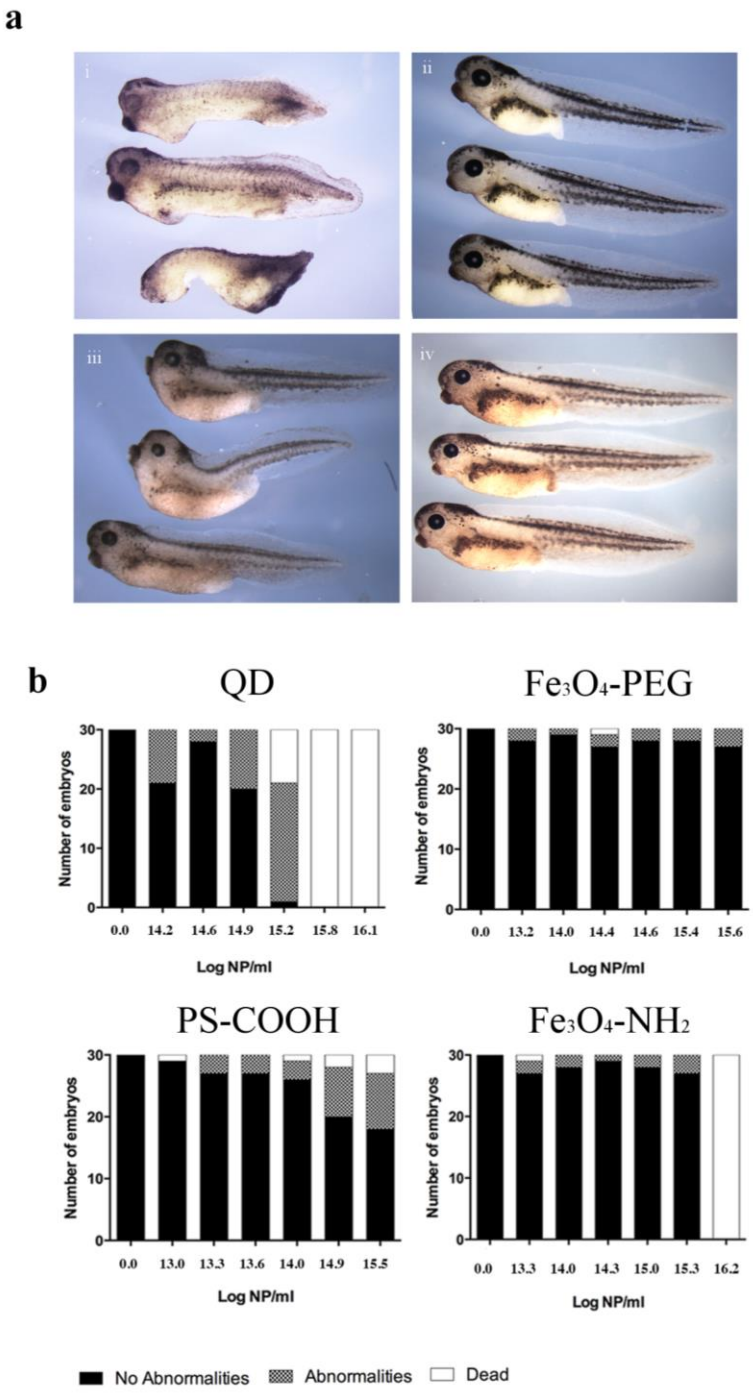

Figure 4.4.3. *X. laevis* phenotypic assay at NF 15 – 38. (a) Representative images of embryos selected at NF stage 15 and left to develop in $10^{15.8}$ NP/ml QD, $10^{15.6}$ NP/ml Fe_3O_4-PEG, $10^{15.5}$ NP/ml PS-COOH, and $10^{15.3}$ NP/ml Fe_3O_4-NH_2 NP solution until NF stage 38. After fixation embryos were imaged and analysed for any developmental abnormalities or death. (b) A total of 30 embryos were analysed for each concentration of NP to semi-quantify NP toxicity in *X. laevis.*

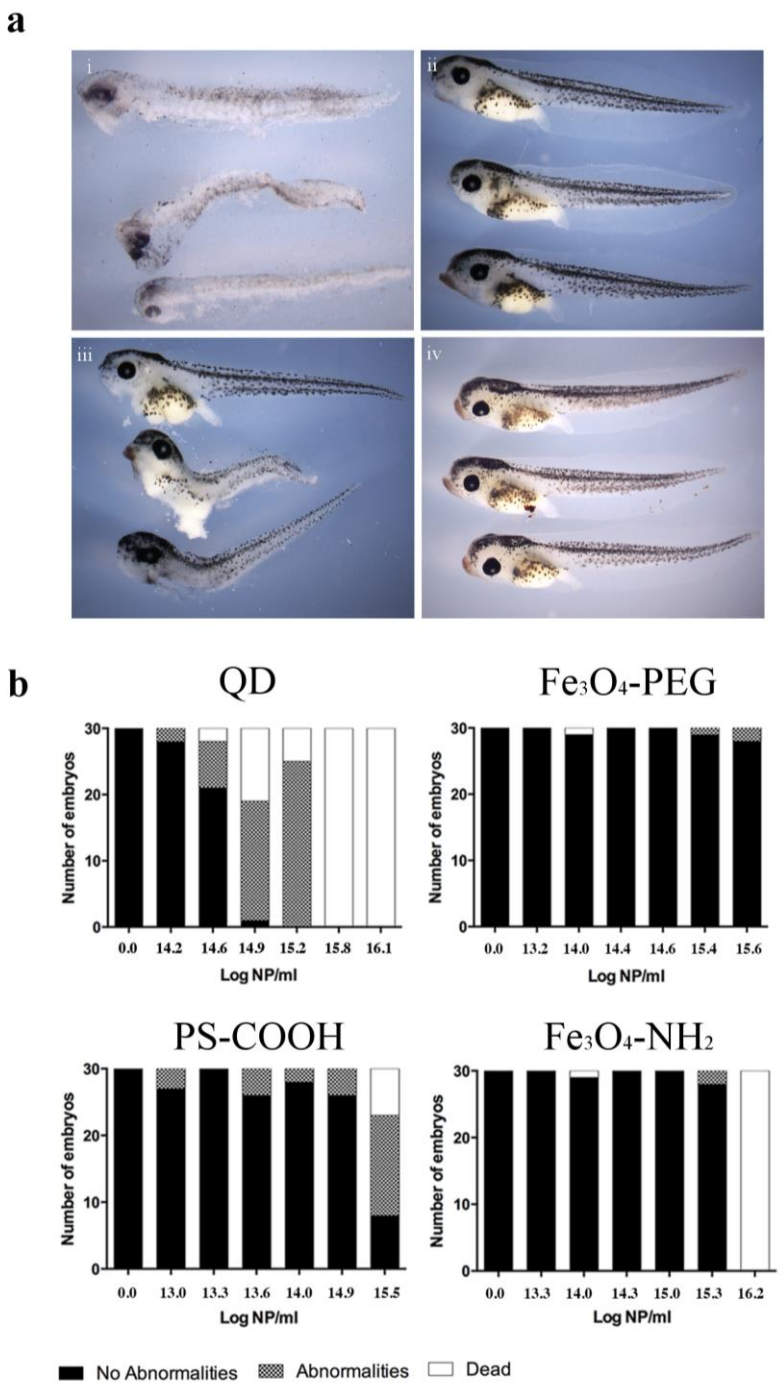

Figure 4.4.4. *X. laevis* phenotypic assay at NF 38 – 45. (a) Representative images of embryos selected at NF stage 38 and left to develop in $10^{15.8}$ NP/ml QD, $10^{15.6}$ NP/ml Fe_3O_4-PEG, $10^{15.5}$ NP/ml PS-COOH, and $10^{15.3}$ NP/ml Fe_3O_4-NH_2 NP solution until NF stage 45. After fixation embryos were imaged and analysed for any developmental abnormalities or death. (b) A total of 30 embryos were analysed for each concentration of NP to semi-quantify NP toxicity in *X. laevis.*

At QD concentrations in excess of $10^{15.2}$ NP/ml, all embryos were dead before reaching the selected NF stage, and there were clear signs of stunted growth, loss of melanocytes, eye deformities, and, in particular when exposed to late tailbud embryos (NF 38-45), tissue degradation. Embryo toxicity induced by QDs corresponded with QD toxicity in other mammalian developmental systems (Chan and Shiao, 2008), and with cytotoxicity data (figure 4.3.3). Fe_3O_4-PEG, the particle that we have synthesised for development into a theranostic NP, showed no toxic effects at any stage of *X. laevis* development. Fe_3O_4-NH_2 NPs showed limited toxicity with exposure to the embryos through gastrulation (NF 4-38), the most sensitive stage. At the highest concentration of $10^{16.2}$ NP/ml Fe_3O_4-NH_2 nearly all embryos of all stages were dead and aggregation of the NPs could be seen on the surface of the *X. laevis.* The toxicity of Fe_3O_4-NH_2 in *X. laevis*, at a concentration in excess of 10^{16} NP/ml, is in agreement with cytotoxicity data in the MDCK cell line. Interestingly, PS-COOH NPs, which showed no effect on cell viability by the *in vitro* assays (figure 4.3.2 and 4.3.3), but at the higher concentrations evaluated, $>10^{14}$ NP/ml, high toxicity was observed in the embryos at all stages. At lower concentrations, PS-COOH showed moderate toxicity, particularly when exposed to NF stage 4 embryos (figure 4.4.2).

4.5 Uptake of NPs in *X. laevis*

For Fe_3O_4-PEG and PS-COOH NPs, which showed limited or no toxicity, it was important to investigate uptake of the NPs in *X. laevis* embryos to negate that absence of toxicity was due to a lack of internalisation of the NPs and limited exposure to sensitive organs. NF stage 38 embryos were incubated in a solution of Fe_3O_4-PEG at a concentration of $10^{15.3}$ NP/ml. Once developed to NF stage 45, embryos were fixed

and sectioned (materials and methods 2.4.2 and 2.4.5) before analysis using TEM. Fe_3O_4-PEG NPs were found in both the embryo head sections (figure 4.5.1 b (i) and (ii)) and in the gut sections (figure 4.5.1 b (iii) and (iv)).

PS-COOH uptake was observed in embryos at NF stage 15-38 (figure 4.5.2 a-d) and in NF stage 38-45 (figure 4.5.2 e). Increase in fluorescence could be seen in fixed NF stage 38 embryos in a dose dependent manner (figure 4.5.2 a-d). Importantly, fluorescence was observed in internal structures of the embryo such as the primitive gut and somites, suggesting NP internalisation. Moreover, embryos exposed at NF stage 38 with 10^{15} PS-COOH NPs and anesthetised at NF stage 45, showed aggregates of fluorescent particles moving through the blood stream (movie; stills from movie in figure 4.5.2 e). Larger particle aggregates could be traced moving with the blood flow through the intersomitic blood vessels.

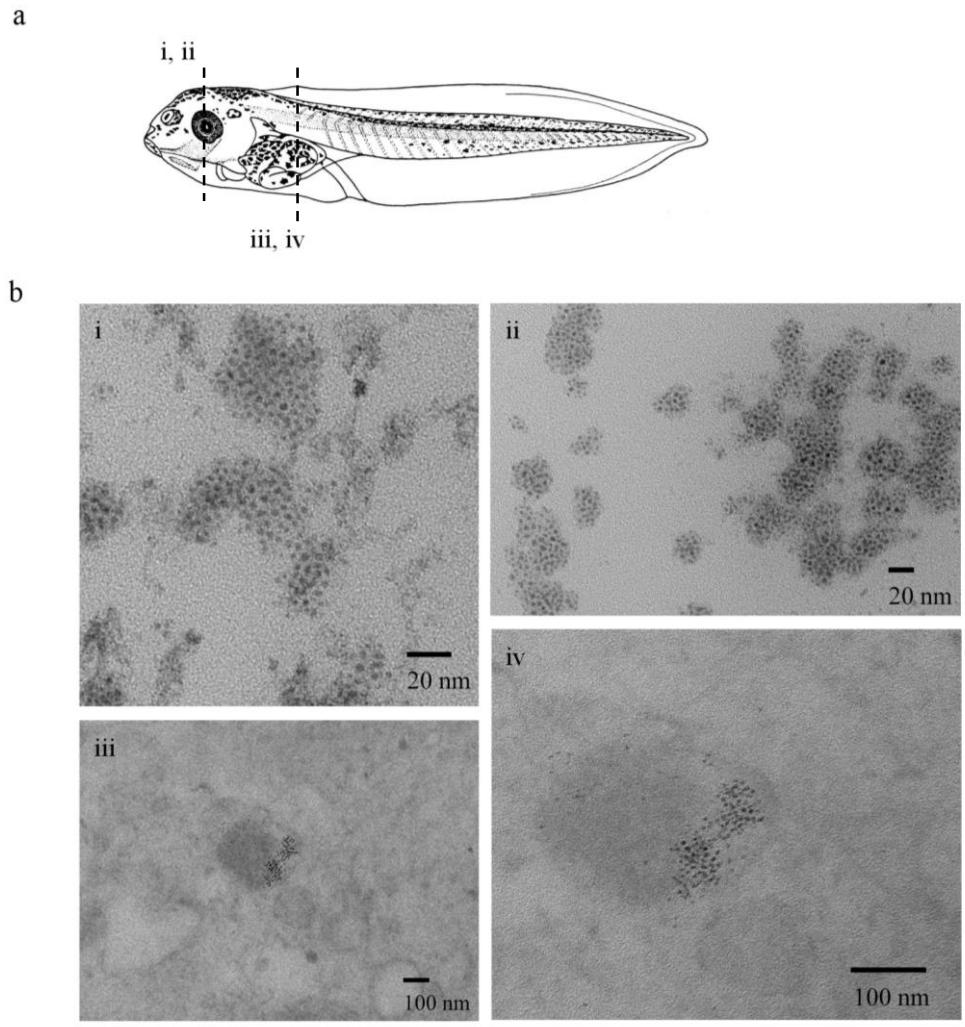

Figure 4.5.1 TEM analysis of Fe_3O_4-PEG uptake in *X. laevis*. (a) Sections were taken from the head and gut of the embryo. (b) Representative images of sections from the head (i, ii) and gut (iii, iv) of NF stage 45 embryos after exposure to $10^{15.3}$ NP/ml Fe_3O_4-PEG NPs at NF stage 38. Size bars as indicated.

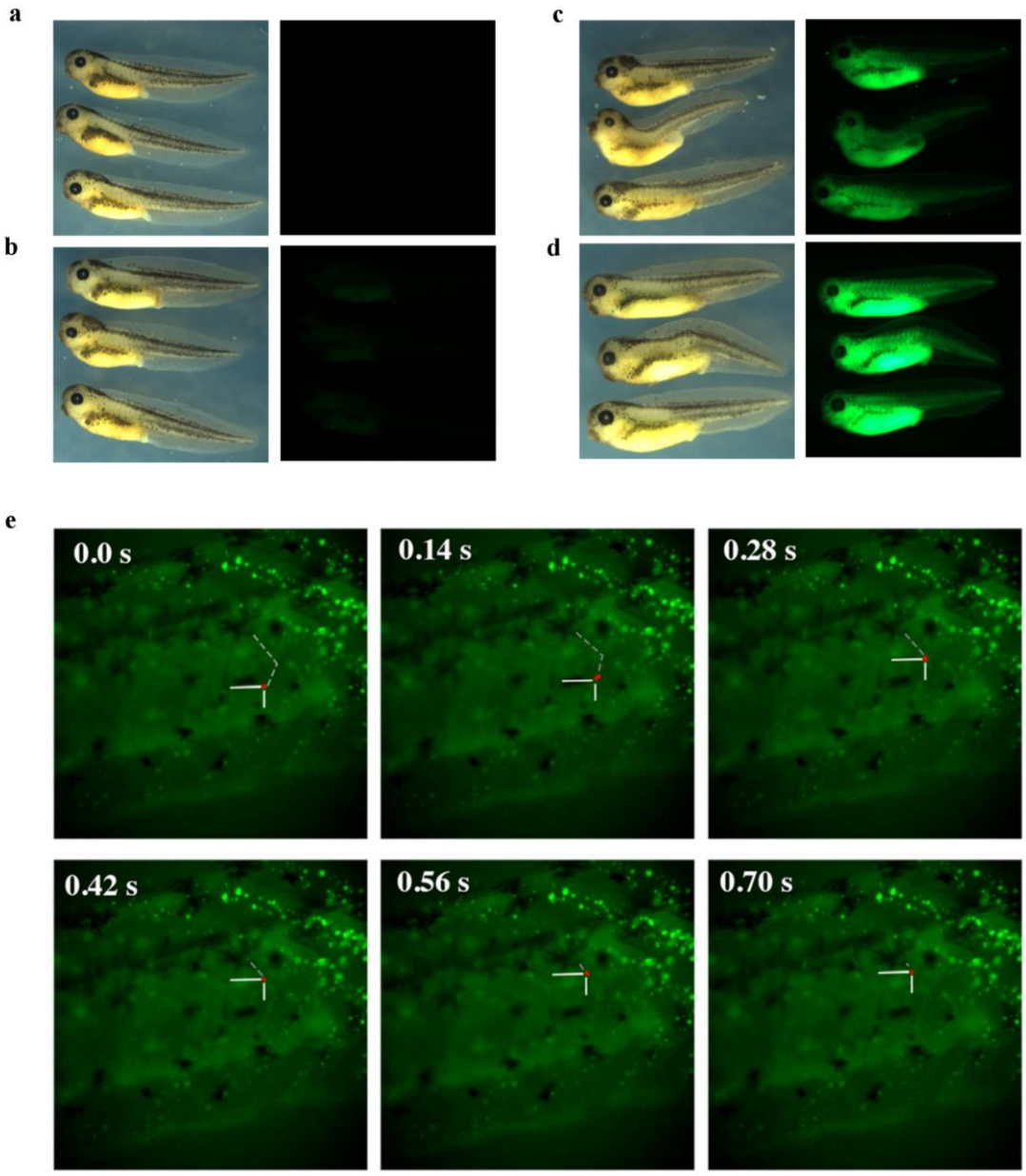

Figure 4.5.2 Fluorescent microscopy analysis of PS-COOH uptake in *X. laevis.* (a-d) *X. laevis* exposed to $10^{14.0}$ (b), $10^{14.9}$ (c), and $10^{15.5}$ (d) NP/ml PS-COOH at NF stage 15 and fixed at NF stage 38. 3 animals shown in each image. Control cells were vehicle treated (a). (e) Frame stills of live embryo movie exposed to $10^{15.5}$ NP/ml at NF stage 38 and imaged live at NF stage 45. Images show the movement of the NP aggregates (marked by the white lines) moving through the intersomitic blood vessel of a developing embryo over 0.70 s. Grey dashed line shows the NP trajectory around the somite.

4.6 Assessment of NP safety in a mammalian system.

After parallel *in vitro* and *X. laevis* phenotypic toxicity assays, in accordance with our protocol (figure 4.1.1), NPs that show low-to-no toxicity progress to further assessment in rodent models. Both Fe_3O_4-PEG and Fe_3O_4-NH_2 particles constituted as viable to progress to mouse toxicological assessment. To validate our toxicity assay, these NPs were sent to the Istituto di Ricerche Farmacologiche "Mario Negri" (IRCCS), in Milan to be administered in mice to assess toxicity effects on specific organs. For iron core NPs, biodistribution in murine target tissue can be easily seen via MRI analysis.

MRI analysis showed that in T2 weighed MRI coronal slices from epigastric and mesogastric regions, both iron oxide NPs accumulated in the liver and kidneys of the NP-treated animals compared to vehicle-treated controls (figure 4.6.1 a + b). Importantly, post-mortem histological sections from the tissues where these NPs accumulated (the liver and kidneys) demonstrated not only that the iron distribution (as assessed by Perl's staining) corroborated the MRI findings, but importantly also failed to reveal any evidence of morphological tissue toxicity (figure 4.6.1 c, 4.6.2), highlighting that these NPs exhibit little-to-no toxicity in mammalian tissues. These findings show that *X. laevis* embryos, in conjunction with cytotoxicity assessment, is a useful tool to predict NP safety prior to administration and further testing in mammalian models.

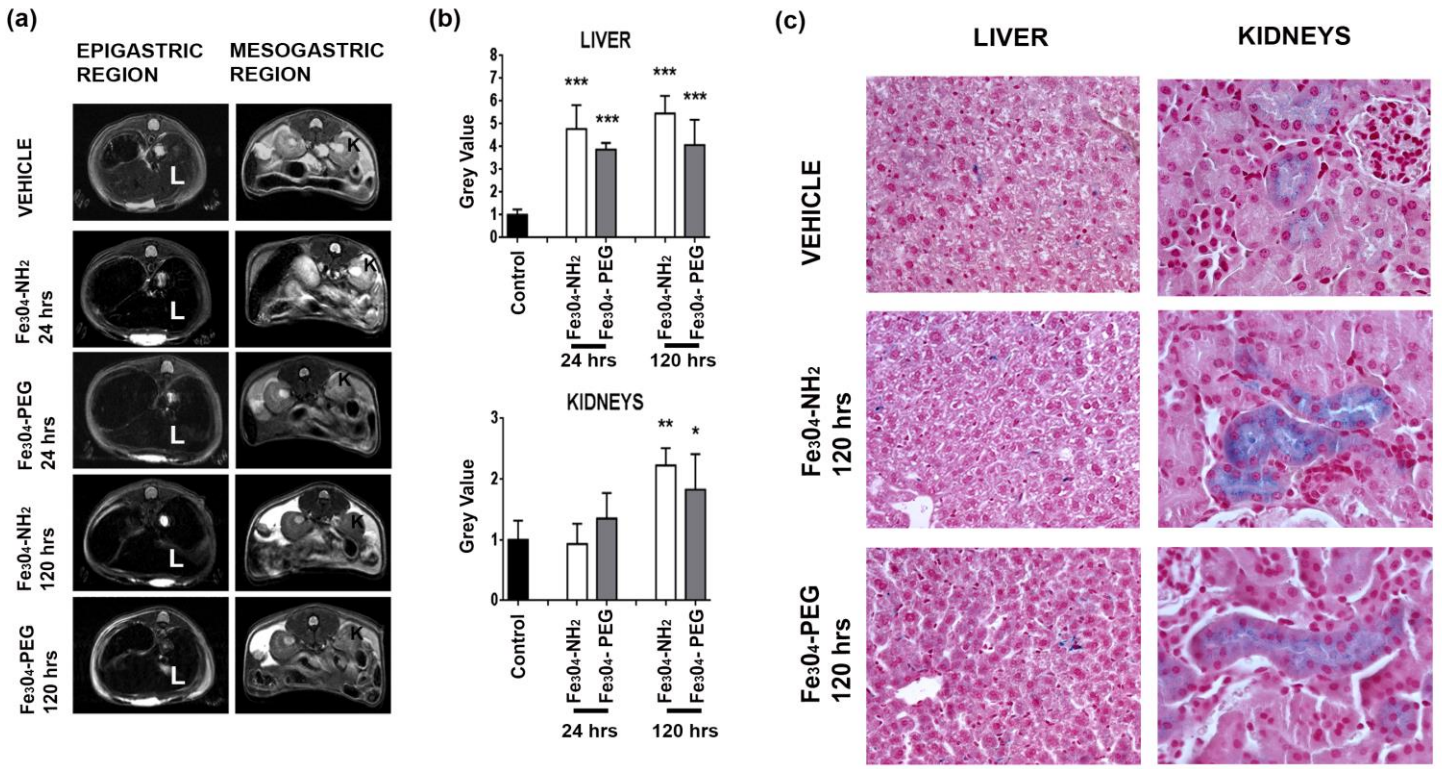

Figure 4.6.1 Assessment of iron oxide NPs in a mammalian model. (a) Representative MRI images showing coronal slices from treated mice corresponding to the epigastric (left column) and mesogatric region (right column). K, kidneys and L, liver (b) Histograms showing the grey levels in liver (upper panel) and kidney (lower panel) measured from vehicle- (black bars), Fe_3O_4-NH_2 NPs (white bars) and Fe_3O_4-PEG NPs treated mice (grey bars) at one or five days after NP administration. Data are expressed as mean ± S.D. * < 0.005; ** < 0.01, ***<0.0001 compared to the vehicle (Student's t-test). (c) Perl's stained tissue sections from target organs in treated animals. Tissues counter-stained with eosin. Representative images shown.

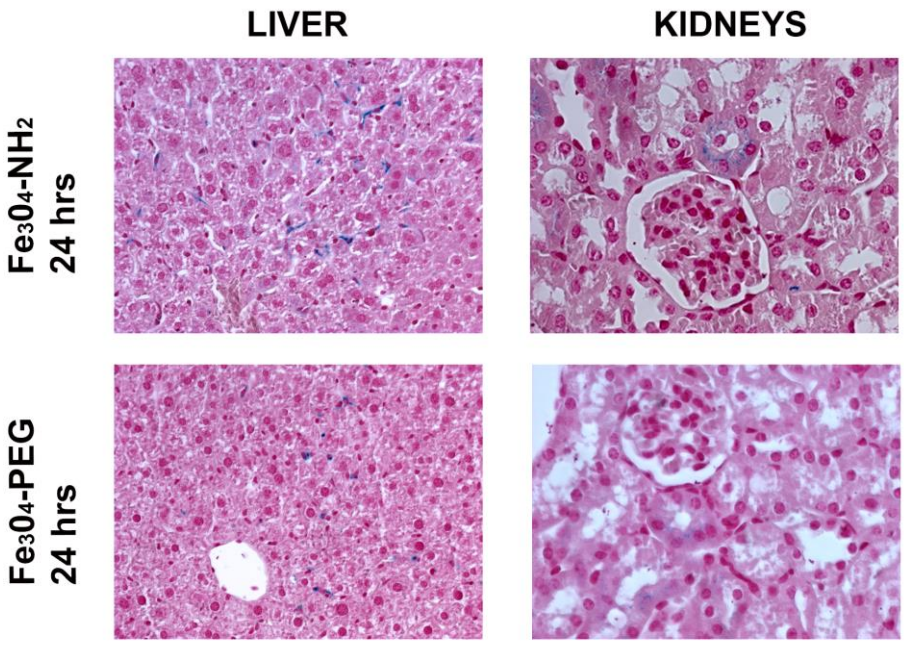

Figure 4.6.2 Comparison of Perl's staining for tissular iron in liver and kidneys of NP treated animals at 24 hrs post-injection.

4.7 Hazard scoring – Combining *in vitro* cytotoxicity with *X. laevis* phenotypic scoring

To compare the overall toxicity of a NP from both *in vitro* and *in vivo* assay data, hazard scores were given depending on assay parameters (table 4.7.1). For both Trypan Blue and MTT assays scoring was based on cell viability. At a given concentration, if the cell viability was >76% a hazard score of 0 was given; 50 – 75% cell viability equated to a hazard score of 1 (x); and <50% cell viability a hazard score of 2 (xx) was awarded. For the *X. laevis* phenotypic assays the hazard score was based on the percentage of healthy embryos, where embryos that were dead or with phenotypic abnormalities were considered unhealthy. A hazard score of 0 was given if >76% of the embryos were healthy; 50 – 75% healthy embryos produced a hazard score of 1 (x); and if there was < 50% healthy embryos then the highest hazard score of 2 (xx) was conferred.

For the cytotoxicity data the hazard score was taken from the mean cell viability in all cell lines from the highest NP concentration. For comparison, we took *X. laevis* analysis from the data produced from tadpole stage (NF stage 38-45) as NPs would be exposed to developed organs in the embryo and consequently more physiologically relevant to adult tissue.

There was a strong correlation between the *in vitro* and *in vivo* results obtained from the highly toxic QDs, with all assays leading to a hazard score of 2 (xx). For both iron core NPs, Fe_3O_4-PEG and Fe_3O_4-NH_2, a hazard score of 0 was given and, again, there was agreement with the cell based assays and the *X. laevis* phenotypic assay.

Table 4.7.1 Hazard score obtained from cell cytotoxicity and *X. laevis* phenotypic assays. Hazard score is based on the parallel analysis of cell viability and percentage healthy embryos.

Hazard	**Hazard Score**	**Cell Viability (%)**	**Healthy Embryo (%)**
0	0	>76	>76
x	1	50 – 75	50 – 75
xx	2	<50	<50

	X. laevis (NF 4-38)	***X. laevis (NF 15-38)***	***X. laevis (NF 38-45)***
QD	xx	xx	xx
PEG-Fe_3O_4	0	0	0
PS-COOH	x	x	xx
NH_2-Fe_3O_4	0	0	0

	MTT	**Trypan Blue**	***X. laevis (NF 38-45)***
QD	xx	xx	xx
PEG-Fe_3O_4	0	0	0
PS-COOH	0	0	xx
NH_2-Fe_3O_4	0	0	0

Interestingly, PS-COOH NPs did not reduce cell viability or produce levels of cleaved PARP-1; however, in the *X. laevis* phenotypic assay, toxicity was observed. After exposure at the early stages of embryo development, NF 4 and 15, a hazard score of 1 (x) was awarded. After exposure to the tailbud embryos, NF 38-45, a higher toxicity was observed and, as less than 50% of the embryos were deemed as healthy, a hazard score of 2 was given (xx). This suggests that using the *X. laevis* in parallel to traditional cytotoxicity assays early on in the development of a novel NP can help to identify false negatives produced by cell-based assays.

4.8 Discussion

Increasingly, there is a higher demand for the accurate assessment of NP toxicity. The increase in development of novel nanotherapeutics continues to rise at a considerable rate, and yet remarkably few are deemed safe for biomedical applications. Often nanotherapeutics undergo quick and easy cell-based toxicity assessments in the hope that this reveals potential toxicity of the NP. It is not until these novel NPs reach a more robust toxicological screening, such as in a rodent model, that the formulation is deemed unsafe; after considerable time and cost for development of the NP. As such, the need for animal models that can produce effective and accurate toxicity data, and act as a bridge between conventional *in vitro* cell-based assays and higher mammalian models, has been established here. Alternatives to the traditional 2D monoculture toxicity assays have been suggested, for example the development of 3D and co-culture *in vitro* cell-based models to mimic functions of living tissues (Lee et al., 2009). A key area of this is to assess nephrotoxicity, often seen in adverse drug responses, by producing 3D kidney tissue (Astashkina et al., 2014, Lee et al., 2009,

Movia et al., 2011, Muller et al., 2010, Pampaloni et al., 2007, Smalley et al., 2006). However, although this work has its place in nanotoxicology, tissue mimetic models fail to reproduce complete systemic interactions between different organ systems found in *in vivo* models.

Early vertebrate developmental models provide whole *in vivo* systems that can accurately assess NP toxicity after interaction with complete organ systems with the benefit of rapid and high-throughput potential. Early vertebrate developmental models, such as *Xenopus* and zebrafish, are available in research departments and provide a cheap alternative to rodent models. Specifically, *Xenopus* has the advantage of being physiologically relevant to mammals with organs that are typically affected in human diseases (skin, lymphatic system, nervous system, gastrointestinal tract, cardiovascular system, primitive kidneys, hepatic system, and circulatory system) (Wheeler and Liu, 2012). Moreover, at a time where there are initiatives to reduce the amount of higher vertebrate models, early stage *Xenopus* embryos do not require an animal licence to work on, and are described under EU directive as not protected as non-human vertebrate models. We have shown that large volumes of *X. laevis* embryos can be tested in multi-well formats, allowing multiple NPs at a large range of concentrations to be tested alongside each other; a feat which is impossible to achieve in higher vertebrate models. In this study, a 24-well format was used with each well containing 5 embryos. In each experiment, 10 embryos were analysed for each NP at each concentration, and the process repeated 3 times. With the control, over 800 embryos were analysed on the bench for each stage; over 2500 were analysed over all of the developmental stages (NF 4-38, 15-38, and 38-45). This high capacity of analysis can help to negate false results that may be seen when using small sample

sizes in higher vertebrate animal models, where it is too expensive, too time consuming, or unethical to use such large numbers.

Physico-chemical NP characterisation needs to be established in each assay buffer. Electrostatically stabilised NPs, QDs and Fe_3O_4-NH_2, were affected by the *X. laevis* embryo salt buffer MMR. In particular, Fe_3O_4-NH_2 NPs showed excessive aggregation in MMR at the highest concentration of $10^{16.2}$ NP/ml (figure 4.2.4), leading to precipitation. Limited toxicity can be seen at concentrations $<10^{16.2}$ NP/ml, whereas the majority of embryos die across all NF stages when exposed to the aggregated Fe_3O_4-NH_2 NPs at concentrations $> 10^{16.2}$ (figure 4.4.2, 4.4,3, and 4.4.4). This suggests the toxic effect is a result of colloidal instability rather than the nanomaterial itself. Moreover, Fe_3O_4-NH_2 NPs aggregate less in the presence of proteins from the RMPI + 10% FCS cell media. This correlates to a milder toxic effect in cells treated with Fe_3O_4-NH_2 (figure 4.3.2, 4.3.3), further suggesting instability of Fe_3O_4-NH_2 as the cause of toxicity rather than the material itself. This highlights how important it is to fully characterise NPs in assay buffers in order to understand NP behaviour *in vitro* and *in vivo.*

Cytotoxicity results were as expected from literature, with CdSe QDs causing dose dependant toxicity, and both PS-COOH and Fe_3O_4 core NPs showing low-to-no toxicity (Liu et al., 2013, Shiohara et al., 2004). Differences in *in vitro* toxicity could be observed across the cell lines. After MTT analysis, MDCK (non-cancerous cell line) appeared more sensitive to NP cytotoxicity than A549 and SK-MEL-28 (cancerous cell lines) (figure 4.3.3), highlighting the need to perform toxicity assessment in a range of cell lines. Robust immortalised cells are often used as the only initial screening of NP safety and these can lead to false negative results. This, in

part, goes some way in explaining the disparity between *in vivo* and *in vitro* results (Kroll et al., 2009).

Discounting the effects of aggregation seen at high concentrations of Fe_3O_4-NH_2, we saw a strong correlation between *in vitro* and *in vivo* results for all NPs tested. *X. laevis* phenotypic toxicity assessment was also in agreement with what has been reported in the literature, with CdSe QD material reported as toxic and iron oxide core showing low-to-no toxicity (Liu et al., 2013, Shiohara et al., 2004). There is some discrepancy with *in vitro* and *in vivo* results after treatment with PS-COOH. Cytotoxicity assessment shows no significant loss of cell viability after PS-COOH exposure measured by Trypan Blue and MTT assays (figure 4.3.2 and 4.3.3) and no cleaved PARP-1 was observed. However, phenotypic abnormalities and embryo death was observed at the higher PS-COOH NP concentrations. We found NF 4-35 staged embryos were particularly sensitive to PS-COOH (figure 4.4.2). This contradiction emphasises the need for an integrated *in vitro* and *in vivo* toxicity assessment to insure identification of false negatives. In fact, there is evidence to suggest that with PS-COOH NPs toxic effects may be seen due to carboxylic functionalisation of the polystyrene core and the interaction with plasma proteins (Clancy et al., 2010, Oslakovic et al., 2012).

Generally, in the *X. laevis* phenotypic assay NPs were more toxic to embryos exposed at early developmental time points (NF 4-38 and NF 15-38; figure 4.4.3 and 4.4.4), when the embryos were undergoing sensitive morphological changes. Although testing NP safety on these early stage embryos may not best assess toxicity to adult mammals, it can be adapted to evaluate teratogenesis. In literature, teratogenesis has been observed at both gastrula and neurala staged embryos after *X. laevis* embryos were microinjected with carboxyl functionalised nanodiamond NPs between NF stage

1 and 3 (Marcon et al., 2010). Other studies using metal oxide NPs (CuO, ZnO, etc.) have evaluated teratogenesis in *X. laevis* using the FETAX assay and reported major toxicity effects in the gastrointestinal tract (Nations et al., 2011). While FETAX focuseson the teratogenic effects to mid blastula stage embryos, we have demonstrated *X. laevis* as a versatile model that can be used to predict toxicity of nanomaterials beyond teratogenic effects. In our assessment, NF 38-45 would be more suitable than early stage embryos for use as a prognostic toxicity model as at NF 38 and beyond, the gills and mouth are open and the skin is more porous leading to possible respiratory and oral tract exposure (Dickinson and Sive, 2006). We have also demonstrated that NPs with different cores and functionalisation (Fe_3O_4 and PS-COOH NPs) are internalised by different staged *X. laevis* embryos (figure 4.5.1 and 4.5.2), and key internal organs were exposed to the NPs.

We have developed a scoring system that allows *X. laevis* embryos to be used as a rapid and simple model for NP-mediated toxicity assessment (figure 4.1.1). This scoring system has been integrated with the results from the cytotoxicity data to facilitate optimal prediction for the NP toxicity in mammalian systems (table 4.7.1). As both Fe_3O_4 core NPs predicated low-to-no toxicity after combined scores from cytotoxicity and *X. laevis* phenotypic assessment, we evaluated these NPs in rodent models to validate our model. As both PS-COOH and QDs caused toxicity *in vivo,* they did not progress to testing in a rodent model as per our described workflow (figure 4.1.1). Fe_3O_4 cored NPs (NH_2 and PEG functionalised) were injected intravenously into mice. MRI was used to assess bioaccumulation of the NPs and identify the organs exposed to NPs; mostly, iron oxide was found in the parenchyma of the kidneys and the liver. Histochemical staining of liver and kidney tissue confirmed the MRI results. Moreover, despite long-term accumulation of both iron cored NPs, no gross

histopathological defects were observed, demonstrating that there were no toxicological effects from the NPs in these organs. The results from intravenously injected mice validate our findings from the integrated toxicity protocol (figure 4.6.1 and 4.6.2). However, to better understand if *X. laevis* can be used in place of a rodent model, more comprehensive *in vivo* toxicity assays must be undertaken with known toxic NPs to understand the parallels with the *X. laevis* phenotypic assay and a rodent model; specifically, with NPs at a therapeutically relevant concentration range.

Overall, we have shown that *X. laevis* can be integrated alongside *in vitro* analysis to produce an accurate and effective screening tool for novel nanomaterials. This approach helps to bridge the gap between *in vitro* and *in vivo* analysis for nano-toxicity. We believe *Xenopus* is a readily available laboratory model that has a unique flexibility in regards to external embryo development, cost, embryo numbers, and ethical considerations. We have shown *X. laevis* can be easily integrated into a standardised toxicity assessment and, ultimately, will minimise the time and cost of using higher vertebrate toxicity models at an early stage in nanomaterial design. Further optimisation of the protocol could see it being used to identify bioaccumulation of NPs in *X. laevis* and gain information that contributes to a better understanding of new nanotherapies in whole organism systems (Webster et al., 2016).

4.9 References

Ahire, J. H., Behray, M., Webster, C. A., Wang, Q., Sherwood, V., Saengkrit, N., Ruktanonchai, U., Woramongkolchai, N. & Chao, Y. 2015. Synthesis of Carbohydrate Capped Silicon Nanoparticles and their Reduced Cytotoxicity, In Vivo Toxicity, and Cellular Uptake. *Adv Healthc Mater,* 4**,** 1877-86.

Anselmo, A. C. & Mitragotri, S. 2016. Nanoparticles in the Clinic. *Bioengineering & Translational Medicine***,** n/a-n/a.

Asharani, P. V., Lian Wu, Y., Gong, Z. & Valiyaveettil, S. 2008. Toxicity of silver nanoparticles in zebrafish models. *Nanotechnology,* 19**,** 255102.

Astashkina, A. I., Jones, C. F., Thiagarajan, G., Kurtzeborn, K., Ghandehari, H., Brooks, B. D. & Grainger, D. W. 2014. Nanoparticle toxicity assessment using an in vitro 3-D kidney organoid culture model. *Biomaterials,* 35**,** 6323-6331.

Bacchetta, R., Santo, N., Fascio, U., Moschini, E., Freddi, S., Chirico, G., Camatini, M. & Mantecca, P. 2012. Nano-sized CuO, TiO2 and ZnO affect Xenopus laevis development. *Nanotoxicology,* 6**,** 381-398.

Bargmann, C. I. 1998. Neurobiology of the Caenorhabditis elegans genome. *Science,* 282**,** 2028-2033.

Blitz, I. L., Andelfinger, G. & Horb, M. E. 2006. Germ layers to organs: Using Xenopus to study "later" development. *Seminars in Cell & Developmental Biology,* 17**,** 133-145.

Boisselier, E. & Astruc, D. 2009. Gold nanoparticles in nanomedicine: preparations, imaging, diagnostics, therapies and toxicity. *Chemical Society Reviews,* 38**,** 1759-1782.

Brenner, S. 1974. The genetics of Caenorhabditis elegans. *Genetics,* 77**,** 71-94.

Brigger, I., Dubernet, C. & Couvreur, P. 2012. Nanoparticles in cancer therapy and diagnosis. *Advanced drug delivery reviews,* 64**,** 24-36.

Carlson, C., Hussain, S. M., Schrand, A. M., Braydich-Stolle, L. K., Hess, K. L., Jones, R. L. & Schlager, J. J. 2008. Unique cellular interaction of silver nanoparticles: size-dependent generation of reactive oxygen species. *J Phys Chem B,* 112**,** 13608-19.

Chan, W. H. & Shiao, N. H. 2008. Cytotoxic effect of CdSe quantum dots on mouse embryonic development. *Acta Pharmacol Sin,* 29**,** 259-66.

Clancy, A. A., Gregoriou, Y., Yaehne, K. & Cramb, D. T. 2010. Measuring properties of nanoparticles in embryonic blood vessels: Towards a physicochemical basis for nanotoxicity. *Chemical Physics Letters,* 488**,** 99-111.

Coradeghini, R., Gioria, S., Garcia, C. P., Nativo, P., Franchini, F., Gilliland, D., Ponti, J. & Rossi, F. 2013. Size-dependent toxicity and cell interaction mechanisms of gold nanoparticles on mouse fibroblasts. *Toxicology Letters,* 217**,** 205-216.

Davidson, L. A. & Keller, R. E. 1999. Neural tube closure in Xenopus laevis involves medial migration, directed protrusive activity, cell intercalation and convergent extension. *Development,* 126**,** 4547-4556.

Derfus, A. M., Chan, W. C. W. & Bhatia, S. N. 2004. Probing the cytotoxicity of semiconductor quantum dots. *Nano Letters,* 4**,** 11-18.

Desai, N. 2012. Challenges in Development of Nanoparticle-Based Therapeutics. *The AAPS Journal,* 14**,** 282-295.

Di Silvio, D., Rigby, N., Bajka, B., Mayes, A., Mackie, A. & Baldelli Bombelli, F. 2015. Technical tip: high-resolution isolation of nanoparticle-protein corona complexes from physiological fluids. *Nanoscale,* 7**,** 11980-11990.

Dickinson, A. J. & Sive, H. 2006. Development of the primary mouth in Xenopus laevis. *Dev Biol,* 295**,** 700-13.

Dressler, G. R. 2006. The cellular basis of kidney development. *Annual Review of Cell and Developmental Biology,* 22**,** 509-529.

Fahmy, T. M., Samstein, R. M., Harness, C. C. & Mark Saltzman, W. 2005. Surface modification of biodegradable polyesters with fatty acid conjugates for improved drug targeting. *Biomaterials,* 26**,** 5727-36.

Filippi, C., Pryde, A., Cowan, P., Lee, T., Hayes, P., Donaldson, K., Plevris, J. & Stone, V. 2015. Toxicology of ZnO and TiO2 nanoparticles on hepatocytes: Impact on metabolism and bioenergetics. *Nanotoxicology,* 9**,** 126-134.

George, S., Xia, T. A., Rallo, R., Zhao, Y., Ji, Z. X., Lin, S. J., Wang, X., Zhang, H. Y., France, B., Schoenfeld, D., Damoiseaux, R., Liu, R., Lin, S., Bradley, K. A., Cohen, Y. & Nal, A. E. 2011. Use of a High-Throughput Screening Approach Coupled with In Vivo Zebrafish Embryo Screening To Develop Hazard Ranking for Engineered Nanomaterials. *ACS nano,* 5**,** 1805-1817.

Greene, N. D. & Copp, A. J. 2014. Neural tube defects. *Annual review of neuroscience,* 37**,** 221.

Guo, G. N., Liu, W., Liang, J. G., He, Z. K., Xu, H. B. & Yang, X. L. 2007. Probing the cytotoxicity of CdSe quantum dots with surface modification. *Materials Letters,* 61**,** 1641-1644.

Hardin, J. & Keller, R. 1988. The behaviour and function of bottle cells during gastrulation of Xenopus laevis. *Development,* 103**,** 211-230.

Heckman, K. L., Decoteau, W., Estevez, A., Reed, K. J., Costanzo, W., Sanford, D., Leiter, J. C., Clauss, J., Knapp, K. & Gomez, C. 2013. Custom cerium oxide nanoparticles protect against a free radical mediated autoimmune degenerative disease in the brain. *ACS nano,* 7**,** 10582-10596.

Hsieh, J.-H., Sedykh, A., Huang, R., Xia, M. & Tice, R. R. 2015. A data analysis pipeline accounting for artifacts in Tox21 quantitative high-throughput screening assays. *Journal of biomolecular screening,* 20**,** 887-897.

Hull, M., Kennedy, A. J., Detzel, C., Vikesland, P. & Chappell, M. A. 2012. Moving beyond mass: the unmet need to consider dose metrics in environmental nanotoxicology studies. *Environ Sci Technol,* 46**,** 10881-2.

Hussain, S. M., Hess, K. L., Gearhart, J. M., Geiss, K. T. & Schlager, J. J. 2005. In vitro toxicity of nanoparticles in BRL 3A rat liver cells. *Toxicol In Vitro,* 19**,** 975-83.

Ivask, A., Kurvet, I., Kasemets, K., Blinova, I., Aruoja, V., Suppi, S., Vija, H., Kakinen, A., Titma, T., Heinlaan, M., Visnapuu, M., Koller, D., Kisand, V. & Kahru, A. 2014. Size-Dependent Toxicity of Silver Nanoparticles to Bacteria, Yeast, Algae, Crustaceans and Mammalian Cells In Vitro. *Plos One,* 9.

Javle, M. & Curtin, N. 2011. The role of PARP in DNA repair and its therapeutic exploitation. *British journal of cancer,* 105**,** 1114-1122.

Joris, F., Manshian, B. B., Peynshaert, K., De Smedt, S. C., Braeckmans, K. & Soenen, S. J. 2013. Assessing nanoparticle toxicity in cell-based assays: influence of cell culture parameters and optimized models for bridging the in vitro-in vivo gap. *Chemical Society Reviews,* 42**,** 8339-8359.

Kasemets, K., Suppi, S., Mantecca, P. & Kahru, A. 2014. Charge and size-dependent toxicity of silver nanoparticles to yeast cells. *Toxicology Letters,* 229**,** S193-S194.

Kim, K. T., Zaikova, T., Hutchison, J. E. & Tanguay, R. L. 2013. Gold nanoparticles disrupt zebrafish eye development and pigmentation. *Toxicol Sci,* 133**,** 275-88.

Kim, T. H., Kim, M., Park, H. S., Shin, U. S., Gong, M. S. & Kim, H. W. 2012. Size-dependent cellular toxicity of silver nanoparticles. *Journal of Biomedical Materials Research Part A,* 100A**,** 1033-1043.

Kroll, A., Pillukat, M. H., Hahn, D. & Schnekenburger, J. 2009. Current in vitro methods in nanoparticle risk assessment: limitations and challenges. *Eur J Pharm Biopharm,* 72**,** 370-7.

Lanza, G. M., Winter, P. M., Caruthers, S. D., Hughes, M. S., Cyrus, T., Marsh, J. N., Neubauer, A. M., Partlow, K. C. & Wickline, S. A. 2006. Nanomedicine opportunities for cardiovascular disease with perfluorocarbon nanoparticles.

Leconte, I. & Mouche, I. 2013. Frog embryo teratogenesis assay on Xenopus and predictivity compared with in vivo mammalian studies. *Methods Mol Biol,* 947**,** 403-21.

Lee, J., Lilly, G. D., Doty, R. C., Podsiadlo, P. & Kotov, N. A. 2009. In vitro toxicity testing of nanoparticles in 3D cell culture. *Small,* 5**,** 1213-21.

Lin, M., Pei, H., Yang, F., Fan, C. & Zuo, X. 2013. Applications of gold nanoparticles in the detection and identification of infectious diseases and biothreats. *Advanced Materials,* 25**,** 3490-3496.

Liu, G., Gao, J. H., Ai, H. & Chen, X. Y. 2013. Applications and Potential Toxicity of Magnetic Iron Oxide Nanoparticles. *Small,* 9**,** 1533-1545.

Lovric, J., Bazzi, H. S., Cuie, Y., Fortin, G. R., Winnik, F. M. & Maysinger, D. 2005. Differences in subcellular distribution and toxicity of green and red emitting CdTe quantum dots. *J Mol Med (Berl),* 83**,** 377-85.

Marcon, L., Riquet, F., Vicogne, D., Szunerits, S., Bodart, J. F. & Boukherroub, R. 2010. Cellular and in vivo toxicity of functionalized nanodiamond in Xenopus embryos. *Journal of Materials Chemistry,* 20**,** 8064-8069.

Mohan, N., Chen, C. S., Hsieh, H. H., Wu, Y. C. & Chang, H. C. 2010. In Vivo Imaging and Toxicity Assessments of Fluorescent Nanodiamonds in Caenorhabditis elegans. *Nano Letters,* 10**,** 3692-3699.

Monteiro-Riviere, N. A., Inman, A. O. & Zhang, L. W. 2009. Limitations and relative utility of screening assays to assess engineered nanoparticle toxicity in a human cell line. *Toxicol Appl Pharmacol,* 234**,** 222-35.

Mornet, S., Vasseur, S., Grasset, F. & Duguet, E. 2004. Magnetic nanoparticle design for medical diagnosis and therapy. *Journal of Materials Chemistry,* 14**,** 2161-2175.

Mosmann, T. 1983. Rapid colorimetric assay for cellular growth and survival: application to proliferation and cytotoxicity assays. *Journal of immunological methods,* 65**,** 55-63.

Mouche, I., Malesic, L. & Gillardeaux, O. 2011. FETAX assay for evaluation of developmental toxicity. *Methods Mol Biol,* 691**,** 257-69.

Movia, D., Prina-Mello, A., Bazou, D., Volkov, Y. & Giordani, S. 2011. Screening the Cytotoxicity of Single-Walled Carbon Nanotubes Using Novel 3D Tissue-Mimetic Models. *ACS nano,* 5**,** 9278-9290.

Muller, L., Riediker, M., Wick, P., Mohr, M., Gehr, P. & Rothen-Rutishauser, B. 2010. Oxidative stress and inflammation response after nanoparticle exposure: differences between human lung cell monocultures and an advanced three-dimensional model of the human epithelial airways. *Journal of the Royal Society Interface,* 7**,** S27-S40.

Nations, S., Long, M., Wages, M., Canas, J., Maul, J. D., Theodorakis, C. & Cobb, G. P. 2011. Effects of ZnO nanomaterials on Xenopus laevis growth and development. *Ecotoxicology and environmental safety,* 74**,** 203-210.

Nel, A., Xia, T., Madler, L. & Li, N. 2006. Toxic potential of materials at the nanolevel. *Science,* 311**,** 622-627.

Oberdorster, G., Oberdorster, E. & Oberdorster, J. 2005. Nanotoxicology: An emerging discipline evolving from studies of ultrafine particles. *Environmental Health Perspectives,* 113**,** 823-839.

Oslakovic, C., Cedervall, T., Linse, S. & Dahlback, B. 2012. Polystyrene nanoparticles affecting blood coagulation. *Nanomedicine,* 8**,** 981-6.

Pampaloni, F., Reynaud, E. G. & Stelzer, E. H. K. 2007. The third dimension bridges the gap between cell culture and live tissue. *Nature Reviews Molecular Cell Biology,* 8**,** 839-845.

Qiao, R. R., Yang, C. H. & Gao, M. Y. 2009. Superparamagnetic iron oxide nanoparticles: from preparations to in vivo MRI applications (vol 19, pg 6274, 2009). *Journal of Materials Chemistry,* 19**,** 9286-9286.

Shiohara, A., Hoshino, A., Hanaki, K., Suzuki, K. & Yamamoto, K. 2004. On the cyto-toxicity caused by quantum dots. *Microbiol Immunol,* 48**,** 669-75.

Smalley, K. S., Lioni, M. & Herlyn, M. 2006. Life isn't flat: taking cancer biology to the next dimension. *In Vitro Cell Dev Biol Anim,* 42**,** 242-7.

Strober, W. 2001. Trypan blue exclusion test of cell viability. *Curr Protoc Immunol,* Appendix 3**,** Appendix 3B.

Tewari, M., Wolf, F. W., Seldin, M. F., O'shea, K. S., Dixit, V. M. & Turka, L. A. 1995. Lymphoid expression and regulation of A20, an inhibitor of programmed cell death. *J Immunol,* 154**,** 1699-706.

Tomlinson, M. L., Hendry, A. E. & Wheeler, G. N. 2012. Chemical genetics and drug discovery in Xenopus. *Methods Mol Biol,* 917**,** 155-66.

Venditto, V. J. & Szoka, F. C. 2013. Cancer nanomedicines: So many papers and so few drugs! *Advanced drug delivery reviews,* 65**,** 80-88.

Walczyk, D., Bombelli, F. B., Monopoli, M. P., Lynch, I. & Dawson, K. A. 2010. What the Cell "Sees" in Bionanoscience. *Journal of the American Chemical Society,* 132**,** 5761-5768.

Wang, H. H., Wick, R. L. & Xing, B. S. 2009. Toxicity of nanoparticulate and bulk ZnO, Al2O3 and TiO2 to the nematode Caenorhabditis elegans. *Environmental Pollution,* 157**,** 1171-1177.

Webster, C. A., Di Silvio, D., Devarajan, A., Bigini, P., Micotti, E., Giudice, C., Salmona, M., Wheeler, G. N., Sherwood, V. & Bombelli, F. B. 2016. An early developmental vertebrate model for nanomaterial safety: bridging cell-based and mammalian toxicity assessment. *Nanomedicine (Lond),* 11**,** 643-56.

Wheeler, G. N. & Brändli, A. W. 2009. Simple vertebrate models for chemical genetics and drug discovery screens: Lessons from zebrafish and Xenopus. *Developmental Dynamics,* 238**,** 1287-1308.

Wheeler, G. N. & Liu, K. J. 2012. Xenopus: an ideal system for chemical genetics. *Genesis,* 50**,** 207-18.

Zou, H., Zhang, Q. W., Xing, M. L., Gao, X. J., Zhou, L. F., Tollerud, D. J., Tang, S. C. & Zhang, M. B. 2015. Relationships between number, surface area, and mass concentrations of different nanoparticles in workplaces. *Environmental Science-Processes & Impacts,* 17**,** 1470-1481.

Chapter 5.

Development of a targeted nanoparticle drug delivery system for the treatment of metastatic melanoma

5. Development of a targeted nanoparticle drug delivery system for the treatment of metastatic melanoma

5.1 Introduction

Incidence rates of metastatic melanoma have been increasing rapidly over the past four decades and, as a result, is increasing faster than any other form of cancer (Lens and Dawes, 2004). Melanoma is the ninth most common cancer in Europe and the 19th most common cancer worldwide (Bombelli et al., 2014). Prognosis is generally good if diagnosed early and can be cured by surgery before the tumour has invaded. However, if the melanoma has metastasised and the tumours are unresectable, long-term prognosis is poor. Once the tumour has developed into a late-stage metastatic disease, there are limited successful therapeutic options. Unresectable metastatic melanoma has a 3-year overall survival rate of less than 15% with conventional treatments (Balch et al., 2009).

Increased understanding of the molecular mechanisms of melanoma cells has led to the development of novel targeted therapies. Recently, new drugs have shown promising results in clinical trials (Chapman et al., 2011, Hodi et al., 2010, Robert et al., 2011). Amongst these are the FDA approved BRAF inhibitors dabrafenib and vemurafenib (Carrera et al., 2015, Kainthla et al., 2014, Roos et al., 2014). Approximately 50% of melanoma contain abhorrent BRAF production leading to cell survival, proliferation, differentiation, and migration (Sullivan and Flaherty, 2011). BRAF is a component of the mitogen-activated protein kinase (MAPK) signal transduction cascade (figure 5.1.1).

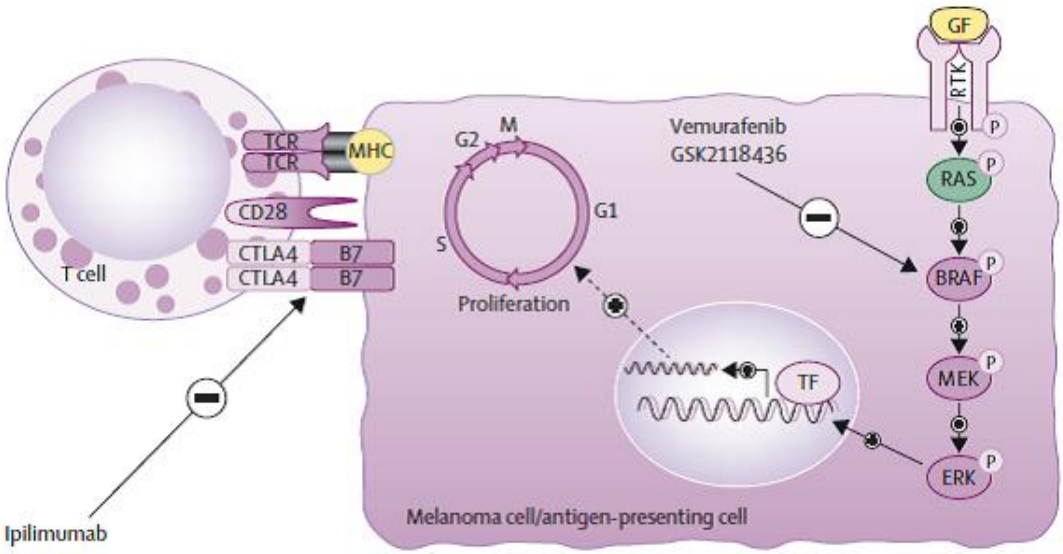

Figure 5.1.1 Current targeted immunotherapies for the treatment of metastatic melanoma. As BRAF is mutated in approximately 50% of metastatic melanomas, there is a lot of research into inhibitors for the MAP kinase signalling pathway. FDA approved vemurafenib and dabrafenib inhibit the mutant BRAF kinase and selumetinib inhibits MEK kinase to block transcription factor (TF) activation for continued proliferation. Ipilimumab is a monoclonal antibody that inhibits cytotoxic T lymphocyte antigen (CTLA-4) to increase T cell activity with the tumour tissue. CTLA-4 signalling inhibits T cell activation after binding to antigen presenting cells (Bombelli et al., 2014).

Upon activation of receptor tyrosine kinases (RTKs) by extracellular stimuli, RAS, a small G protein, is activated by phosphorylation. Sequential activation of BRAF and MEK follows, eventually leading to the phosphorylation of ERK which, in turn, is able to activate several transcription factors (Shaul and Seger, 2007). Abhorrent expression of the MAPK signalling pathway molecules can lead to uncontrolled activation of these transcription factors; if this is the case, drugs are designed to specifically inhibit the actions of mutated proteins (Roberts and Der, 2007). Both dabrafenib and vemurafenib inhibit the BRAF protein to reduce cell growth and division and are approved for use in late-stage, unresectable melanoma with $BRAF^{V600E}$ mutation (figure 5.1.1). However, these therapies are restricted to patients with $BRAF^{V600E}$ mutations and are not applicable to ~ 50% of melanoma suffers. MEK inhibitors are amongst the most promising new targeted therapeutics; trametinib is approved for use in BRAF mutated patients that have metastasised melanoma that cannot be removed by surgery (Robert et al., 2015) and selumetinib is in phase 3 clinical trials (NCT01974752; (Carvajal et al., 2014).

Immunotherapy is a treatment option that aims to increase the activity of a patient's immune system in order to fight cancer cells (Ito and Chang, 2013). Ipilimumab is an immunotherapy that inhibits cytotoxic T lymphocyte antigen (CTLA-4) (Acharya and Jeter, 2013). CTLA-4 is a receptor expressed on the surface of T cells and is a negative regulator of T cell activation. Once CTLA-4 is inhibited by ipilimumab, T cell activity in the tumour is enhanced (Keilholz, 2008). Other targets are being investigated to disrupt other immune checkpoints. Currently, there are several immunotherapies in clinical trials, which aim to inhibit programmed cell death-1 (PD-1) in patients with melanoma (NCT02626065, NCT02676869, NCT02335918, NCT01176474). PD-1 is an immunoinhibitory receptor which

suppresses T-cell growth, survival, and effector responses. Inhibiting PD-1 results in an increase in immune response to in the tumor environment (Parry et al., 2005). In clinical trials, anti-PD-1 therapies induced a greater response compared to chemotherapies and kinase inhibitors (Brahmer et al., 2012, Topalian et al., 2012). In contrast to CTLA-4 inhibition, anti-PD-1 therapies produce a less aggressive autoimmune response in patients (Zitvogel and Kroemer, 2012).

Despite the development of novel targeted therapeutics for melanoma and their promise in patients, they are restricted by their low response and high relapse rates due to the formation of drug resistant tumour cell populations. Partial and complete regression after treatment with ipilimumab was reported in patients with stage IV melanoma previously untreated (Schartz et al., 2010). Drug resistant populations of melanoma have also been observed after treatment with Vemurafenib. Although there is an initial regression of the tumour after Vemurafenib administration, most patients relapse with lethal drug-resistant form of melanoma (Das Thakur et al., 2013). As a result, work must be done to develop novel drugs capable of targeting different pathways to eradicate the tumour before drug resistance occurs and that provide higher response rates. As previously discussed (section 1.3), working in the nanoscale provides many advantages to the drug delivery of cancer therapeutics (Bombelli et al., 2014). Amongst these advantages is the ability of a NP drug delivery system to passively and actively target a tumour and a specific cell type. A targeted NP can be developed to act as both a therapeutic and a diagnostic tool (termed theranostic). A further advantage is the possibility to encapsulate multiple drugs to greatly improve patient response and bypass drug resistance.

Several nanotherapeutics have been developed for unresectable melanomas. Albumin-stabilised paclitaxel nanoparticles (NPs) are in phase II clinical trials

(NCT00081042, NCT00738361) and have improved progression free survival rates. Paclitaxel is a general cytotoxic chemotherapeutic used for the treatment of several cancers which targets the cytoskeleton of the cell, specifically tubulin, to trigger cell death (Arnal and Wade, 1995). Although a potent anti-cancer drug, paclitaxel is limited by the serious side-effects it causes. This is partly due to the toxicity of the polyethoxylated castor oil used as a carrier. Abraxane is an FDA approved NP albumin-bound paclitaxel, which negates the need for polyethoxylated castor oil as a carrier and decreasing the systemic toxicity of the drug (Wang et al., 2013).

More specific therapeutics have been added to paclitaxel for a more effective treatment. Albumin stabilised paclitaxel NPs in combination with carboplatin (NCT00404235; (Kottschade et al., 2011, Perez et al., 2009), vascular endothelial growth factor (VEGF) inhibitors (NCT00462423; (Miller et al., 2007), and a combination of both VEGF inhibitors with carboplatin (NCT00626405; (Kottschade et al., 2013) have all improved overall survival rates in melanoma patients.

NPs have numerous advantages as a drug delivery system in oncology (section 1.3). NPs in a certain size range can exploit the leaky vasculature and the poor lymphatic drainage of the tumour environment. Passive accumulation of NPs in the tumour due to this physiology is known as the enhanced permeability and retention (EPR) effect (Brigger et al., 2012). Furthermore, NPs can be functionalised to target cell types to deliver drugs specifically and reduce systemic toxicity (Wang and Thanou, 2010). There are several targeting options for melanoma nanotherauptics. Aminopeptidase N (CD13) (Chen et al., 2010), fibrin-fibronectin (Simberg et al., 2007), neuropilin (Sugahara et al., 2009), and integrins (Hood et al., 2002), are all associated with upregulation in the tumour cell vasculature. Laminin is expressed on the surface of melanoma cells and upregulated during invasion and metastasis (Sarfati

et al., 2011). A promising target is to take advantage of the upregulation of the melanin pigmentation signalling pathway. Melanocortin-1 receptor (MC1R) is expressed on the cell surface of melanocytes (Suzuki et al., 1996). In normal human melanocytes expression of MC1R is restricted to a few hundreds of molecules on the cell surface (Donatien et al., 1992), but it is upregulated on > 80% of melanoma cells (Cai et al., 2005).

MC1R is a one of five melanocortin receptors (MC1R-MC5R) which are G-protein-coupled receptors (GPCR). Melanocortins have a wide range of physiological roles and are expressed in different tissues; MC1R in the skin and hair (Garcia-Borron et al., 2005), MC2R in the adrenal glands (Almeida et al., 2014), MC3R and MC4R in the hypothalamus (Millington, 2007), and MC5R in the kidneys (Tafreshi et al., 2013). Ordinarily, MC1R is predominantly a regulator of melanogenesis (Suzuki et al., 1996) upon binding of the peptide agonist α-melanocyte stimulating hormone (α-MSH). Ligand binding results in upregulation of cAMP, converted from cytoplasmic ATP by the intracellular messenger adenylyl cyclase (AC). In turn, cAMP activates protein-kinase A (PKA), which translocates to the nucleus. At the nucleus, PKA phosphorylates cAMP-response-element binding protein (CREB) transcription factors. CREB binds to the CRE region at promoter sites upstream of key genes to activate expression. Microphthalmia-associated transcription factor (MITF) is a transcription factor that is activated by CREB (Chin, 2003); figure 5.1.2). MITF activates tyrosinase, the rate-limiting enzyme in melanogensis. MITF also plays a pivotal role in melanoma oncogenesis (Levy et al., 2006).

MC1R contains small extracellular loops (Ringholm et al., 2004), which are thought to play a role in increasing binding affinity and ligand recognition of MC1R agonists (Chhajlani et al., 1996). The ligand-binding site of MC1R is contained in the

transmembrane fragments of the receptor where there is a region of highly charged aromatic residues containing Glu94 in transmembrane region 2, Asp117 and Asp 121 both in transmembrane region 3. The Arg residue of the α-MSH pharmacophore core (His-Phe-Arg-Trp) binds to these MC1R transmembrane regions (Haskell-Luevano et al., 1996, Prusis et al., 1995, Prusis et al., 1997).

Other melanocortin agonists, including α-, β-, γ-MSH, and the adrenocorticotropic hormone (ACTH), contain the same pharmacophore core. Due to this high degree of homology between the agonists, there is difficulty in designing a ligand that is highly specific for MC1R alone. The synthetic analogue of α-MSH, Nle4-D-Phe7 (NDP-MSH) has been demonstrated to be selective ligand for MC1R. Moreover, it is more potent than native α-MSH and is resistant to degradation (Hadley et al., 1985, Sawyer et al., 1980).

In this study, Fe_3O_4-α-MSH NP (Fe_3O_4-PEP; developed in chapter 3) functionalised with the NDP-MSH analogue will be used to actively target MC1R on the surface of melanoma cells and specifically deliver a combination of the MEK inhibitor selumetinib and the cytotoxic drug paclitaxel. One of the main challenges when using cultured cells for molecular biology is the presence of cell culture artefacts and lack of heterogeneity compared to the *in vivo* situation. It is widely reported that the genome of cultured cells varies greatly from primary cells and tends to be more uniform. Traditional monolayer culture systems often fail to reproduce *in vivo* conditions and have an altered gene expression (Bork et al., 2010). This lack of stability in the expression of genes can produce false results in molecular biology techniques such as Western Immunoblotting. When producing a targeted therapy, it is important to understand the target cell as close to *in vivo* as possible. To this end, we

have developed a novel protocol to isolate melanoma cells directly from resected tissue from patients with suspected metastatic melanoma.

In this chapter, MC1R was found to be expressed in melanoma cell lines and over expressed in malignant melanoma. The targeted Fe_3O_4-PEP NP, containing the MC1R ligand α-MSH, was taken up more readily in melanoma cells than the non-targeted Fe_3O_4-PEG NP. The chemotherapeutic drug, PTX, was encapsulated into the Fe_3O_4-PEG/Fe_3O_4-PEP system. Moreover, Fe_3O_4 NPs successfully delivered PTX to melanoma cells leading to cell death.

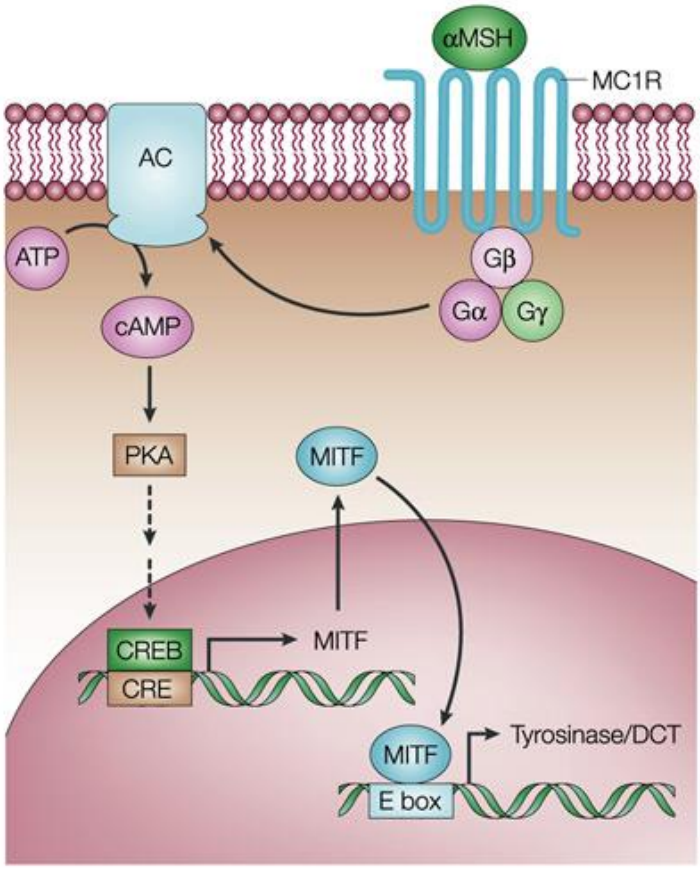

Figure 5.1.2 MC1R signalling pathway. Upon binding of the agonist α-MSH, the heterotrimeric G-protein complexes down stream of MC1R activate AC. AC catalyses the conversion of cytoplasmic ATP to cyclic AMP (cAMP). In turn, cAMP activates PKA. After translocation to the nucleus, PKA phosphorylates the transcription factor CREB. Upon binding to CRE, CREB promotes the expression of several genes. A key target for CREB is the transcription factor MITF. Expression of MITF activates tyrosinase, the rate-limiting enzyme in melanogenesis (Chin, 2003).

5.2 MC1R expression in melanoma

Expression levels of MC1R mRNA have previously been analysed using the microarray dataset GDS1375 from the NCBI Gene Expression Omnibus database (Edgar et al., 2002) (figure 5.2.1.a. Sherwood unpublished). The samples were regarded as normal skin, benign nevi, and melanoma. Compared to normal and benign data sets there was a significant increase in MC1R mRNA expression levels in the melanoma tissue.

Western Immunoblotting was used to confirm the presence of MC1R protein in melanoma and melanocyte cell lines. M202, M229, M285, A375, and SK-MEL-28 melanoma cells, and HEMA-lp melanocyte cells all had MC1R protein expression. HEMA-lp MC1R protein expression appeared reduced when compared to melanoma cells as expected (reference). Levels of MC1R have been shown to vary across different melanoma cells (Smith et al., 2001) and Western blot analysis shows SK-MEL-28 has particularly high levels of MC1R protein expression (figure 5.2.1.b). Interestingly, the negative control of A549 lung cancer, MDA-MB-231 breast cancer, and HEK 293 human embryonic kidney cells showed positive for MC1R protein. Interestingly, MC1R protein has previously been identified in non-melanocytic cells presumed to be ‘negative’ for MC1R (Roberts et al., 2006). MC1R protein expression has also been demonstrated CIR-A2 LCL (lymphoblastoid B-cells) but was shown to be intracellular and not expressed on the cell surface (Salazar-Onfray et al., 2002). Overall, the data suggests that MC1R could represent a suitable tart receptor for mediating NP uptake in melanoma cells.

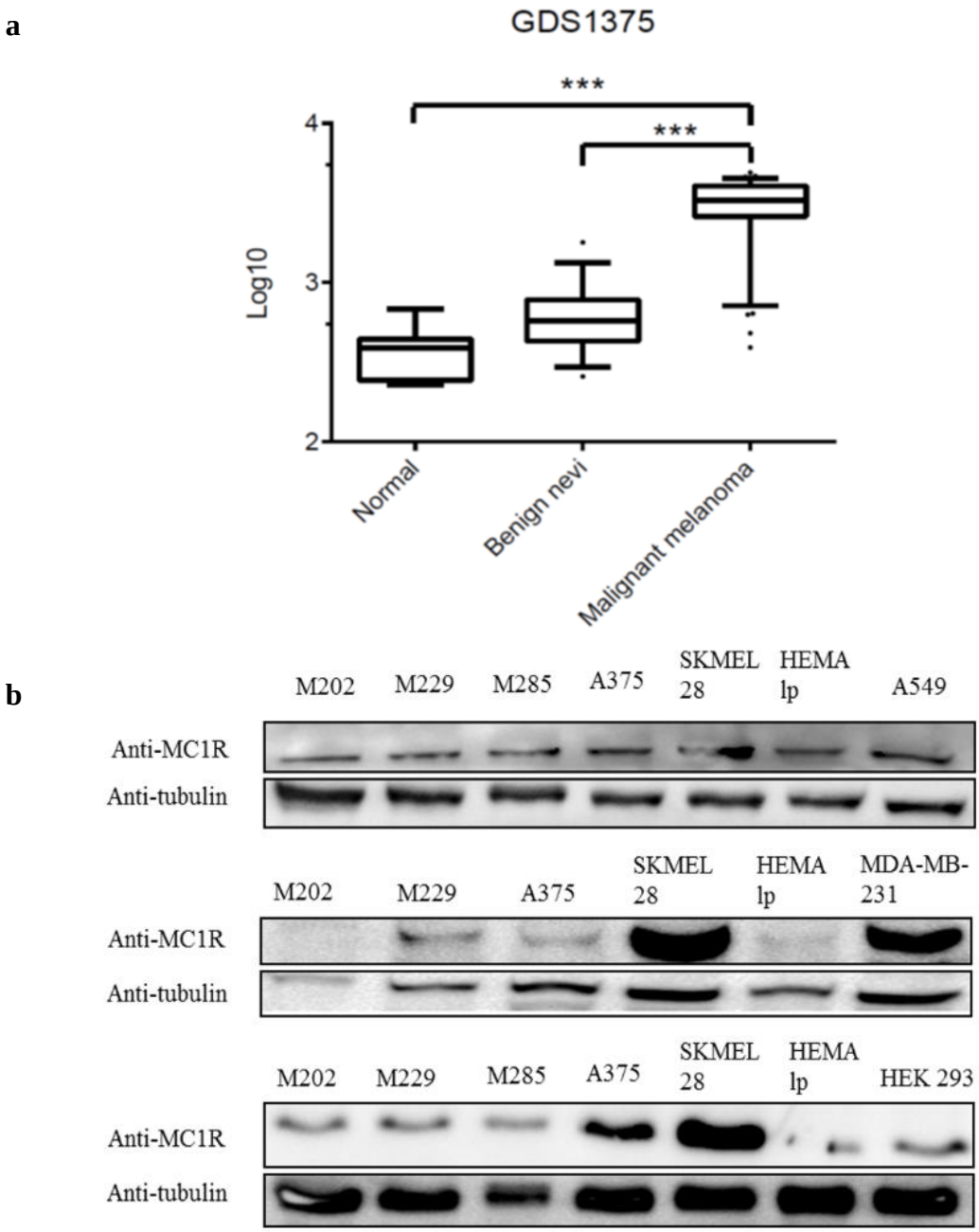

Figure 5.2.1 mRNA and protein expression of MC1R in tissue and melanoma cells (a). Microarray data from Gene Expression Omnibus (GEO) dataset GDS1375, normal/benign vs melanoma. Bars represent 95th and 5th percentile (Sherwood unpublished). (b). Representative Western Immunoblot showing protein levels of MC1R in melanoma cell lines (M202, M229, M285, A375, and SK-MEL-28) and non-cancerous melanocytes (HEMA-lp). Tubulin was used as a loading control.

5.3 Nile red (NR) encapsulation into Fe_3O_4-core NPs

In order to monitor MC1R-mediated uptake of Fe_3O_4 NPs in melanoma cells fluorescent labelling of NPs was required. To do this a hydrophobic dye, nile red (NR) was used. NR is a lipophilic molecule (Mw 318.37) with strong fluorescent properties and was non-covalently absorbed into the hydrophobic shell of the previously synthesised Fe_3O_4-PEG NPs *via* method 2.1.8. In this work, NR was used as a proof of concept for the encapsulation of small hydrophobic molecules. It has the additional advantage of being highly fluorescent which was used to visualise encapsulation using a spectrophotometer (figure 5.3.1). Minimal background fluorescence was seen in Fe_3O_4-PEG and Fe_3O_4-PEP. After addition of NR and purification, both Fe_3O_4-PEG and Fe_3O_4-PEP produced similar fluorescent emission intensities at 520 nm after excitation at 480 nm. Furthermore, NR being relatively insoluble in H_2O could not be dispersed in the aqueous solution. Fluorescent emission measurements showed that NR before and after dialysis did not dissolve in H_2O and so no fluorescence intensity was observed (figure 5.3.2). After NR encapsulation, Fe_3O_4-PEG-NR showed a fluorescence spectrum with a maximum of emission at 620 nm after excitation at 480 nm. A slight decrease in fluorescence intensity was seen after Fe_3O_4-PEG-NR was dialysed through a 3-5 kDa nitrocellulose membrane overnight in PBS. Fe_3O_4-core NPs containing NR in their shell provided a powerful tool to investigate the targeted uptake of Fe_3O_4-PEP NPs in melanoma.

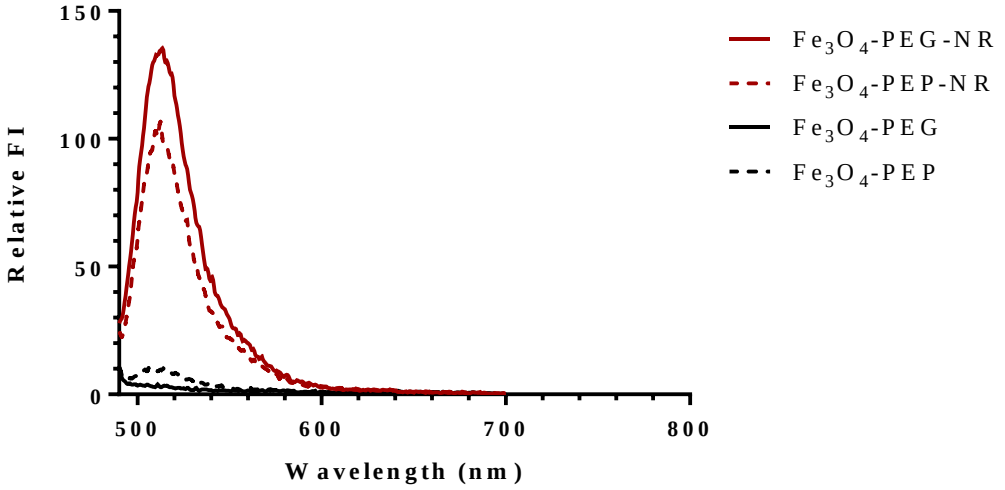

Figure 5.3.1 Encapsulation of NR in Fe_3O_4 NPs. An excitation of 480 nm was used and relative fluorescence intensity (FI) was measured to compare NR encapsulation in Fe_3O_4-PEG-NR and Fe_3O_4-PEP-NR. Fe_3O_4 NPs without NR were used as a control (with and without α-MSH peptide).

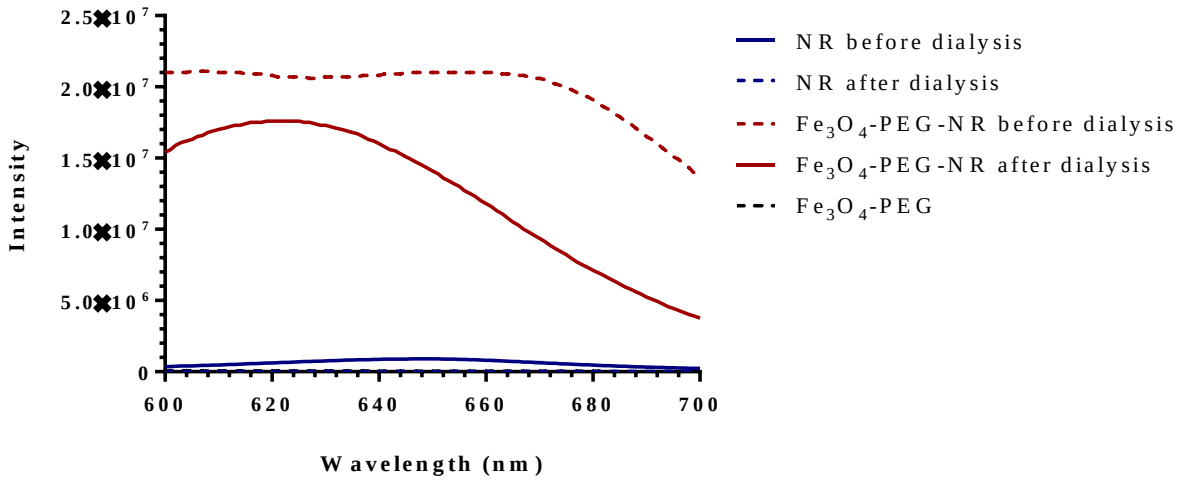

Figure. 5.3.2 Purification of Fe_3O_4-PEG-NR. Fluorescence intensity was measured after excitation at 480 nm to compare NR in Fe_3O_4-PEG-NR before and after 24 h dialysis in a 3-5 kDa nitrocellulose membrane against PBS at room temperature. This was compared to NR in H_2O and Fe_3O_4 alone.

5.4 Cellular uptake of targeted Fe_3O_4-α-MSH NPs in tumour cells

After successful encapsulation of NR, Fe_3O_4-PEG-NR NPs were used to study uptake of NPs in melanoma cells. It was important to use a method of encapsulation, such as trapping the NR in the hydrophobic core, that did not affect the surface chemistry of the NP which could have inadvertently affected cellular uptake. Firstly, confocal microscopy was used to see if Fe_3O_4-PEG-NR can be used for imaging and uptake analysis. A2058 melanoma cells were seeded at 2 x 10^4 cells per well in 12 well plates and left to seed overnight. Fe_3O_4-PEG-NR NPs were added at a final concentration of 1.4 x 10^{12} NP/ml in serum free media. Cells were incubated with NPs for 24 h before confocal microscopy. After 24 h incubation, Fe_3O_4-PEG-NR NPs freely entered A2058 cells and were ubiquitously seen in the cytoplasm of the cells (red images, figure 5.4.1). Reflected light also identified the presence of Fe_3O_4 from the core of the NPs within the cytoplasm (green, figure 5.4.1) (Shevtsov et al., 2014). Although there was limited evidence of co-localisation of NR and reflected light of Fe_3O_4, Fe_3O_4-PEG-NR NPs appear to be delivering the NR molecule into the cells. Moreover, it showed that hydrophobic molecules are readily released from the nanoformulation upon delivery to the melanoma cells, which is likely to be MC1R-mediated.

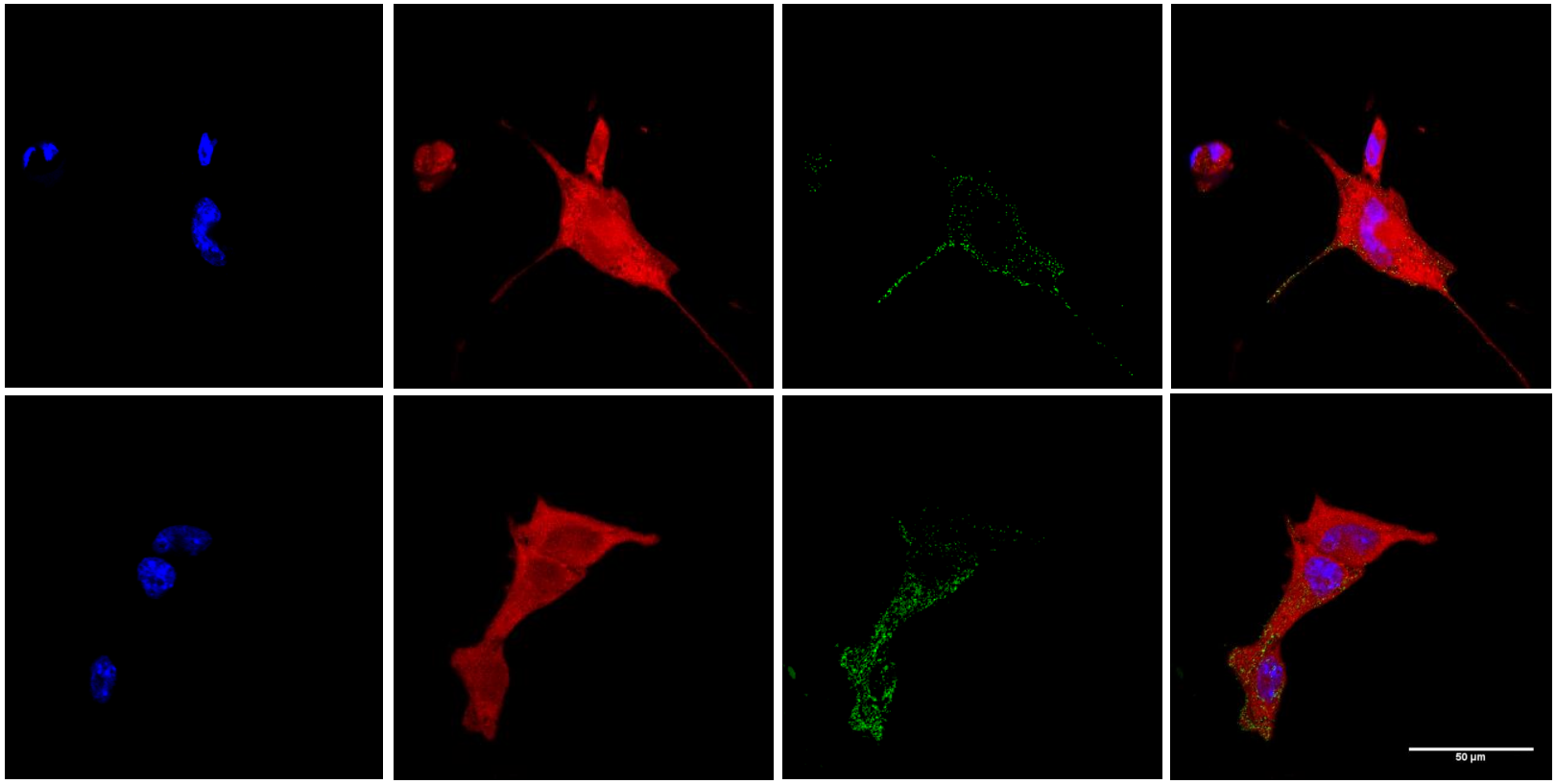

Figure 5.4.1 Confocal microscopy of IOX-PEG-NR uptake in A2058 melanoma cells. Hoechst 33342 stained nucleus (blue), NR (red) from the Fe_3O_4-PEG-NR NPs, and reflected light from Fe_3O_4 core of NP. Merged channels on far right. Scale bar 50 µm is the same for all images. Images are examples from 2 fields of view.

Uptake of Fe_3O_4-PEP-NR with the α-MSH targeting peptide attached was compared to the control of Fe_3O_4-PEG-NR to determine active uptake. As Fe_3O_4 NPs have been shown to deliver NR to cells (figure 5.4.1), flow cytometery was used to quantify internal fluorescence from internalised NR after NP delivery. B16F10 and A2058 melanoma; A549 lung cancer (control cell line); and HEMA-lp melanocyte cell lines were used in these studies. NPs were added to cells at 70-80% confluency at a final NP concentration of 1.4 x 10^{12} NP/ml. The fixed cells were then analysed using a flow cytometer. Fe_3O_4-PEG-NR and Fe_3O_4-PEP-NR uptake over time was measured by comparing the fluorescence geometric means (GM). Increasing the amount of fluorescence causes a shift in the histogram peak that can be quantified by comparing the position of the peak, known as the geometric mean, along the x-axis. NP uptake was evaluated at time points 30 min, 1 h, 3 h, and 5 h.

In B16F10 melanoma cells, Fe_3O_4-PEG-NR caused the GM of FL4 to increase modestly over 5 h. At 30 min, FL4 GM has increased by 1.4-fold difference compared to vehicle control (figure 5.4.2). Fe_3O_4-PEP-NR however, increased FL4 GM by a 9.4-fold difference (figure 5.4.3). The non-targeting Fe_3O_4-PEG-NR caused the FL4 GM to increase to 3.0, 4.5, and 4.3-fold difference from 1, 3, and 5 h through non-MC1R-mediated uptake. FL4 GM from the targeted Fe_3O_4-PEP-NR however increased to 10.0, 15.0, 15.6-fold difference from 1, 3, and 5 h respectively.

Similar results were seen in A2058 human melanoma cells. After the first half an hour of NP incubation, Fe_3O_4-PEG-NR caused an FL4 GM increase of 1.6-fold difference (figure 5.4.4) compared to Fe_3O_4-PEP-NR which caused an FL4 GM increase of 6.0 (figure 5.4.5). Over 5 h there was no significant increase in FL4 GM in A2058 cells incubated with Fe_3O_4-PEG-NR; fold differences in FL4 GM were 1.4, 1.7, and 1.7 for 1, 3, and 5 h respectively.

The non-melanoma cell line, A549 lung cancer, showed no significant difference in FL4 GM over the 5 hours between Fe_3O_4-PEG-NR and Fe_3O_4-PEP-NR (figure 5.4.6, 5.4.7). Fold difference in FL4 GM after A549 incubation with Fe_3O_4-PEG-NR was 1.1, 2.0, 2.2, and 3.1 for 0.5, 1, 3, and 5 h respectively. Similarly, the fold-difference in FL4 GM after A549 incubation with Fe_3O_4-PEP-NR was 1.2, 2.1, 2.8, and 3 for 0.5, 1, 3, and 5 h respectively.

After comparing histograms (figure 5.4.8) and the fold change in FL4 GM (figure 5.4.9), it is clear that some non-MC1R-mediated uptake of Fe_3O_4-core NPs occurs in all cell lines evaluated. In B16F10, A2058, and A549 cells FL4 increase, due to internalisation of NR, can be seen up to 4-fold difference compared to control after incubation with Fe_3O_4-PEG-NR. Interestingly, Fe_3O_4-PEP-NR in the A549 non-melanoma cells is comparable to the NPs without the targeting peptide. In conjunction with the increased fluorescence and the faster rate of uptake with targeted Fe_3O_4-PEP-NR in B16F10 and A2058 melanoma cells compared to Fe_3O_4-PEG-NR it suggests that uptake beyond that of the 4-fold difference in FL4 GM is active targeting from the interaction between α-MSH peptide on the surface of Fe_3O_4-PEP-NR and MC1R on the melanoma cell surface.

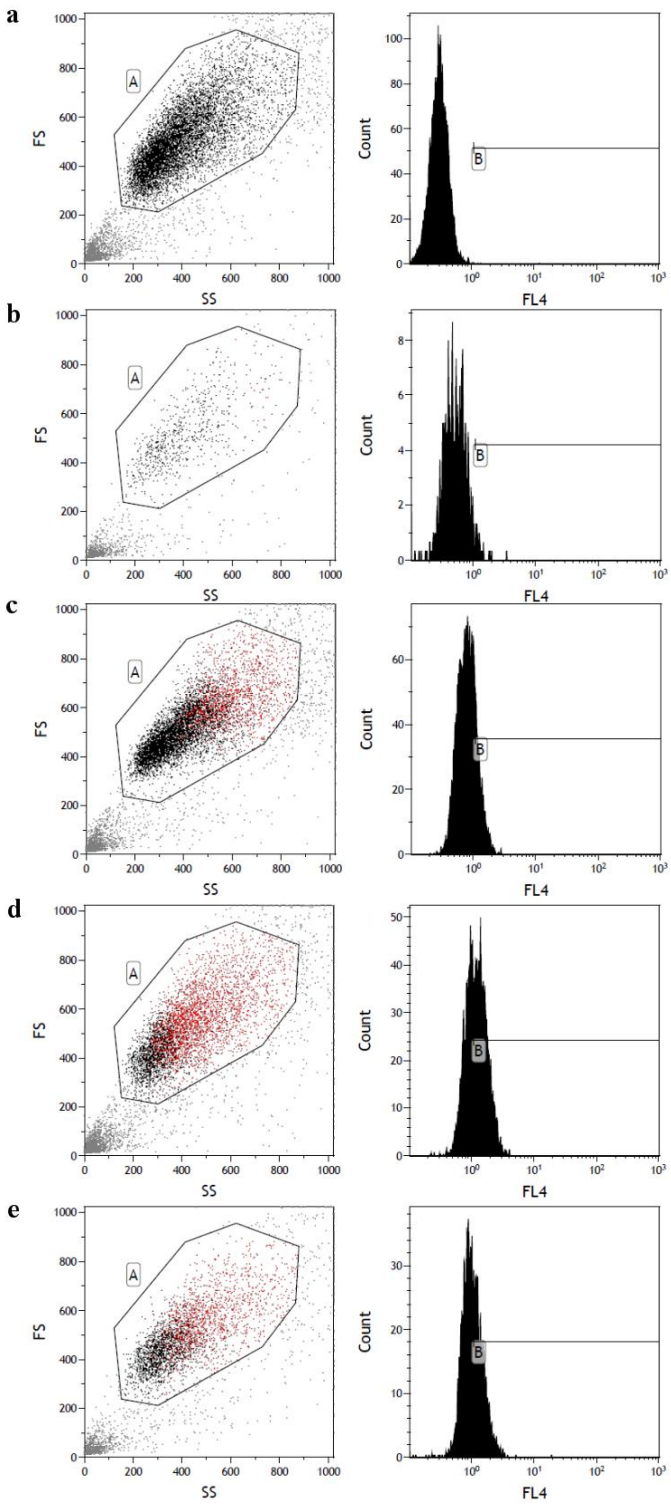

Figure 5.4.2 Flow cytometry time uptake analysis of Fe_3O_4-PEG-NR in B16F10. (a) Control Fe_3O_4-PEG. (b) Fe_3O_4-PEG-NR 0.5 h. (c) Fe_3O_4-PEG-NR 1 h. (d) Fe_3O_4-PEG-NR 3 h. (e) Fe_3O_4-PEG-NR 5 h. Dot plot (left) shows linear FS against linear SS with the cell population selected for analysis (gate A). Histogram shows relative count against log FL4 with cells positive for FL4 in gate B.

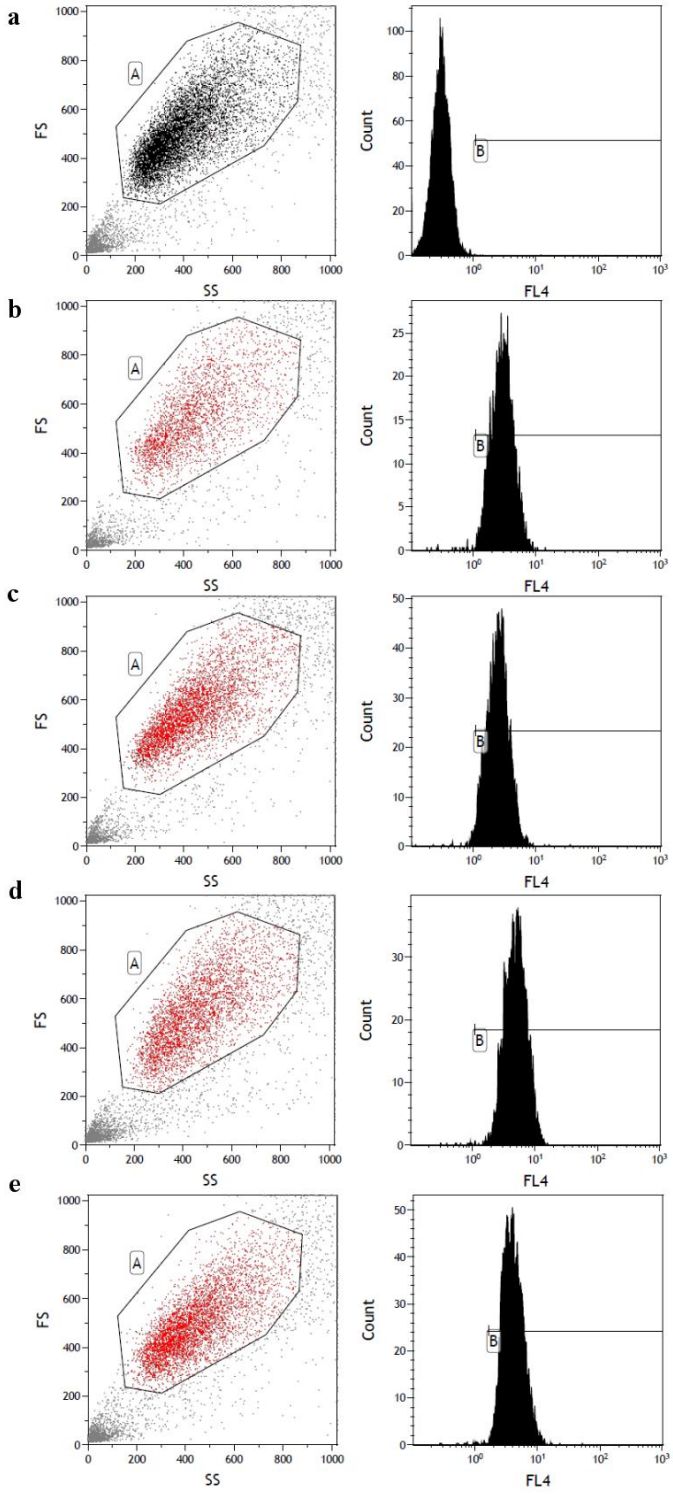

Figure 5.4.3 Flow cytometry time uptake analysis of Fe_3O_4-PEP-NR in B16F10. (a) Control Fe_3O_4-PEP. (b) Fe_3O_4-PEP-NR 0.5 h. (c) Fe_3O_4-PEP-NR 1 h. (d) Fe_3O_4-PEP-NR 3 h. (e) Fe_3O_4-PEP-NR 5 h. Dot plot (left) shows linear FS against linear SS with the cell population selected for analysis (gate A). Histogram shows relative count against log FL4 with cells positive for FL4 in gate B.

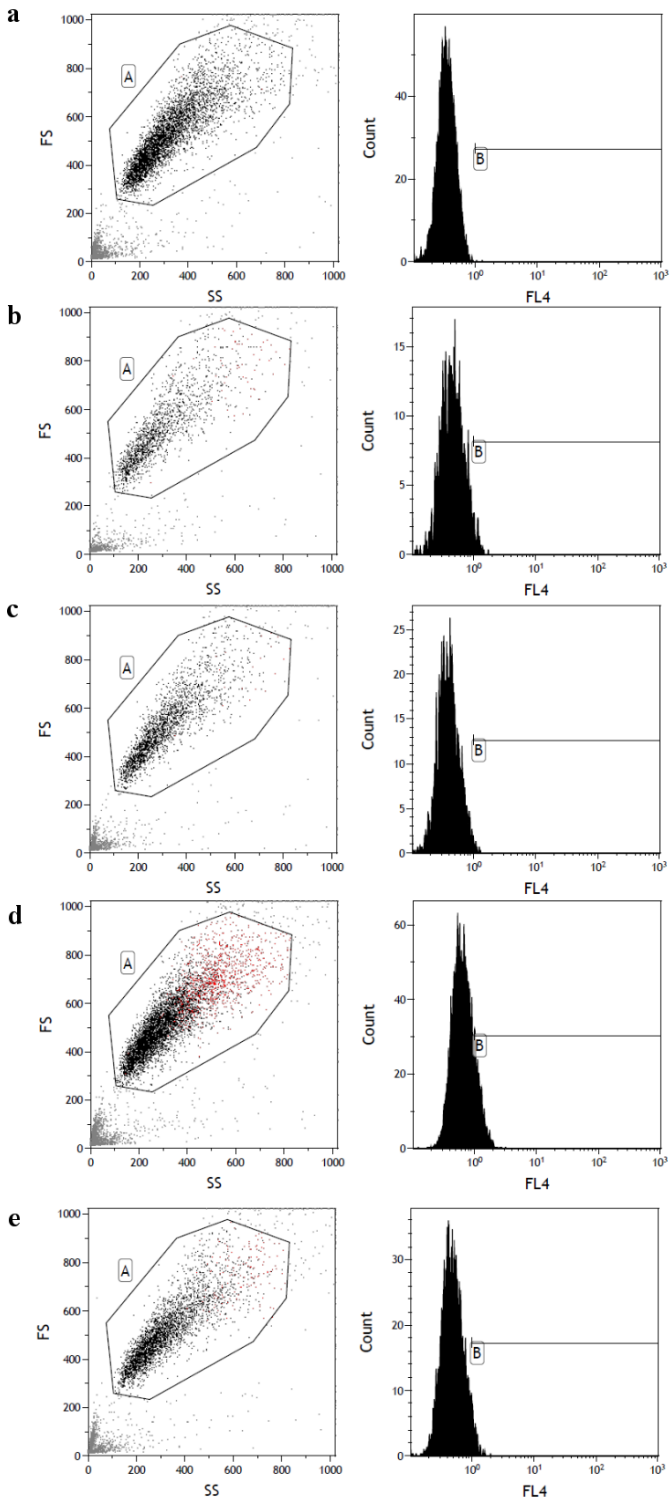

Figure 5.4.4 Flow cytometry time uptake analysis of Fe_3O_4-PEG-NR in A2058. (a) Control Fe_3O_4-PEG. (b) Fe_3O_4-PEG-NR 0.5 h. (c) Fe_3O_4-PEG-NR 1 h. (d) Fe_3O_4-PEG-NR 3 h. (e) Fe_3O_4-PEG-NR 5 h. Dot plot (left) shows linear FS against linear SS with the cell population selected for analysis (gate A). Histogram shows relative count against log FL4 with cells positive for FL4 in gate B.

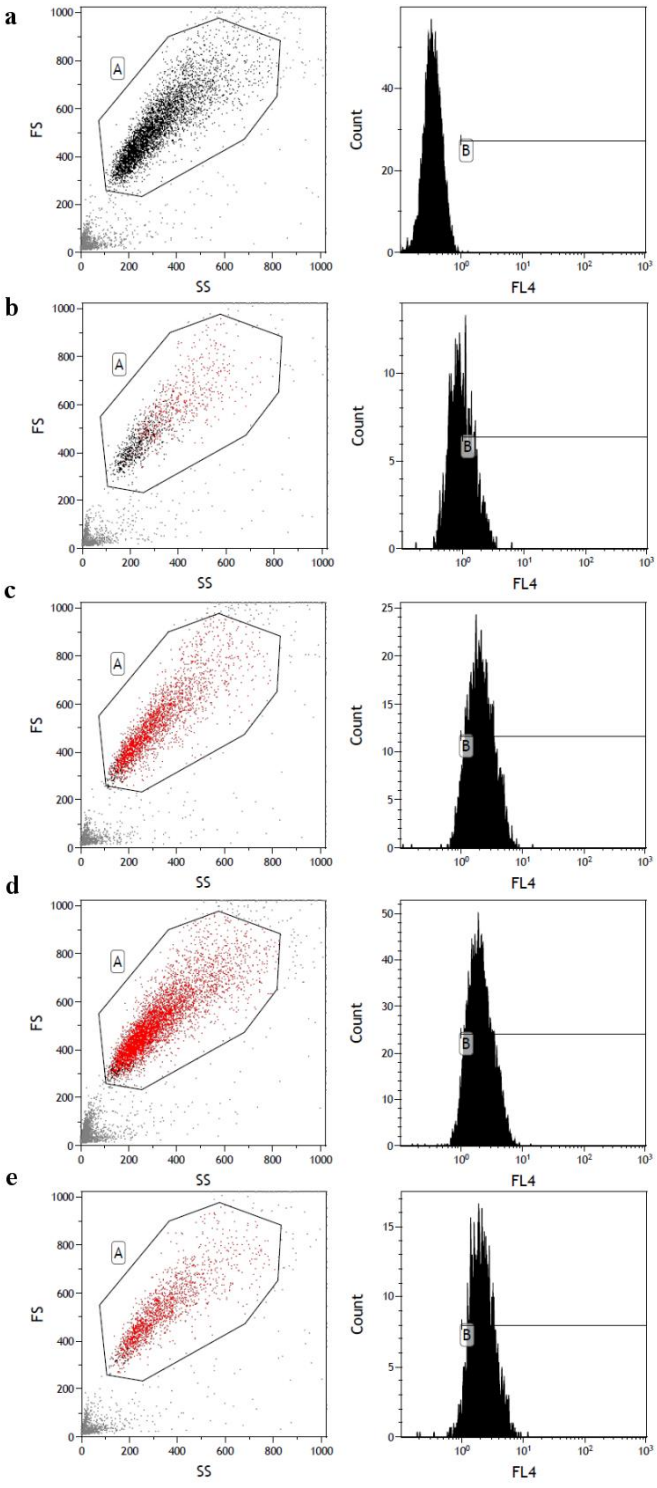

Figure 5.4.5 Flow cytometry time uptake analysis of Fe_3O_4-PEP-NR in A2058. (a) Control Fe_3O_4-PEP. (b) Fe_3O_4-PEP-NR 0.5 h. (c) Fe_3O_4-PEP-NR 1 h. (d) Fe_3O_4-PEP-NR 3 h. (e) Fe_3O_4-PEP-NR 5 h. Dot plot (left) shows linear FS against linear SS with the cell population selected for analysis (gate A). Histogram shows relative count against log FL4 with cells positive for FL4 in gate B.

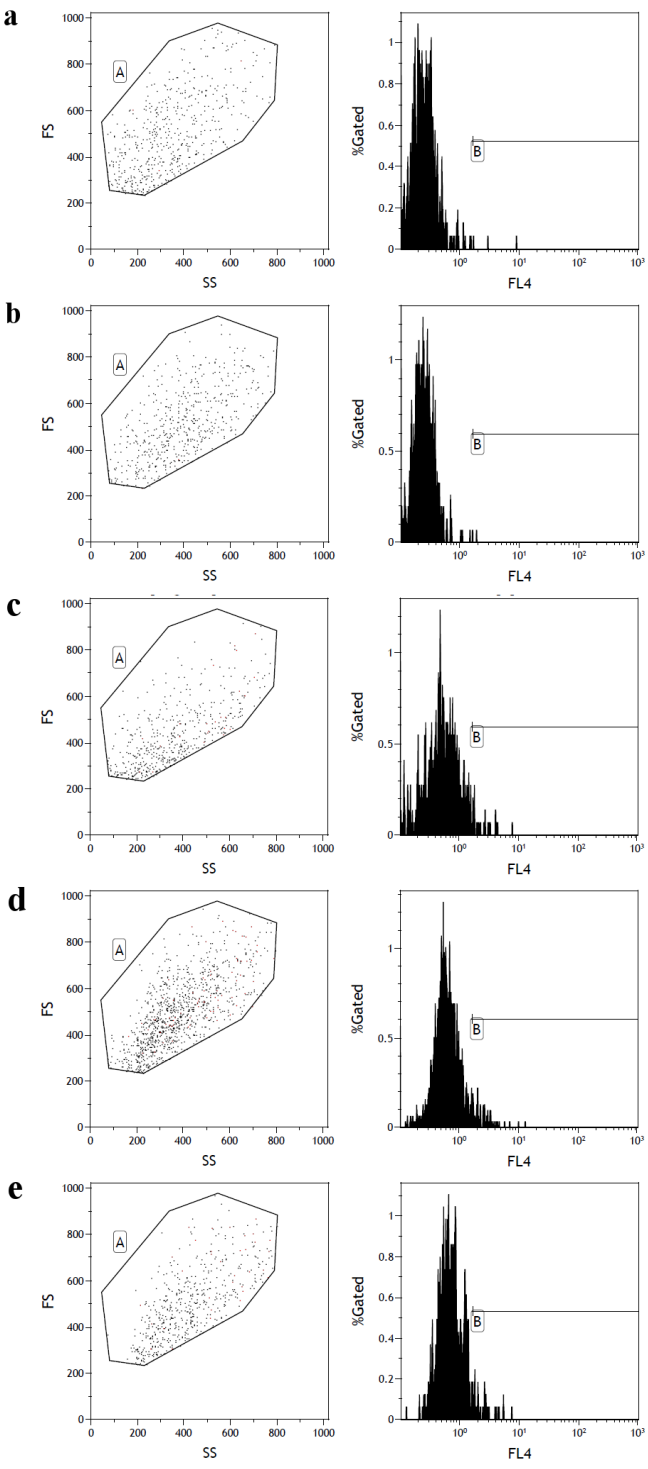

Figure 5.4.6 Flow cytometry time uptake analysis of Fe_3O_4-PEG-NR in A549. (a) Control Fe_3O_4-PEG. (b) Fe_3O_4-PEG-NR 0.5 h. (c) Fe_3O_4-PEG-NR 1 h. (d) Fe_3O_4-PEG-NR 3 h. (e) Fe_3O_4-PEG-NR 5 h. Dot plot (left) shows linear FS against linear SS with the cell population selected for analysis (gate A). Histogram shows relative count against log FL4 with cells positive for FL4 in gate B.

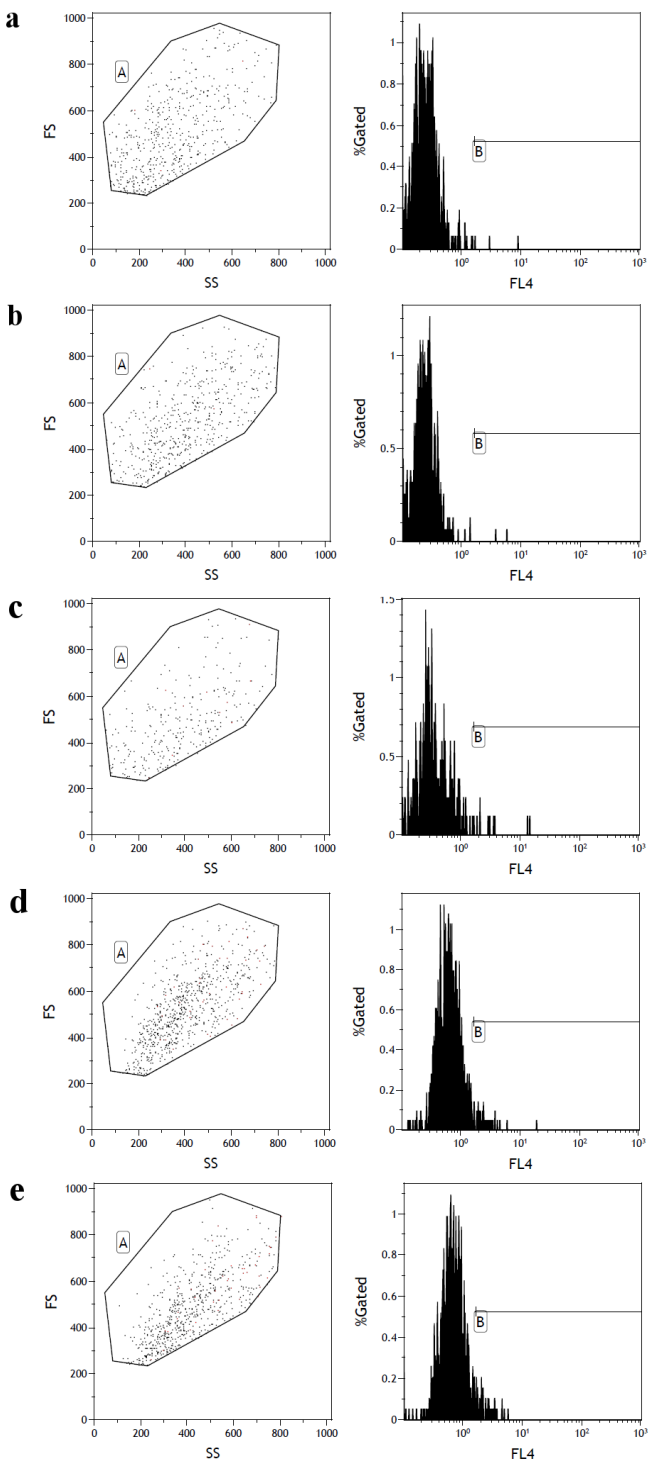

Figure 5.4.7 Flow cytometry time uptake analysis of Fe_3O_4-PEP-NR in A549. (a) Control Fe_3O_4-PEP. (b) Fe_3O_4-PEP-NR 0.5 h. (c) Fe_3O_4-PEP-NR 1 h. (d) Fe_3O_4-PEP-NR 3 h. (e) Fe_3O_4-PEP-NR 5 h. Dot plot (left) shows linear FS against linear SS with the cell population selected for analysis (gate A). Histogram shows relative count against log FL4 with cells positive for FL4 in gate B.

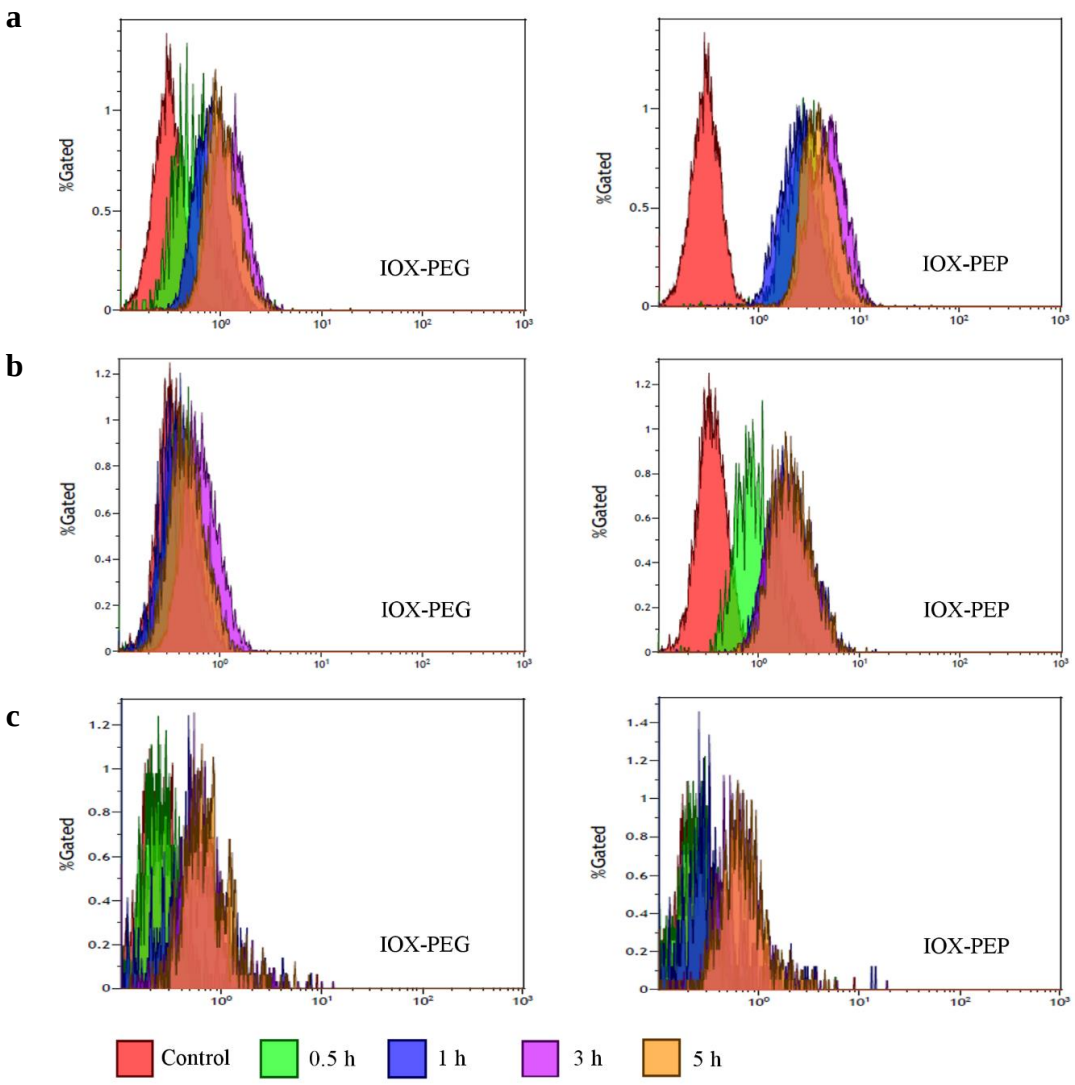

Figure 5.4.8 Representative histograms of flow cytometry time uptake analysis of Fe_3O_4-PEG-NR and Fe_3O_4-PEP-NR (a) B16F10, (b) A2058, and (c) A549 cell lines. Each histogram compares the log FL4 (x axis) with control (red), 0.5 h (green), 1 h (blue), 3 h (pink), and 5 h (orange).

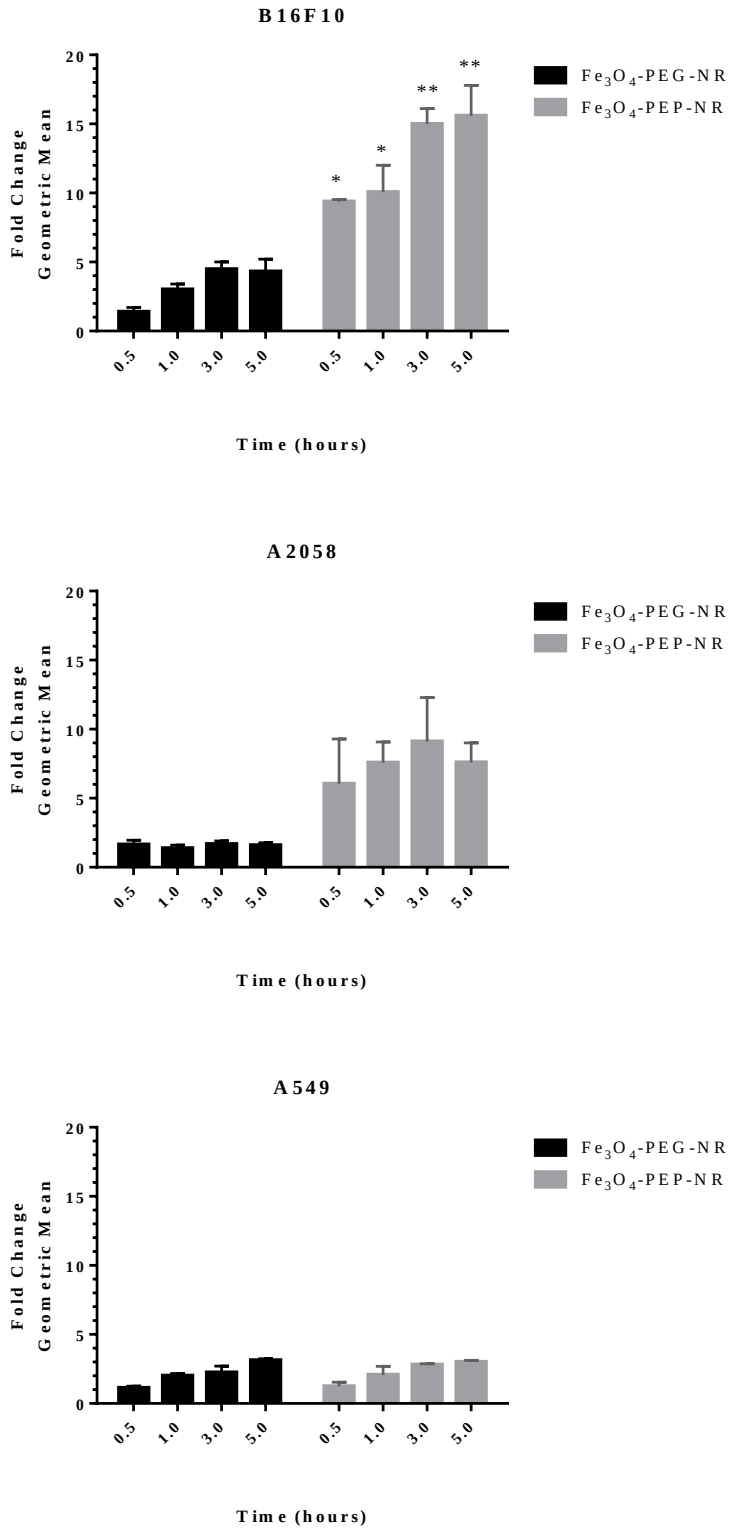

Figure 5.4.9 Quantification of flow cytometry time uptake analysis. Fold change of the geometric mean from the flow cytometry histograms was calculated after normalising to control. In B16F10, A2058, and A549, Fe_3O_4-PEG-NR and Fe_3O_4-PEP-NR uptake was compared over 0.5, 1, 3, and 5 h incubation. Mean ± SD, n = 6. p = <0.05 *, <0.01 **.

5.5 Uptake of NPs in melanocytes cells

Human epidermal melanocytes (HEMA-lp) were grown in Medium 254 supplemented with Human Melanocyte Growth Supplement (HMGS) as described in method 2.3.1. The morphology of HEMA-lp cells was assessed to insure they were fully differentiated (figure 4.5.1). HEMA-lp cells were slender with dendrites containing terminal swellings. Melanocytes grown with limited serum appear fibroblast-like in morphology (Donatien et al.).

As MC1R is also expressed in normal melanocytes (figure 5.2.1.), we used flow cytometry to see if the targeted Fe_3O_4-PEP-NR NP also had increased uptake in HEMA-lp cells compared to the non-targeted Fe_3O_4-PEG-NR. After 5 h incubation with both NPs, there was no significant increase in uptake between Fe_3O_4-PEG-NR and Fe_3O_4-PEP-NR. The fold difference, compared to control, in FL4 GM for Fe_3O_4-PEG-NR was 1.5 and 1.9 for Fe_3O_4-PEP-NR (figure 5.5.2); suggesting that both NPs were likely being taken up through non-MC1R-mediated pathways at the same rate.

Overall, after 5 h there was an increase in uptake of Fe_3O_4-PEP NPs in melanoma cells (B16F10 and A2058) compared to Fe_3O_4-PEG NPs. There was no increase in difference in uptake between Fe_3O_4-PEP and Fe_3O_4-PEG NPs in non-melanocytic cells (A549 and HEMA-lp). Across all cell lines there was a comparable level of uptake for Fe_3O_4-PEG NPs (figure 5.5.3).

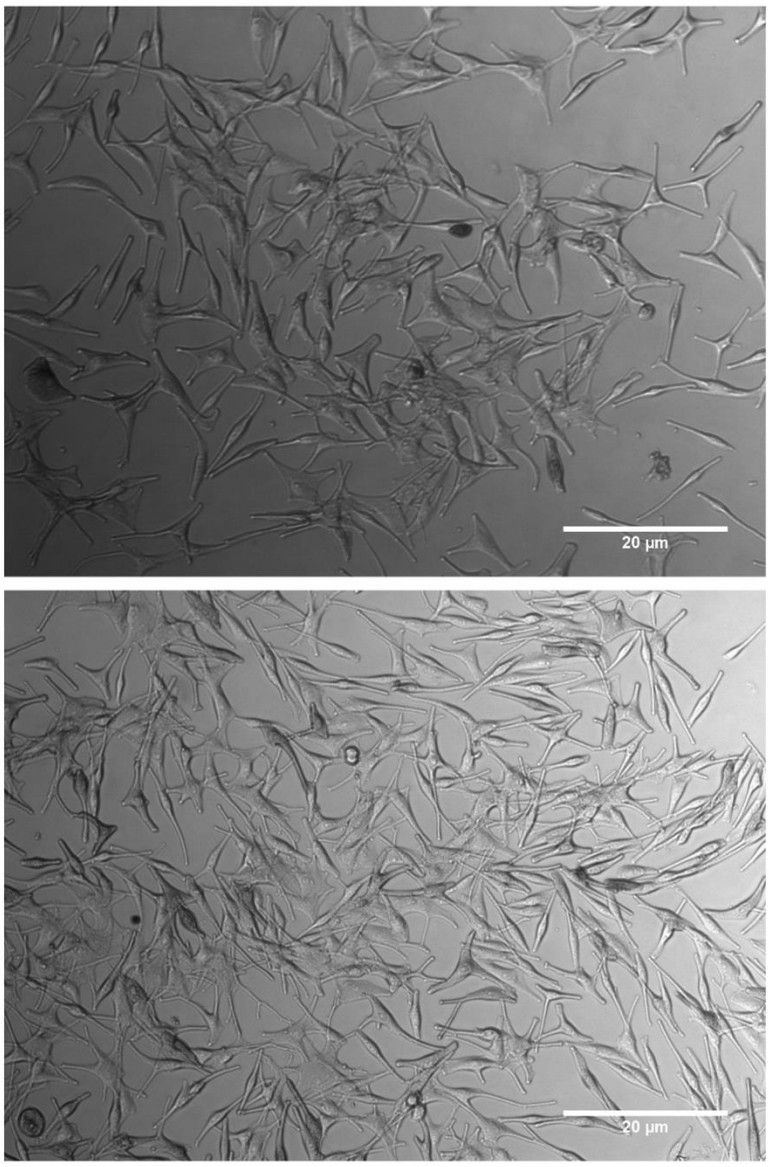

Figure 5.5.1 Morphology of HEMA-lp cells. Melanocytes were grown in Medium 254 supplemented with Human Melanocyte Growth Supplement (HMGS). Melanocytes were fully differentiated with dendritic processes. Images taken from different fields of view. Scale bar 20 µm.

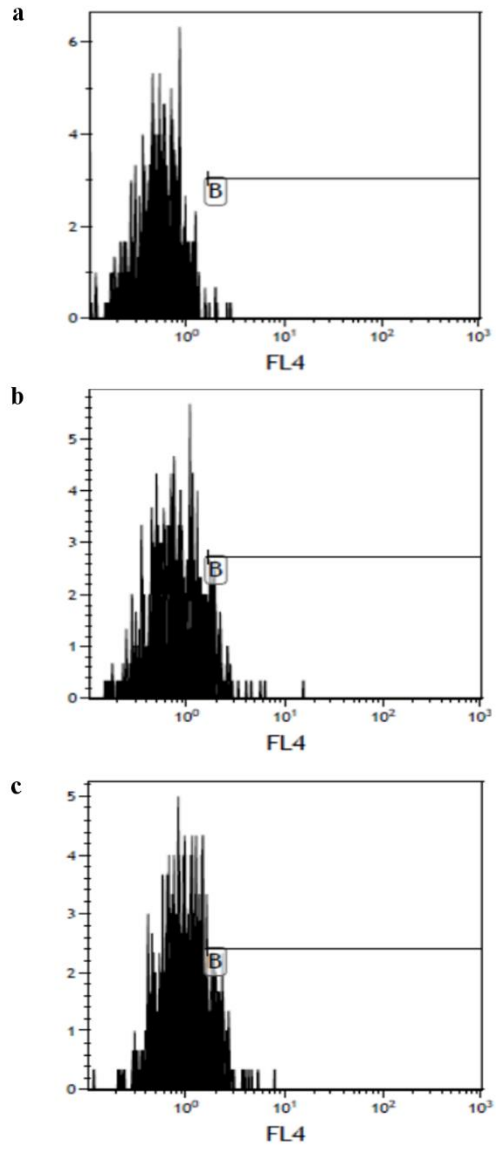

Figure 5.5.2 Flow cytometry time uptake analysis of Fe_3O_4-PEG-NR and Fe_3O_4-PEP-NR in HEMA-lp. (a). control HEMA-lp cells. (b) HEMA-lp cells after 5 h incubation with Fe_3O_4-PEG-NR. (c). HEMA-lp cells after 5 h incubation with Fe_3O_4-PEP-NR. Histogram shows relative count against log FL4 with cells positive for FL4 in gate B.

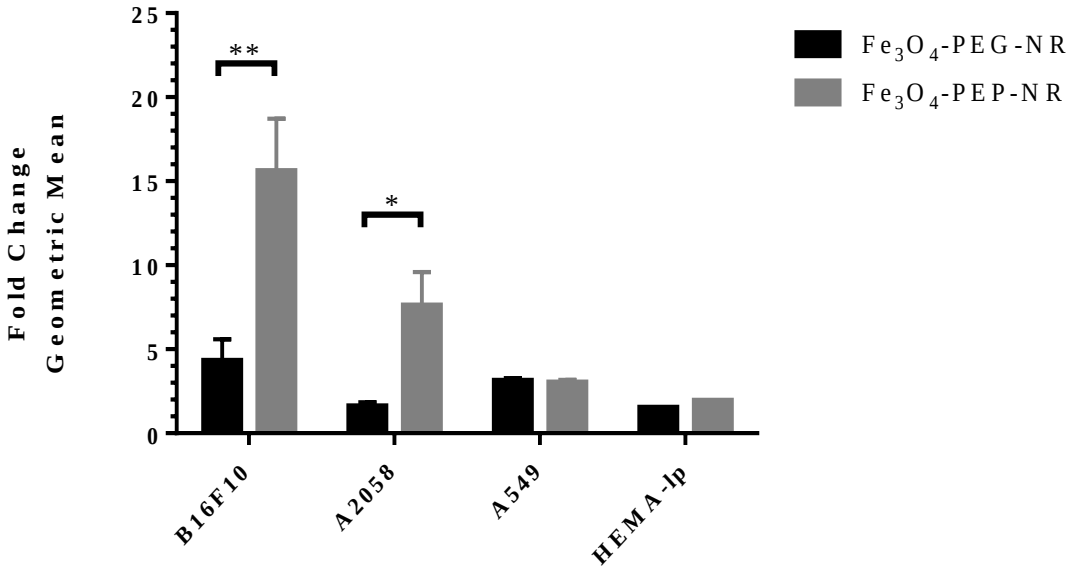

Figure 5.5.3 Quantification of 5 h flow cytometry time uptake analysis. Fold change of the geometric mean from the flow cytometry histograms was calculated after normalising to control. In B16F10, A2058, A549, and HEMA-lp cells, Fe_3O_4-PEG-NR and Fe_3O_4-PEP-NR uptake was compared after 5 h. Mean ± SD, n = 6. p = <0.05 *, <0.01 **.

5.6 MC1R-mediated uptake of Fe_3O_4-PEP-NR NPs

Initially, to confirm the increase of cellular uptake of Fe_3O_4-PEP NPs in melanoma cells was due to MC1R-mediated internalisation, gene knockdown of MC1R was attempted. siRNA can be introduced into the cell *via* transfection where it can silence the expression of genes by inducing the degradation of mRNA. After transfection of siRNA for 48, 72, and 96 h, MC1R protein was still detected in A2058 cells (figure 5.6.1).

As MC1R was difficult to knockdown, an alternative method was used to show MC1R-mediated uptake. To confirm receptor-mediated internalisation, cells were blocked with an excess of peptide prior to NP incubation. For 30 mins, 200 μg/ml α-MSH was used to block MC1-receptors on the surface of cells. As a negative control, the scrambled peptide of α-MSH was used. Fe_3O_4-PEG-NR and Fe_3O_4-PEP-NR NPs were then added in serum free media for 5 h incubation. In B16F10, there was no significant difference between the control Fe_3O_4-PEG-NR and the cells treated with either α-MSH or the scrambled peptide (figure 5.6.2). There was a significant decrease in the fold change FL4 GM between the control (non-blocked) Fe_3O_4-PEP-NR and the cells that had been pre-blocked with α-MSH and incubated with Fe_3O_4-PEP-NR (figure 5.6.3). However, there was also a decrease in uptake after prior incubation with the scrambled peptide similar to α-MSH. In A549, there was no difference between non-blocked, α-MSH, and scrambled peptide for both Fe_3O_4-PEG-NR and Fe_3O_4-PEP-NR NPs (figure 5.6.4, 5.6.5).

In B16F10 cells, FI from both Fe_3O_4-PEG-NR and Fe_3O_4-PEP-NR NPs was high, making it difficult to see the differences between the control cells that were not

blocked and cells blocked with α-MSH or scrambled peptide. To further investigate peptide blocking of MC1R, NR was decreased from 0.5% (v/v) to 0.1% (v/v) in NPs. In B16F10 and A2058 melanoma cells, Fe_3O_4-PEP uptake was increased significantly compared to Fe_3O_4-PEG (control; figure 5.6.8). After blocking with 200 μg/ml α-MSH for 30 min, Fe_3O_4-PEP internalisation was reduced to levels comparable to the control. Moreover, incubating the cells with 200 μg/ml of scrambled peptide did not block Fe_3O_4-PEP internalisation (figure 5.6.8). In A549 cells, although uptake of Fe_3O_4-PEP was higher than control, there was no significant difference between Fe_3O_4-PEP, Fe_3O_4-PEP with α-MSH, and Fe_3O_4-PEP with scrambled peptide.

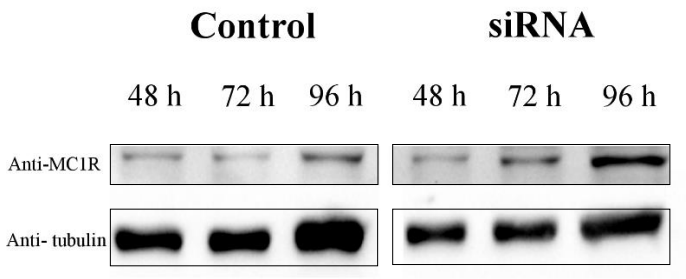

Figure 5.6.1 Western Immunoblot of siRNA knockdown of MC1R in A2058 melanoma cells. MC1R expression was analysed in A2058 cells after transfection with MC1R siRNA for 48, 72, and 96 h.

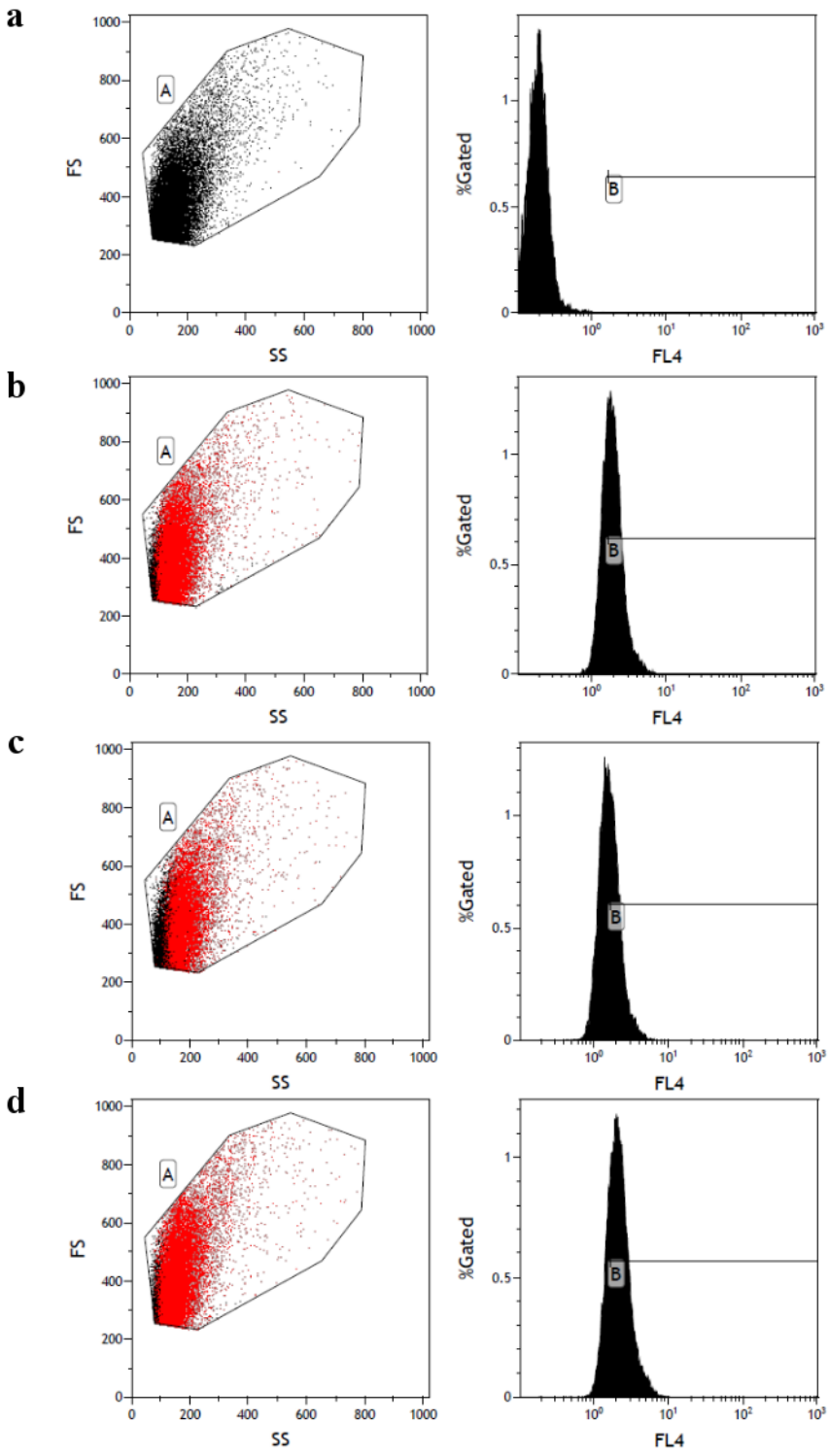

Figure 5.6.2 Peptide blocking in B16F10 after Fe_3O_4-PEG-NR incubation. Dot plot (left) of B16F10 cell population and log FL4 histogram after incubation of Fe_3O_4-PEG-NR for 5 h. (a) Control cells, (b) Fe_3O_4-PEG-NR, (c) Fe_3O_4-PEG-NR with α-MSH block, (d) Fe_3O_4-PEG-NR with scrambled block.

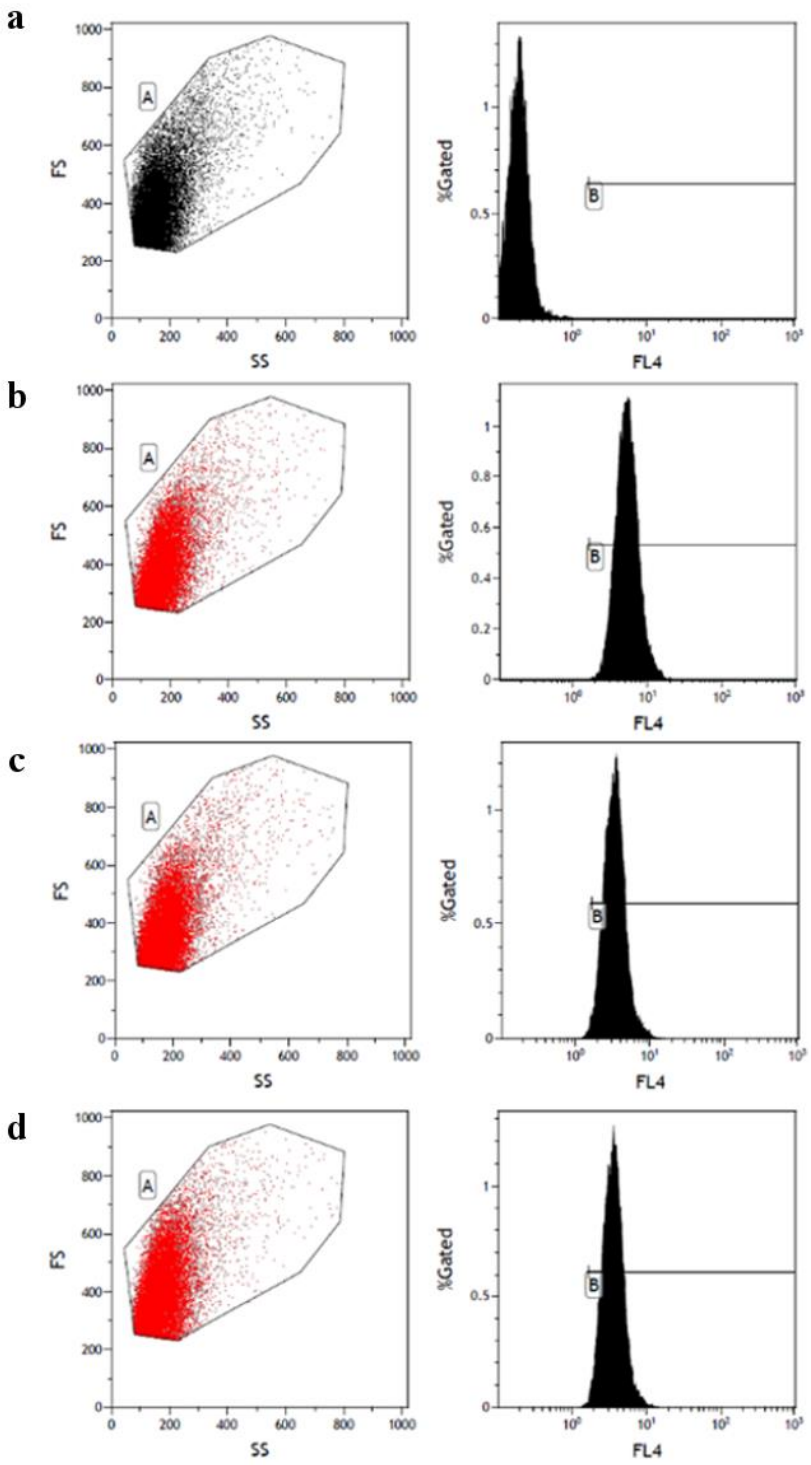

Figure 5.6.3 Peptide blocking in B16F10 after Fe_3O_4-PEP-NR incubation. Dot plot (left) of B16F10 cell population and log FL4 histogram after incubation of Fe_3O_4-PEP-NR for 5 h. (a) Control cells, (b) Fe_3O_4-PEP-NR, (c) Fe_3O_4-PEP-NR with α-MSH block, (d) Fe_3O_4-PEP-NR with scrambled block.

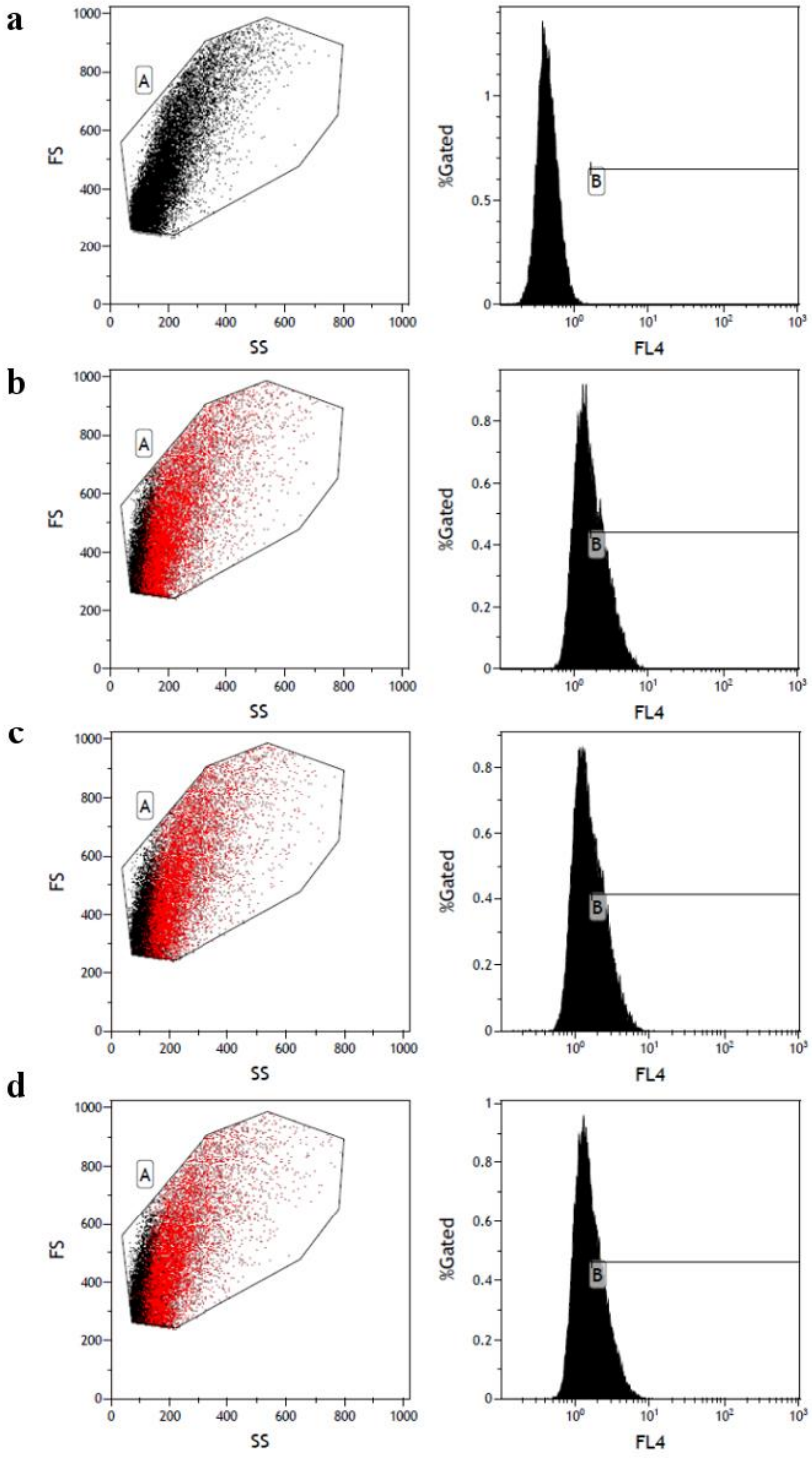

Figure 5.6.4 Peptide blocking in A549 after Fe_3O_4-PEG-NR incubation. Dot plot (left) of A549 cell population and log FL4 histogram after incubation of Fe_3O_4-PEG-NR for 5 h. (a) Control cells, (b) Fe_3O_4-PEG-NR, (c) Fe_3O_4-PEG-NR with α-MSH block, (d) Fe_3O_4-PEG-NR with scrambled block.

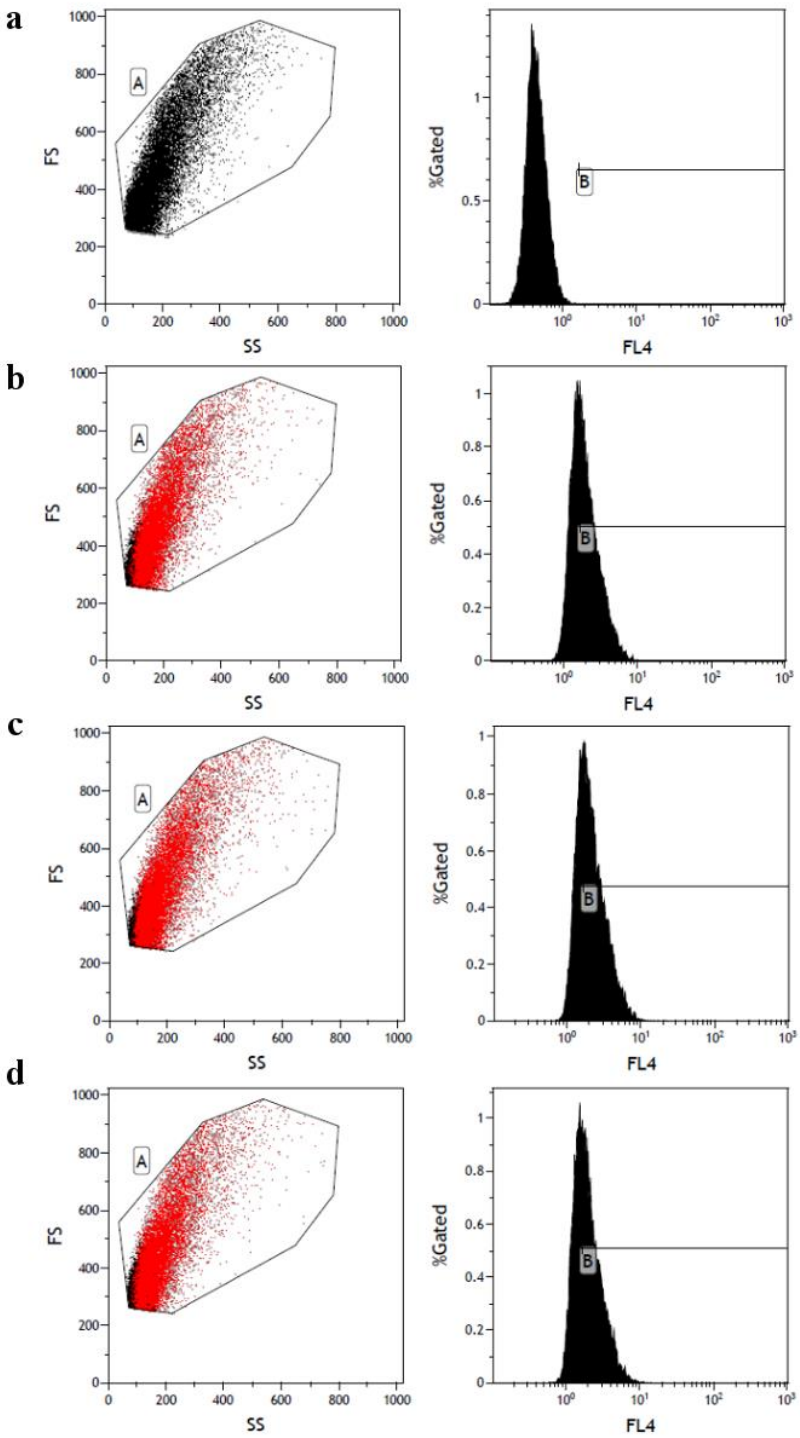

Figure 5.6.5 Peptide blocking in A549 after Fe_3O_4-PEP-NR incubation. Dot plot (left) of A549 cell population and log FL4 histogram after incubation of Fe_3O_4-PEP-NR for 5 h. (a) Control cells, (b) Fe_3O_4-PEP-NR, (c) Fe_3O_4-PEP-NR with α-MSH block, (d) Fe_3O_4-PEP-NR with scrambled block.

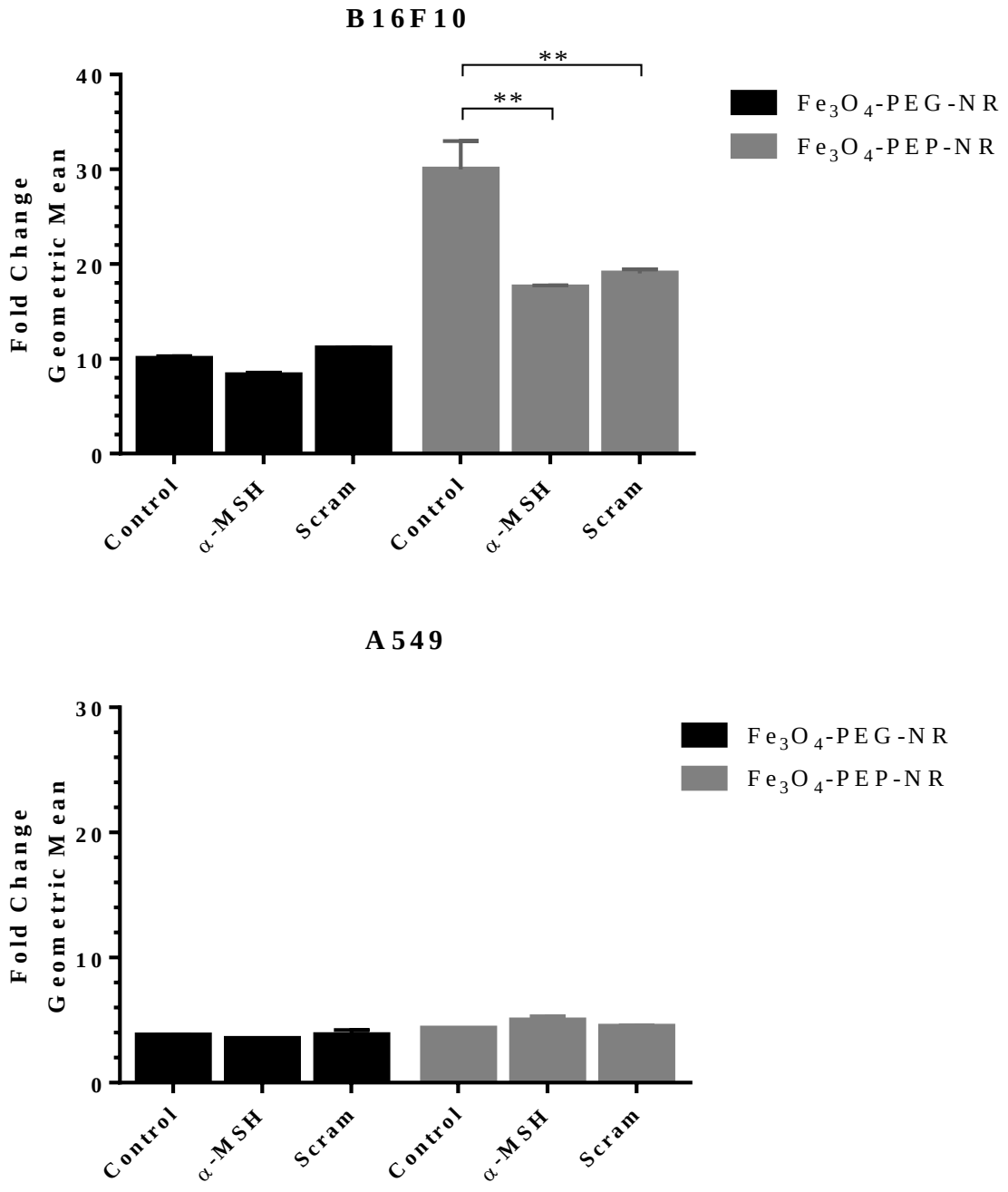

Figure 5.6.6 Peptide blocking in B16F10 and A549 after Fe_3O_4-PEG-NR and Fe_3O_4-PEP-NR incubation. Fold difference of FL4 GM. α-MSH and scrambled peptide 200 µg/ml for 30 min was used to block NP uptake. After peptide exposure, Fe_3O_4-PEG-NR and Fe_3O_4-PEP-NR NPs were incubated for 5 h before flow analysis. Mean ± SD, n = 6, p = <0.01 **.

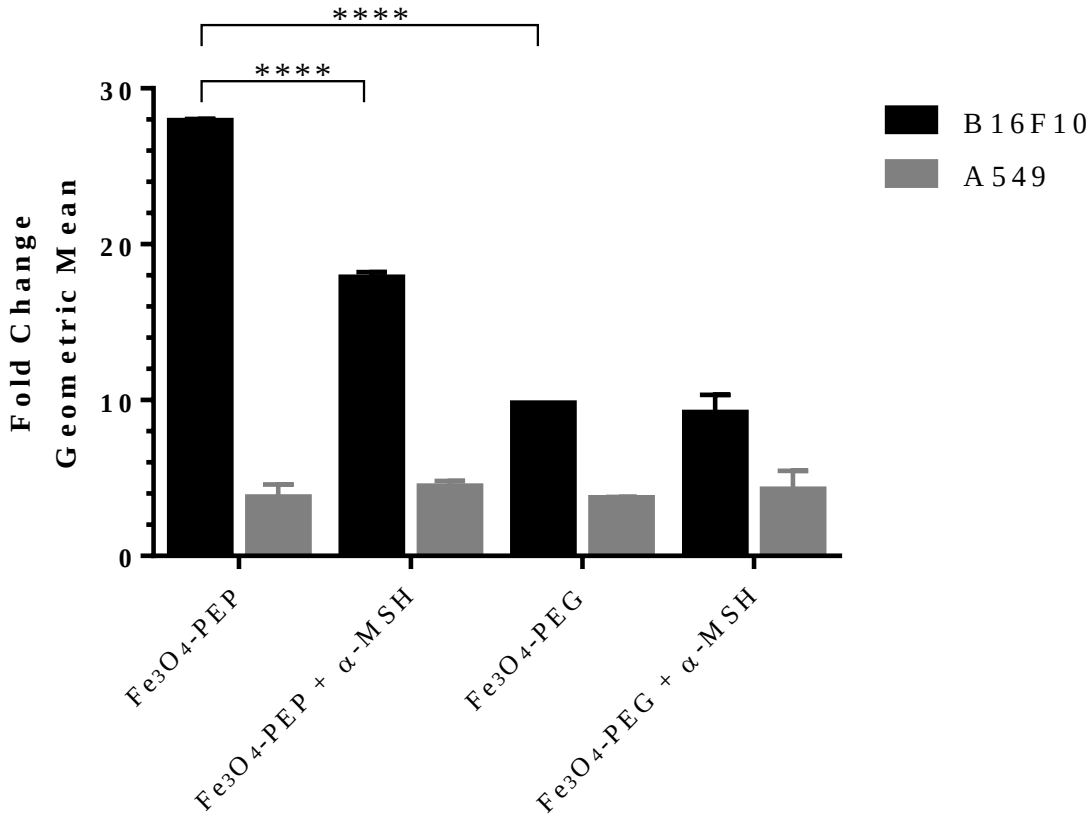

Figure 5.6.7 Comparison of α-MSH peptide blocking in B16F10 and A549 after Fe_3O_4-PEG-NR and Fe_3O_4-PEP-NR incubation. Fold difference of FL4 GM. α-MSH peptide 200 µg/ml for 30 min was used to block NP uptake. After peptide exposure, Fe_3O_4-PEG-NR and Fe_3O_4-PEP-NR NPs with 0.5% NR were incubated for 5 h before flow analysis. Mean ± SD, n = 6. p = <0.0001 ****.

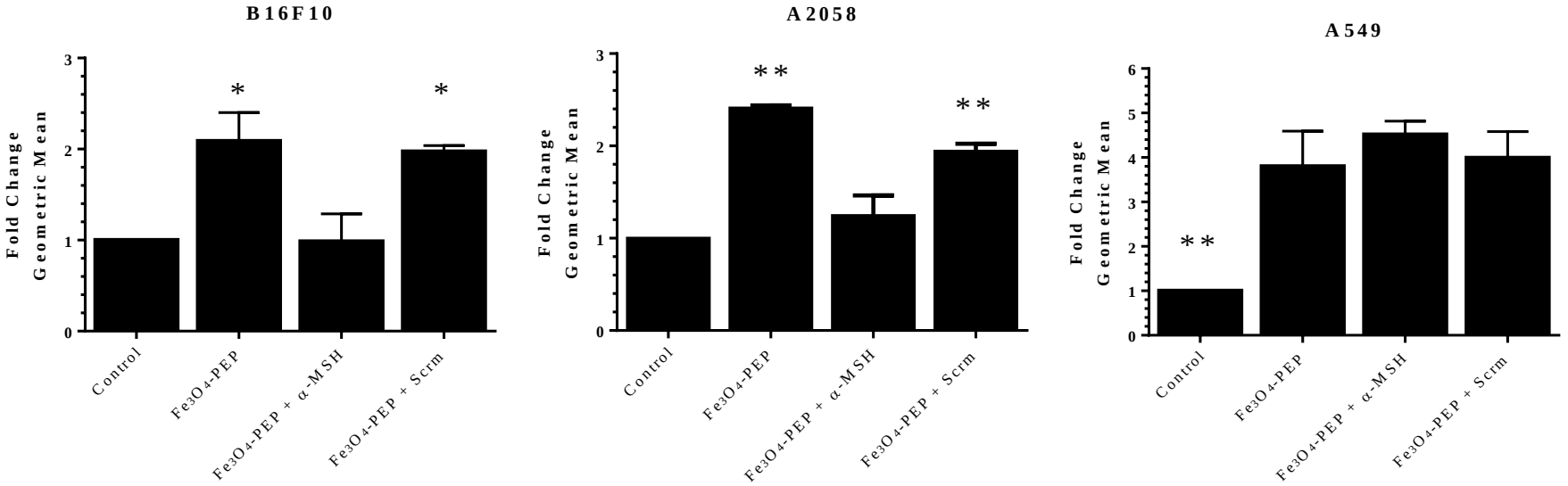

Figure 5.6.8 Comparison of α-MSH peptide blocking and scrambled peptide. Fold difference of FL4 GM. α-MSH peptide 200 µg/ml for 30 min was used to block NP uptake. Scrambled α-MSH peptide was used as a control. After peptide exposure, Fe_3O_4-PEP-NR NPs with 0.1% NR were incubated for 5 h before flow analysis. Mean ± SD, n = 6. p = <0.05 *, <0.01 ** compared to blocking with α-MSH peptide.

5.7 Encapsulation of a chemotherapeutic drug in Fe_3O_4 NPs

Encapsulation of the hydrophobic drug PTX was achieved by method 2.1.8. For Fe_3O_4-PEG-PTX and Fe_3O_4-PEP-PTX, there was a theoretical final concentration of 50 µM and a NP concentration of $10^{12.4}$ NP/ml. The stability of NPs was analysed using DLS measurements after addition of PTX; measurements were compared to the same batch of Fe_3O_4-PEG without drug (figure 5.7.1) with a Zave hydrodynamic diameter, d_H, of 55.0 nm and a PDI of 0.2. After addition of PTX, Fe_3O_4-PEG-PTX DLS measurements showed a slight increase in the hydrodynamic diameter from 55 nm to 61 nm. PDI also increased from 0.2 to 0.3 (figure 5.7.2).

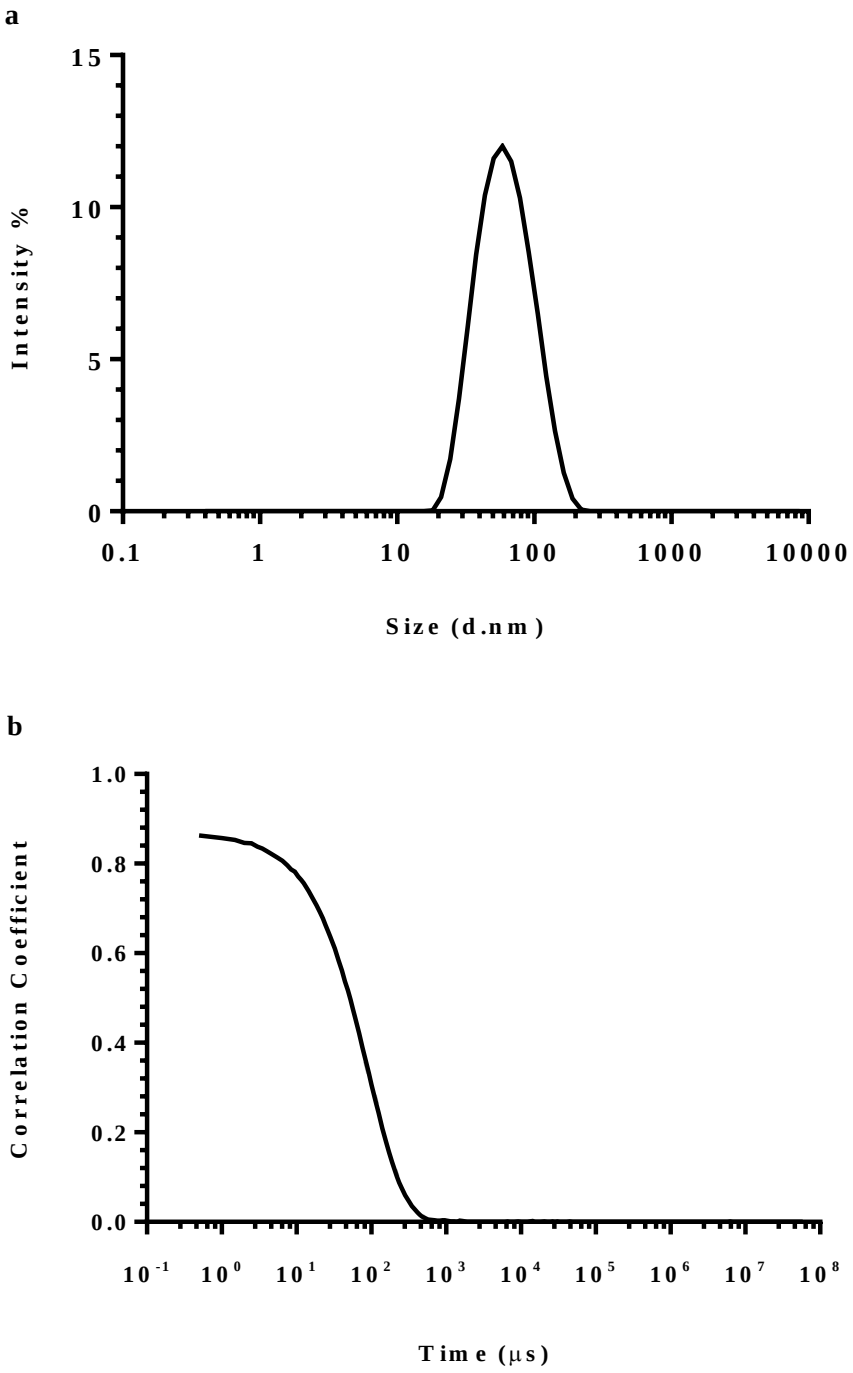

Figure 5.7.1 Representative DLS size and polydispersity analysis of Fe_3O_4-PEG. Size distribution of Fe_3O_4-PEG by intensity (a) and raw correlation data (b). Fe_3O_4-PEG had a Z ave 55 nm and PDI of 0.2.

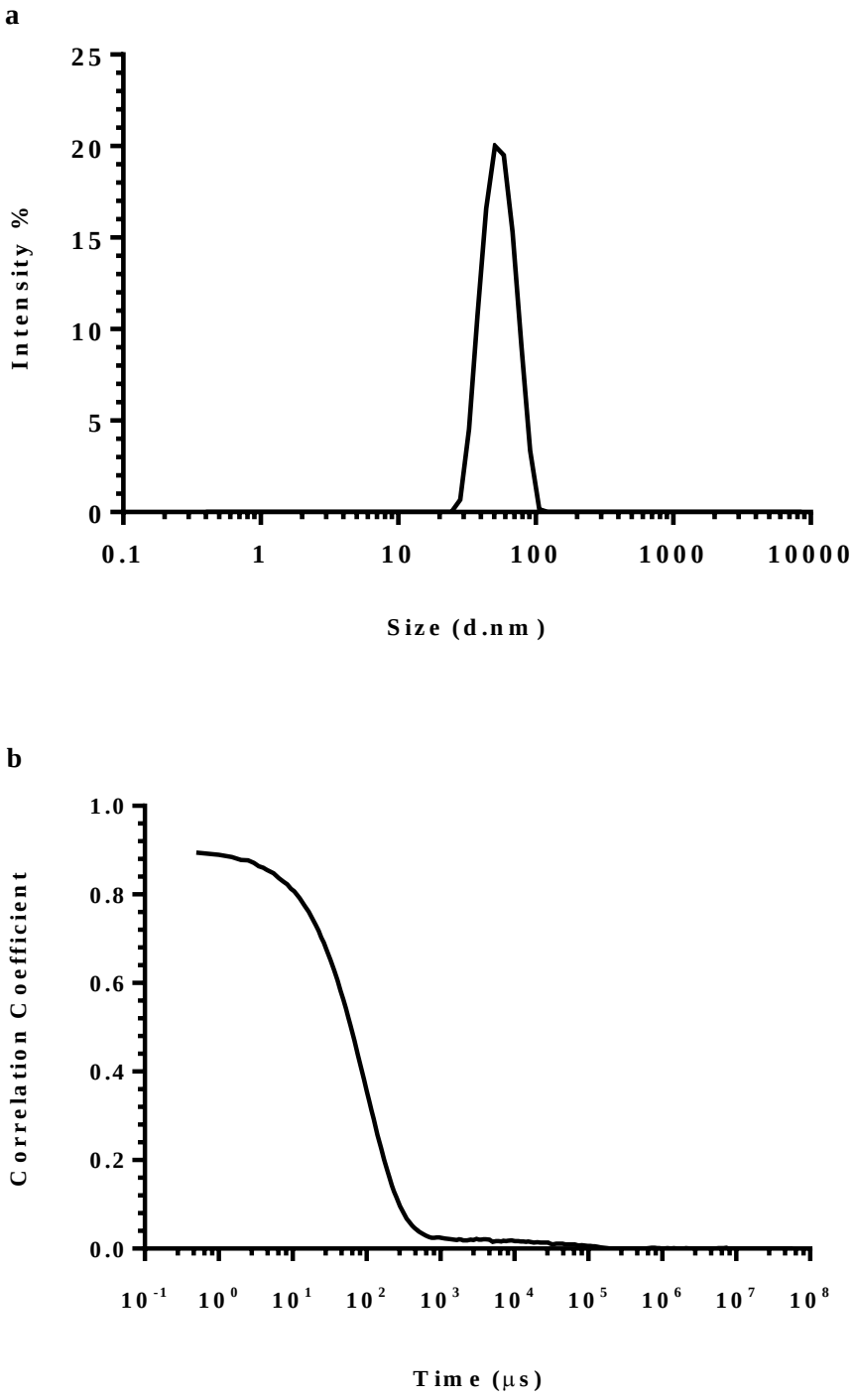

Figure 5.7.2 Representative DLS size and polydispersity analysis of Fe_3O_4-PEG-PTX. Size distribution of Fe_3O_4-PEG-PTX by intensity (a) and raw correlation data (b). Fe_3O_4-PEG-PTX had a Z ave 61 nm and PDI of 0.3.

5.8 *In vitro* efficacy studies of drug loaded Fe_3O_4 NPs

To preliminary evaluate the successful encapsulation of PTX in NPs, A549 and A2058 cell lines were incubated with Fe_3O_4-PEG-PTX and Fe_3O_4-PEP-PTX. These were normalised to the vehicle of NP without PTX. For cell viability assays, a theoretical concentration range between 750 nM and 0.3 nM of PTX was used, assuming 100% of PTX was encapsulated in the NPs. In A549 cells, Fe_3O_4-PEG-PTX and Fe_3O_4-PEP-PTX caused a marked decrease in cell viability after 72 h of incubation (figure 5.8.1); at a PTX concentration of 750 nM average cell viability was 46.4% Fe_3O_4-PEG-PTX, 72.1% Fe_3O_4-PEP-PTX, and 80.2% PTX alone. In A2058 melanoma cells, PTX encapsulated in Fe_3O_4-core NPs had a higher efficacy than PTX alone. Moreover, targeted Fe_3O_4-PEP-PTX NPs appeared more potent than Fe_3O_4-PEG-PTX.

Dose dependent toxicity of both NPs provides evidence that PTX is associated with Fe_3O_4-PEG and Fe_3O_4-PEP. In order to accurately assess the efficacy of each NP, the encapsulation of PTX must be quantified. However, as Fe_3O_4-PEP-PTX was more potent than PTX in melanoma cells and Fe_3O_4-PEP had an increased uptake in melanoma cells compared to non-melanoma cells *via* MC1R-mediated internalisation, the Fe_3O_4-PEP-PTX is an exciting prospect as a drug delivery system for the treatment of melanoma. This system has the potential for increasing drug efficacy compared to standard chemotherapy agents.

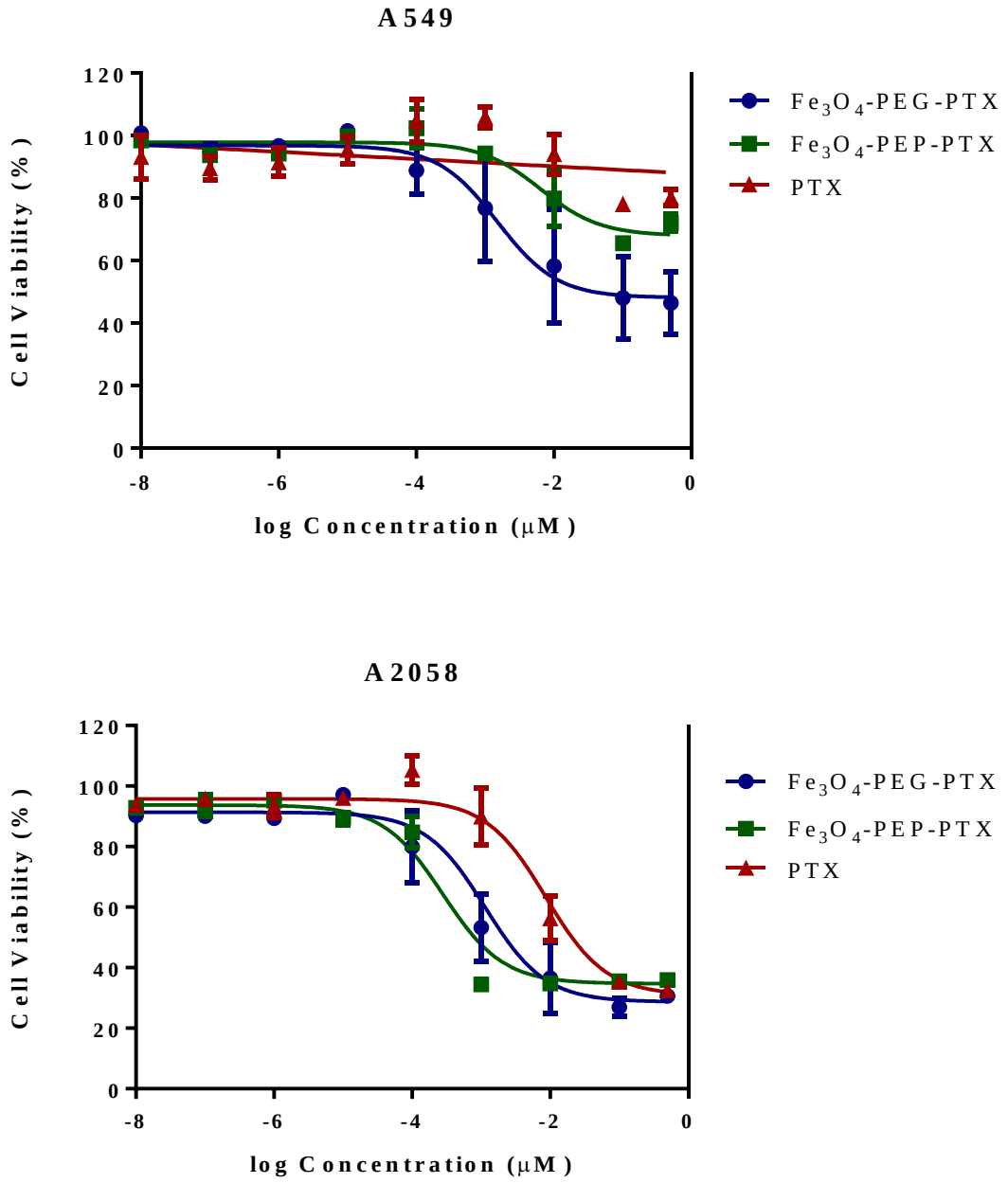

Figure 5.8.1 Cell viability of PTX loaded Fe_3O_4 core NPs in A549 and A2058 cell lines. After 72 h incubation with either Fe_3O_4-PEG-PTX, Fe_3O_4-PEP-PTX or PTX alone. All values normalised to vehicle, mean ± SD, n = 9.

5.9 Isolation of melanocytes from patient tissue

Typically, cultured cell lines provide a poor model for predicating drug efficacy in patients due to loss of heterogeneity (Kryh et al., 2011, Yaffe, 1968). We wanted to develop a methodology to assess drug efficacy as close to the patient as possible by isolating melanoma cells without prior culturing. This should provide a system that is better for assessing the efficacy of the Fe_3O_4 NP drug delivery system in patients. Patients diagnosed with cutaneous melanoma had given prior consent for biopsied tissue, after sentinel lymph node biopsy, to be used for our research. HTA-compliant Norwich Biorepository (HTA licence 11208; National Research Ethics Service reference, 08/H0304/85) ethical approval was obtained. All procedures of patient-derived melanoma cells were approved by the UEA Faculty of Medicine and Health ethics committee (Ref: 2013/2014-03HT).

Neural/glial antigen 2 (NG2), also known as melanoma chondroitin sulphate proteoglycan (MCSP), is expressed on the surface of the majority (90%) of malignant melanoma (Li et al., 2003, Russell et al., 2013). NG2 is thought to play a role in cell proliferation, adhesion, and migration (Russell et al., 2013). For this reason, NG2 was chosen as a novel marker for melanoma cells. As tissue was taken from the patient's lymph node, the lymphocyte common antigen (CD45) was used as a control (Nandedkar et al., 1998). Successfully isolated melanoma cells will be used to evaluate specificity of the Fe_3O_4-α-MSH NP (Fe_3O_4-PEP) in a model closer to the patient tissue than commercial cultured cells. As a result, the Fe_3O_4-PEP will be validated as a viable drug delivery system.

Patient tissue was collected fresh from lymphadenectomy and transferred directly to cell culture in HBSS supplemented with 2% FCS, 100 U/ml penicillin, and 100 µg/ml streptomycin. Tissue was then dissociated by breaking down collagen IV of the basal lamina, DNA, and hyaluronic acid of the connective tissue. After digestion and filtration through a 70 µm nylon filter, cells were separated into a single cell suspension (figure 5.9.1). The cell morphology suggested a range of cell types and cell debris (figure 5.9.1).

To isolate melanoma cells, the sample was stained using fluorescent antibodies targeted against NG2 and CD45 before separating cell types with FACS. First, the cell population was selected from the FS and SS dot plot, avoiding the cell debris at the origin of the x and y axis (figure 5.9.2.a.i). The single cells were then re-analysed to check the population and the cells from this gate only were used for separating $NG2^+$ and $NG2^-$ cells (figure 5.9.2.a.ii). The FL2 channel was used to identify cells positive for NG2 (y axis) and FL4 channel was used to identify $CD45^+$ cells (figure 5.9.2.a.iii). The representative data shows 45.0% of the gated single cells were positive for NG2; identified by the cluster of f events with a high FI detected by the FL2 channel (y axis). A large proportion of cells, 46.2%, were $NG2^-$ and a small population had a high relative FI detected by the FL4 channel (x axis), indicating the presence of lymphocytes. Interestingly, there was a population of cells $NG2^+/CD45^-$. These cell could be $NG2^+$ melanoma cells engulfed by $CD45^+$ lymphocytes however, as the aim was to isolate melanoma cells, the $NG2^+/CD45^+$ population were not included in the $NG2^+$ sorting. $NG2^+/CD45^-$ cells (top gate, figure 5.9.2.a.iii.) were isolated into a centrifuge tube containing supplemented RPMI-1640. Into a separate centrifuge tube, also containing supplemented RPMI-1640, the $NG2^-$ population was sorted (bottom gate, figure 5.9.2.a.iii). The separate samples were then reanalysed (figures 2.9.2.b,

2.9.2.c) to confirm the FACS machine was calibrated correctly. $NG2^-$ cells were correctly separated into centrifuge tube (figure 2.9.2.b.iii) and $NG2^+$ cells (figure 2.9.2.c.iii) were correctly separated into a different centrifuge tube.

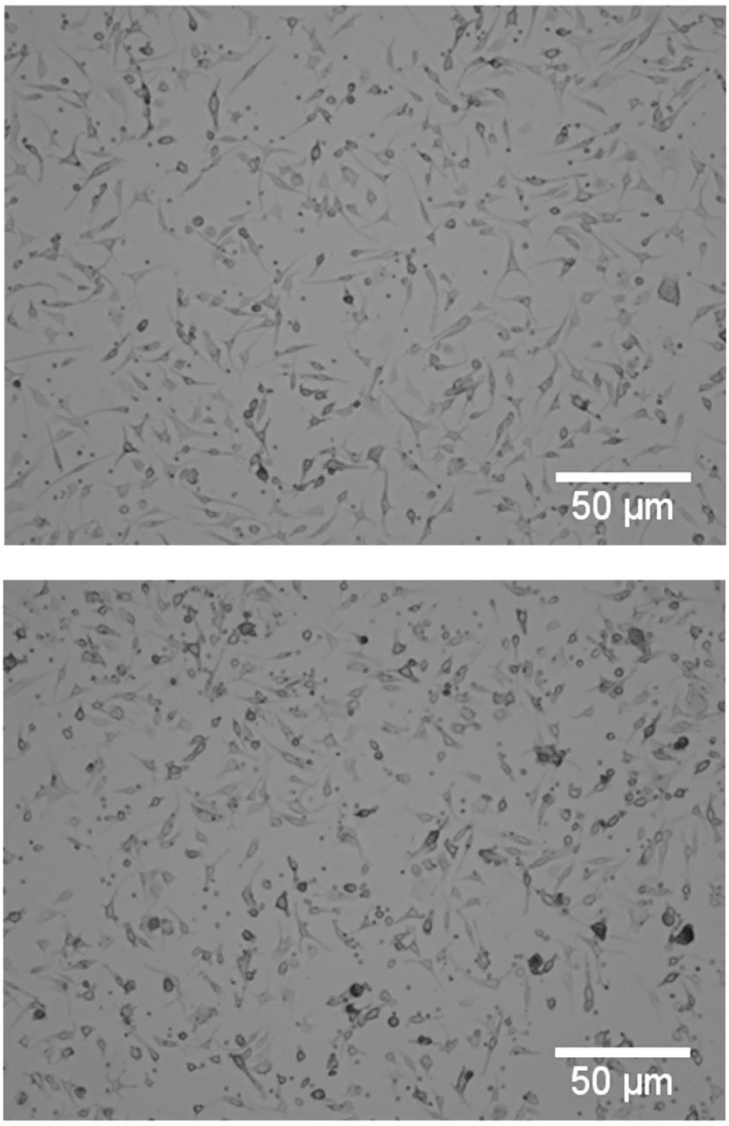

Figure 5.9.1 Patient sample after digestion and before FACs. Tissue was digested and separated into single cells.

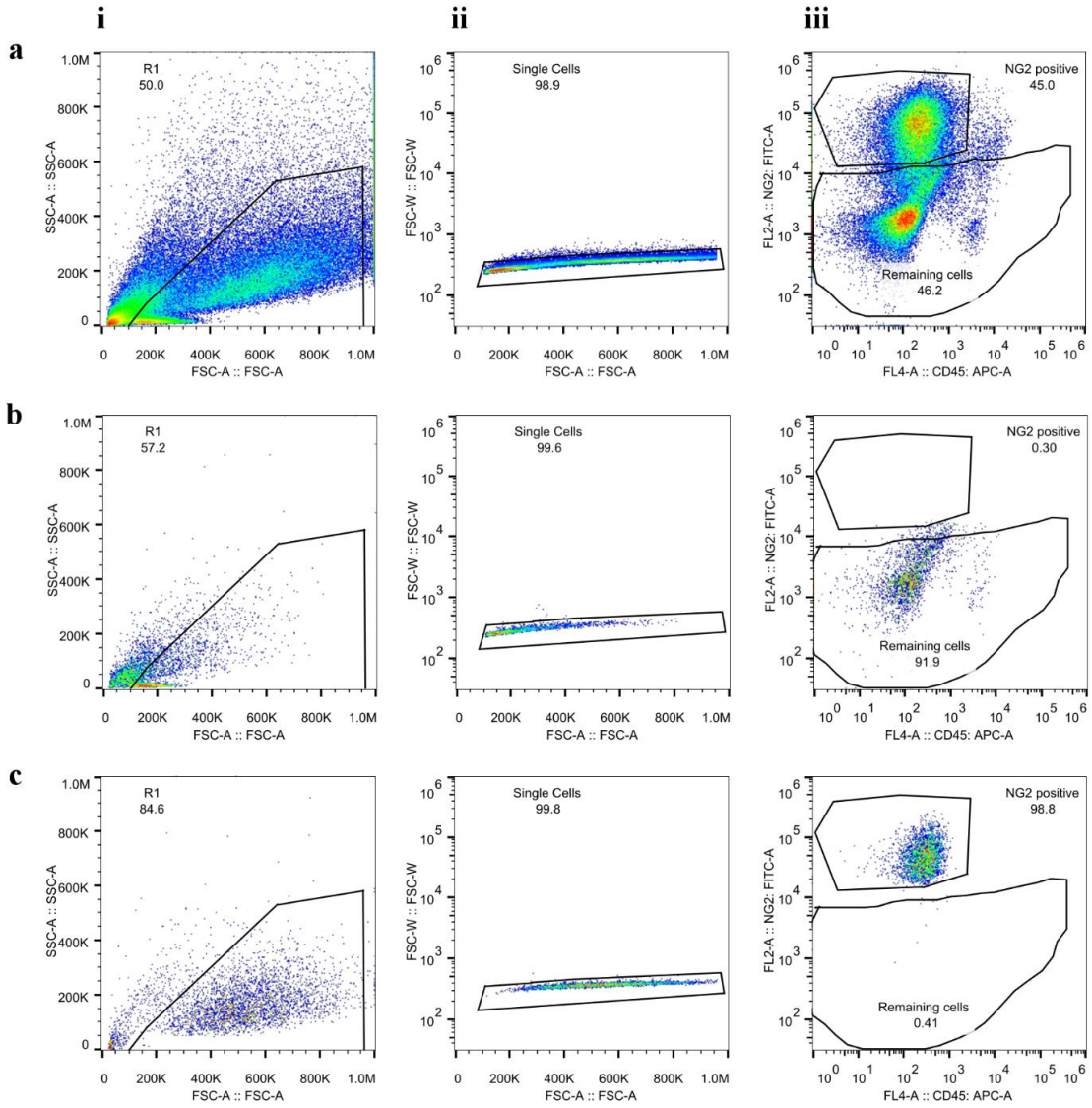

Figure 5.9.2 Digested patient tissue sample sorted by FACs into NG2$^+$ and NG2$^-$ cells. (a.i) cells were gated based on the dot plot against side scatter and forward scatter, (a.ii) the population of single cells were then gated for analysis, (a.iii) FL2 on y axis (NG2$^+$) against FL4 on x axis (CD45). Cells were gated for NG2$^+$ and remaining cells. (b, c) cells were then analysed after sorting. (b) Cells analysed after being selected as NG2$^-$, and (c) cells analysed after being selected as NG2$^+$.

After cell seeding for 24 h post FACS, the morphology of the two populations is clearly different (figure 5.9.3). $NG2^+$ cells have started to attach to the culture surface, evident by the flattened shape of the cells, whereas $NG2^-$ cells appear smaller and not attached to the culture surface. $NG2^+$ morphology continued to change over 2, 3, and 4 days as they started to differentiate (figure 5.9.4.a). After 6 days, $NG2^+$ cells had differentiated and proliferated (figure 5.9.4.b). The cells then appeared elongated and multi polar, comparable to the morphology of common cultured melanoma cells. These cells were then lysed and the presence of MC1R and Melan A protein was analysed using Western Immunoblotting (figure 5.9.4.c). $NG2^-$ and A549 (negative control) cells showed no evidence of Melan A protein expression. MC1R protein was also not found in the cell lysate of $NG2^-$ cells. The positive cells however, showed protein expression of Melan A and MC1R. Overall, it appears from the morphology and the presence of melanoma markers that sorting for NG2 has successfully isolated the melanoma from non-melanoma cells.

Importantly, the development of this method will enable us to ultimately test our novel anti-melanoma nanotherapy using a system that can isolate pure melanoma cells harvested from the patient biopsy material, several hours post-surgery.

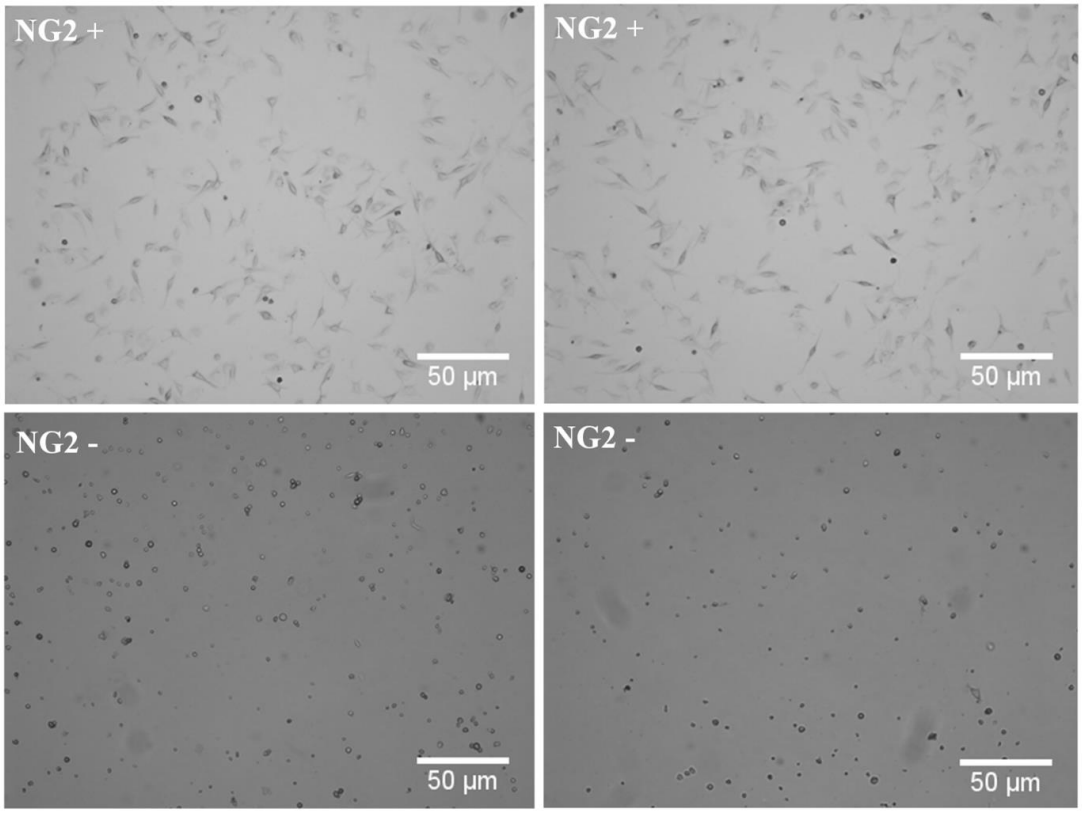

Figure 5.9.3 Patient cells after sorted by FACs into NG2^{+} and NG2^{-} populations. Cells were seeded for 24 h after FACs before imaging to assess cell morphology. Images from different fields of view of the sample patient sample. Scale bar 50 µm.

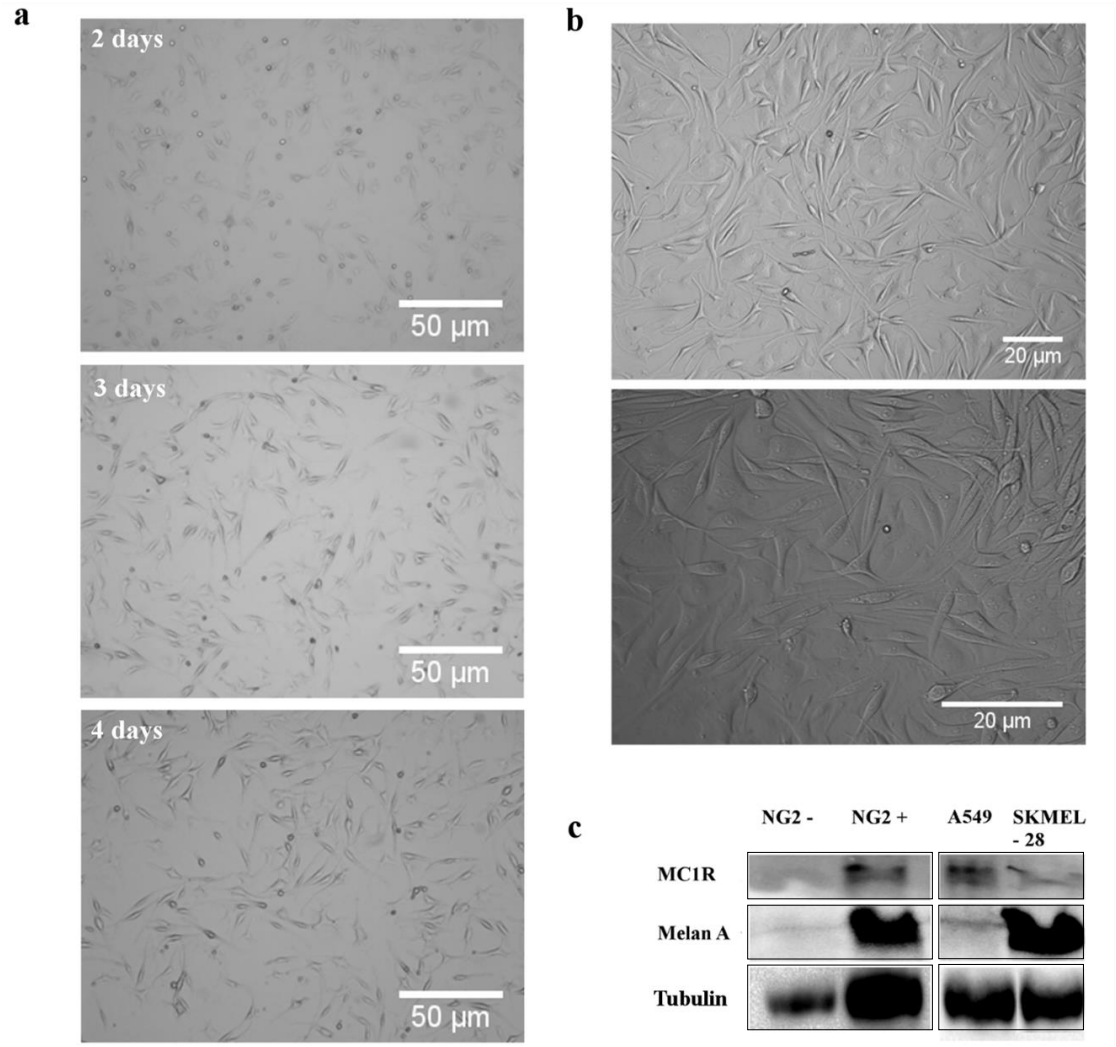

Figure 5.9.4 Characterisation of patient cells after sorted by FACs into $NG2^+$ and $NG2^-$ populations. (a) Cell morphology of $NG2^+$ cells after sorting and seeded for 2, 3, and 4 days. $NG2^+$ cells were seeded after FACs and the morphology assessed for 2, 3, and 4 days. Error bars 50 µm. (b) $NG2^+$ cells seeded after FACs and incubated for 6 days to assess cell morphology. (c) Western Immunoblot analysis of MC1R and Melan A protein levels in $NG2^-$, $NG2^+$, A549 lung cancer, and SK-MEL-28 melanoma cells. Tubulin was used as loading control.

5.10 Discussion

Targeted NPs are beginning to show great promise as drug delivery systems for the treatment of a wide variety of cancers (Kim et al., 2013, Lee et al., 2013, Lee et al., 2014, Sung et al., 2007). For melanoma, MC1R is a promising target (Tafreshi et al., 2012). We checked the expression of MC1R in a range of melanoma cell lines. M202, M229, M285, A375, and SK-MEL-28 all showed protein expression of MC1R (figure 5.2.1). However, MC1R was also seen in A549 lung cancer, MDA-MB-231 breast cancer, and HEK 293 embryonic kidney cells. Several other studies have also shown MC1R expression in non-melanocytic cell lines (Roberts et al., 2006, Salazar-Onfray et al., 2002, Tafreshi et al., 2012). Roberts et al. identified mRNA levels of MC1R in non-melanocytic cell lines including HEK 293, Colo 205 (colon), MCC 14/2 (Merkel cell carcinoma), H69 (lung), LCL (lymphoblastoid), and NHKs (human keratinocytes). After decreasing the number of amplification cycles, mRNA was not identified in the non-cancerous non-melanocytic cells, but observed in melanoma cells and human melanocytes. This suggests low levels of leaky MC1R gene expression in non-melanocytic cells and higher expression in melanoma and melanocytes. Moreover, after confocal microscopy and ligand binding assays intracellular levels of MC1R protein was observed in non-melanocytic cells. In melanoma and melanocytes, on the other hand, MC1R was found on the cell surface (Roberts et al., 2006). Extracellular expression of MC1R deviated from melanoma cells to non-melanoma cells only in *in vitro* cultured cells. It is often the case that, with an unstable genome, transferred cells for cell culture have an altered phenotype.

In this study, NR was used as a small hydrophobic molecule for proof-of-concept encapsulation into the outer shell of Fe_3O_4-PEG NP. Moreover, it had the added advantage of fluorescent properties that could be utilised for NP uptake studies into melanoma cells. As NR is insoluble in H_2O, addition of the molecule into Fe_3O_4-PEG aqueous solution forced NR into the hydrophobic shell of the NPs (figure 5.3.1.). In a solution without NPs, NR aggregated on the surface of the centrifuge tube or the dialysis membrane. As a result, only NR encapsulated in the Fe_3O_4-core NPs was dispersed in the solution (figure 5.3.2).

After encapsulation, we used the Fe_3O_4-PEG-NR as a tool to investigate NP uptake in cells. After A2058 melanoma cells were incubated with Fe_3O_4-PEG-NR cells, NR was seen intracellularly alongside Fe_3O_4-core (figure 5.4.1). As NR is a dye specifically designed for microscopy it is easy to using the confocal microscope. The Fe_3O_4-core particles, seen using reflected light, are not optimised to be seen using this type of microscopy. As a result, the NR is clearer to see than the NPs (figure 5.4.1) and it is difficult to see if there is co-localisation of the two. However, as NR is lipophilic it is safe to assume the NR either remains in the Fe_3O_4-PEG NP or is released once in the cell into adiposomes, intracellular lipids (Greenspan et al., 1985). A limitation with the use of NR as the only way to quantify the internalisation of NPs was the uncertainty that the NR stayed associated with the NP before internalisation in the cell. Internalised NR stains the hydrophobic domains of the cell (Greenspan et al., 1985), but internalisation could occur as either Fe_3O_4-NR or as free NR.

We wanted to investigate the specificity of this uptake by comparing the targeted Fe_3O_4-PEP NPs to the non-targeted Fe_3O_4-PEG NPs in both melanoma and control cells. Flow cytometry was used to quantify the cellular uptake of the NR associated with the NP. One of the advantages of using nanomaterials as drug delivery

systems in oncology is the accumulation of NPs into the tumour environment through the EPR effect (section 1.3.2). NPs are able to enter the cell through four pathways: clathrin/caveolar-mediated endocytosis, phagocytosis, macropinocytosis, and pinocytosis (Oh and Park, 2014). As a result, it was expected that the non-targeted Fe_3O_4-PEG-NR NPs cellular uptake would be observed in both melanoma and non-melanocytic cell lines through non-MC1R-mediated uptake such as pinocytosis; and the same can be said for targeted Fe_3O_4-PEP-NR NPs. However, due to the active targeting through MC1R receptor-mediated endocytosis, the rate of cellular uptake should be increased compared to other uptake mechanisms (Wileman et al., 1985). To this end, we compared cellular uptake of targeted and non-targeted NPs over time. In both melanoma cells assessed, the rate of uptake was increased. Fe_3O_4-PEP-NR NPs were internalised quicker than the non-targeted Fe_3O_4-PEG-NR NPs, whereas the non-melanocytic A549 cells showed no difference in cellular uptake between Fe_3O_4-PEG-NR and Fe_3O_4-PEP-NR NPs. Uptake in A549 increased steadily from 30 min to 1 h, where it remained at a constant level. This NP uptake can be viewed as non-MC1R-mediateduptake through uptake mechanisms such as pinocytosis. Although the extracellular presence of MC1R protein on non-melanocytic cells is disputed (Roberts et al., 2006), it is promising to see that despite the detection of MC1R protein there is no significant difference in A549 cellular uptake between Fe_3O_4-PEG-NR and Fe_3O_4-PEP-NR NPs. Furthermore, the majority of literature outlining the successful targeting of α-MSH to MC1R *in vitro* has been shown in mouse melanoma cells (Leung, 2004, Qin et al., 2014, Vannucci et al., 2012). Encouragingly, specific targeting of MC1R using our Fe_3O_4-PEP-NR system appears to be working in both mouse (B16F10) and human (A2058) melanoma cell lines. These results indicate the system is a viable candidate for *in vivo* uptake studies.

As melanocytes have cell surface expression of MC1R, albeit at a lower level than on melanoma cells (Donatien et al., 1992), the uptake in HEMA-lp cells was also investigated. It would be disadvantageous for Fe_3O_4-PEP drug loaded NPs to target healthy human cells. There was minimal uptake of both Fe_3O_4-PEG-NR and Fe_3O_4-PEP-NR NPs after 5 h incubation, and no significant difference in cellular internalisation between the non-targeted and targeted NPs (figure 5.4.8). Healthy cells have a lower metabolism and uptake molecules at a slower rate than cancer cells. In this respect, it was expected that healthy human melanocytes will have a slower endocytic activity than cancer cells and it is beneficial that our data show low Fe_3O_4 NP internalisation in the non-cancerous melanocytes and no detectable increase with the Fe_3O_4-PEP-NR targeted NP (figure 5.5.3). Data from the flow cytometry strongly suggests that if after Fe_3O_4-PEP NPs accumulate in the tumour microenvironment through EPR, then the increase rate of uptake will deliver any drug payload to the melanocytic cells; avoiding healthy non-cancer cells such as melanocytes.

Further experiments were undertaken to demonstrate that Fe_3O_4-PEP NPs were internalised through MC1R-mediated endocytosis. To block MC1R prior to incubation with Fe_3O_4-PEP NPs, B16F10 and A549 cells were incubated with an excess of α-MSH peptide (figure 5.6.7). As expected, blocking non-melanocytic A549 control cells with an excess of α-MSH had no effect on the internalisation of both Fe_3O_4-PEG-NR and Fe_3O_4-PEP-NR NPs; demonstrating non-MC1R-mediated endocytosis. In the melanocytic B16F10 cell line, blocking with an excess of α-MSH prior to Fe_3O_4-PEG-NR incubation caused no effect; again signifying NP internalisation is by means other than MC1R-mediated endocytosis. Although the peptide blocking of MC1R did not decrease the relative FI from Fe_3O_4-PEP-NR to the same FI as Fe_3O_4-PEG-NR (figure 5.6.7), there was a marked decrease in internalisation of Fe_3O_4-PEP-NR to Fe_3O_4-PEP-

NR with the peptide block. This indicates that Fe_3O_4-PEP-NR is mostly being internalised *via* MC1R. After optimisation of the amount of NR from 0.5% to 0.1% NR, blocking with α-MSH did decrease the relative FI after Fe_3O_4-PEP incubation to the same as control NPs for both melanoma cell lines (figure 5.6.8). This suggests that with the higher amount of NR (0.5%) there may be free NR being internalised into the cell. At 0.1% NR, Fe_3O_4-PEP-NR can be successfully block with an excess of α-MSH providing evidence that Fe_3O_4-PEP-NR NPs are internalised through MC1R and the relative FI from the flow cytometry is not from free NR.

After establishing uptake specificity to melanoma cells, a chemotherapeutic drug was encapsulated into the NPs. PTX was loaded into Fe_3O_4-PEG and Fe_3O_4-PEP NPs using the same principles as encapsulation of NR. Although encapsulation of PTX was not specifically quantified, lower IC50 values than PTX alone and the dose dependent loss of cell viability in A549 and A2058 cells lines suggests that a significant amount of the original concentration of PTX was successfully encapsulated into the Fe_3O_4-core NPs. There was no significant difference after incubation with either Fe_3O_4-PEG-PTX and Fe_3O_4-PEP-PTX NPs for 72 h in both cell lines. At 72 h incubation, it is feasible to suggest that comparable amounts of both the targeted and non-targeted NPs have entered the cell. As a result, cells are exposed to the delivered PTX for a similar time. To improve understanding of efficacy of PTX loaded NPs, incubation times must be optimised. The next step would be to incubate the particles for a time point where there is a difference in NP internalisation. Flow cytometry data (figure 5.4.9) would suggest that after <5 h incubation of Fe_3O_4-PEP-PTX more PTX would be delivered to melanoma cells than after the same incubation time of Fe_3O_4-PEG-PTX. If this were the case, at the lower incubation time, Fe_3O_4-PEP-PTX would be more potent to melanoma cells than Fe_3O_4-PEG-PTX. Further work also needs to

be done to quantify the concentration of PTX encapsulated into Fe_3O_4-core NP to properly understand the amount of drug delivered to the cell.

To understand uptake and drug efficacy of the Fe_3O_4 delivery system, we wanted to test as close to the patient as possible. In order to do that, we established a method for isolating melanoma cells from resected tissue containing multiple cell types. Melanoma cells were sorted, using FACS, by discriminating against $NG2^+$ and $NG2^-$ cell populations (figure 5.6.2). Cell morphology was clearly different between the $NG2^+$ and $NG2^-$ cells (figure 5.6.3). $NG2^+$ cells then went on to proliferate and differentiate after seeding from 2 to 6 days (figure 5.6.4, 5.6.5.a). After differentiation, elongation and polarisation of the cells provided cell morphology similar to recognised melanoma cell lines (figure 5.6.5.a). Moreover, protein expression of $NG2^+$ cells was consistent with melanoma (figure 5.6.5.b). Further characterisation of $NG2^+$/$NG2^-$ cells is needed to convincingly confirm isolation of melanoma cells, but initial results show promise. A limiting step with the protocol was obtaining appropriate tissue. The amount of melanoma cells from resection varied greatly between samples. However, with the melanoma cell isolation protocol working, it leads the way for exciting experiments using the Fe_3O_4 drug system.

5.11 References

Acharya, U. H. & Jeter, J. M. 2013. Use of ipilimumab in the treatment of melanoma. *Clinical Pharmacology : Advances and Applications,* 5**,** 21-27.

Almeida, M. Q., Kaupert, L. C., Brito, L. P., Lerario, A. M., Mariani, B. M., Ribeiro, M., Monte, O., Denes, F. T., Mendonca, B. B. & Bachega, T. A. 2014. Increased expression of ACTH (MC2R) and androgen (AR) receptors in giant bilateral myelolipomas from patients with congenital adrenal hyperplasia. *BMC Endocr Disord,* 14**,** 42.

Arnal, I. & Wade, R. H. 1995. How does taxol stabilize microtubules? *Curr Biol,* 5**,** 900-8.

Balch, C. M., Gershenwald, J. E., Soong, S. J., Thompson, J. F., Atkins, M. B., Byrd, D. R., Buzaid, A. C., Cochran, A. J., Coit, D. G., Ding, S., Eggermont, A. M., Flaherty, K. T., Gimotty, P. A., Kirkwood, J. M., Mcmasters, K. M., Mihm, M. C., Jr., Morton, D. L., Ross, M. I., Sober, A. J. & Sondak, V. K. 2009. Final version of 2009 AJCC melanoma staging and classification. *J Clin Oncol,* 27**,** 6199-206.

Bombelli, F. B., Webster, C. A., Moncrieff, M. & Sherwood, V. 2014. The scope of nanoparticle therapies for future metastatic melanoma treatment. *Lancet Oncol,* 15**,** e22-32.

Bork, S., Pfister, S., Witt, H., Horn, P., Korn, B., Ho, A. D. & Wagner, W. 2010. DNA methylation pattern changes upon long-term culture and aging of human mesenchymal stromal cells. *Aging Cell,* 9**,** 54-63.

Brahmer, J. R., Tykodi, S. S., Chow, L. Q., Hwu, W. J., Topalian, S. L., Hwu, P., Drake, C. G., Camacho, L. H., Kauh, J., Odunsi, K., Pitot, H. C., Hamid, O., Bhatia, S., Martins, R., Eaton, K., Chen, S., Salay, T. M., Alaparthy, S., Grosso, J. F., Korman, A. J., Parker, S. M., Agrawal, S., Goldberg, S. M., Pardoll, D. M., Gupta, A. & Wigginton, J. M. 2012. Safety and activity of anti-PD-L1 antibody in patients with advanced cancer. *N Engl J Med,* 366**,** 2455-65.

Brigger, I., Dubernet, C. & Couvreur, P. 2012. Nanoparticles in cancer therapy and diagnosis. *Advanced drug delivery reviews,* 64**,** 24-36.

Cai, M., Mayorov, A. V., Cabello, C., Stankova, M., Trivedi, D. & Hruby, V. J. 2005. Novel 3D pharmacophore of alpha-MSH/gamma-MSH hybrids leads to selective human MC1R and MC3R analogues. *J Med Chem,* 48**,** 1839-48.

Carrera, C., Puig-Butille, J. A., Tell-Marti, G., Garcia, A., Badenas, C., Alos, L., Puig, S. & Malvehy, J. 2015. Multiple BRAF Wild-Type Melanomas During Dabrafenib Treatment for Metastatic BRAF-Mutant Melanoma. *JAMA Dermatol,* 151**,** 544-8.

Carvajal, R. D., Sosman, J. A., Quevedo, J. F., Milhem, M. M., Joshua, A. M., Kudchadkar, R. R., Linette, G. P., Gajewski, T. F., Lutzky, J., Lawson, D. H., Lao, C. D., Flynn, P. J., Albertini, M. R., Sato, T., Lewis, K., Doyle, A., Ancell, K., Panageas, K. S., Bluth, M., Hedvat, C., Erinjeri, J., Ambrosini, G., Marr, B., Abramson, D. H., Dickson, M. A., Wolchok, J. D., Chapman, P. B. & Schwartz, G. K. 2014. Effect of selumetinib vs chemotherapy on progression-free survival in uveal melanoma: a randomized clinical trial. *JAMA,* 311**,** 2397-405.

Chapman, P. B., Hauschild, A., Robert, C., Haanen, J. B., Ascierto, P., Larkin, J., Dummer, R., Garbe, C., Testori, A., Maio, M., Hogg, D., Lorigan, P., Lebbe, C., Jouary, T., Schadendorf, D., Ribas, A., O'day, S. J., Sosman, J. A., Kirkwood, J. M., Eggermont, A. M., Dreno, B., Nolop, K., Li, J., Nelson, B., Hou, J., Lee, R. J., Flaherty, K. T., Mcarthur, G. A. & Group, B.-S. 2011. Improved survival with vemurafenib in melanoma with BRAF V600E mutation. *N Engl J Med,* 364**,** 2507-16.

Chen, Y., Wu, J. J. & Huang, L. 2010. Nanoparticles Targeted With NGR Motif Deliver c-myc siRNA and Doxorubicin for Anticancer Therapy. *Molecular Therapy,* 18**,** 828-834.

Chhajlani, V., Xu, X., Blauw, J. & Sudarshi, S. 1996. Identification of ligand binding residues in extracellular loops of the melanocortin 1 receptor. *Biochem Biophys Res Commun,* 219**,** 521-5.

Chin, L. 2003. The genetics of malignant melanoma: lessons from mouse and man. *Nat Rev Cancer,* 3**,** 559-570.

Das Thakur, M., Salangsang, F., Landman, A. S., Sellers, W. R., Pryer, N. K., Levesque, M. P., Dummer, R., Mcmahon, M. & Stuart, D. D. 2013. Modelling vemurafenib resistance in melanoma reveals a strategy to forestall drug resistance. *Nature,* 494**,** 251-255.

Donatien, P., Surlève-Bazeille, J. E., Thody, A. J. & Taïeb, A. Growth and differentiation of normal human melanocytes in a TPA-free, cholera toxin-free, low-serum medium and influence of keratinocytes. *Archives of Dermatological Research,* 285**,** 385-392.

Donatien, P. D., Hunt, G., Pieron, C., Lunec, J., Taieb, A. & Thody, A. J. 1992. The expression of functional MSH receptors on cultured human melanocytes. *Arch Dermatol Res,* 284**,** 424-6.

Edgar, R., Domrachev, M. & Lash, A. E. 2002. Gene Expression Omnibus: NCBI gene expression and hybridization array data repository. *Nucleic Acids Res,* 30**,** 207-10.

Garcia-Borron, J. C., Sanchez-Laorden, B. L. & Jimenez-Cervantes, C. 2005. Melanocortin-1 receptor structure and functional regulation. *Pigment Cell Res,* 18**,** 393-410.

Greenspan, P., Mayer, E. P. & Fowler, S. D. 1985. Nile red: a selective fluorescent stain for intracellular lipid droplets. *The Journal of Cell Biology,* 100**,** 965-973.

Hadley, M. E., Mieyr, J. H., Martin, B. E., Castrucci, A. M., Hruby, V. J., Sawyer, T. K., Powers, E. A. & Rao, K. R. 1985. [Nle4, D-Phe7]-alpha-MSH: a superpotent melanotropin with prolonged action on vertebrate chromatophores. *Comp Biochem Physiol A Comp Physiol,* 81**,** 1-6.

Haskell-Luevano, C., Sawyer, T. K., Trumpp-Kallmeyer, S., Bikker, J. A., Humblet, C., Gantz, I. & Hruby, V. J. 1996. Three-dimensional molecular models of the hMC1R melanocortin receptor: complexes with melanotropin peptide agonists. *Drug Des Discov,* 14**,** 197-211.

Hodi, F. S., O'day, S. J., Mcdermott, D. F., Weber, R. W., Sosman, J. A., Haanen, J. B., Gonzalez, R., Robert, C., Schadendorf, D., Hassel, J. C., Akerley, W., Van Den Eertwegh, A. J., Lutzky, J., Lorigan, P., Vaubel, J. M., Linette, G. P., Hogg, D., Ottensmeier, C. H., Lebbe, C., Peschel, C., Quirt, I., Clark, J. I., Wolchok, J. D., Weber, J. S., Tian, J., Yellin, M. J., Nichol, G. M., Hoos, A. & Urba, W. J. 2010. Improved survival with ipilimumab in patients with metastatic melanoma. *N Engl J Med,* 363**,** 711-23.

Hood, J. D., Bednarski, M., Frausto, R., Guccione, S., Reisfeld, R. A., Xiang, R. & Cheresh, D. A. 2002. Tumor regression by targeted gene delivery to the neovasculature. *Science,* 296**,** 2404-7.

Ito, F. & Chang, A. E. 2013. Cancer Immunotherapy: Current Status and Future Directions. *Surgical Oncology Clinics of North America,* 22**,** 765-783.

Kainthla, R., Kim, K. B. & Falchook, G. S. 2014. Dabrafenib for treatment of BRAF-mutant melanoma. *Pharmgenomics Pers Med,* 7**,** 21-9.

Keilholz, U. 2008. CTLA-4: negative regulator of the immune response and a target for cancer therapy. *J Immunother,* 31**,** 431-9.

Kim, S. M., Im, G. H., Lee, D.-G., Lee, J. H., Lee, W. J. & Lee, I. S. 2013. Mn2+-doped silica nanoparticles for hepatocyte-targeted detection of liver cancer in T1-weighted MRI. *Biomaterials,* 34**,** 8941-8948.

Kottschade, L. A., Suman, V. J., Amatruda, T., Mcwilliams, R. R., Mattar, B. I., Nikcevich, D. A., Behrens, R., Fitch, T. R., Jaslowski, A. J. & Markovic, S. N. 2011. A phase II trial of nab‐paclitaxel (ABI‐007) and carboplatin in patients with unresectable stage IV melanoma. *Cancer,* 117**,** 1704-1710.

Kottschade, L. A., Suman, V. J., Perez, D. G., Mcwilliams, R. R., Kaur, J. S., Amatruda, T. T., Geoffroy, F. J., Gross, H. M., Cohen, P. A. & Jaslowski, A. J. 2013. A randomized phase 2 study of temozolomide and bevacizumab or nab‐paclitaxel, carboplatin, and bevacizumab in patients with unresectable stage IV melanoma. *Cancer,* 119**,** 586-592.

Kryh, H., Carén, H., Erichsen, J., Sjöberg, R.-M., Abrahamsson, J., Kogner, P. & Martinsson, T. 2011. Comprehensive SNP array study of frequently used neuroblastoma cell lines; copy neutral loss of heterozygosity is common in the cell lines but uncommon in primary tumors. *BMC Genomics,* 12**,** 1-11.

Lee, G. Y., Qian, W. P., Wang, L., Wang, Y. A., Staley, C. A., Satpathy, M., Nie, S., Mao, H. & Yang, L. 2013. Theranostic Nanoparticles with Controlled Release of Gemcitabine for Targeted Therapy and MRI of Pancreatic Cancer. *ACS Nano,* 7**,** 2078-2089.

Lee, J., Chatterjee, D. K., Lee, M. H. & Krishnan, S. 2014. Gold nanoparticles in breast cancer treatment: Promise and potential pitfalls. *Cancer Letters,* 347**,** 46-53.

Lens, M. B. & Dawes, M. 2004. Global perspectives of contemporary epidemiological trends of cutaneous malignant melanoma. *British Journal of Dermatology,* 150**,** 179-185.

Leung, K. 2004. Poly(ethylene glycol)-coated gold nanocages bioconjugated with [Nle4,d-Phe7]-alpha-melanotropin-stimulating hormone. *Molecular Imaging and Contrast Agent Database (MICAD).* Bethesda (MD).

Levy, C., Khaled, M. & Fisher, D. E. 2006. MITF: master regulator of melanocyte development and melanoma oncogene. *Trends in Molecular Medicine,* 12**,** 406-414.

Li, Y., Madigan, M. C., Lai, K., Conway, R. M., Billson, F. A., Crouch, R. & Allen, B. J. 2003. Human uveal melanoma expresses NG2 immunoreactivity. *Br J Ophthalmol,* 87**,** 629-32.

Miller , K., Wang , M., Gralow , J., Dickler , M., Cobleigh , M., Perez , E. A., Shenkier , T., Cella , D. & Davidson , N. E. 2007. Paclitaxel plus Bevacizumab versus Paclitaxel Alone for Metastatic Breast Cancer. *New England Journal of Medicine,* 357**,** 2666-2676.

Millington, G. W. 2007. The role of proopiomelanocortin (POMC) neurones in feeding behaviour. *Nutr Metab (Lond),* 4**,** 18.

Nandedkar, M. A., Palazzo, J., Abbondanzo, S. L., Lasota, J. & Miettinen, M. 1998. CD45 (leukocyte common antigen) immunoreactivity in metastatic undifferentiated and neuroendocrine carcinoma: a potential diagnostic pitfall. *Mod Pathol,* 11**,** 1204-10.

Oh, N. & Park, J.-H. 2014. Endocytosis and exocytosis of nanoparticles in mammalian cells. *International Journal of Nanomedicine,* 9**,** 51-63.

Parry, R. V., Chemnitz, J. M., Frauwirth, K. A., Lanfranco, A. R., Braunstein, I., Kobayashi, S. V., Linsley, P. S., Thompson, C. B. & Riley, J. L. 2005. CTLA-4 and PD-1 receptors inhibit T-cell activation by distinct mechanisms. *Molecular and cellular biology,* 25**,** 9543-9553.

Perez, D. G., Suman, V. J., Fitch, T. R., Amatruda, T., Morton, R. F., Jilani, S. Z., Constantinou, C. L., Egner, J. R., Kottschade, L. A. & Markovic, S. N. 2009. Phase 2 trial of carboplatin, weekly paclitaxel, and biweekly bevacizumab in patients with unresectable stage IV melanoma. *Cancer,* 115**,** 119-127.

Prusis, P., Frandberg, P. A., Muceniece, R., Kalvinsh, I. & Wikberg, J. E. 1995. A three dimensional model for the interaction of MSH with the melanocortin-1 receptor. *Biochem Biophys Res Commun,* 210**,** 205-10.

Prusis, P., Schioth, H. B., Muceniece, R., Herzyk, P., Afshar, M., Hubbard, R. E. & Wikberg, J. E. 1997. Modeling of the three-dimensional structure of the human

melanocortin 1 receptor, using an automated method and docking of a rigid cyclic melanocyte-stimulating hormone core peptide. *J Mol Graph Model,* 15**,** 307-17, 334.

Qin, C., Liu, H., Chen, K., Hu, X., Ma, X., Lan, X., Zhang, Y. & Cheng, Z. 2014. Theranostics of malignant melanoma with 64CuCl2. *J Nucl Med,* 55**,** 812-7.

Ringholm, A., Klovins, J., Rudzish, R., Phillips, S., Rees, J. L. & Schioth, H. B. 2004. Pharmacological characterization of loss of function mutations of the human melanocortin 1 receptor that are associated with red hair. *J Invest Dermatol,* 123**,** 917-23.

Robert, C., Karaszewska, B., Schachter, J., Rutkowski, P., Mackiewicz, A., Stroiakovski, D., Lichinitser, M., Dummer, R., Grange, F., Mortier, L., Chiarion-Sileni, V., Drucis, K., Krajsova, I., Hauschild, A., Lorigan, P., Wolter, P., Long, G. V., Flaherty, K., Nathan, P., Ribas, A., Martin, A.-M., Sun, P., Crist, W., Legos, J., Rubin, S. D., Little, S. M. & Schadendorf, D. 2015. Improved Overall Survival in Melanoma with Combined Dabrafenib and Trametinib. *New England Journal of Medicine,* 372**,** 30-39.

Robert, C., Thomas, L., Bondarenko, I., O'day, S., Weber, J., Garbe, C., Lebbe, C., Baurain, J. F., Testori, A., Grob, J. J., Davidson, N., Richards, J., Maio, M., Hauschild, A., Miller, W. H., Jr., Gascon, P., Lotem, M., Harmankaya, K., Ibrahim, R., Francis, S., Chen, T. T., Humphrey, R., Hoos, A. & Wolchok, J. D. 2011. Ipilimumab plus dacarbazine for previously untreated metastatic melanoma. *N Engl J Med,* 364**,** 2517-26.

Roberts, D. W., Newton, R. A., Beaumont, K. A., Helen Leonard, J. & Sturm, R. A. 2006. Quantitative analysis of MC1R gene expression in human skin cell cultures. *Pigment Cell Res,* 19**,** 76-89.

Roberts, P. J. & Der, C. J. 2007. Targeting the Raf-MEK-ERK mitogen-activated protein kinase cascade for the treatment of cancer. *Oncogene,* 26**,** 3291-3310.

Roos, W. P., Quiros, S., Krumm, A., Merz, S., Switzeny, O. J., Christmann, M., Loquai, C. & Kaina, B. 2014. B-Raf inhibitor vemurafenib in combination with temozolomide and fotemustine in the killing response of malignant melanoma cells. *Oncotarget,* 5**,** 12607-20.

Russell, K. C., Tucker, H. A., Bunnell, B. A., Andreeff, M., Schober, W., Gaynor, A. S., Strickler, K. L., Lin, S., Lacey, M. R. & O'connor, K. C. 2013. Cell-surface expression of neuron-glial antigen 2 (NG2) and melanoma cell adhesion

molecule (CD146) in heterogeneous cultures of marrow-derived mesenchymal stem cells. *Tissue Eng Part A,* 19**,** 2253-66.

Salazar-Onfray, F., Lopez, M., Lundqvist, A., Aguirre, A., Escobar, A., Serrano, A., Korenblit, C., Petersson, M., Chhajlani, V., Larsson, O. & Kiessling, R. 2002. Tissue distribution and differential expression of melanocortin 1 receptor, a malignant melanoma marker. *Br J Cancer,* 87**,** 414-22.

Sarfati, G., Dvir, T., Elkabets, M., Apte, R. N. & Cohen, S. 2011. Targeting of polymeric nanoparticles to lung metastases by surface-attachment of YIGSR peptide from laminin. *Biomaterials,* 32**,** 152-61.

Sawyer, T. K., Sanfilippo, P. J., Hruby, V. J., Engel, M. H., Heward, C. B., Burnett, J. B. & Hadley, M. E. 1980. 4-Norleucine, 7-D-phenylalanine-alpha-melanocyte-stimulating hormone: a highly potent alpha-melanotropin with ultralong biological activity. *Proc Natl Acad Sci U S A,* 77**,** 5754-8.

Schartz, N. E., Farges, C., Madelaine, I., Bruzzoni, H., Calvo, F., Hoos, A. & Lebbe, C. 2010. Complete regression of a previously untreated melanoma brain metastasis with ipilimumab. *Melanoma Res,* 20**,** 247-50.

Shaul, Y. D. & Seger, R. 2007. The MEK/ERK cascade: From signaling specificity to diverse functions. *Biochimica et Biophysica Acta (BBA) - Molecular Cell Research,* 1773**,** 1213-1226.

Shevtsov, M. A., Nikolaev, B. P., Yakovleva, L. Y., Marchenko, Y. Y., Dobrodumov, A. V., Mikhrina, A. L., Martynova, M. G., Bystrova, O. A., Yakovenko, I. V. & Ischenko, A. M. 2014. Superparamagnetic iron oxide nanoparticles conjugated with epidermal growth factor (SPION–EGF) for targeting brain tumors. *International Journal of Nanomedicine,* 9**,** 273-287.

Simberg, D., Duza, T., Park, J. H., Essler, M., Pilch, J., Zhang, L., Derfus, A. M., Yang, M., Hoffman, R. M., Bhatia, S., Sailor, M. J. & Ruoslahti, E. 2007. Biomimetic amplification of nanoparticle homing to tumors. *Proceedings of the National Academy of Sciences of the United States of America,* 104**,** 932-936.

Smith, A. G., Box, N. F., Marks, L. H., Chen, W., Smit, D. J., Wyeth, J. R., Huttley, G. A., Easteal, S. & Sturm, R. A. 2001. The human melanocortin-1 receptor locus: analysis of transcription unit, locus polymorphism and haplotype evolution. *Gene,* 281**,** 81-94.

Sugahara, K. N., Teesalu, T., Karmali, P. P., Kotamraju, V. R., Agemy, L., Girard, O. M., Hanahan, D., Mattrey, R. F. & Ruoslahti, E. 2009. Tissue-penetrating delivery of compounds and nanoparticles into tumors. *Cancer cell,* 16**,** 510-520.

Sullivan, R. J. & Flaherty, K. T. 2011. BRAF in Melanoma: Pathogenesis, Diagnosis, Inhibition, and Resistance. *J Skin Cancer,* 2011**,** 423239.

Sung, J. C., Pulliam, B. L. & Edwards, D. A. 2007. Nanoparticles for drug delivery to the lungs. *Trends in Biotechnology,* 25**,** 563-570.

Suzuki, I., Cone, R. D., Im, S., Nordlund, J. & Abdel-Malek, Z. A. 1996. Binding of melanotropic hormones to the melanocortin receptor MC1R on human melanocytes stimulates proliferation and melanogenesis. *Endocrinology,* 137**,** 1627-33.

Tafreshi, N. K., Huang, X., Moberg, V. E., Barkey, N. M., Sondak, V. K., Tian, H., Morse, D. L. & Vagner, J. 2012. Synthesis and characterization of a melanoma-targeted fluorescence imaging probe by conjugation of a melanocortin 1 receptor (MC1R) specific ligand. *Bioconjug Chem,* 23**,** 2451-9.

Tafreshi, N. K., Silva, A., Estrella, V. C., Mccardle, T. W., Chen, T., Jeune-Smith, Y., Lloyd, M. C., Enkemann, S. A., Smalley, K. S., Sondak, V. K., Vagner, J. & Morse, D. L. 2013. In vivo and in silico pharmacokinetics and biodistribution of a melanocortin receptor 1 targeted agent in preclinical models of melanoma. *Mol Pharm,* 10**,** 3175-85.

Topalian, S. L., Hodi, F. S., Brahmer, J. R., Gettinger, S. N., Smith, D. C., Mcdermott, D. F., Powderly, J. D., Carvajal, R. D., Sosman, J. A., Atkins, M. B., Leming, P. D., Spigel, D. R., Antonia, S. J., Horn, L., Drake, C. G., Pardoll, D. M., Chen, L., Sharfman, W. H., Anders, R. A., Taube, J. M., Mcmiller, T. L., Xu, H., Korman, A. J., Jure-Kunkel, M., Agrawal, S., Mcdonald, D., Kollia, G. D., Gupta, A., Wigginton, J. M. & Sznol, M. 2012. Safety, activity, and immune correlates of anti-PD-1 antibody in cancer. *N Engl J Med,* 366**,** 2443-54.

Vannucci, L., Falvo, E., Fornara, M., Di Micco, P., Benada, O., Krizan, J., Svoboda, J., Hulikova-Capkova, K., Morea, V., Boffi, A. & Ceci, P. 2012. Selective targeting of melanoma by PEG-masked protein-based multifunctional nanoparticles. *Int J Nanomedicine,* 7**,** 1489-509.

Wang, H., Cheng, G., Du, Y., Ye, L., Chen, W., Zhang, L., Wang, T., Tian, J. & Fu, F. 2013. Hypersensitivity reaction studies of a polyethoxylated castor oil-free, liposome-based alternative paclitaxel formulation. *Mol Med Rep,* 7**,** 947-52.

Wang, M. & Thanou, M. 2010. Targeting nanoparticles to cancer. *Pharmacological Research,* 62**,** 90-99.

Wileman, T., Harding, C. & Stahl, P. 1985. Receptor-mediated endocytosis. *Biochem J,* 232**,** 1-14.

Yaffe, D. 1968. Retention of differentiation potentialities during prolonged cultivation of myogenic cells. *Proceedings of the National Academy of Sciences,* 61**,** 477-483.

Zitvogel, L. & Kroemer, G. 2012. Targeting PD-1/PD-L1 interactions for cancer immunotherapy. *Oncoimmunology,* 1**,** 1223-1225.

Chapter 6.

Discussion

6.1 Discussion

The use of conventional chemotherapeutics and radiation in oncology is widely regarded as out-dated (Hanahan and Weinberg, 2011). For the treatment of melanoma, resection of the tumour still represents the best chance of survival. Once metastasised, prognosis is poor; the 5-year survival rate for stage 4 melanoma is approximately 15-20% (Dickson and Gershenwald, 2011). Before 2011, the chemotherapeutic drug dacarbazine (DTIC) was part of a standardised treatment. However, DTIC produced a tumour response in only 10-15% of patients and furthermore, did not increase progression-free survival (Middleton et al., 2000). A significant advancement in the genes and molecular mechanisms involved in melanoma tumorigenesis, the tumour microenvironment, and melanoma progression, contributed to the development of more targeted melanoma drugs (Flaherty et al., 2012). The discovery that the tumour in 50 % of melanoma patients harboured the BRAF Val600 mutation led to targeted drugs that inhibit the MAPK signalling pathway, of which BRAF is a component. These drugs include vemurafenib, dabrafenib, and trametinib. Although tumour response can be seen in patients treated with BRAF inhibitors, there is typically only a minimal increase in the median survival (5-7 months; (Jang and Atkins, 2013). This relapse due to the formation of tumour resistance. Changes in BRAF, such as abhorrent upregulation of mutated BRAF and the truncation of the BRAF protein (leading to an increase in kinase activity) accounts for drug resistance in 30% of patients (Poulikakos et al., 2011, Shi et al., 2012). As a result, attention is now focused on developing combinational therapies such as BRAF inhibitors with immunotherapy (including iplimumab and anti-PD1 antibody).

The use of multifunctional nanoparticles (NPs) in oncology is being explored as a way to overcome the limitations conventional chemotherapeutics. Importantly, NP drug delivery systems are able to accumulate in the tumour primarily through the enhanced permeability and retention (EPR) effect and be taken up in cancer cells more readily than in healthy cells; a strategy which limits systemic toxicity. Moreover, by combining several drugs into the nanoformulation, NPs are able to overcome common resistance mechanisms which can lead to patient relapse.

Fe_3O_4 NPs are being developed as drug delivery systems for a range of cancers due to the unique properties of the material; specifically, when Fe_3O_4 is capable of exhibiting superparamagnetic (SPM) properties. For example, Fe_3O_4 cores have been shown to work well as MRI contrast agents (Gamarra et al., 2010, Wang et al., 2009). This approach is particularly useful as a diagnostic tool as the current procedure (sentinel lymph node biopsy) is invasive to the patient. Moreover, Fe_3O_4 NPs have also demonstrated that they can be used for further therapeutic benefits through thermal ablation treatment (Lin et al., 2014).

The synthesis method outlined in chapter 3 produced highly monodispersed Fe_3O_4 NPs that were within a size range to exhibit superparamagnetic (SPM) properties (Xuan et al., 2009). Moreover, they were functionalised to be water soluble and stable in a biologically relevant environment, which is a mandatory requirement for intravenous administration. The DLS data showed no aggregation of Fe_3O_4-PEG NPs in the presence of proteins, which would suggest Fe_3O_4-PEG NPs would be stable in the blood stream. The use of PEG as stabilising agent is widely accepted to prevent clearance through the RES system and prolong circulation time (Xie et al., 2007).

Before further development, Fe_3O_4 NPs were assessed for potential toxicity. Currently, there is no standardised toxicity assessment for NPs, and this has hindered

the advancement of NPs to clinical use (Nyström and Fadeel, 2012). To address this, in chapter 4 we showed that the combination of cytotoxicity assays with a *X. laevis* phenotypic abnormality assay provided accurate toxicity data that was comparable to using a mouse model (Webster et al., 2016). The assay could rapidly identify NP-induced toxicity that would otherwise be missed with conventional cytotoxicity assays at an early stage of multi-functional NP development. This work correlates with initiatives that aim to reduce the number of animals used in medical research as higher vertebrate models are replaced by the more primitive organism *X. laevis* at the early stages of toxicity assessment. Other research groups have also investigated using lower phylogenetic organisms for nanotoxicology asessement. For example, with similar advantages to using *X. laevis,* zebrafish has been proposed as another suitable toxicity model (Chen et al., 2016, Fako and Furgeson, 2009, Wehmas et al., 2015). The research presented in chapter 3 advances the knowledge of the use of developmental animal models in nanotoxicology and provides evidence that parallel cytotoxicity, and *in vivo* analysis is needed for accurate nanotoxicity assessment. Fe_3O_4 NPs that we developed in chapter 3 were put through this robust toxicity protocol. After parallel assessment with cytotoxic and *X. laevis* phenotypic assays, Fe_3O_4 NPs showed no signs of potential toxicity in these systems. These results were reinforced using a rodent model.

The main aim of this work was to produce a NP that could specifically target melanoma cells. To achieve this, we sought to target the upregulated melanocortin 1 receptor (MC1R; (Cai et al., 2005) using the agonist α-MSH. FT-IR analysis confirmed attachment of the α-MSH-PEG conjugate on the surface of Fe_3O_4 NPs. Successful encapsulation of the hydrophobic dye nile red (NR) into the outer shell of Fe_3O_4 NPs resulted in the dye being dispersed in an aqueous solution with two main advantages.

Firstly, it allowed Fe_3O_4 NPs to be visualised for uptake experiments through confocal microscopy and flow cytometry, as well as acting as a prove of concept that hydrophobic drugs would also successfully reside in the hydrophobic part of the NP shell.

Fe_3O_4-PEG NPs were passively internalised in A2058 melanoma cells, as visualised using confocal microscopy. Reflective light and fluorescence (from NR), showed that the NR was encapsulated in the NP, and both the Fe_3O_4 NPs and NR were internalised in the cell (further evidence of co-localisation of Fe_3O_4 and NR can be seen in the appendix). Other options for visualisation of Fe_3O_4 NPs included attachment of a fluorescent labelled PEG to the surface of the NP. Although this would provide more direct evidence of NP uptake, there was a concern that any modification of the NP surface would affect the reliability of the targeted uptake results.

Flow cytometry confirmed that Fe_3O_4-PEP NPs (targeted NPs) were internalised more readily than Fe_3O_4-PEG NPs (non-targeted NPs) in melanoma cells. Moreover, after blocking MC1R with an excess of α-MSH, we observed that Fe_3O_4-PEP NP uptake was receptor mediated. Further work needs to be done to optimise Fe_3O_4-PEP NP uptake in melanoma cells. Fe_3O_4-PEP NPs contained a theoretical 10% PEG-PEP (compared to PEG alone) attached to the surface. Different ratios of PEG-PEP to PEG need to be explored to provide optimal melanoma targeting without risking the stability of the NP.

Fe_3O_4 NPs have shown to successfully target solid tumours passively by exploiting the enhanced permeability effects *in vivo* (Chertok et al., 2008, Larsen et al., 2009, Yu et al., 2008) and, with the relevant size and the same PEG coating, it is expected that our Fe_3O_4 NPs will also accumulate in a solid tumour. Once in the tumour environment, Fe_3O_4-PEP NPs will be selectively internalised by MC1R

overexpressing melanoma cells. Au NPs, conjugated to the same NDP-MSH peptide as we have used in this study, have shown NPs are selectively delivered to melanoma cells by microscopy (Lu et al., 2009). Mice injected with the Au–NDP-MSH NPs markedly reduced tumour size compared to Au-PEG NPs or saline alone after photothermal ablation (Lu et al., 2009). A major focus for the future work of this project would be to investigate the melanoma-targeting capabilities of Fe_3O_4-PEP NPs a rodent model in order to confirm NP *in vivo* uptake and biodistribution. The substantial work carried out in chapter 5 to confirm the specificity of Fe_3O_4-PEP NPs to melanoma cells would suggest that equally promising results would be seen *in vivo*.

A major concern with studying NP uptake via an overexpressed protein target is the translation from *in vitro* to *in vivo.* Although MC1R appears to be a promising targeted both *in vitro* and *in vivo* (Lu et al., 2009), the literature reports concern over the accurate identification and quantification of MC1R in melanoma cell lines (Roberts et al., 2006). As a result, the receptor blocking experiments in chapter 5 were important to show receptor mediated uptake of Fe_3O_4 NPs. Additionally, chapter 5 reports a methodology for the isolation of melanoma cells from human tissue samples. Successful isolation would allow NPs to be tested as close to clinically relevant melanoma cells as possible. The methodology separated melanoma cells from tissue containing multiple cell types by isolating cells expressing human glial antigen 2 (NG2). These cells were characterised as melanoma cells by Western Immunoblot, which showed that $NG2^+$ cells expressed the melanoma markers MelanA and MC1R. Continuation of this work would aim to show an increase in receptor mediated uptake of Fe_3O_4-PEP NPs in $NG2^+$ cells compared to $NG2^-$ cells; thus confirming that once accumulated within the solid tumour, Fe_3O_4 NPs would preferentially target the melanoma cells rather than the local healthy tissue.

As a result of successful NR encapsulation, the hydrophobic and cytotoxic drug paclitaxel (PTX) was encapsulated by the same method. Although the concentration of PTX was not formally quantified, a dose dependent loss of cell viability in cell lines confirmed that PTX was associated with the Fe_3O_4 NPs. Going forward, PTX, or any other drug encapsulated in the NP, must be accurately quantified. Furthermore, several groups have looked at temperature/pH – dependent drug release from a nanoformulation (Chang et al., 2013, Kamaly et al., 2016, Xing et al., 2012), which is important to considered. The foremost aim for the continued development of our Fe_3O_4 NP system, is the encapsulation of synergist drugs. There are numerous viable drugs that could be encapsulated into our nanosystem that have demonstrated to work effectively as combinational therapies. Amongst these is combining PTX with other, more targeted, drugs. Axitinib, a vascular endothelial growth factor (VEGF) inhibitor, alongside PTX led to an increase in standardised uptake value in patients with stage IV or unresectable stage III melanoma (Algazi et al., 2015). PTX with trametinib improved progression free and overall survival in non-*BRAF* mutated advanced melanoma (Coupe et al., 2015). Other drug combinations have been explored in melanoma patients. Phase III clinical trials have shown an increase in overall survival rate with treatment of dabrafenib and trametinib (Robert et al., 2015), nivolumab and ipilimumab (Larkin et al., 2015), and ipilimumab and dacarbazine (Maio et al., 2015).

In summary, this work has achieved the aim to produce a novel NP that specifically targets melanoma. The Fe_3O_4 NP is stable and safe, as tested by our nanotoxicity protocol, and appears to be preferentially internalised by MC1R expressing melanoma cells. The work presented here provides a solid platform for development of this NP tool as a multimodel drug delivery system and furthers the field of NP treatments for metastatic melanoma. Furthermore, by modification of

targeting moieties and drug choice, the system can be adapted to different mutational status of the cancer. Significantly, the nanoformulation developed here can be used as a future personalised medicine.

6.2 References

Algazi, A. P., Cha, E., Ortiz-Urda, S. M., Mccalmont, T., Bastian, B. C., Hwang, J., Pampaloni, M. H., Behr, S., Chong, K., Cortez, B., Quiroz, A., Coakley, F., Liu, S. & Daud, A. I. 2015. The combination of axitinib followed by paclitaxel/carboplatin yields extended survival in advanced BRAF wild-type melanoma: results of a clinical/correlative prospective phase II clinical trial. *Br J Cancer,* 112**,** 1326-1331.

Cai, M., Mayorov, A. V., Cabello, C., Stankova, M., Trivedi, D. & Hruby, V. J. 2005. Novel 3D pharmacophore of alpha-MSH/gamma-MSH hybrids leads to selective human MC1R and MC3R analogues. *J Med Chem,* 48**,** 1839-48.

Chang, B., Chen, D., Wang, Y., Chen, Y., Jiao, Y., Sha, X. & Yang, W. 2013. Bioresponsive Controlled Drug Release Based on Mesoporous Silica Nanoparticles Coated with Reductively Sheddable Polymer Shell. *Chemistry of Materials,* 25**,** 574-585.

Chen, Y., Hu, X., Sun, J. & Zhou, Q. 2016. Specific nanotoxicity of graphene oxide during zebrafish embryogenesis. *Nanotoxicology,* 10**,** 42-52.

Chertok, B., Moffat, B. A., David, A. E., Yu, F., Bergemann, C., Ross, B. D. & Yang, V. C. 2008. Iron oxide nanoparticles as a drug delivery vehicle for MRI monitored magnetic targeting of brain tumors. *Biomaterials,* 29**,** 487-496.

Coupe, N., Corrie, P., Hategan, M., Larkin, J., Gore, M., Gupta, A., Wise, A., Suter, S., Ciria, C., Love, S., Collins, L. & Middleton, M. R. 2015. PACMEL: A phase 1 dose escalation trial of trametinib (GSK1120212) in combination with paclitaxel. *European Journal of Cancer,* 51**,** 359-366.

Dickson, P. V. & Gershenwald, J. E. 2011. Staging and Prognosis of Cutaneous Melanoma. *Surgical oncology clinics of North America,* 20**,** 1-17.

Fako, V. E. & Furgeson, D. Y. 2009. Zebrafish as a correlative and predictive model for assessing biomaterial nanotoxicity. *Advanced Drug Delivery Reviews,* 61**,** 478-486.

Flaherty, K. T., Hodi, F. S. & Fisher, D. E. 2012. From genes to drugs: targeted strategies for melanoma. *Nature Reviews Cancer,* 12**,** 349-361.

Gamarra, L., Amaro, E., Alves, S., Soga, D., Pontuschka, W. M., Mamani, J., Carneiro, S., Brito, G. E. D. S. & Figueiredo Neto, A. M. 2010. Characterization of the biocompatible magnetic colloid on the basis of Fe3O4 nanoparticles coated with dextran, used as contrast agent in magnetic resonance imaging. *Journal of nanoscience and nanotechnology,* 10**,** 4145-4153.

Hanahan, D. & Weinberg, Robert a. 2011. Hallmarks of Cancer: The Next Generation. *Cell,* 144**,** 646-674.

Jang, S. & Atkins, M. B. 2013. Which drug, and when, for patients with BRAF-mutant melanoma? *The lancet oncology,* 14**,** e60-e69.

Kamaly, N., Yameen, B., Wu, J. & Farokhzad, O. C. 2016. Degradable Controlled-Release Polymers and Polymeric Nanoparticles: Mechanisms of Controlling Drug Release. *Chemical Reviews,* 116**,** 2602-2663.

Larkin, J., Chiarion-Sileni, V., Gonzalez, R., Grob, J. J., Cowey, C. L., Lao, C. D., Schadendorf, D., Dummer, R., Smylie, M., Rutkowski, P., Ferrucci, P. F., Hill, A., Wagstaff, J., Carlino, M. S., Haanen, J. B., Maio, M., Marquez-Rodas, I., Mcarthur, G. A., Ascierto, P. A., Long, G. V., Callahan, M. K., Postow, M. A., Grossmann, K., Sznol, M., Dreno, B., Bastholt, L., Yang, A., Rollin, L. M., Horak, C., Hodi, F. S. & Wolchok, J. D. 2015. Combined Nivolumab and Ipilimumab or Monotherapy in Untreated Melanoma. *New England Journal of Medicine,* 373**,** 23-34.

Larsen, E. K. U., Nielsen, T., Wittenborn, T., Birkedal, H., Vorup-Jensen, T., Jakobsen, M. H., Østergaard, L., Horsman, M. R., Besenbacher, F., Howard, K. A. & Kjems, J. 2009. Size-Dependent Accumulation of PEGylated Silane-Coated Magnetic Iron Oxide Nanoparticles in Murine Tumors. *ACS Nano,* 3**,** 1947-1951.

Lin, L.-S., Cong, Z.-X., Cao, J.-B., Ke, K.-M., Peng, Q.-L., Gao, J., Yang, H.-H., Liu, G. & Chen, X. 2014. Multifunctional Fe3O4@Polydopamine Core–Shell Nanocomposites for Intracellular mRNA Detection and Imaging-Guided Photothermal Therapy. *ACS Nano,* 8**,** 3876-3883.

Lu, W., Xiong, C., Zhang, G., Huang, Q., Zhang, R., Zhang, J. Z. & Li, C. 2009. Targeted photothermal ablation of murine melanomas with melanocyte-stimulating hormone analog-conjugated hollow gold nanospheres. *Clin Cancer Res,* 15**,** 876-86.

Maio, M., Grob, J.-J., Aamdal, S., Bondarenko, I., Robert, C., Thomas, L., Garbe, C., Chiarion-Sileni, V., Testori, A. & Chen, T.-T. 2015. Five-year survival rates for treatment-naive patients with advanced melanoma who received ipilimumab plus dacarbazine in a phase III trial. *Journal of Clinical Oncology***,** JCO. 2014.56. 6018.

Middleton, M. R., Grob, J., Aaronson, N., Fierlbeck, G., Tilgen, W., Seiter, S., Gore, M., Aamdal, S., Cebon, J. & Coates, A. 2000. Randomized phase III study of temozolomide versus dacarbazine in the treatment of patients with advanced metastatic malignant melanoma. *Journal of Clinical Oncology,* 18**,** 158-158.

Nyström, A. M. & Fadeel, B. 2012. Safety assessment of nanomaterials: Implications for nanomedicine. *Journal of Controlled Release,* 161**,** 403-408.

Poulikakos, P. I., Persaud, Y., Janakiraman, M., Kong, X., Ng, C., Moriceau, G., Shi, H., Atefi, M., Titz, B. & Gabay, M. T. 2011. RAF inhibitor resistance is mediated by dimerization of aberrantly spliced BRAF (V600E). *Nature,* 480**,** 387-390.

Robert, C., Karaszewska, B., Schachter, J., Rutkowski, P., Mackiewicz, A., Stroiakovski, D., Lichinitser, M., Dummer, R., Grange, F., Mortier, L., Chiarion-Sileni, V., Drucis, K., Krajsova, I., Hauschild, A., Lorigan, P., Wolter, P., Long, G. V., Flaherty, K., Nathan, P., Ribas, A., Martin, A.-M., Sun, P., Crist, W., Legos, J., Rubin, S. D., Little, S. M. & Schadendorf, D. 2015. Improved Overall Survival in Melanoma with Combined Dabrafenib and Trametinib. *New England Journal of Medicine,* 372**,** 30-39.

Roberts, D. W., Newton, R. A., Beaumont, K. A., Helen Leonard, J. & Sturm, R. A. 2006. Quantitative analysis of MC1R gene expression in human skin cell cultures. *Pigment cell research,* 19**,** 76-89.

Shi, H., Moriceau, G., Kong, X., Lee, M.-K., Lee, H., Koya, R. C., Ng, C., Chodon, T., Scolyer, R. A. & Dahlman, K. B. 2012. Melanoma whole-exome sequencing identifies V600EB-RAF amplification-mediated acquired B-RAF inhibitor resistance. *Nature communications,* 3**,** 724.

Wang, L., Neoh, K., Kang, E., Shuter, B. & Wang, S. C. 2009. Superparamagnetic Hyperbranched Polyglycerol-Grafted Fe3O4 Nanoparticles as a Novel Magnetic Resonance Imaging Contrast Agent: An In Vitro Assessment. *Advanced Functional Materials,* 19**,** 2615-2622.

Webster, C. A., Di Silvio, D., Devarajan, A., Bigini, P., Micotti, E., Giudice, C., Salmona, M., Wheeler, G. N., Sherwood, V. & Bombelli, F. B. 2016. An early developmental vertebrate model for nanomaterial safety: bridging cell-based and mammalian toxicity assessment. *Nanomedicine,* 11**,** 643-656.

Wehmas, L. C., Anders, C., Chess, J., Punnoose, A., Pereira, C. B., Greenwood, J. A. & Tanguay, R. L. 2015. Comparative metal oxide nanoparticle toxicity using embryonic zebrafish. *Toxicology Reports,* 2**,** 702-715.

Xie, J., Xu, C., Kohler, N., Hou, Y. & Sun, S. 2007. Controlled PEGylation of monodisperse Fe3O4 nanoparticles for reduced non-specific uptake by macrophage cells. *Advanced Materials,* 19**,** 3163-3166.

Xing, L., Zheng, H., Cao, Y. & Che, S. 2012. Coordination polymer coated mesoporous silica nanoparticles for pH-responsive drug release. *Advanced Materials,* 24**,** 6433-6437.

Xuan, S., Wang, Y.-X. J., Yu, J. C. & Cham-Fai Leung, K. 2009. Tuning the Grain Size and Particle Size of Superparamagnetic Fe3O4 Microparticles. *Chemistry of Materials,* 21**,** 5079-5087.

Yu, M. K., Jeong, Y. Y., Park, J., Park, S., Kim, J. W., Min, J. J., Kim, K. & Jon, S. 2008. Drug-loaded superparamagnetic iron oxide nanoparticles for combined cancer imaging and therapy in vivo. *Angewandte Chemie International Edition,* 47**,** 5362-5365.

Chapter 7.

Appendix

7.1 Additional *in vitro* NP uptake images

As a member of the project to develop a novel targeted nanotherapy for the treatment of melanoma, Dr Paola Sánchez Moreno confirmed results seen in chapter 5. This section presents confocal images taken by Dr Sánchez Moreno at the *Politecnico di Milano* (currently unpublished). NP uptake was performed using serum free media for A2058 cell line and complete media (including 10 % serum) for B16F10 cells.

a

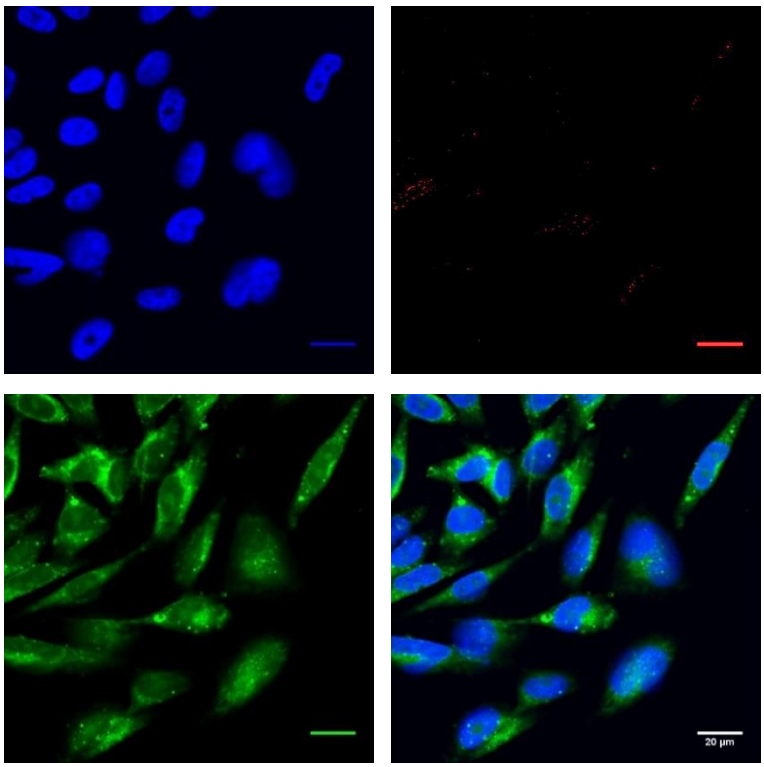

b

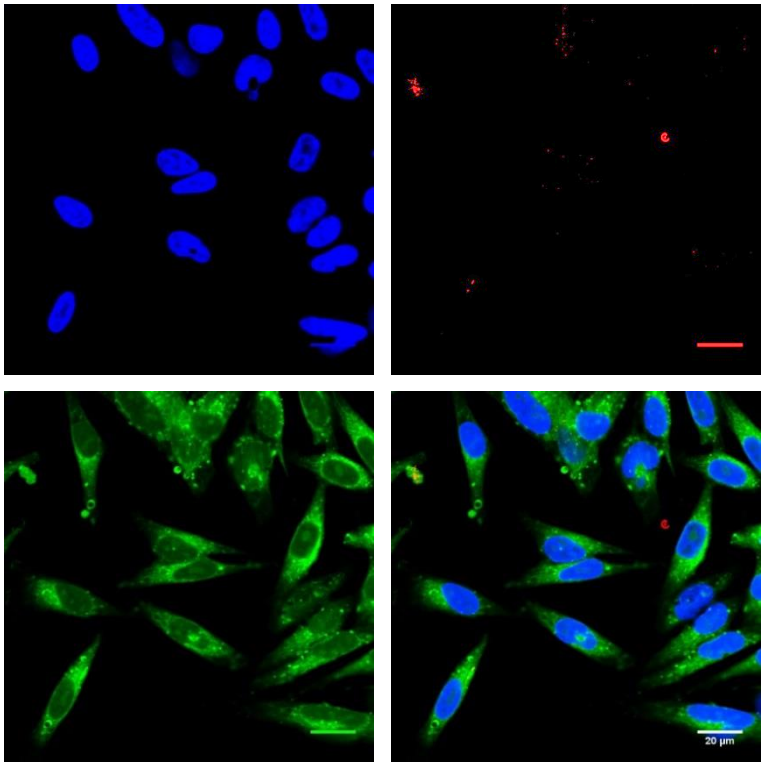

Figure A1 Confocal microscopy of Fe_3O_4-PEG NPs in A2058 melanoma cells. Nucleus stained with Hoechst 33342 (blue), Fe_3O_4 reflective light (red), and cell mask (green). Scale bar size stated. Panel a and b show different representative images.

a

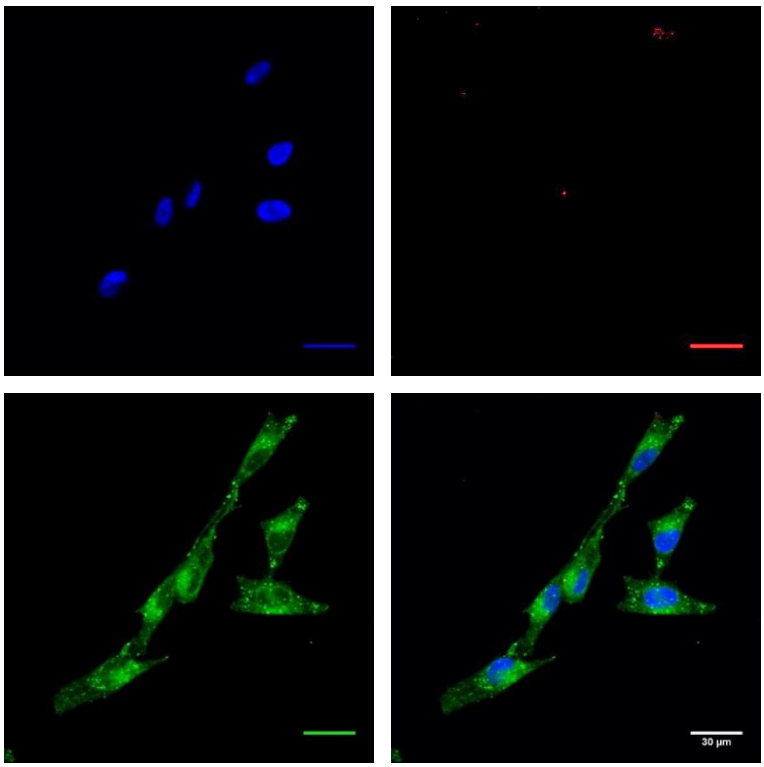

b

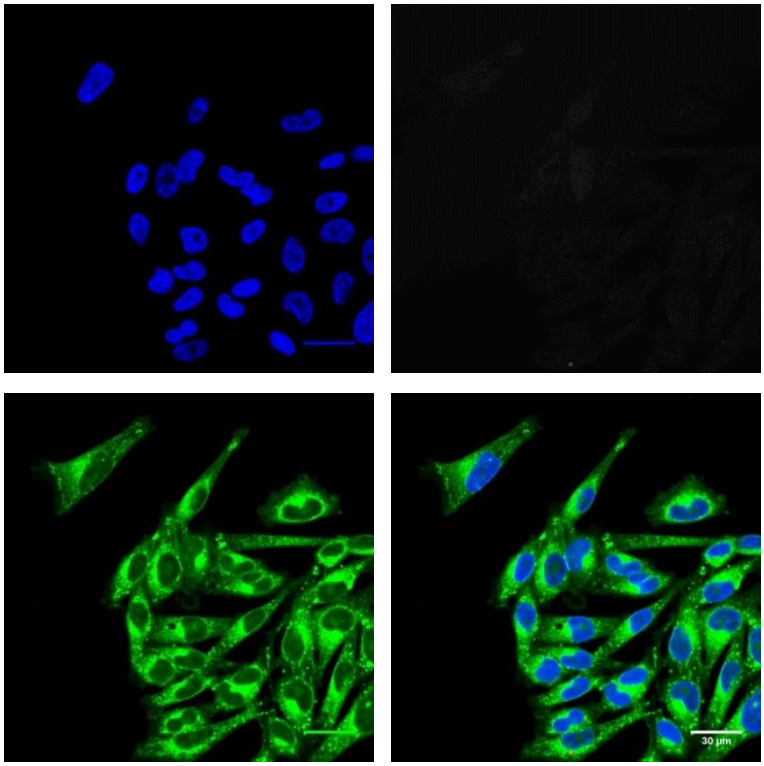

Figure A2 Confocal microscopy of Fe_3O_4-PEG NPs in A2058 melanoma cells pre-blocked with excess peptide. Nucleus stained with Hoechst 33342 (blue), Fe_3O_4 reflective light (red), and cell mask (green). Scale bar size stated. Panel a and b show different representative images.

a

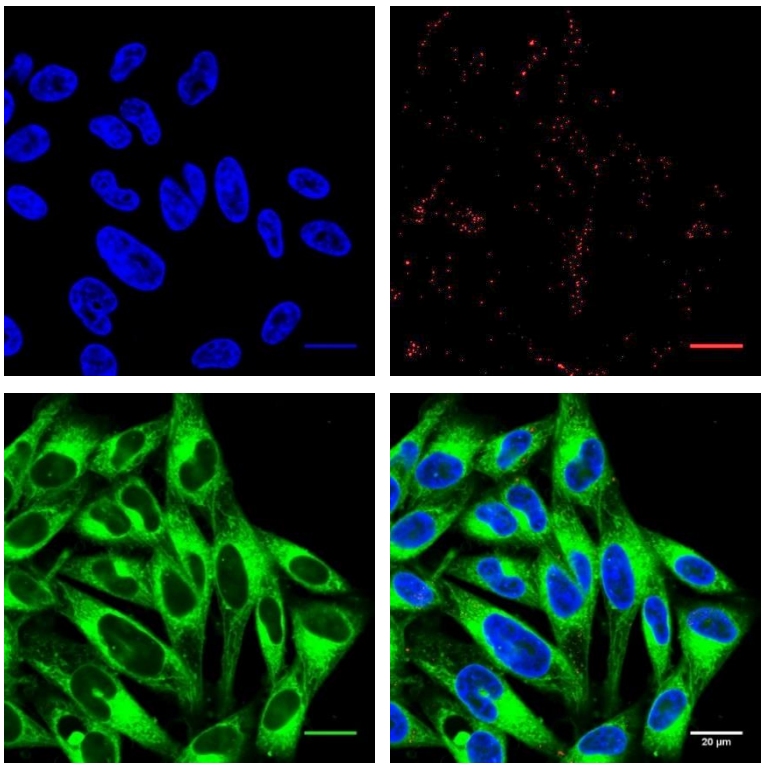

b

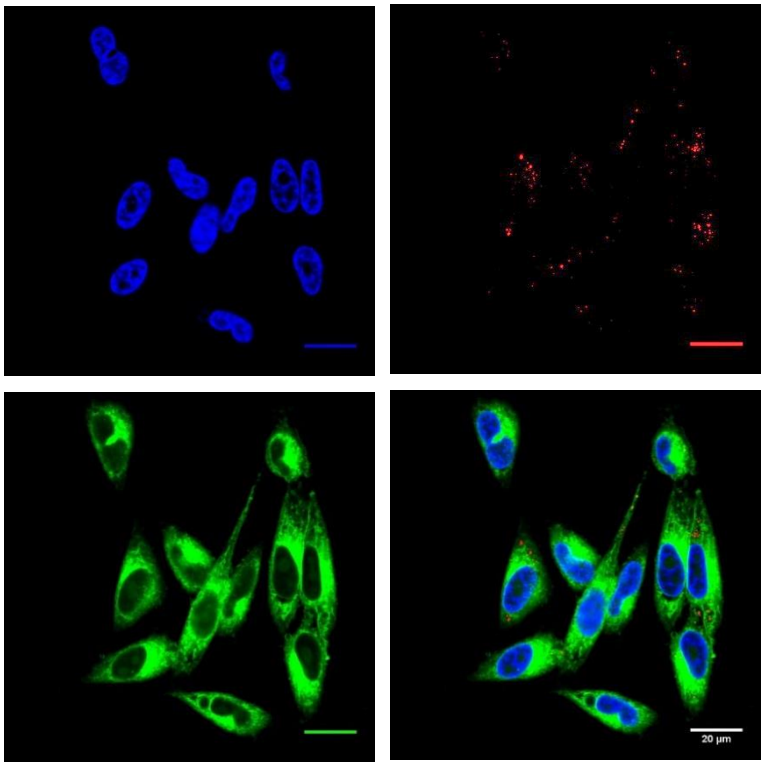

Figure A3 Confocal microscopy of Fe_3O_4-PEP NPs in A2058 melanoma cells. Nucleus stained with Hoechst 33342 (blue), Fe_3O_4 reflective light (red), and cell mask (green). Scale bar size stated. Panel a and b show different representative images.

a

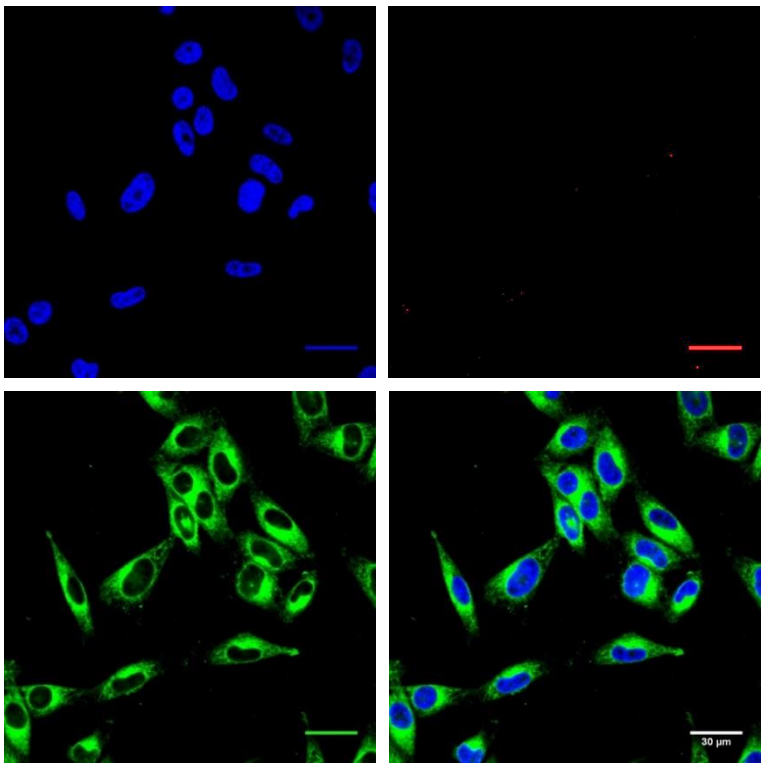

b

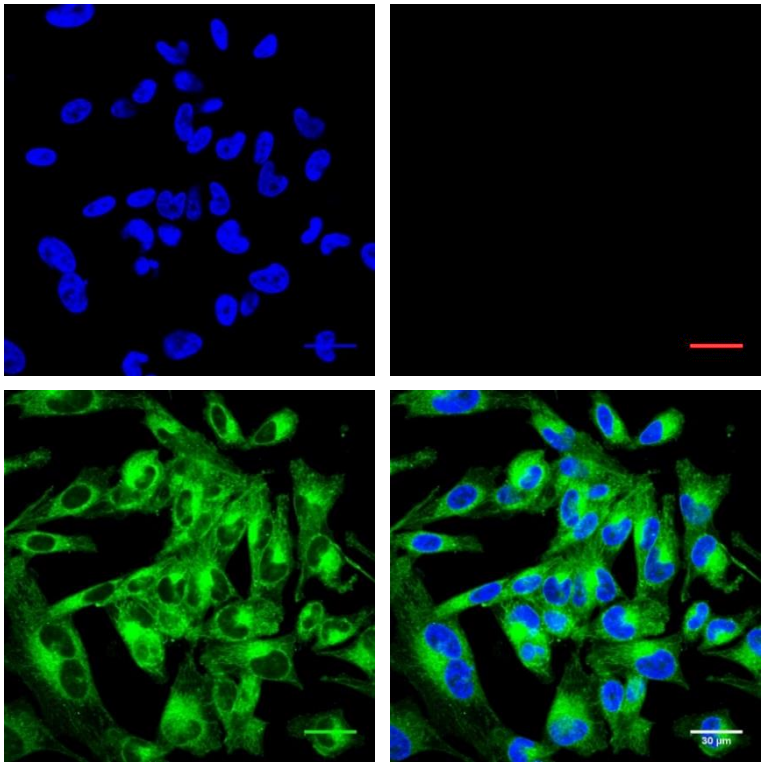

Figure A4 Confocal microscopy of Fe_3O_4-PEP NPs in A2058 melanoma cells pre-blocked with excess peptide. Nucleus stained with Hoechst 33342 (blue), Fe_3O_4 reflective light (red), and cell mask (green). Scale bar size stated. Panel a and b show different representative images.

a

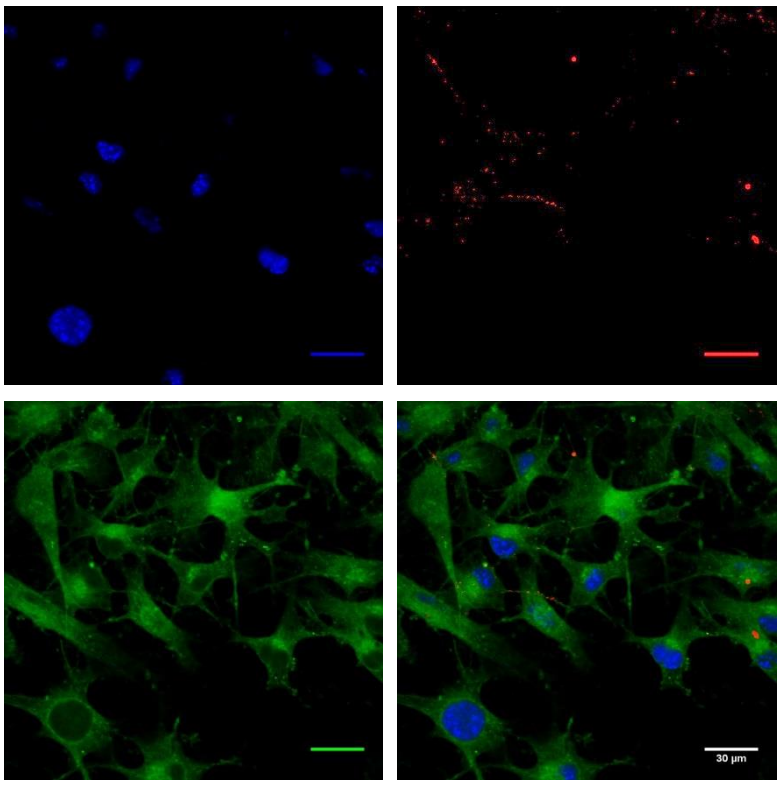

b

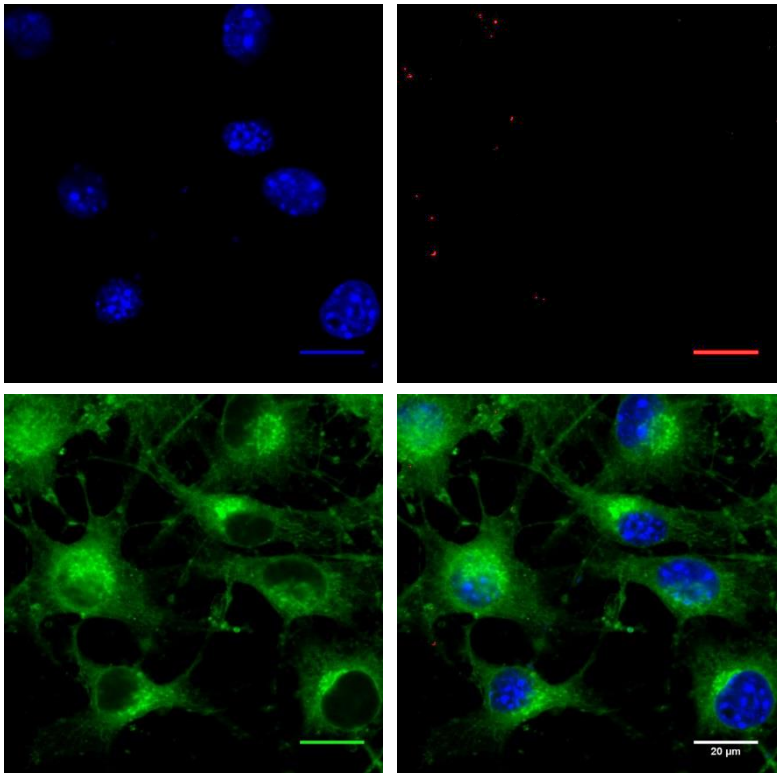

Figure A5 Confocal microscopy of Fe_3O_4-PEG NPs in B16F10 melanoma cells. Nucleus stained with Hoechst 33342 (blue), Fe_3O_4 reflective light (red), and cell mask (green). Scale bar size stated. Panel a and b show different representative images.

a

b

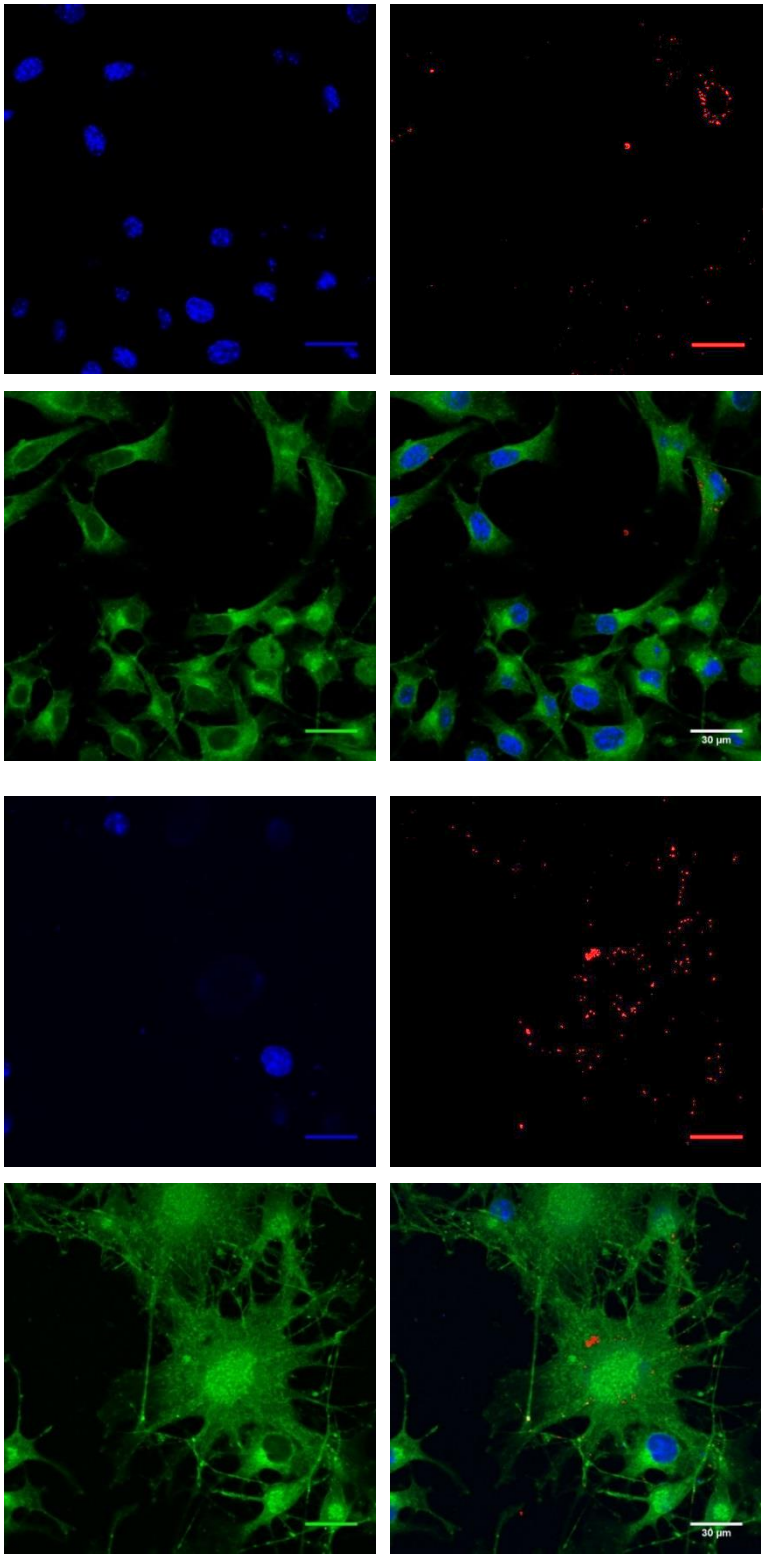

Figure A6 Confocal microscopy of Fe_3O_4-PEG NPs in B16F10 melanoma cells re-blocked with excess peptide. Nucleus stained with Hoechst 33342 (blue), Fe_3O_4 reflective light (red), and cell mask (green). Scale bar size stated. Panel a and b show different representative images.

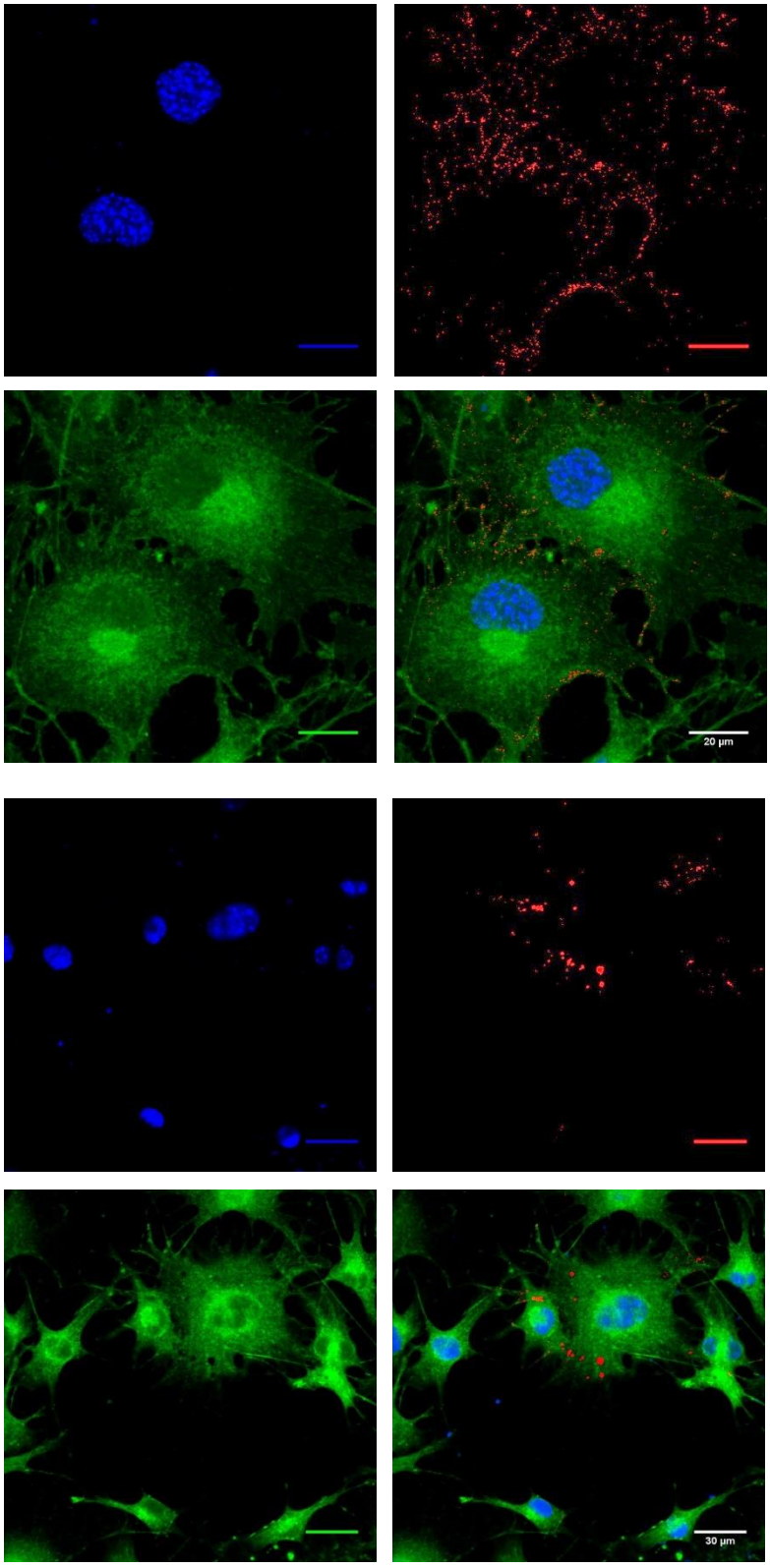

Figure A7 Confocal microscopy of Fe_3O_4-PEP NPs in B16F10 melanoma cells. Nucleus stained with Hoechst 33342 (blue), Fe_3O_4 reflective light (red), and cell mask (green). Scale bar size stated. Panel a and b show different representative images.

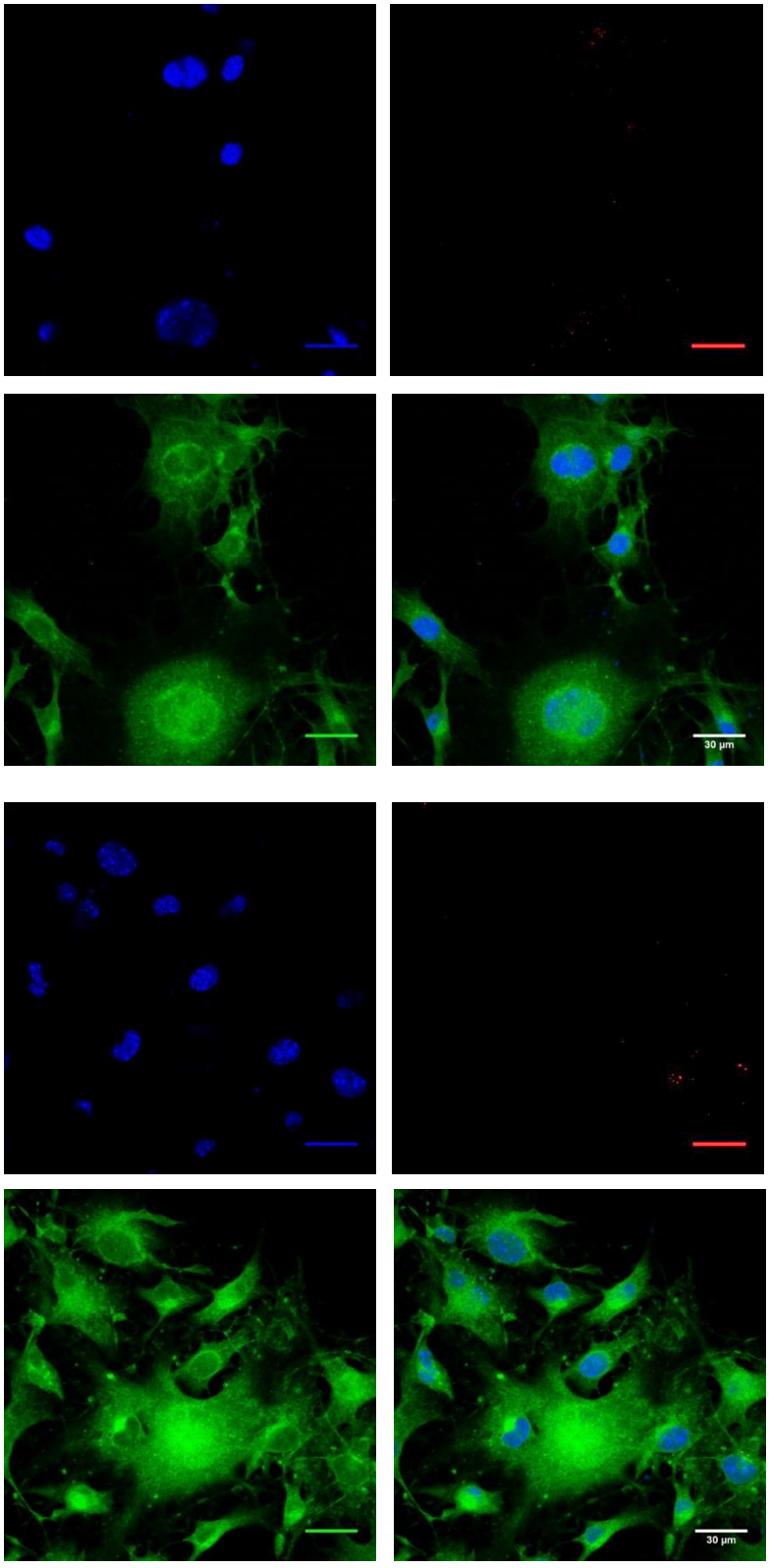

Figure A8 Confocal microscopy of Fe_3O_4-PEG NPs in B16F10 melanoma cells re-blocked with excess peptide. Nucleus stained with Hoechst 33342 (blue), Fe_3O_4 reflective light (red), and cell mask (green). Scale bar size stated. Panel a and b show different representative images.